



EUROPEAN COMMISSION  
JOINT RESEARCH CENTRE

Institute for Environment and Sustainability  
Inland and Marine Waters Unit  
I-21020 Ispra(VA) Italy

Special Publication No. I.02.161

# **Sensitivity of an ocean-atmosphere model of Adriatic Sea to coupling scheme and resolution of the atmospheric model**

Dissertation

zur Erlangung des Doktorgrades  
der Naturwissenschaften im Fachbereich Geowissenschaften  
der Universität Hamburg

vorgelegt von

Srdjan Dobricic

aus

Dubrovnik, Kroatien

Hamburg

2002

**Mission:**

The mission of the Institute for Environment and Sustainability is to provide scientific and technical support to EU strategies for the protection of the environment and sustainable development. Employing an integrated approach to the investigation of the air, water and soil contaminants, its goal are sustainable management of water resources, protection and maintenance of drinking, waters, good functioning of aquatic ecosystems, and good ecological quality of surface waters.

**LEGAL NOTICE**

Neither the European Commission nor any person acting on behalf of the Commission is responsible for the use which might be made of the following information.

A great deal of additional information on the European Union is available on the Internet. It can be accessed through the Europa server (<http://europa.eu.int>)

S.P.I.02.161

©European Communities, 2002

Reproduction is authorized provided the source is acknowledged

*Printed in Italy*

Dr. Steven Eisenreich  
HoU, Inland and marine Waters  
Institute of Environment and Sustainability

Als Dissertation angenommen vom Fachbereich Geowissenschaften  
der Universität Hamburg

auf Grund der Gutachten von Prof. Dr. Jürgen Sündermann  
und PD Dr. Heinke Schlünzen

Hamburg, den 19. November 2002

Prof. Dr. U. Bismayer

Dekan  
des Fachbereichs Geowissenschaften

## Abstract

The main objective of this study is to produce the information about physical properties of the Adriatic Sea using a coupled ocean-atmosphere limited-area model, and to assess its sensitivity to the coupling scheme in comparison with its sensitivity to changes in the horizontal resolution of the atmospheric model. The oceanographic model outputs were validated with good agreement using satellite observations and climatological analyses; while the validation of atmospheric model outputs reveals good agreement with climatological calculations and estimates and with measurements at meteorological stations. The sensitivity analysis demonstrates that the coupled model gives a superior simulation of oceanographic parameters, in particular close to the sea surface, in comparison with the one-way forcing, even with a high-resolution atmospheric model. On the other hand, the improvement of the simulation of atmospheric parameters at coastal meteorological stations due to the coupling scheme is less significant.



# Contents

<b>1</b>	<b>Introduction</b>	<b>5</b>
1.1	Geography, climatology from data and previous modelling studies of the Adriatic Sea . . . . .	5
1.2	Motivation for this study . . . . .	10
<b>2</b>	<b>Description of the coupled model</b>	<b>14</b>
2.1	Ocean model . . . . .	14
2.1.1	Main model equations . . . . .	14
2.1.2	Numerical implementation . . . . .	15
2.2	Atmospheric model . . . . .	22
2.2.1	Main model equations . . . . .	22
2.2.2	Numerical schemes . . . . .	24
2.3	Coupling scheme . . . . .	31
<b>3</b>	<b>Model set-up</b>	<b>33</b>
3.1	Ocean model set-up . . . . .	33
3.1.1	Horizontal and vertical resolution, time step and bottom topography . . . . .	33
3.1.2	River runoff . . . . .	34
3.1.3	Initial and boundary conditions . . . . .	37
3.2	Atmospheric model set-up . . . . .	39
3.2.1	Horizontal and vertical resolution, topography and land-sea mask . . . . .	39
3.2.2	Initial and boundary data . . . . .	41
3.2.3	Surface fields . . . . .	42
3.3	Control experiment set-up . . . . .	43

<b>4</b>	<b>Discussion and validation of model results</b>	<b>46</b>
4.1	Discussion and validation of oceanographic model results . . . . .	46
4.2	Discussion and validation of atmospheric model results . . . . .	60
<b>5</b>	<b>Sensitivity experiments</b>	<b>85</b>
5.1	Differences between experiments . . . . .	85
5.2	Sensitivity of oceanographic outputs . . . . .	86
5.2.1	Surface temperature . . . . .	86
5.2.2	Surface currents . . . . .	110
5.2.3	Total transport stream function . . . . .	123
5.2.4	Temperature at 100m depth . . . . .	133
5.3	Sensitivity of atmospheric outputs . . . . .	136
5.3.1	Temperature at 2m . . . . .	136
5.3.2	Sea level pressure . . . . .	139
5.3.3	Surface wind . . . . .	147
<b>6</b>	<b>Summary and conclusions</b>	<b>151</b>

# Chapter 1

## Introduction

The diverse economic activities in the Adriatic Sea, which include industry, fishing, transport and tourism, and the high density of the population along its coasts, require the assessment of the oceanographic environmental conditions with the highest possible precision. For instance, oceanographic environmental conditions determine the eutrophication which is the main environmental problem in the Adriatic Sea (EEA 1999). Furthermore, in the Adriatic Sea physical processes significantly influence biogeochemical processes (Zavaratelli et al. 2001), and the description of high fluxes of material in a complex coastal area like the Adriatic Sea requires additional high quality information about the interaction between the sea and the atmosphere.

### 1.1 Geography, climatology from data and previous modelling studies of the Adriatic Sea

The Adriatic Sea is a semi-enclosed sea connected with the rest of the Mediterranean through the Otranto Channel at the south. It has the elongated shape in the north-west direction starting from the Otranto Channel at the south-east. The length of the Adriatic Sea is approximately 700km and its mean width is approximately 200km. Its bottom topography is displayed in Fig.1.1. The north part of the Adriatic Sea is shallow with the average depth of 30m. The bottom has a gentle slope between the very shallow northern part and the central part with the 200m deep Pomo Depression. Further to the south-east the central part is divided from the southern part by the 120m deep Palagruza Sill. The

Southern Adriatic Depression with the maximum depth of approximately 1200m is connected to the Mediterranean by the 100km wide and approximately 500m deep Otranto Channel. While the western coast of the Adriatic is shallow and sandy, the eastern coast is rocky with the larger bottom slope along the coast.

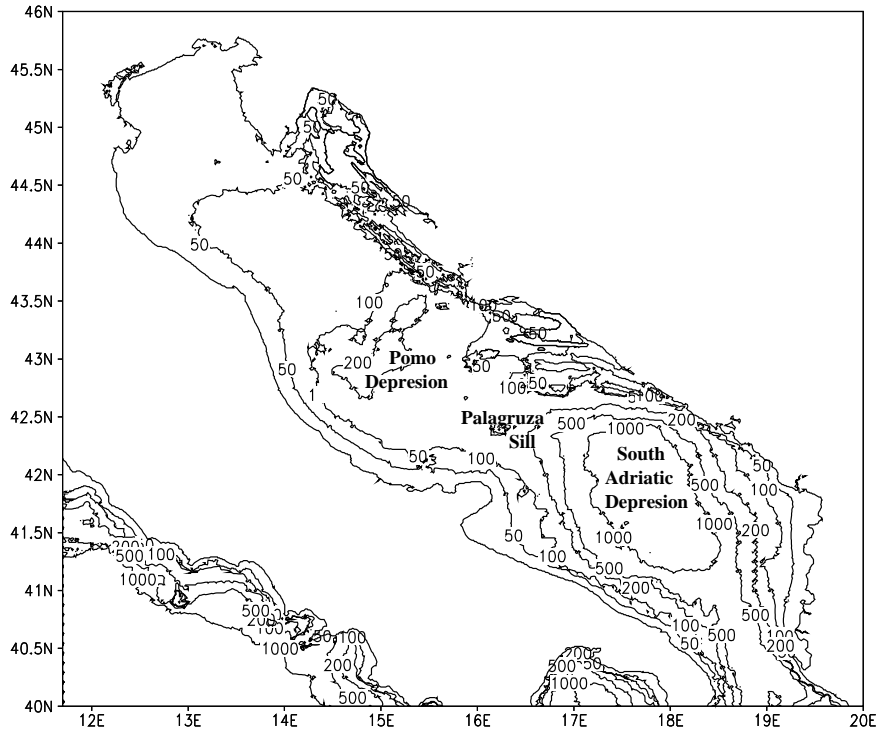


Figure 1.1: The bottom topography (depth in m) of the Adriatic Sea.

The Adriatic Sea is surrounded by the Apennines on the west, by the Alps on the north and by the Julian Alps and the Dinaric Alps on the east (Fig.1.2). This complex topographic surrounding determines a complicated and orography controlled wind field over the Adriatic Sea. The most prominent winds are the north-east wind (Bora), and the south-east wind (Scirocco). The Bora wind is a strong episodic downslope katabatic wind blowing from the eastern coast towards the sea. It is strongly channelled by mountain ridges and valleys along the eastern coast. On the other hand, the Scirocco wind blows almost uniformly over the Adriatic Sea. However, due to the mountain blocking by the Dinaric Alps and the Julian Alps at the eastern coast, the maximum of the wind velocity is close to the eastern coast in the middle of the Adriatic Sea. Furthermore, due to the blocking by the Alps on the north, in the Northern Adriatic the south-east direction of the Scirocco wind may change into the north-east direction. At the end of summer

the north-western wind (Maestral) blows along the eastern coast.

Several rivers discharge into the Adriatic. On the eastern coast the river inflow is mostly spread along its southern part in Albania, while on the western coast major rivers are in the northern part of basin. The largest river is Po with the river mouth at the north-western edge of the Adriatic Sea (Fig.1.2).



Figure 1.2: The topography surrounding the Adriatic.

Artegianni et al. (1997a,1997b) performed an analysis of seasonal climatological physical properties of the Adriatic Sea, based on historical data sets. In the first part of their study Artegianni et al. (1997a) analysed the heat and momentum fluxes by arbitrarily combining several historical atmospheric data sets and using a bulk formula selected by Castellari et al. (1998). They calculated the climatological yearly averaged heat loss in the Adriatic of about  $-19Wm^{-2}$ . This value is in relatively good agreement with the climatological heat loss of  $-22Wm^{-2}$  previously estimated by May (1986). In Artegianni et al. (1997a) the maximum heat loss is along the western coast during winter-spring months. To achieve the climatologically steady state, in which the temperature does not deviate from the climatological mean, the large annual surface cooling in the Adriatic Sea requires the inflow of the relatively warm water through the Otranto Strait

from the south.

In another study Maggiore et al. (1998) analysed the heat fluxes in the Adriatic Sea using ECMWF analyses in a four-year period (1991-1994). Their calculation results in a similar four-year mean heat flux of  $-17\text{Wm}^{-2}$ , but there is a relatively large oscillation in yearly averaged values, which change between the yearly averaged heat loss of  $-26\text{Wm}^{-2}$  in 1993 and the yearly averaged heat gain of  $4\text{Wm}^{-2}$  in 1994.

Both studies, Artegiani et al. (1997a) and Maggiore et al. (1998), show a large seasonal change of the heat flux over the Adriatic Sea, governed by the change in the magnitude of the short wave radiation. The Adriatic Sea loses heat from October until March with the maximum heat loss in December and it gains heat during the rest of the year with the maximum heat gain in June. Maggiore et al. (1998) found that the major change of the yearly averaged value between single years was the consequence of the large yearly change in the sensible heat and the latent heat components of the total heat flux.

In the Adriatic Sea the river runoff and the precipitation exceed the evaporation, resulting in the positive fresh water flux. Zore-Armanda (1969) estimated the yearly averaged fresh water flux at approximately  $0.5m$ , while Raicich (1996) estimated that the yearly averaged fresh water flux was between  $0.65m$  and  $1.1m$ . Furthermore, Raicich (1996) estimated that the yearly river runoff was  $1.17m$  and that the yearly averaged evaporation and the yearly averaged precipitation had similar magnitudes. Artegiani et al. (1997a) also found a small yearly averaged difference between the evaporation and the precipitation of  $0.15m$ . On the other hand, in the calculation by Maggiore et al. (1998) the yearly averaged difference between the evaporation and the precipitation is  $0.88m$ , resulting in a large reduction in the estimate for the yearly averaged fresh water flux in the Adriatic. Large differences between the fresh water fluxes calculated in different studies are the consequence of large differences between the latent heat fluxes and the precipitation data originating from different meteorological data sets.

We may define three main water masses in the Adriatic Sea: surface, intermediate and deep (Artegiani et al. 1997b). The hydrological characteristics of the surface water mass are mainly defined by the positive fresh water flux at the surface, the hydrological characteristics of the intermediate water are mainly defined by the inflow of the Levantine intermediate water and those of the deep water by the dense water formation and the deep circulation.

The circulation in the Adriatic Sea is mainly cyclonic (Zore 1956, Buljan and

Zore-Armanda 1976, Artegiani et al. 1997b, Poulain 2001) with the northward flow along the eastern coast and the southward return flow along the western coast. The circulation creates three cyclonic gyres with centres in the southern, in the central and in the northern section (e.g. Artegiani et al. 1997b). The most pronounced surface current is the Western Adriatic Current starting from the Po river mouth. In winter it is confined to the coast and it is limited to the North Adriatic, while in summer it is the most intense spreading more offshore and towards the South Adriatic. The South-eastern Adriatic Current is the most intense in autumn. The position of main gyres and surface currents is sketched in Fig.1.3.

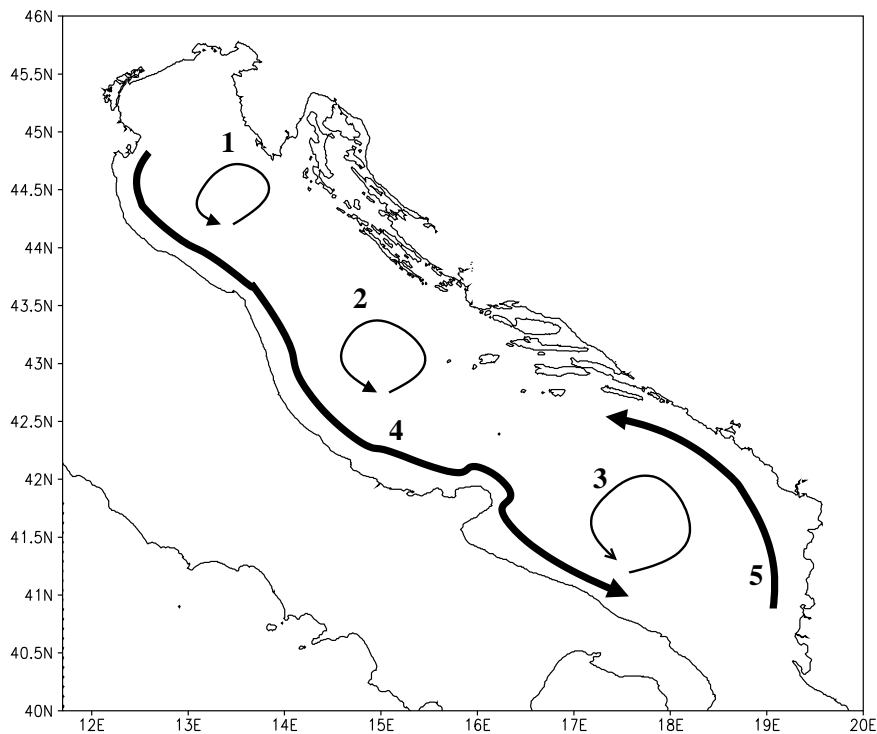


Figure 1.3: Main features of the surface circulation. Northern, central and southern cyclonic gyres are labelled 1, 2 and 3. The Western Adriatic Current is labelled 4 and the South-eastern Adriatic Current is labelled 5.

Modelling studies of the circulation in the Adriatic Sea started by Malanotte-Rizzoli and Bergamasco (1983), who found that during winter both thermohaline and wind forcing influenced the circulation in the North Adriatic. Several process studies have investigated the impact of the most dominant winds on the circulation in the Adriatic Sea using numerical models (Schimpf et al. 1992, Bone

1993, Kuzmic 1991, Orlic et al. 1994, Bergamasco and Gacic 1996). Vested et al. (1996) applied a process study with a numerical model, to investigate the dense water formation process in the North Adriatic, and Kourafalou (1999) made a process study with an ocean model to investigate the spreading of the Po river plume under the influence of the most dominant winds. The relative importance of the influence of the wind and of the river inflow on the winter circulation in the North Adriatic is investigated in a process study by Zavaratelli et al. (1999) and in a case study by Beg-Paklar et al. (2001).

In a modelling study Zavaratelli et al. (2002) performed simulations of the Adriatic Sea circulation in diagnostic and prognostic modes, using realistic heat flux and wind stress forcing fields. Their study confirmed the importance of both the barotropic and baroclinic forcing on the surface circulation in the Adriatic. Furthermore, it emphasised the importance of the atmospheric forcing which strongly influences the large spatial and temporal variability of the circulation.

## 1.2 Motivation for this study

To model the ocean circulation in coastal areas surrounded by the complex topography like the Adriatic Sea, it is necessary to provide the meteorological forcing which accounts for the complex influence of local conditions and which reflects the high temporal and spatial variability of forcing fields. However, the traditional approach is often limited to the use of the available meteorological forcing data from relatively coarse resolution global circulation models (e.g. Zavaratelli et al. 2002). The highest horizontal resolution of surface fields available from global circulation models is approximately 50 kilometres in the case of the re-analyses and the analyses originating from the T213 ECMWF model, but the typical horizontal resolution of these models for the Adriatic Sea is of the order of 100 kilometres. These typical resolutions of global data sets may be insufficient to accurately describe all important processes that govern the circulation in coastal areas.

One possibility to improve the accuracy of the ocean model simulation is to apply atmospheric limited area models with the high horizontal resolution in the area surrounding the sea (e.g. Horton et al. 1997). These models may have lateral boundary conditions calculated by global circulation models with coarser horizontal resolution. In this way it is possible to provide meteorological forcing

data sets with locally higher temporal and spatial resolutions than those available from global data sets.

However, even with this improvement the meteorological forcing is calculated using the sea surface temperature which is different from that which is later simulated by the ocean model. The heat flux computed by the atmospheric model is completely independent of the sea surface temperature simulated by the ocean model. A possible consequence of this inaccuracy in the computation of surface heat and momentum fluxes is that the temperature and the circulation in the ocean model may deviate from the realistic value. One solution for this problem is to add an artificial term in the prognostic equation for the temperature in order to relax the surface temperature towards the climatological value (e.g. Oberhuber 1988). However, in areas with the strong advection of temperature at the surface of the ocean, the inclusion of the relaxation term may introduce large errors (Killworth et al. 2000).

Another solution and the step forward in the oceanographic simulation in coastal areas may be the interactive simulation by directly coupling the ocean and the limited area atmospheric model. In this case the ocean-atmosphere interaction is explicitly simulated by the coupled model, and surface heat and momentum fluxes are calculated using the sea surface temperature simulated by the ocean model and atmospheric parameters simulated by the atmospheric model. In this way all simulated parameters are dependent on each other through common physical parameterisations.

Relatively coarse resolution global coupled ocean-atmosphere models have become an important tool for global climate simulations. One of the major problems appearing in global climate simulations with coupled ocean-atmosphere models is the occurrence of large climate drifts during the simulation of the current climate. Climate drifts have been alleviated by the use of flux adjustments (e.g. Sausen et al. 1988, Manabe et al. 1991). Recently, several models have demonstrated the ability to produce present climate simulations without flux adjustments, which do not diverge from the observed climate (e.g. Barthelet et al. 1998, Boville and Gent 1998). The main reason for the improvement of the simulation quality is the increased horizontal resolution of global coupled models and the improved parameterisation schemes.

On the other hand, in simulations of the circulation in coastal areas, limited area coupled ocean-atmosphere models have been used much less frequently. Hordur (1997) coupled a non-hydrostatic atmospheric model with a coastal ocean

model. Lionello and Malguzzi (1997) coupled the BOLAM atmospheric limited area model with the Princeton Ocean Model to perform forecasts in the Mediterranean. In Nitz (1998) the METRAS non-hydrostatic atmospheric model was coupled with the German Bight oceanographic model to study the sensitivity of surface fluxes and their influence on the oceanographic simulation to the coupling scheme. Bender et al. (2000) and Bao et al. (2000) performed hurricane simulations using high resolution coupled ocean-atmosphere models. In Dobricic et al. (1998) a coupled limited area model was developed using the ISPRAMIX ocean model and it was tested in the Adriatic in the simulation of the high sea level in Venice with the coastal flooding. A common feature of all simulations with high resolution coupled limited area ocean-atmosphere models in coastal areas is that they are performed only for a relatively short simulation period which is usually only several hours or days long. The main reason for performing only short term simulations is that the use of the high horizontal resolution atmospheric model typically requires very fast computers.

Contrary to previous studies with high resolution limited area coupled models, the main objective of this study is to investigate the influence of the coupling method on the simulation of oceanographic fields in the Adriatic Sea for the longer simulation time period of one year. In this way, using statistical analyses, it may become possible to more precisely quantify and better understand the influence of the interactive ocean-atmosphere coupling on the improvement in the simulation result.

In the study, the outputs of simulated fields originating from the coupled model simulation in the Adriatic Sea will be validated and statistically compared with outputs originating from simulations by the one-way forcing. The improvements in accuracy of the simulation obtained by the coupled model will be compared with the improvements obtained only by the use of the higher horizontal resolution in the atmospheric model.

The coupled model is described in Chapter 2., starting with the description of model equations and numerical schemes used in the oceanographic model and in the atmospheric model. The description of the coupling scheme is given in the last section of Chapter 2.

The model set-up in the Adriatic Sea is described in Chapter 3. It gives information on the horizontal and on the vertical resolution of the oceanographic model, on the low and on the high horizontal resolution atmospheric model set-up and on initial and boundary data sets. One subsection describes the method used

to calculate the fresh water inflow from rivers that discharge into the Adriatic Sea. The last section of Chapter 3. contains the description of the calculation of surface heat and momentum fluxes from ECMWF reanalyses used in the control experiment.

In Chapter 4. oceanographic outputs of the coupled model are compared with measurements, climatological data and with results of other modelling studies in the Adriatic. Surface heat fluxes are compared with other calculations and climatological estimates. Furthermore, measurements at several meteorological stations along the coast of the Adriatic Sea are used to validate meteorological parameters simulated by the atmospheric model.

In Chapter 5. oceanographic and atmospheric outputs of the model experiments are compared with observations and climatological data to evaluate the sensitivity of the model results to the use of the fully coupled scheme to compute surface heat fluxes and the wind stress.

# Chapter 2

## Description of the coupled model

### 2.1 Ocean model

#### 2.1.1 Main model equations

The ISPRAMIX ocean model is a free surface model developed for coastal applications. Initially, it has been partially based on the model of Backhaus (1985) and the model of Nihoul (1986). Its development and numerical schemes are described in Eifler and Schimpf (1992) and Demirov et al. (1998). The main model equations are based on the hydrostatic and Boussinesq approximations:

$$\frac{\partial \mathbf{v}}{\partial t} + \nabla(\mathbf{v} \cdot \mathbf{v}) + \frac{\partial}{\partial z}(w\mathbf{v}) + f\mathbf{k} \times \mathbf{v} = \frac{1}{\rho_0}\nabla p + \frac{\partial}{\partial z}\left(\varepsilon_v^m \frac{\partial}{\partial z}\mathbf{v}\right) + \mathbf{F}_v \quad (2.1)$$

$$\frac{\partial p}{\partial z} = -g\rho \quad (2.2)$$

$$\nabla \cdot \mathbf{v} + \frac{\partial w}{\partial z} = 0 \quad (2.3)$$

$$\frac{\partial T}{\partial t} + \nabla \cdot (\mathbf{v}T) + \frac{\partial}{\partial z}(wT) = \frac{\partial}{\partial z}\left(\varepsilon_v^h \frac{\partial T}{\partial z}\right) + \nabla \cdot (\varepsilon_h^h \nabla T) \quad (2.4)$$

$$\frac{\partial S}{\partial t} + \nabla \cdot (\mathbf{v}S) + \frac{\partial}{\partial z}(wS) = \frac{\partial}{\partial z}\left(\varepsilon_v^h \frac{\partial S}{\partial z}\right) + \nabla \cdot (\varepsilon_h^h \nabla S) \quad (2.5)$$

$$\rho = \rho(T, S, p). \quad (2.6)$$

In (2.1-2.6)  $\mathbf{v}$  is the horizontal velocity vector,  $w$  is the vertical velocity component,  $p$  is the pressure,  $\rho$  is the density,  $\rho_0$  is the reference density,  $T$  is the potential temperature,  $S$  is the salinity,  $\varepsilon_v^m$  and  $\varepsilon_v^h$  are the vertical turbulent

viscosity and the vertical turbulent diffusivity,  $\varepsilon_h^h$  is the horizontal turbulent diffusivity,  $\mathbf{F}_v$  is the horizontal viscosity and  $I$  is the short wave solar radiation. The equation of state (2.6) is the UNESCO formula (UNESCO 1981). At the bottom and at the coast the no-slip boundary condition is specified for the velocity, and the no-flux boundary condition for tracers  $T$  and  $S$ . Fluxes of the momentum, the heat and the salt at the surface are:

$$\varepsilon_v^m \frac{\partial \mathbf{v}}{\partial z} = -\frac{\tau_s}{\rho_0}, \quad \varepsilon_v^h \frac{\partial T}{\partial z} = -\frac{Q_s^h}{C_p \rho_0} \quad \text{and} \quad \varepsilon_v^h \frac{\partial S}{\partial z} = -Q_s^S, \quad (2.7)$$

where  $\tau_s$  is the wind stress.

## 2.1.2 Numerical implementation

### *Space discretisation*

It is assumed that the top surface follows the free sea surface and that all numerical cells have variable vertical thickness due to the sea surface movement. The vertical coordinate is defined by:

$$\sigma = \left(1 + \frac{\eta}{H}\right)z, \quad (2.8)$$

where  $\sigma$  is the vertical coordinate,  $\eta$  is the surface elevation and  $H$  is the depth of the ocean corresponding to the zero surface elevation. Assuming that the bottom is composed of the topography represented by boxes, the relation between the vertical velocity  $\dot{\sigma}$  in the  $\sigma$  coordinate system and the vertical velocity  $w$  in the  $z$  coordinate system is given by:

$$\dot{\sigma} = \left(1 + \frac{\eta}{H}\right)w + \dot{\eta} \frac{z}{H}. \quad (2.9)$$

The vertical coordinate is schematically displayed in Fig.2.1.

Model equations are discretised using the C-grid in horizontal. Discretised equations are:

$$\delta_t(hu) - hf\bar{v}^{\lambda\phi} - \varphi^u = h\delta_z(\varepsilon_v^m \delta_z u) \quad (2.10)$$

$$\delta_t(hv) + hf\bar{u}^{\lambda\phi} - \varphi^v = h\delta_z(\varepsilon_v^m \delta_z v) \quad (2.11)$$

$$\delta_t(h) + \delta_\lambda(uh) + \frac{1}{\cos\phi} \delta_\phi(vh \cos\phi) + h\delta_z \tilde{w} = 0, \quad (2.12)$$

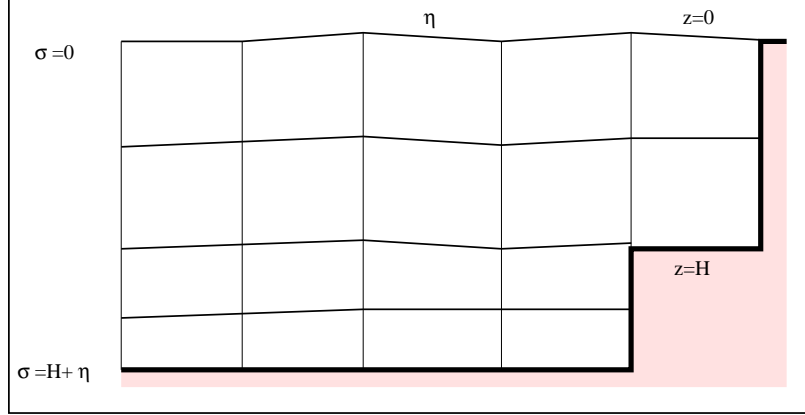


Figure 2.1: The sketch of the model vertical coordinate.

$$\delta_t(hT) + \mathcal{L}(T) - h\nabla(\varepsilon_h^h \nabla T) = h\delta_z(\varepsilon_v^h \delta_z T) \quad (2.13)$$

$$\delta_t(hS) + \mathcal{L}(S) - h\nabla(\varepsilon_h^h \nabla S) = h\delta_z(\varepsilon_v^h \delta_z S), \quad (2.14)$$

where

$$\varphi^u = -\mathcal{L}(u) + \frac{huv \tan \phi}{a} - \delta_\lambda P + hF^u, \quad (2.15)$$

$$\varphi^v = -\mathcal{L}(v) + \frac{hu^2 \tan \phi}{a} - \delta_\phi P + hF^v, \quad (2.16)$$

$$\tilde{w} = w + \delta_t \tilde{z} + u\delta_\lambda \tilde{z} + \frac{v}{\cos \phi} \delta_\phi(\tilde{z} \cos \phi), \quad (2.17)$$

$$\mathcal{L}(\alpha) = \delta_\lambda(hu\alpha) + \frac{1}{\cos \phi} \delta_\phi(hu\alpha \cos \phi) + h\delta_z(\tilde{w}\alpha) \quad (2.18)$$

In (2.10-2.18)  $\lambda$  and  $\phi$  are the longitude and the latitude,  $a$  is the earth radius,  $h$  is the model layer thickness and  $\delta$  indicates the finite differencing operator.

The horizontal advection of scalars may be calculated using the first order accurate upwind scheme, the central differencing scheme, the third order accurate upwind scheme (Leonard 1979) and the MPDATA scheme (Smolarkiewicz and Grabowski 1990). The momentum advection may be calculated using the energy conservative central differencing scheme or the first order accurate upwind scheme.

### ***Time integration***

The integration with time of momentum equations and the continuity equation is performed by splitting the calculation into the two-dimensional calculation

of the external waves from vertically integrated momentum and continuity equations using the micro (short) time step and into the three-dimensional prognostic calculation of momentum components and tracers using the macro (long) time step.

The two-dimensional calculation is made using the explicit forward-backward time stepping for gravity waves with the micro time step limited by the speed of gravity waves in the deepest point of the model. At each micro time step the Coriolis term is calculated using an implicit scheme for the evaluation of horizontally averaged vertically integrated momentum components (Backhaus 1985). The vertical integral of advection and viscous terms is calculated at the beginning of the marching by the micro time step, and it is kept constant during the macro time step.

The advection and the horizontal diffusion are calculated using the forward in time scheme and the vertical diffusion is calculated using the implicit integration with time.

### ***Boundary conditions***

At internal coastal boundaries the zero gradient boundary condition is used for tracers and surface elevation. The momentum component perpendicular to the coast is set to zero at the coastal boundary, and this value is used in the calculation of the horizontal diffusion.

At the open boundary the Orlanski radiational boundary condition is applied for the surface elevation and vertically integrated velocity components (Demirov et al. 1999), and for tracers there is a possibility to chose between the inflow-outflow condition, the zero gradient condition and the relaxation towards the boundary value for tracers.

### ***Parameterisation of vertical mixing***

The turbulence model used in ISPRAMIX is based on the prognostic equation for the turbulent kinetic energy  $K$  and relations for the turbulent length scale  $L$ , the vertical viscosity  $\varepsilon_v^m$  and the vertical diffusivity  $\varepsilon_v^h$ . The model is developed by Eifler (1993) and Eifler et al. (1991) starting from the model of Nihoul (1986).

The prognostic equation for the turbulent kinetic energy is:

$$\begin{aligned} \frac{\partial K}{\partial t} + \nabla \cdot (\mathbf{v}K) + \frac{\partial}{\partial z}(wK) - \frac{\partial}{\partial z} \left( \varepsilon_v^m \frac{\partial K}{\partial z} \right) - \nabla \cdot (\varepsilon_v^h \nabla K) = \\ \varepsilon_v^m \left[ \left( \frac{\partial u}{\partial z} \right)^2 + \left( \frac{\partial v}{\partial z} \right)^2 \right] + \frac{g}{\rho_0} \varepsilon_v^m \frac{\partial \rho}{\partial z} - DIS. \end{aligned} \quad (2.19)$$

On the right side of 2.19, the first term represents the production of the turbulent kinetic energy by the velocity shear, the second term represents the enhancement or the dumping of the turbulent kinetic energy by the buoyancy, and the third term represents the dissipation of the turbulent kinetic energy. The no-flux boundary condition is used for  $K$  at internal boundaries. At open boundaries the zero gradient boundary condition is used for  $K$ .

The turbulent viscosity and the turbulent dissipation are parameterised using a Kolmogorov-Prandtl type relation (Kolmogorov 1942, Prandtl 1945):

$$\varepsilon_v^m = c_\varepsilon L K^{1/2}, \quad (2.20)$$

$$\varepsilon_v^h = c_H \varepsilon_v^m \quad (2.21)$$

and

$$DIS = \frac{c_d K^{3/2}}{L}, \quad (2.22)$$

where  $c_H^{-1}$  is the turbulent Prandtl number, and  $c_\varepsilon$  and  $c_d = c_\varepsilon^3$  are empirical constants. The diagnostic formulation for the turbulent mixing length depends on the stratification of the ocean (Eifler et al. 1991). In the well mixed layer close to the surface and in the bottom boundary layer the turbulent mixing length  $L$  is calculated from the Blackadar (1962) formula:

$$L = \frac{kz}{1 + \frac{kz}{c_2 h_{ml}}}. \quad (2.23)$$

In 2.23  $k$  is the von Karman constant,  $h_{ml}$  is the thickness of the surface of the bottom mixed layer and  $z$  is the distance from the surface or from the bottom. In the strongly stratified ocean, between the surface and the bottom mixed layers,  $L$  is diagnosed from:

$$L = c_3 \left( \frac{K}{-\frac{g}{\rho_0} \frac{\partial \rho}{\partial z}} \right)^{1/2}, \quad (2.24)$$

where  $c_3$  is obtained from the requirement of the continuity of the vertical profile of the turbulent mixing length at the bottom of the surface mixed layer.

### *Skin layer parameterisation*

In nature, at the several millimetres thick surface layer, the vertical exchange of the momentum and heat differs from the vertical mixing in the mixed layer below it. In conditions when there is no breaking of surface waves, the exchange of the momentum and the heat is determined by the molecular viscosity and the molecular diffusion, which are much weaker than the turbulent viscosity and the turbulent diffusion. As a consequence, there is a steep vertical gradient of physical parameters close to the sea surface. On the other hand, the vertical resolution of the ocean model is too coarse to explicitly calculate the vertical profile of physical parameters close to the surface. Therefore, the influence of the skin layer is parameterised in the model as a sub-scale feature (Eifler 1993, Eifler and Schrimpf 1992) in the form of the shape function (Fig.2.2). The parameterisation

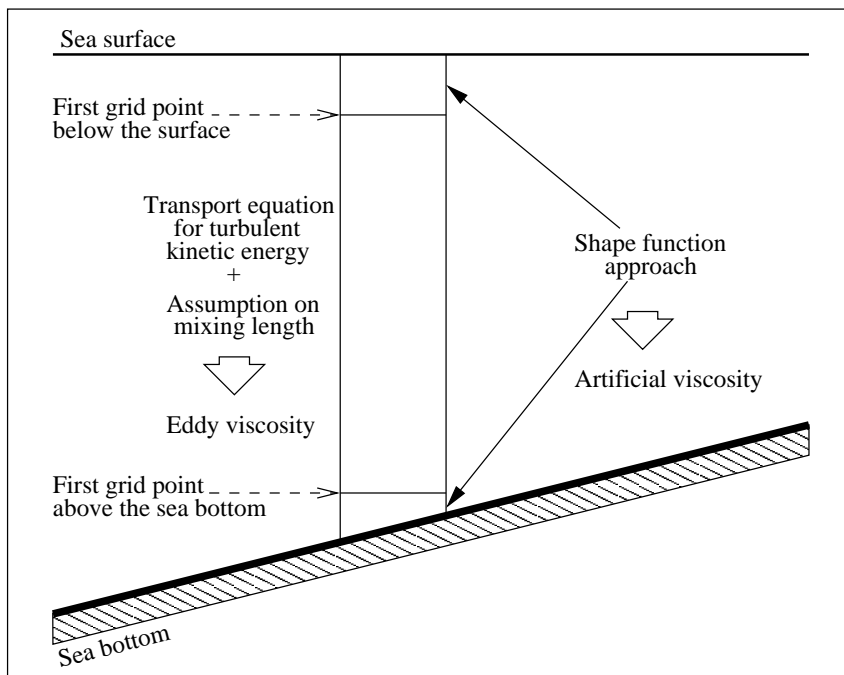


Figure 2.2: The illustration of the turbulence parameterisation with the near-interface shape function (from Eifler and Schrimpf 1992).

which is applied at both the surface and the bottom skin layers is based on assumptions that the velocity and the temperature, expressed in terms of non-dimensional parameters, have a universal distribution depending on boundary

layer variables and that there is a near-interface constant flux layer between the interface and the model level which is the closest to it. The non-dimensional form of the velocity, the potential temperature and the distance from the interface are given by:

$$u^+ = \frac{u - u_i}{u^*}, \quad (2.25)$$

$$\theta^+ = \frac{|T_i - T|c_p\rho_0 u^*}{q_i} \quad (2.26)$$

and

$$z^+ = \frac{z u^*}{\nu}, \quad (2.27)$$

where  $u_i$  and  $T_i$  are the interface velocity and temperature,  $u$  and  $T$  are the velocity and the temperature at the distance  $z$  from the interface and  $u^*$  is the interface friction velocity defined by:

$$u^* = \left( \frac{\tau_i}{\rho_0} \right)^{1/2}. \quad (2.28)$$

The assumption that there is a near-interface constant flux layer between the interface and the model level which is the closest to it, permits the substitution of the eddy viscosity in the layer close to the interface by the artificial viscosity  $\varepsilon_*^m$ . The following relation for  $\varepsilon_*^m$  may be derived (Eifler 1993):

$$\varepsilon_*^m = \nu \frac{\tau \Delta z^+}{\tau_i \Delta u^+}, \quad (2.29)$$

where  $\Delta z^+/\Delta u^+$  and  $\tau$  are computed from the previous time step. In the viscous region the non-dimensional velocity  $u^+$  is calculated from (Eifler 1993):

$$u^+ = 3u_0^+ \frac{z^+}{z_0^+} \left[ 1 - \frac{z^+}{z_0^+} + \frac{1}{3} \left( \frac{z^+}{z_0^+} \right)^2 \right], \quad (2.30)$$

when

$$u^+ = 3u_0^+ \frac{z^+}{z_0^+} \quad 0 \leq z^+ \leq z_0^+ = 3u_0^+. \quad (2.31)$$

At the bottom a constant value for  $u_0$  is used and at the top surface it is calculated from (Eifler 1993):

$$u_0^+ = \frac{4}{3} \left( \frac{\lambda u^*}{\nu} \right)^{1/3} = \frac{4}{3} (\lambda_0^+)^{1/3}, \quad (2.32)$$

where  $\lambda$  is the wavelength of the momentum, heat and mass transfer governing young waves. When  $z^+$  is beyond the viscous layer thickness  $z_0^+$ , a logarithmic is added:

$$u^+ = u_0^+ + \frac{1}{\kappa} \ln \left( \frac{z^+}{z_0^+} \right). \quad (2.33)$$

The near-surface heat transport is parameterised using the same approach as for the momentum. It is only parameterised at the sea surface, because it is assumed that the heat flux between the water and the bottom is zero. The artificial conductivity  $\varepsilon_*^h$  is defined by:

$$\varepsilon_*^h = \nu \frac{q}{q_i} \frac{\Delta z^+}{\Delta \theta^+}, \quad (2.34)$$

where  $q_i$  and  $q$  represent the flux of the heat at the interface and below it. The temperature profile close to the sea surface is given as a function of the Prandtl number  $Pr = \rho_0 c_p \nu / k_h$ , with  $k_h$  representing the heat conductivity:

$$\theta^+ = 3\theta_0^+ \left( \frac{z^+ Pr^{1/3}}{z_0^+} \right) \left[ 1 - \left( \frac{z^+ Pr^{1/3}}{z_0^+} \right) + \frac{1}{3} \left( \frac{z^+ Pr^{1/3}}{z_0^+} \right)^2 \right], \quad (2.35)$$

for

$$0 \leq z^+ \leq z_0^+ / Pr^{1/3}, \quad (2.36)$$

where

$$\theta^+ = \frac{|T_i - T| c_p \rho_0 u^*}{q_i}, \quad (2.37)$$

$$\theta_0^+ = u_0^+ Pr^{2/3}. \quad (2.38)$$

In the remaining part of the viscous layer, for:

$$z_0^+ / Pr^{1/3} < z^+ \leq z_0^+, \quad (2.39)$$

$\theta^+$  equals  $\theta_0^+$ . When  $\Delta z^+$  is larger than the viscous layer thickness  $z_0^+$  the logarithmic part has to be added to  $\theta^+$ :

$$\theta^+ = \theta_0^+ + \frac{1}{\kappa c_H} \ln \frac{z^+}{z_0^+}. \quad (2.40)$$

## 2.2 Atmospheric model

### 2.2.1 Main model equations

The model solves prognostic equations for the surface pressure, the temperature, the water mixing ratio, the cloud water and ice, the velocity and the turbulent kinetic energy. Furthermore, the model contains a prognostic model for the temperature and the moisture of the soil and the vegetation .

Following Laprise (1992) model equations are written for the non-hydrostatic compressible flow with the option to use the hydrostatic approximation. The vertical coordinate is defined by:

$$\eta = \frac{\pi - \pi_T}{\pi_S - \pi_T} \frac{\pi_r(z) - \pi_T}{\pi_r(0) - \pi_T}. \quad (2.41)$$

In (2.41)  $\pi$  is the hydrostatic pressure. Subscripts  $S$  and  $T$  indicate surface and top values, subscript  $r$  indicates the reference value and  $z$  is the elevation of the surface topography. The vertical coordinate is defined in a way that it is possible to combine the terrain following approach with step mountains (Mesinger 1984). The vertical coordinate is displayed in Fig.2.3.

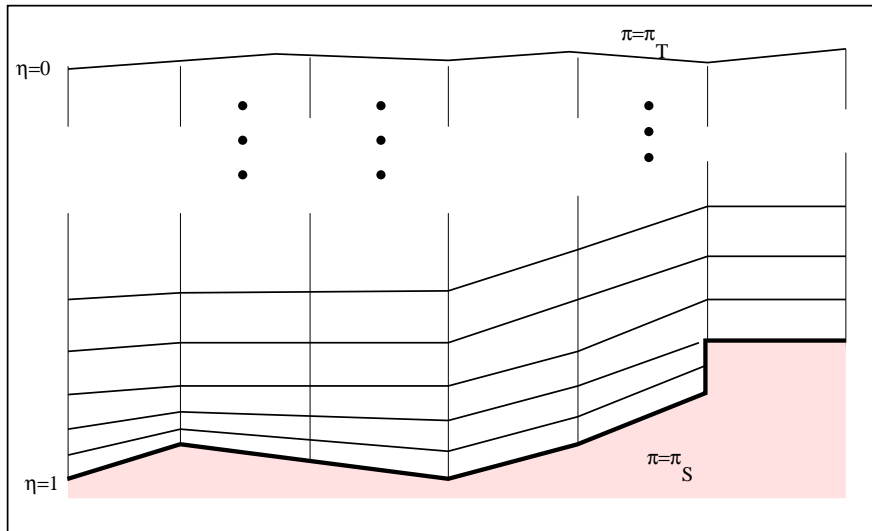


Figure 2.3: The vertical  $\eta$  coordinate

Prognostic equations in the model, written in the model vertical coordinate system, are:

$$\frac{d\mathbf{v}}{dt} + f\mathbf{k} \times \mathbf{v} + \frac{RT}{p} \nabla p + \eta_r \nabla \Phi = \mathbf{F}_v, \quad (2.42)$$

$$\frac{dp}{dt} + \frac{C_p p}{C_V} \left( \nabla \cdot \mathbf{v} + \frac{p \eta_r}{RT} \nabla \Phi \cdot \frac{\partial \mathbf{v}}{\partial \eta} - \frac{g p \eta_r}{RT} \frac{\partial w}{\partial \eta} \right) = \frac{Q p}{C_V T} + F_T, \quad (2.43)$$

$$\gamma \frac{dw}{dt} - g \eta_r \frac{\partial(p - \pi)}{\partial \eta} = \gamma F_w, \quad (2.44)$$

$$\frac{dT}{dt} - \frac{RT}{p C_p} \frac{dp}{dt} = \frac{Q}{C_p}, \quad (2.45)$$

$$\frac{\partial \pi_S}{\partial t} + \nabla \cdot \int_{\eta_T}^{\eta_S} \mathbf{v} \eta_r d\eta' = 0, \quad (2.46)$$

$$\frac{dq}{dt} = R_q, \quad (2.47)$$

where

$$\frac{d}{dt} = \mathbf{v} \cdot \nabla + \dot{\eta} \frac{\partial}{\partial \eta}, \quad (2.48)$$

and

$$\eta_r = \frac{\eta}{\pi - \pi_T}. \quad (2.49)$$

In (2.42-2.49)  $\mathbf{v}$  is the horizontal wind vector,  $w$  is the vertical velocity,  $p$  is the pressure,  $T$  is the temperature and  $q$  is the specific humidity. Terms  $\mathbf{F}_v$ , and  $F_w$  indicate viscous processes and terms  $F_T$  and  $F_q$  indicate the diffusion and the external forcing. By setting  $\gamma = 0$  and  $p = \pi$  the system becomes hydrostatic. Diagnostic equations in the model are:

$$\dot{\pi} = \mathbf{v} \cdot \nabla \pi - \nabla \cdot \int_{\eta_T}^{\eta} \mathbf{v} \eta_r d\eta', \quad (2.50)$$

$$\dot{\eta} = \nabla \cdot \int_{\eta_T}^{\eta} \mathbf{v} \eta_r d\eta' - \nabla \cdot \int_{\eta_T}^{\eta_S} \mathbf{v} \eta_r d\eta', \quad (2.51)$$

$$\Phi = \Phi_S + \eta_r \int_{\eta_S}^{\eta} \frac{RT}{p} d\eta', \quad (2.52)$$

and

$$R = R_d(1 + 0.608q), \quad (2.53)$$

where  $R_d$  is the gas constant for the dry air.

## 2.2.2 Numerical schemes

### *Spatial differencing*

The horizontal discretisation is made using the fully staggered C-grid (Arakawa and Lamb 1977). Also, the model grid is fully staggered in the vertical, with the vertical velocity and the turbulent kinetic energy calculated at layer interfaces and the horizontal momentum and scalars calculated at the middle of vertical layers. In horizontal momentum equations and in the continuity equation the pressure gradient and the horizontal velocity divergence are well simulated on the horizontal C-grid, but the calculation of the Coriolis term requires the averaging of momentum components. The averaging of the Coriolis term is made using the energy conservative scheme of Arakawa and Lamb (1977).

The advection of scalars and momentum components is calculated using the central differencing in space. The momentum advection scheme conserves the energy and the potential enstrophy (Arakawa and Lamb 1981).

### *Time integration*

The time stepping is split-explicit (Gadd 1978) with the longer time step for the physical forcing and the advection, and the shorter time step for the geostrophic adjustment by gravity-inertia waves. The increments of prognostic parameters due to the physics and the advection are calculated before the time stepping by the short time step, which solves the adjustment by gravity-inertia waves. They are averaged over the long time step and used as the external forcing at each short time step.

The adjustment by fast gravity waves is solved using the forward-backward scheme in time for momentum and continuity equations, while the Coriolis term is solved using the predictor-corrector scheme. The advection with the longer time step is solved using the predictor-corrector scheme. The vertical diffusion is calculated using the implicit scheme, while the horizontal diffusion is calculated using the forward in time scheme.

### *Boundary conditions*

The sponge boundary condition is applied at five points along lateral bound-

aries for the temperature, the specific humidity and the wind velocity. The horizontal velocity divergence is filtered at each short time step to reduce the gravity wave noise originating from the lateral boundaries.

### ***Horizontal diffusion and viscosity***

The biharmonic horizontal diffusion is applied to the fields of the temperature, the specific humidity and the cloud water content, while the biharmonic horizontal viscosity is applied on the fields of horizontal momentum components. The fourth order accurate biharmonic diffusion and viscosity are obtained by two successive applications of the second order diffusion and viscosity. The diffusion term for a parameter  $\alpha$  has the form  $K\nabla^2(K\nabla^2\alpha)$ .

### ***Vertical diffusion and viscosity***

The vertical diffusion and viscosity are parameterised as functions of the turbulent kinetic energy and the mixing length scale. The turbulent kinetic energy is calculated from the prognostic formula:

$$\frac{d}{dt}\left(\frac{q^2}{2}\right) - \frac{\partial}{\partial z}\left[lqS_q\frac{\partial}{\partial z}\left(\frac{q^2}{2}\right)\right] = P_s + P_b - \epsilon. \quad (2.54)$$

In (2.54)  $q^2/2$  is the turbulent kinetic energy,  $l$  is the mixing length,  $S_q$  is a constant, and  $P_s$ ,  $P_b$  and the dissipation  $\epsilon$  are defined from:

$$P_s = -\overline{wu}\frac{\partial U}{\partial z} - \overline{wv}\frac{\partial V}{\partial z}, \quad P_b = \beta g\overline{w\theta_v}, \quad \epsilon = \frac{q^3}{B_1 l}, \quad (2.55)$$

where

$$-\overline{wu} = K_M\frac{\partial U}{\partial z}, \quad -\overline{wv} = K_M\frac{\partial V}{\partial z}, \quad -\overline{w\theta_v} = K_H\frac{\partial \theta_v}{\partial z}. \quad (2.56)$$

Vertical diffusion and viscosity coefficients  $K_M$  and  $K_H$  are defined using stability functions of Mellor and Yamada (1982):

$$K_M = lqS_M, \quad K_H = lqS_H, \quad (2.57)$$

where  $S_M$  and  $S_H$  are defined from:

$$S_M(6A_1A_2G_M) + S_H(1 - 3A_2B_2G_H + 12A_1A_2G_H) = A_2, \quad (2.58)$$

$$S_M(1 + 6A_1^2G_M - 9A_1A_2G_H) - S_H(12A_1^2G_H + 9A_1A_2G_H) = A_1(1 - 3C_1), \quad (2.59)$$

where  $\beta$ ,  $A_1$ ,  $A_2$ ,  $B_1$ ,  $B_2$  and  $C_1$  are empirical constants, and  $G_M$  and  $G_H$  are obtained from:

$$G_M = \frac{l^2}{q^2} \left[ \left( \frac{\partial U}{\partial z} \right)^2 + \left( \frac{\partial V}{\partial z} \right)^2 \right], \quad G_H = -\frac{l^2}{q^2} \beta g \frac{\partial \theta_v}{\partial z}. \quad (2.60)$$

The mixing length  $l$  is diagnosed from the Blackadar (1962) formula:

$$l = l_0 \frac{\kappa z}{\kappa z + l_0}. \quad (2.61)$$

At land points stability functions are calculated by the Paulson (1970) formula:

$$\Psi_M = \begin{cases} -5\zeta & , 0 \leq \zeta < 1 \\ 2\ln\left(\frac{1+x}{2}\right) + \ln\left(\frac{1+x^2}{2}\right) - \frac{2}{\tan(x)} + \frac{\pi}{2} & , -5 < \zeta < 0 \end{cases} \quad (2.62)$$

and

$$\Psi_H = \begin{cases} -5\zeta & , 0 \leq \zeta < 1 \\ 2\ln\left(\frac{1+x^2}{2}\right) & , -5 < \zeta < 0. \end{cases} \quad (2.63)$$

In (2.62-2.63)  $x = (1 - 16\zeta)^{1/4}$ ,  $\zeta = z/L$ , and  $L$  is the Monin-Obukhov length.

Over the sea stability functions are used in the Mellor-Yamada 2 closure scheme (Lobocki 1993). Stability functions are:

$$\Psi_M = \begin{cases} \frac{\zeta}{R_{FC}} - 2.076 \left( 1 - \frac{1}{\zeta+1} \right) & , 0 \leq \zeta < 1 \\ -0.96\ln(1 - 4.5\zeta) & , -5 < \zeta < 0 \end{cases} \quad (2.64)$$

and

$$\Psi_H = \begin{cases} \frac{\zeta R_{IC}}{R_{FC}^2 \Phi_T(0)} - 2.076 \left( 1 - e^{-1.2\zeta} \right) & , 0 \leq \zeta < 1 \\ -0.96\ln(1 - 4.5\zeta) & , -5 < \zeta < 0, \end{cases} \quad (2.65)$$

where  $R_{IC}$  is the gradient Richardson numbers,  $R_{FC}$  is the flux Richardson number and  $\Phi(0)$  is the dimensionless velocity gradient for neutral conditions.

In addition, a viscose sub-layer is introduced over the sea (Janjic 1994). The bottom boundary condition is defined using the sub-layer (Liu et al. 1979) defined by:

$$U_0 = \frac{U_s + \frac{K_M z_U}{\Xi \Delta z} U_m}{1 + \frac{K_M z_U}{\Xi \Delta z}} \quad (2.66)$$

$$\theta_0 = \frac{\theta_s + \frac{K_H z_\theta}{\Xi \Delta z} \theta_m}{1 + \frac{K_H z_\theta}{\Xi \Delta z}} \quad (2.67)$$

$$q_0 = \frac{q_s + \frac{K_H z_q \theta_m}{\lambda \Delta z}}{1 + \frac{K_H z_q}{\lambda \Delta z}}. \quad (2.68)$$

Subscripts 0,  $S$  and  $m$  indicate values at the top of the viscous layer, at the sea surface and at the lowest model layer. In (2.66- 2.68)  $\vartheta$ ,  $\Xi$  and  $\lambda$  are molecular diffusivity for the momentum, the heat and the water vapour, and  $z_U$ ,  $z_\theta$  and  $z_q$  are corresponding depths of the viscous sub-layers. They are obtained from:

$$z_U = \frac{\xi \vartheta}{u_*} \left[ M \left( \frac{z_0 u_*^{1/4}}{\vartheta} \right) \right] \quad (2.69)$$

$$z_\theta = \frac{\xi \Xi}{u_*} \left[ M \left( \frac{z_0 u_*^{1/4}}{\vartheta} \right) Pr^{1/2} \right] \quad (2.70)$$

$$z_q = \frac{\xi \lambda}{u_*} \left[ M \left( \frac{z_0 u_*^{1/4}}{\vartheta} \right) Sc^{1/2} \right]. \quad (2.71)$$

In (2.69-2.71)  $Pr = \vartheta / \Xi$  and  $Sc = \vartheta / \lambda$  are the Prandtl and the Schmidt numbers and  $M$  is a constant which depends on the friction velocity  $u_*$ . Three regimes are defined depending on  $u_*$ . The first regime includes the sub-layer for all parameters with the low  $u_*$ , the second includes the sub-layer only for the heat and humidity for intermediate values of  $u_*$ , and the last excludes the sub-layer for high values of  $u_*$ .

### ***Radiation parameterisation***

The long-wave radiation is parameterised by the use of the broadband emissivity method (Stephens 1978). Emissivity functions, which depend on the water vapour and temperature, are calculated by the interpolation from known profiles given in look-up tables. Upward and downward fluxes are calculated from:

$$F_\uparrow = \int_0^1 B d\epsilon_\uparrow, \quad \text{and} \quad F_\downarrow = \int_0^1 B \epsilon_\downarrow, \quad (2.72)$$

where  $B$  is the Planck function and  $\epsilon$  is the emissivity. The absorption of the cloud is parameterised assuming that the cloud is the grey body (Stephens 1978). The change of the temperature with time due to the heating rate from the long wave radiation is obtained from:

$$\frac{\partial T}{\partial t} = \frac{g}{C_p} \frac{\partial}{\partial p} (F_\uparrow - F_\downarrow). \quad (2.73)$$

The downward short-wave radiation flux is calculated from:

$$F_S = S \cos(\phi) - \int_p^{p_t} (A_c + A_s) dp, \quad (2.74)$$

where  $S$  is the solar constant,  $\phi$  is the solar zenith angle, and  $A_c$  and  $A_s$  represent the cloud and the clear sky albedo and absorption. The cloud albedo and absorption are calculated from look-up tables obtained from Stephens (1978), and the clear sky water vapour absorption is calculated from look-up tables by Lacis and Hansen (1974). The local change of the temperature due to the absorption of the short wave radiation is:

$$\frac{\partial T}{\partial t} = \frac{g}{C_p} \frac{\partial F_S}{\partial p}. \quad (2.75)$$

### ***Large scale cloud water and ice***

The large scale cloud water and ice are parameterised by Zhao and Carr (1997) using a single equation for the cloud ice mixing ratio. Each computational box contains either water or ice depending on the temperature in the box. The prognostic equation for the cloud ice mixing ratio  $m$  and the terms in prognostic equations for temperature and specific humidity are:

$$\frac{dm}{dt} = C_b + C_g - P - E_c \quad (2.76)$$

$$\frac{dq}{dt} = \dots - (C_b + C_g - E_c - E_r) \quad (2.77)$$

$$\frac{dT}{dt} = \dots + \frac{L}{C_p} (E_c + E_r - C_b - C_g) - \frac{L_f}{C_p} P_{sm}, \quad (2.78)$$

where  $E_c$  and  $E_r$  are evaporation rates of the cloud water or ice and of the precipitation,  $C_b$  and  $C_g$  are the convective and the large scale condensation rates,  $P$  is the precipitation production rate of the cloud water or ice,  $P_{sm}$  is the melting rate for the snow,  $L$  is the latent heat of the condensation and  $L_f$  is the latent heat of freezing.

### ***Parameterisation of convection***

The parameterisation of the convection in the atmosphere is based on the main assumption that in the process of the convection vertical profiles of temperature

and specific humidity adjust towards reference states which may be deduced from observations in experimental campaigns (Betts 1986). Furthermore, it is assumed that the vertical integral of the enthalpy does not change during the convection:

$$\int_{p_b}^{p_t} (H_{ref} - H) dp = 0, \quad (2.79)$$

where  $p_b$  and  $p_t$  are the pressure at the bottom and the top of the cloud, and  $H = C_p T + Lq$  is the enthalpy. The convection is parameterised in the model when the conditional instability is diagnosed in the model column using different reference profiles for the ocean and for the land points (Betts 1986).

The adjustment of the temperature and the specific humidity towards reference profiles is performed using the Newtonian relaxation:

$$T_a = T_i + \frac{\Delta t}{\tau} (T_{ref} - T_i) \quad (2.80)$$

and

$$q_a = q_i + \frac{\Delta t}{\tau} (q_{ref} - q_i), \quad (2.81)$$

where the subscript  $a$  indicates the adjusted value, the subscript  $i$  indicates the initial value and  $\tau$  is the relaxation time. In the deep convection, the cloud water  $C_b$  is calculated from the difference between  $q_a$  and  $q_i$ . In the shallow convection same reference profiles are used for the temperature and the specific humidity, but the condensation of the specific humidity does not appear.

### ***Prognostic model for soil and vegetation***

The extended soil and vegetation model of Mahrt and Pan (1984) and Pan and Mahrt (1987) is used to forecast the soil temperature and water content including the vegetation cover influence (Chen et al. 1997). Diffusion equations for the soil temperature  $T$  and the soil water content  $\Theta$  are:

$$C(\Theta) \frac{\partial T}{\partial t} = \frac{\partial}{\partial z} \left( K_t(\Theta) \frac{\partial T}{\partial z} \right) \quad (2.82)$$

and

$$\frac{\partial \Theta}{\partial t} = \frac{\partial}{\partial z} \left( D(\Theta) \frac{\partial \Theta}{\partial z} \right) + \frac{\partial K(\Theta)}{\partial z} + F_\Theta. \quad (2.83)$$

where  $C(\Theta)$  is the volumetric heat capacity,  $K_t(\Theta)$  is the thermal conductivity,  $D(\Theta)$  is the soil water diffusivity,  $K(\Theta)$  is the hydraulic conductivity and  $F_\Theta$

represents sources and sinks of the soil water. Sources of the soil water are the precipitation at the surface and the gravitational percolation from top layers, while sinks of the soil water are the surface runoff, the gravitational percolation towards deep layers, the direct evaporation, the evaporation of the precipitation intercepted by the canopy and the transpiration through the canopy and roots of plants. The canopy water content  $W_C$  is calculated from:

$$\frac{\partial W_c}{\partial t} = \sigma_f P - D - E_c. \quad (2.84)$$

In (2.84)  $\sigma_f$  is the green vegetation fraction,  $P$  is the precipitation,  $D$  is the drip from the vegetation to the ground and  $E_c$  is the evaporation of the precipitation intercepted by the canopy. The evapo-transpiration by the canopy is calculated from:

$$\frac{\partial W_c}{\partial t} = \sigma_f E_p B_c \left[ 1 - \left( \frac{W_c}{S} \right)^n \right], \quad (2.85)$$

where  $S$  is the maximum allowed canopy water content,  $E_p$  is the potential evaporation and  $B_c$  is a function of the canopy resistance.

## 2.3 Coupling scheme

The interaction between the oceanographic and the atmospheric model is applied at the macro time step of the ocean model which is in this application the longest time step in the time integration of the coupled model. The schematic representation of the communication is sketched in Fig.2.4. The sea surface temperature

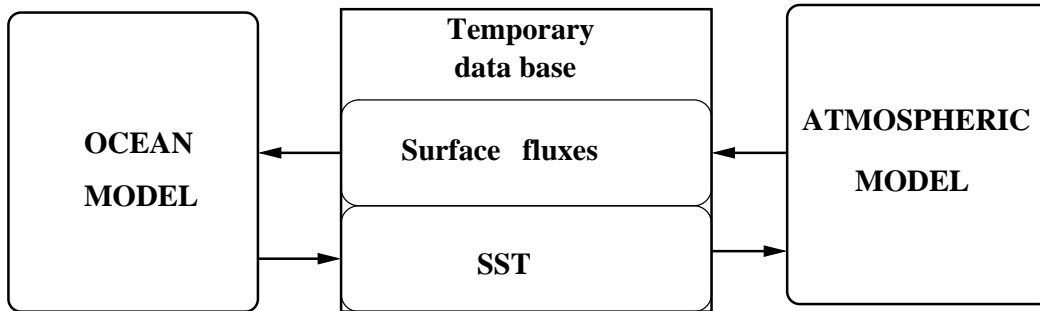


Figure 2.4: The schematic representation of the coupling scheme between the oceanographic and the atmospheric model

simulated by the ocean model is stored in the temporary data base, and then it is used by the atmospheric model as the bottom boundary condition for the calculation of surface fluxes. The surface heat flux and the wind stress calculated using the sea surface temperature field simulated by the ocean model are used as the surface forcing of the ocean model in the next time step.

Typically, the time step for the calculation of physics in the atmospheric model is several times smaller than the macro time step of the ocean model. Surface heat fluxes and wind stress are calculated in the atmospheric model with the constant sea surface temperature during the the macro time step of the ocean model. Then surface fluxes of heat and wind stress are averaged in time over the macro time step, and used in the prognostic equation of the ocean model to obtain a new value for the sea surface temperature at the end of the macro time step. The time splitting is sketched in Fig.2.5.

On the other hand, the horizontal resolution of the ocean model is typically higher than the horizontal resolution of the atmospheric model. Surface heat flux and wind stress calculated on the atmospheric model grid are horizontally interpolated from the atmospheric grid onto the ocean model grid when at least three sea points of the atmospheric model surround the ocean point. Fluxes

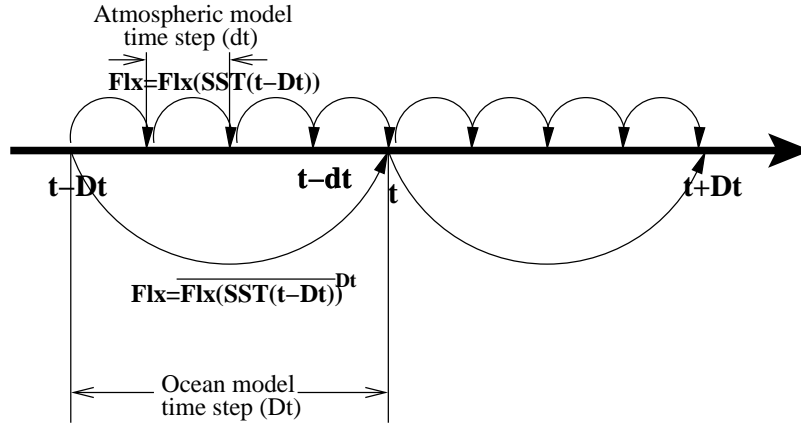


Figure 2.5: The splitting with time of the calculation of surface fluxes and sea surface temperature.

at remaining ocean points are obtained by the extrapolation from nearby ocean points. The sea surface temperature in atmospheric model grid points is obtained as an average of all ocean points that fall on that atmospheric grid point:

$$T_S^A = \sum_{k=1}^m T_k, \quad (2.86)$$

where  $T_S^A$  is the sea surface temperature at the atmospheric grid point, and  $T_k$  is the surface temperature of each of  $m$  ocean model points that fall on the atmospheric model point.

Alternatively, there is a switch in the coupled model to interpolate atmospheric parameters into the ocean model grid, to calculate surface fluxes using the high resolution ocean grid and to average them back onto the atmospheric model grid for the use in the atmospheric model. However, several sensitivity tests have shown that, in comparison with the simpler method applied in this study, this method proposed by Vintzielos and Sadourny (1997) does not result in significant differences in simulation outputs.

# Chapter 3

## Model set-up

### 3.1 Ocean model set-up

#### 3.1.1 Horizontal and vertical resolution, time step and bottom topography

The ocean model horizontal grid, displayed in Fig.3.1, is the latitude-longitude grid with the variable resolution. It covers the whole Adriatic Sea, and at the south it extends into the northern Ionian Sea with the open southern boundary at  $39^{\circ}\text{N}$ . The resolution ranges from 4.5km in the north-western corner to 11km at the south-eastern corner.

The variation in the resolution does not influence the model time step because the North Adriatic is significantly more shallow than the Southern Adriatic and the Ionian Sea. The micro time step, determined by the velocity of free surface gravity waves, is 60s and the macro time step, determined by the advection velocity, is 1800s.

In the vertical the model has 49 levels distributed between the surface and the depth of 1650m. The vertical resolution is the highest at the surface. The first model layer below the surface is at the depth of 1m, and the resolution is gradually increased until it reaches 100m at the deepest layer.

The model bathymetry is obtained from the U.S. Navy 5 minutes data set, corrected in North Adriatic using data extracted from nautical maps and satellite measurements for the coastline. The minimum depth is set to 10m and the bottom depth is adjusted to the depth of the closest vertical level. This was done to ensure that at least several model layers vertically resolve each model point.

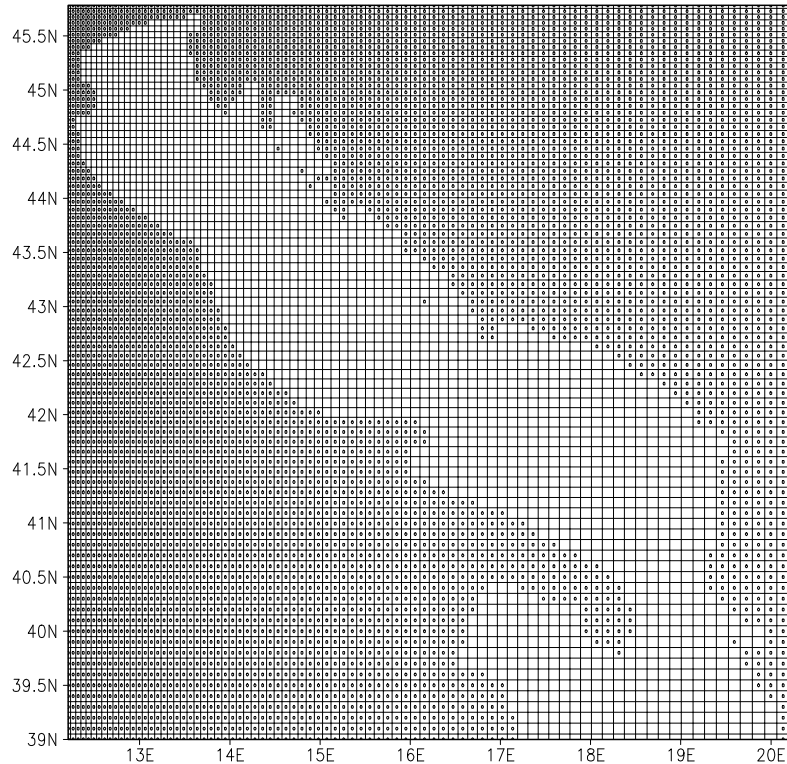


Figure 3.1: The horizontal grid of the ocean model. Grid points marked with dots are land points.

However, only at several points along the western coast of the Adriatic Sea the bottom depth has been corrected using this procedure.

### 3.1.2 River runoff

The river runoff is important for the water balance in the Adriatic and it influences local circulation structures (e.g. Zore-Armanda 1969). It is parameterised in the model using a volume conservation scheme. The change of the fluid mass with time in a model box, due to the river inflow, is given by:

$$\frac{\partial(\rho\Delta V)}{\partial t} = f_r(z)\rho_r, \quad (3.1)$$

where  $\Delta V = \Delta x\Delta y\Delta z$  is the model grid box volume,  $\rho$  is the density of the ocean water,  $f_r(z)$  is the inflow rate at the depth  $z$  of the model grid box and  $\rho_r$  is the density of the fresh water inflowing from the river. The integration of

(3.1) with time, assuming that the river inflow is constant during the integration period, gives the change of the depth of a single grid box with time:

$$\Delta z(t_0 + \Delta t) = z(t_0) + \frac{f_r(z)\Delta t}{\Delta x \Delta y}. \quad (3.2)$$

In (3.2), in consistence with the Boussinesq approximation applied in the ISPRAMIX model, the difference between the density of the ocean and the river water is neglected. The change of the surface elevation at the grid point, due to the fresh water inflow, is obtained by the vertical integration of (3.2):

$$h(t_0 + \Delta t) = h(t_0) + \frac{F_r \Delta t}{\Delta x \Delta y}, \quad (3.3)$$

where  $h$  is the water elevation and  $F_r$  is the river inflow rate.

The change of the tracer concentration in a grid box, due to the river inflow, may be calculated from:

$$\frac{\partial(S\rho\Delta V)}{\partial t} = S_r f_r(z)\rho_r, \quad (3.4)$$

where  $S$  is the tracer. Again, assuming that the density difference between the ocean and the river water is negligible and that the river inflow is constant during the time step  $\Delta t$ , we get the formula for the change of the tracer concentration:

$$\frac{\partial(S\Delta z)}{\partial t} = \frac{S_r F_r \Delta z}{z_r \Delta x \Delta y}. \quad (3.5)$$

In this formula  $z_r$  is the depth of the river mouth, which can be more shallow than the corresponding grid point of the ocean model. After combining (3.2) and (3.5) we get the formula for the change of the tracer concentration with time due to the river inflow:

$$S(t_0 + \Delta t) = S(t_0) - \frac{S(t_0) - S_r}{1 + \frac{z_r \Delta x \Delta y}{F_r \Delta t}}. \quad (3.6)$$

In the ISPRAMIX model the equation (3.2) is used to force the surface elevation at each micro time step, and the equation (3.6) is used to calculate the rate of change of salinity and temperature due to the river inflow at macro time steps.

The most important single fresh water source is the Po river, which creates a large baroclinic gradient along the north-western coast generating and maintaining the Western Adriatic Current (e.g. Kourafalou 1999). However, according to the estimated climatological river runoff made by Raicich (1996), the accumulated fresh water inflow from other rivers, which are not so important as single

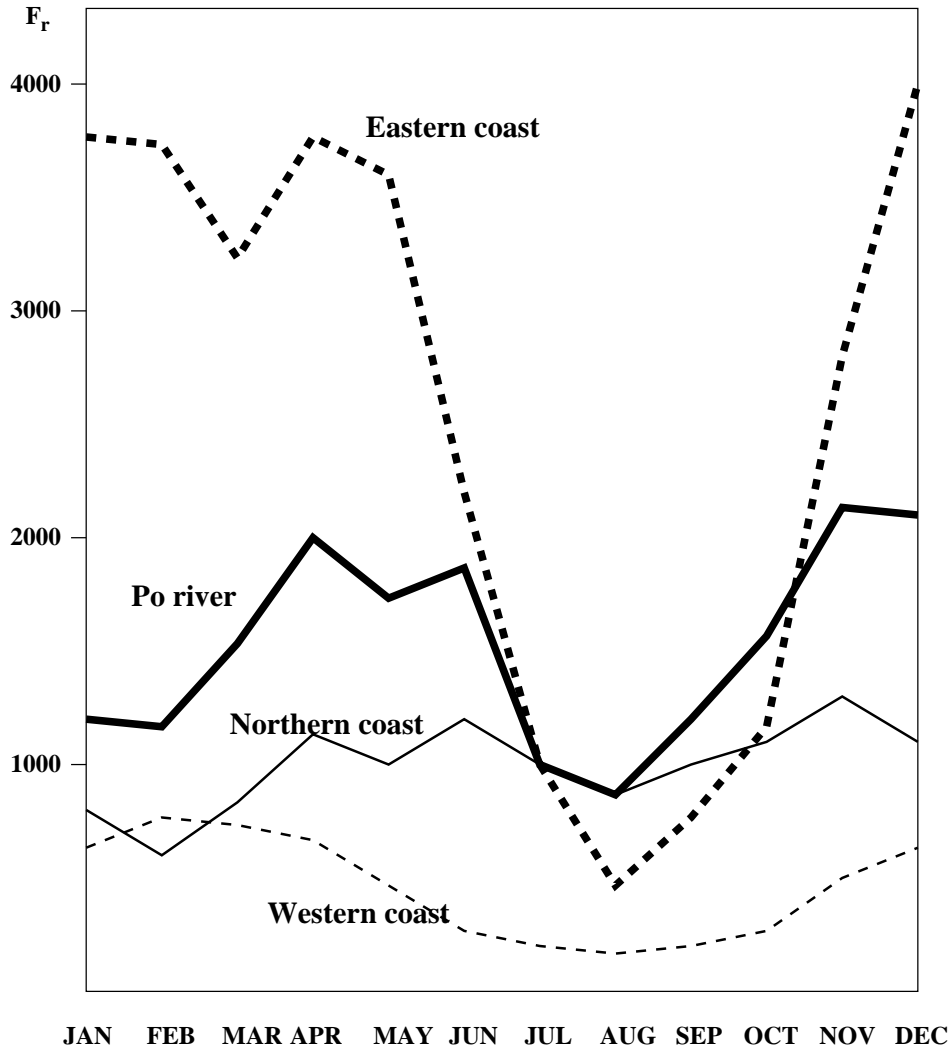


Figure 3.2: The estimated climatological inflow rate ( $m^3s^{-1}$ ) from major rivers in the Adriatic (after Raicich 1994).

sources, is also important for the generation of salinity gradients along the eastern and the northern coast.

Climatological river inflow is estimated by combining several estimates and measurements, mainly using the estimate by Raicich (1994). Estimated climatological mean monthly values of the river runoff are displayed in Fig.3.2. At each macro time step of the model the river inflow rate is calculated as the bilinear interpolation between two nearest months.

### 3.1.3 Initial and boundary conditions

Initial and boundary conditions are obtained from the Mediterranean Oceanographic Data Base (Brasseur et al. 1996) with the horizontal resolution of  $1/4^\circ$ . The model is first initialized with the winter distribution of temperature and salinity bilinearly interpolated in horizontal and in vertical from the climatological field into the model grid. Initial velocity and surface elevation fields are set to zero. Then the model is forced during two perpetual years by fluxes obtained as a monthly average of fluxes calculated by the coarse resolution atmospheric model in the period 1991-1997.

To avoid that the model drifts from the realistic climatological distribution of the temperature and the salinity, the temperature and the salinity are relaxed towards the value linearly interpolated in time between seasonal climatological values by adding extra terms in prognostic equations for tracers. In the prognostic equation for temperature this term has the form:

$$\frac{\partial T}{\partial t} = \dots - k(T - T_c), \quad (3.7)$$

where  $T_c$  is the climatological value linearly interpolated between two nearest climatological seasonal values from analyses by Brasseur et al. (1996). In the case of the constant  $T_c$ , the constant  $k = 10^{-7} s^{-1}$  would result in the e-folding time of approximately 120 days.

Model experiments are initialised by temperature and salinity fields obtained in the initial simulation at the end of the second perpetual year, because it was estimated that in winter there was the least temporal and spatial variability in simulated fields. Starting from this initial distribution, all simulations used realistic surface heat fluxes and wind stress.

Boundary conditions for the temperature and salinity at the southern boundary are linearly interpolated in time between seasonal climatological values. They are used in the case of the inflow through the lateral boundary to calculate the advective flux and in the calculation of the horizontal diffusion at the boundary. The normal component of velocity at the southern boundary is calculated using the zero gradient boundary condition, and the component of velocity parallel to the boundary is set to zero.

In all simulations southern boundary conditions are calculated in a same way as in the initial calculation, and the extra relaxation term, given in (3.7), is set to zero in all experiments.

The change of the surface elevation at the southern boundary due to the tidal forcing is parameterised by the harmonic function that defines the  $M_2$  tide:

$$\eta_{M_2} = \eta_{M_2a} \cos\left(2\pi \frac{t}{T_{M_2}} + \Phi\right), \quad (3.8)$$

where  $\eta_{M_2a}$  is the amplitude,  $\Phi$  is the phase and  $T_{M_2}$  is the period of the  $M_2$  tide. The amplitude  $\eta_{M_2a}$  is approximately estimated to be 0.06m, and the period is 12.42 hours.

## 3.2 Atmospheric model set-up

### 3.2.1 Horizontal and vertical resolution, topography and land-sea mask

There are two atmospheric model configurations. One has a relatively low horizontal resolution and the other has a relatively high horizontal resolution. The low resolution model has the latitudinal resolution of  $0.225^\circ$  and the longitudinal resolution of  $0.3^\circ$ . Its land-sea mask and the topography are displayed in Fig.3.3. The land-sea mask and the topography of the high resolution model, with the latitudinal resolution of  $0.1125^\circ$  and the longitudinal resolution of  $0.15^\circ$ , are displayed in Fig.3.4.

The land-sea mask and the topography of the atmospheric model are obtained from the GTOPO30 data set from the USGS with the lat-lon horizontal resolution of  $30'$ . The elevation at model points is obtained by averaging the elevation of all original elevation values from points that fall into the model point. The land-sea mask is calculated as a maximum of land or sea points that fall on each atmospheric model point.

We can see that there is a large difference in topography between the high and the low resolution model grids. While main topographic features like the Alps, the Julian Alps, the Dinaric Alps and the Apennines (Fig.1.2) are resolved by both model grids, the high resolution model grid resolves much more detail and gives higher topographic gradients, especially along the eastern coast. These details, which highlight the position and the shape of main valleys and ridges along the eastern coast, may be important to better locally simulate Bora wind events (e.g. Bergamasco and Gacic 1996). Furthermore, we may also expect that the model with the higher resolution grid can better simulate other processes at the coast which are influenced by the land-sea-atmosphere interaction.

In the vertical the atmospheric model has 24 terrain following layers. Their depth gradually increases from the bottom to the top of the model atmosphere positioned at the level of  $100mb$ . The layer closest to the surface has the depth of approximately  $20m$  above the ocean, and it is thinner above the topography in proportion to the topographic elevation. The elevation of the highest mountain is approximately  $3000m$  which corresponds approximately to the pressure of  $700mb$  in the standard atmosphere. Using the definition for the model vertical coordinate (2.41) with the top pressure at  $100mb$ , we may estimate that at the point with

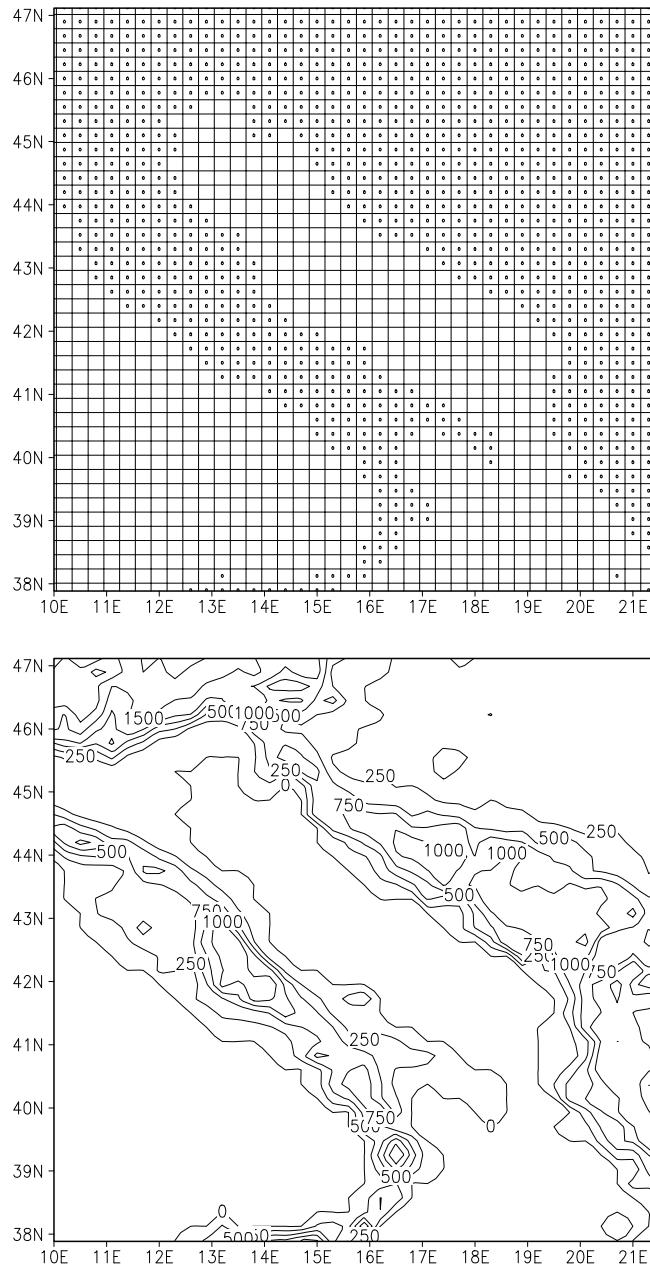


Figure 3.3: Coarse resolution model land-sea mask (up) and topography (down) Land points are marked with dots, and the topography elevation is given in metres.

the highest mountain the layer closest to the surface has the depth which is about two thirds of the depth at the sea level.

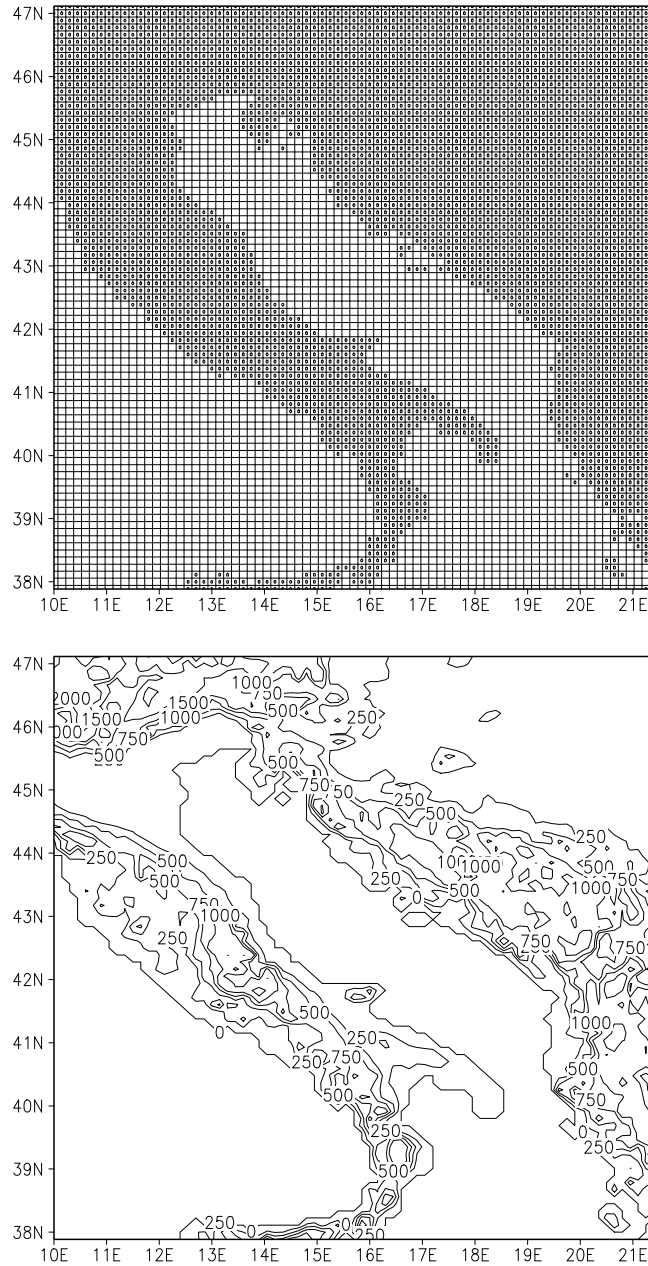


Figure 3.4: High resolution model land-sea mask (up) and topography (down) Land points are marked with dots, and the topography elevation is given in metres.

### 3.2.2 Initial and boundary data

Initial and boundary data are obtained from the ECMWF archive of reanalyses with the horizontal resolution of  $0.5^\circ$ . Boundary conditions for temperature, wa-

ter vapour mixing ratio and wind are available at the time interval of 6 hours. At each model time step boundary values are calculated by the linear interpolation between the ECMWF analyses time steps.

### 3.2.3 Surface fields

The vegetation type is interpolated from the 10 minutes USGS global data set. The soil type is obtained from Wilson (1985) global data set. Deep soil temperature and wetness are interpolated from the climatology of the NCEP/NCAR reanalyses available from Climate Diagnostics Centre.

To provide the sea surface boundary conditions in uncoupled atmospheric model simulations and to validate the results of model experiments daily sea surface temperature analyses are obtained using JPL NASA quality controlled data available with the horizontal resolution of  $9km$ . Only satellite measurements during the night were used to eliminate the eventual influence of the skin effect on the measurement. Due to the presence of clouds, satellite observations at so high temporal resolution often result in large areas with missing data. Full two dimensional daily fields of sea surface temperature are obtained by the objective analysis of daily satellite observations with 4 iterations using the method of Bratseth (1986). This method interpolates measurements with the interpolation error equal to the that obtained using the interpolation based on a statistical method.

The analysis is performed at points of each atmospheric model grid to obtain the atmospheric model sea surface temperature in one-way forcing experiments and also at points of the ocean model grid to evaluate coupled model simulations.

### 3.3 Control experiment set-up

The control experiment is performed to compare its outputs, obtained with the global circulation model surface forcing, with the coupled model outputs. Surface fluxes in the control experiment are calculated using ECMWF reanalyses from the T213 model available with the horizontal resolution of  $0.5^\circ$ . The land-sea mask resulting from the T213 ECMWF model is displayed in Fig.3.5. The calculation

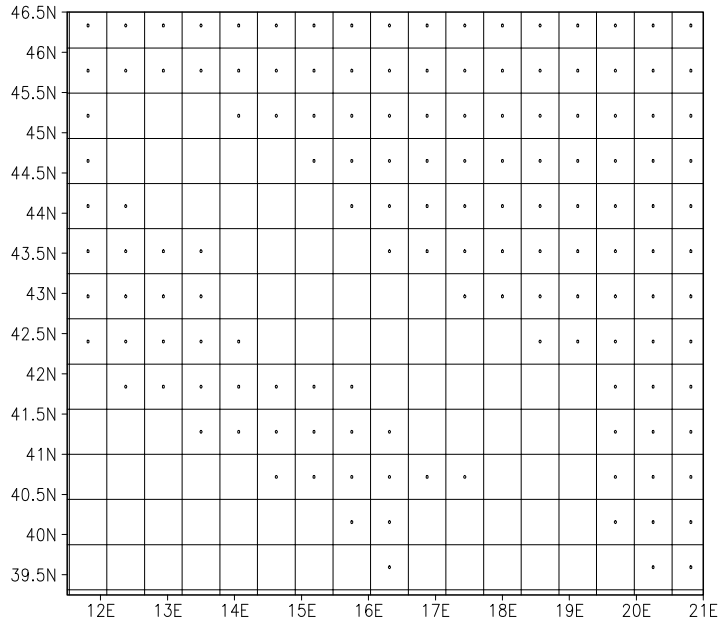


Figure 3.5: The horizontal grid of the T213 ECMWF model. Grid points marked with dots are land points.

of surface forcing is described in Devos (1997). To obtain the latent heat flux, the sensible heat flux and the wind stress it uses the method of Fairall et al. (1996). The turbulent fluxes of sensible heat  $H_s$ , latent heat  $H_l$  and wind stress  $\tau$  are calculated from standard bulk formulae:

$$H_s = \rho_a c_{pa} C_h S (T_s - \Theta), \quad (3.9)$$

$$H_l = \rho_a L_e C_e S (q_s - q). \quad (3.10)$$

$$\tau = \rho_a C_d S (u_s - u). \quad (3.11)$$

In (3.9-3.11)  $\rho_a$  is the density of air,  $L_e$  is the latent heat of evaporation,  $\Theta$  is the potential temperature,  $q$  is the water vapour mixing ratio,  $S$  is the wind speed,

$T_s$  is the temperature at the interface,  $q_s$  is the saturation mixing ratio, and  $C_h$ ,  $C_e$  and  $C_d$  are the transfer coefficients for sensible heat, latent heat and wind stress, which may be partitioned into individual profile components:

$$C_h = c_T^{1/2} c_d^{1/2}, \quad (3.12)$$

$$C_e = c_q^{1/2} c_d^{1/2}, \quad (3.13)$$

$$C_d = c_d^{1/2} c_d^{1/2}. \quad (3.14)$$

Individual components are functions defined from:

$$c_T^{1/2} = c_{Tn}^{1/2} / \left[ 1 - \frac{c_{Tn}^{1/2}}{\alpha\kappa} \Psi_h(\varepsilon) \right], \quad (3.15)$$

$$c_q^{1/2} = c_{qn}^{1/2} / \left[ 1 - \frac{c_{qn}^{1/2}}{\alpha\kappa} \Psi_h(\varepsilon) \right], \quad (3.16)$$

$$c_d^{1/2} = c_{dn}^{1/2} / \left[ 1 - \frac{c_{dn}^{1/2}}{\kappa} \Psi_u(\varepsilon) \right], \quad (3.17)$$

where  $\kappa$  is the von Karman constant,  $\alpha$  accounts for the difference in scalar and velocity constants,  $\Psi$  is the stability function and  $\varepsilon = z_r/L$ , where

$$L^{-1} = \frac{\kappa g}{T u_*^2} (T_* + 0.61 T q_*). \quad (3.18)$$

The subscript  $n$  indicates the value for neutral conditions calculated from the roughness length ( $z_{0T}$ ,  $z_{0q}$ ,  $z_0$ ) and the reference level height  $z_r$ :

$$c_{Tn}^{1/2} = \frac{\alpha\kappa}{\log(z_r/z_{0T})}, \quad (3.19)$$

$$c_{qn}^{1/2} = \frac{\alpha\kappa}{\log(z_r/z_{0q})}, \quad (3.20)$$

$$c_{dn}^{1/2} = \frac{\kappa}{\log(z_r/z_0)}. \quad (3.21)$$

The roughness length  $z_0$  is calculated by Smith (1992) from the combination of formulae of Charnock (1955) and Liu et al. (1979):

$$z_0 = \alpha \frac{u_*^2}{g} + 0.11 \frac{\nu}{u_*}, \quad (3.22)$$

where  $\nu$  is the kinematic viscosity of air. Stability functions are calculated from standard Kansas-type functions  $\psi_{T,uK}$  (Businger et al. 1971) using the formula:

$$\Psi_{T,u} = \frac{1}{1 + \varepsilon^2} \Psi_{T,uK} + \frac{\varepsilon^2}{1 + \varepsilon^2} \Psi_c, \quad (3.23)$$

with  $\Psi_c$  calculated from:

$$\Psi_c = 1.5 \ln \left[ \frac{y^2 + y + 1}{3} \right] - \sqrt{3} \arctan \left[ \frac{2y + 1}{\sqrt{3}} \right] + \frac{\pi}{\sqrt{3}}, \quad (3.24)$$

where

$$y = (1 - \gamma\varepsilon)^{1/3}. \quad (3.25)$$

The average magnitude of the wind speed  $S$  is calculated from the formula:

$$S^2 = u^2 + W_g^2, \quad (3.26)$$

where  $u$  is the magnitude of the average wind speed, and  $W_g$  is the convective scaling velocity computed from:

$$W_g^3 = \frac{g}{T} \left[ \frac{H_s}{\rho_a c_{pa}} + 0.61T \frac{H_l}{\rho_a L_e} \right] z_l. \quad (3.27)$$

In (3.27)  $z_l$  is the depth of the convective boundary layer, and  $H_s$  and  $H_l$  are defined in 3.9 and 3.10.

The short wave radiation at the surface  $Q_s$  is calculated using the combination of methods proposed by Oberhuber (1988) and Reed (1977):

$$Q_s = \frac{k\gamma}{2\pi} \frac{Q_t \cos\phi}{(\cos\phi + 2.7)10^{-3}e_a + 1.085\cos\phi + 0.1}. \quad (3.28)$$

In (3.28)  $Q_t$  is the incoming radiation at the top of the atmosphere,  $\phi$  is the solar zenith angle,  $e_a$  is the water vapour pressure at the surface and  $k$  is the empirically determined absorption and reflection by clouds (Reed 1977):

$$k = 1 - 0.62C + 0.0019\phi_n, \quad (3.29)$$

where  $C$  is the cloud cover ratio available from ECMWF reanalyses, and  $\phi_n$  is the solar zenith angle at noon.

The net long wave radiation at the surface  $R_L$  is calculated using the method of Oberhuber (1988) and taking into account the cloud cover ratio  $C$ :

$$R_L = \epsilon_s \sigma T_a^4 \left( 0.39 - 0.05 \sqrt{\frac{e_a}{100}} \right) \left( 1 - \chi C^2 \right) + 4\epsilon_s T_a^3 (T_s - T_a). \quad (3.30)$$

In (3.30)  $\chi$  is a constant,  $\epsilon_s$  is the emissivity of the water and  $\sigma$  is the Steffan-Bolzman constant.

ECMWF analyses of meteorological parameters were available at the time interval of 6 hours. To obtain hourly values of surface heat fluxes and wind stress, ECMWF fields were linearly interpolated in time at each time step.

# Chapter 4

## Discussion and validation of model results

### 4.1 Discussion and validation of oceanographic model results

The discussion and the validation of the oceanographic model simulation will be made with the results originating from the highest horizontal resolution coupled model experiment. It will be assumed in advance that oceanographic fields simulated by the high resolution coupled model experiment give the most realistic simulation result. However, this premise will be experimentally tested in Chapter 5.

Seasonal fields of the surface temperature simulated by the ocean model are displayed in Fig.4.1. There is a large seasonal oscillation of the mean temperature, due to the large seasonal oscillation of the surface heat fluxes in the Adriatic.

In winter there is a clear north-south gradient in the temperature field. While the temperature along the northern and the north-western coast is lower than  $10^{\circ}C$ , along the south-eastern coast its mean value is about  $14^{\circ}C$ . It can be seen that relatively cold water spreads along the western coast until  $42^{\circ}N$  in a narrow band separated by a high temperature gradient from relatively warm water offshore to the east. In the central Adriatic relatively warm water is transported from the coast towards west by the current that separates from the coast and enters in the cyclonic circulation in the Pomo Depression (Fig.1.1). The separation of the coastal current from the eastern coast and the advection of the warm

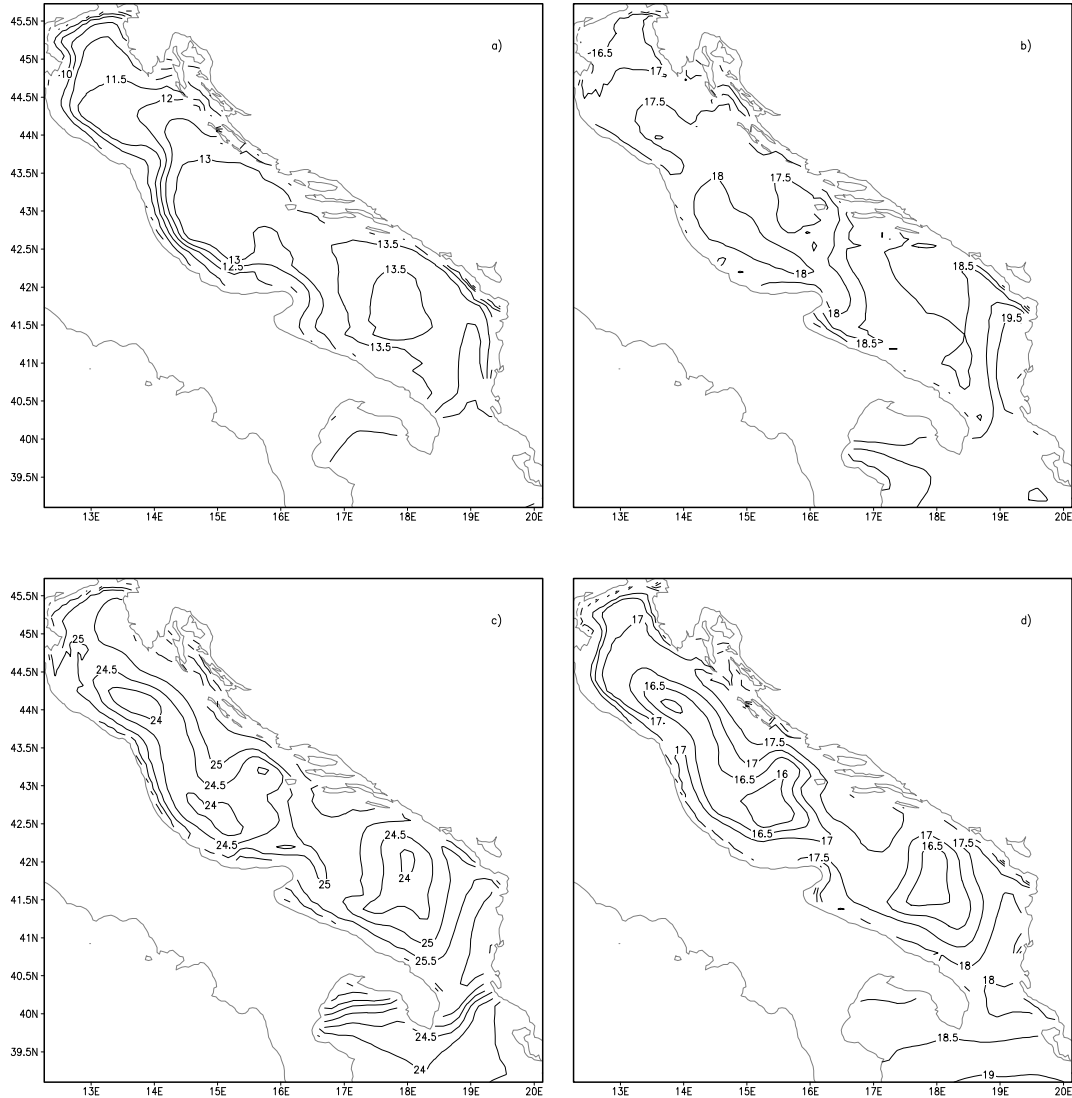


Figure 4.1: Seasonal fields of temperature ( $^{\circ}C$ ) at  $1m$  depth simulated by the high resolution coupled model. a) winter, b) spring, c) summer, d) autumn

water towards the west is visible also in the northern part of the Adriatic, but the warm water does not circulate in the gyre. In the southern part of the Adriatic the cyclonic circulation in the Southern Adriatic Gyre dominates the transport of relatively warm water from the eastern to the western coast and further to the south along the western coast. Along the south-eastern coast relatively warm water is advected from the Ionian sea through the Otranto Strait into the South

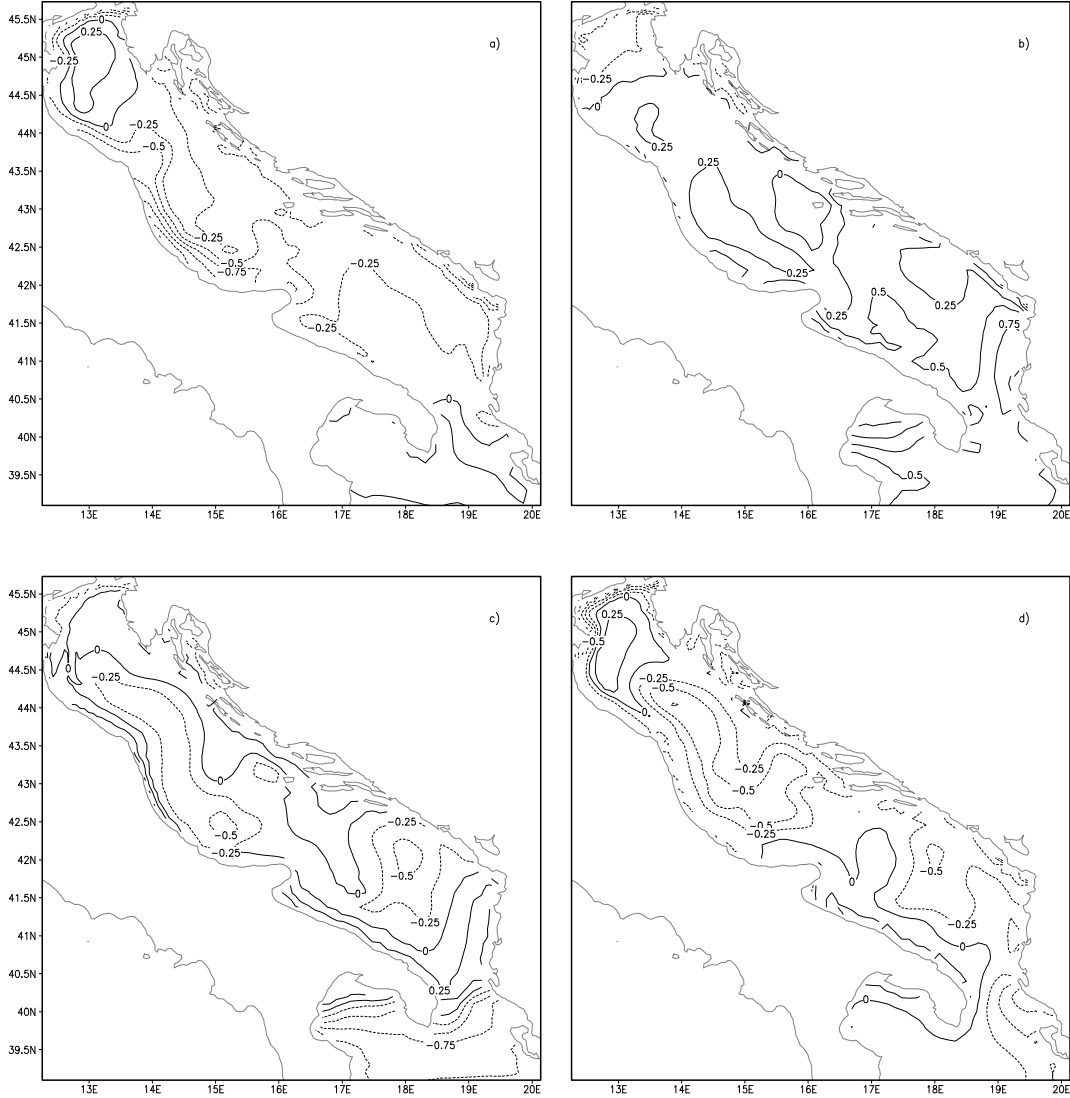


Figure 4.2: Seasonal fields of the difference between the surface temperature simulated by the high resolution coupled model and daily analyses obtained from satellite observations ( $^{\circ}C$ ). a) winter, b) spring, c) summer, d) autumn

Adriatic (Fig.1.2).

In spring the north-south gradient is still evident in the temperature field. However, it is much weaker in the northern part of the Adriatic, and the advection of the cold water from the north part of the Adriatic is significantly reduced and limited only until  $43.5^{\circ}N$ . In the central part of the Adriatic the temperature

in the west is higher than in the east. Still there is the inflow of warm water from the Ionian Sea through the Otranto strait and along the south-eastern coast. In summer, the near-surface temperature becomes warmer along coasts, with relatively colder areas offshore. The horizontal gradient in the northern part of the Adriatic becomes large again, but now, contrary to the winter distribution, the near surface temperature along the western coast is higher than offshore. In autumn, the surface temperature along the western coast in the North Adriatic becomes lower than offshore, and the warm water along the eastern coast separates from the coast and spreads in cyclonic gyres towards the western coast.

In general, the surface temperature spatial distribution and its seasonal variability simulated by the model are in good agreement with climatological estimates based on satellite observations (Fig.2 in Gacic et al. 1997), and based on in situ measurements (Fig.2a in Artegiani et al. 1997b). Also, the model is able to simulate several spatially small scale features which are visible in high resolution satellite images (e.g. Gacic et al. 1997), like the spreading of the cold North Adriatic water in a narrow band along the western coast.

To quantitatively validate the model result, seasonal averages of the difference between the simulated surface temperature in the high resolution coupled model experiment and the surface temperature analysed from satellite observations are displayed in Fig.4.2. We can see that there is a relatively small seasonally averaged difference between the simulated and the analysed surface temperature. Offshore, the absolute value of the difference is less than  $0.5^{\circ}C$ , while along coasts the difference is more significant. The largest difference is in winter along the north-western part of the Adriatic coast, where the simulated value is lower than the analysed along the path of the cold water that spreads from the North Adriatic. The similar difference appears in autumn along the northern coast of the Adriatic Sea.

It is important to notice that, although there was no flux correction and no surface temperature relaxation towards observations in the model simulation, the simulated surface temperature field is in very good agreement with daily analyses based on satellite observations in all seasons. An even more detailed spatial and temporal analysis of differences between the surface temperature simulated by the high resolution coupled model and the analysed surface temperature is performed using the EOF analysis in Subsection 5.1.1. The EOF analysis performed in Subsection 5.1.1 further confirms the high degree of the correspondence between the simulated and the analysed daily fields of the surface temperature throughout

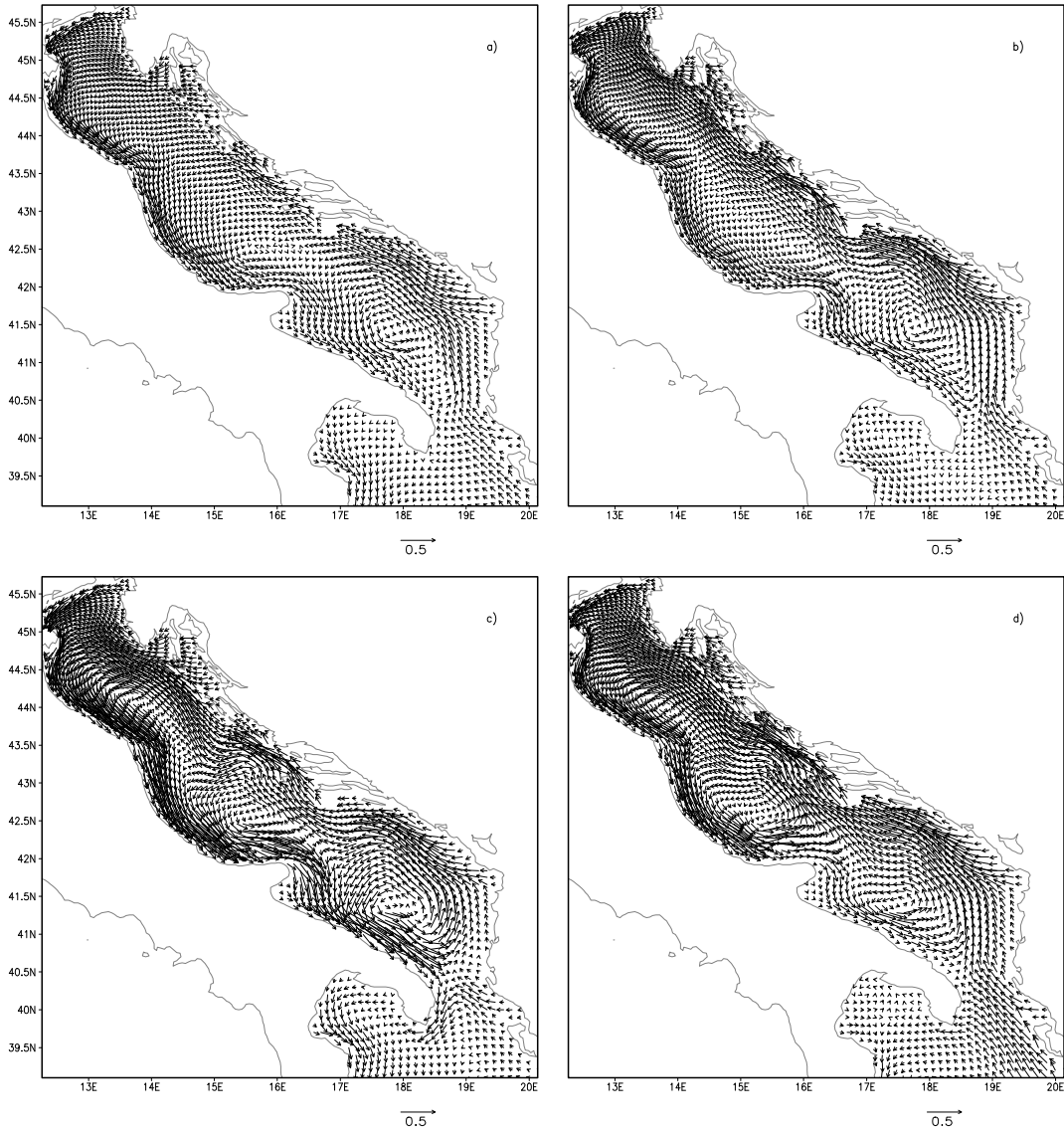


Figure 4.3: Seasonal velocity fields at the surface simulated by the high resolution coupled model ( $ms^{-1}$ ). a) winter, b) spring, c) summer, d) autumn

the year.

Seasonally averaged velocity fields at the surface are displayed in Fig.4.3. The circulation is generally cyclonic and all major structures in the surface circulation are present in averaged fields in all seasons, but their intensity changes. In winter, the western Adriatic current is attached closely to the coast and it extends up to the central part of the Adriatic at  $42^{\circ}N$ . The South-eastern Adriatic Current

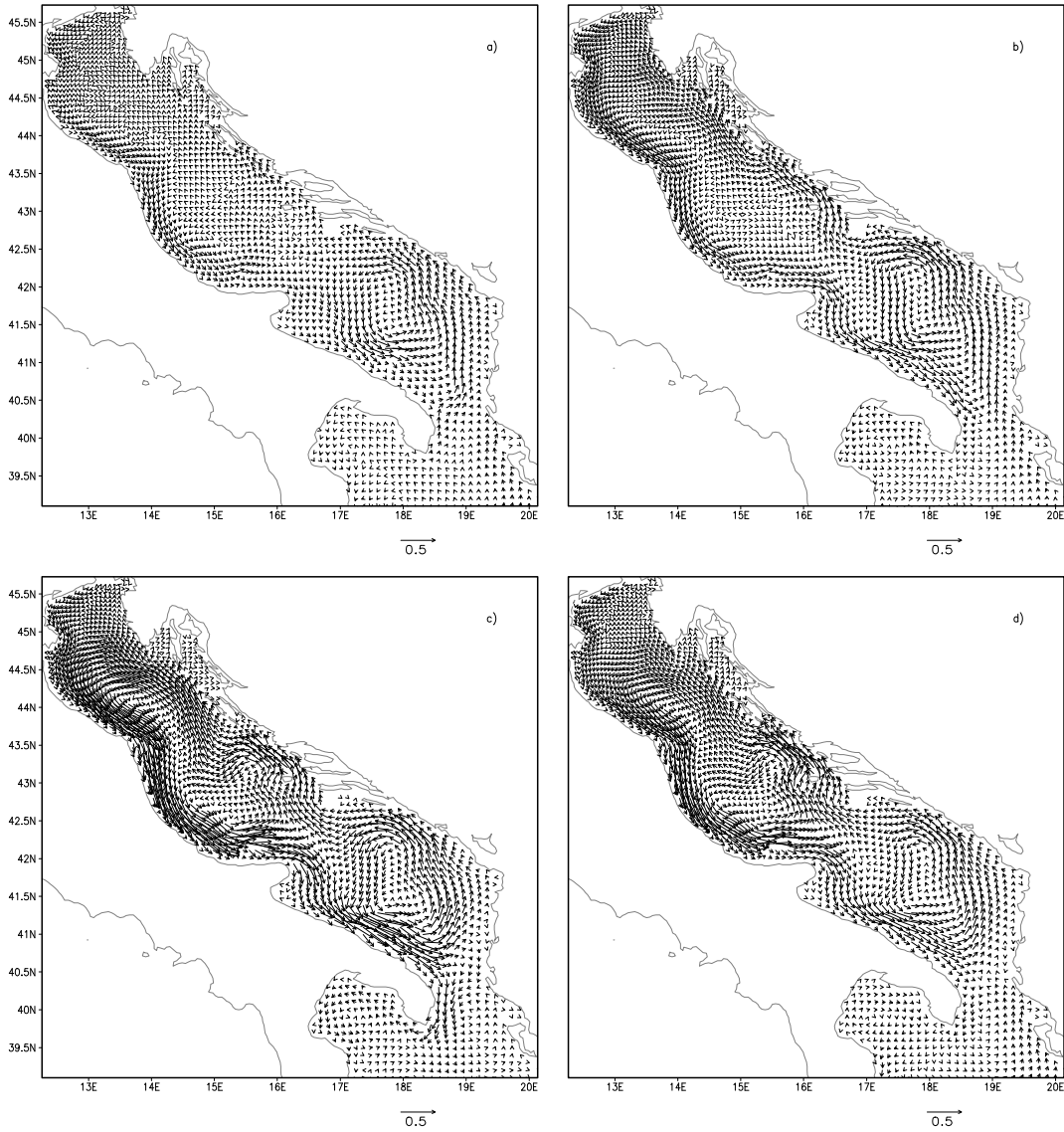


Figure 4.4: Seasonal velocity fields at the depth of 5m simulated by the high resolution coupled model ( $ms^{-1}$ ). a) winter, b) spring, c) summer, d) autumn

is positioned close to the eastern coast in the Ionian Sea, in the Otranto Strait and in the southern part of the Adriatic Sea. The South Adriatic Gyre is clearly visible, but the Central Adriatic Gyre and the North Adriatic Gyre are very weak and almost inexistent. They are visible only as a part of the general cyclonic circulation in the Adriatic. In spring, the flow intensity becomes stronger almost everywhere. The Western Adriatic Gyre is wider and it spreads more to the

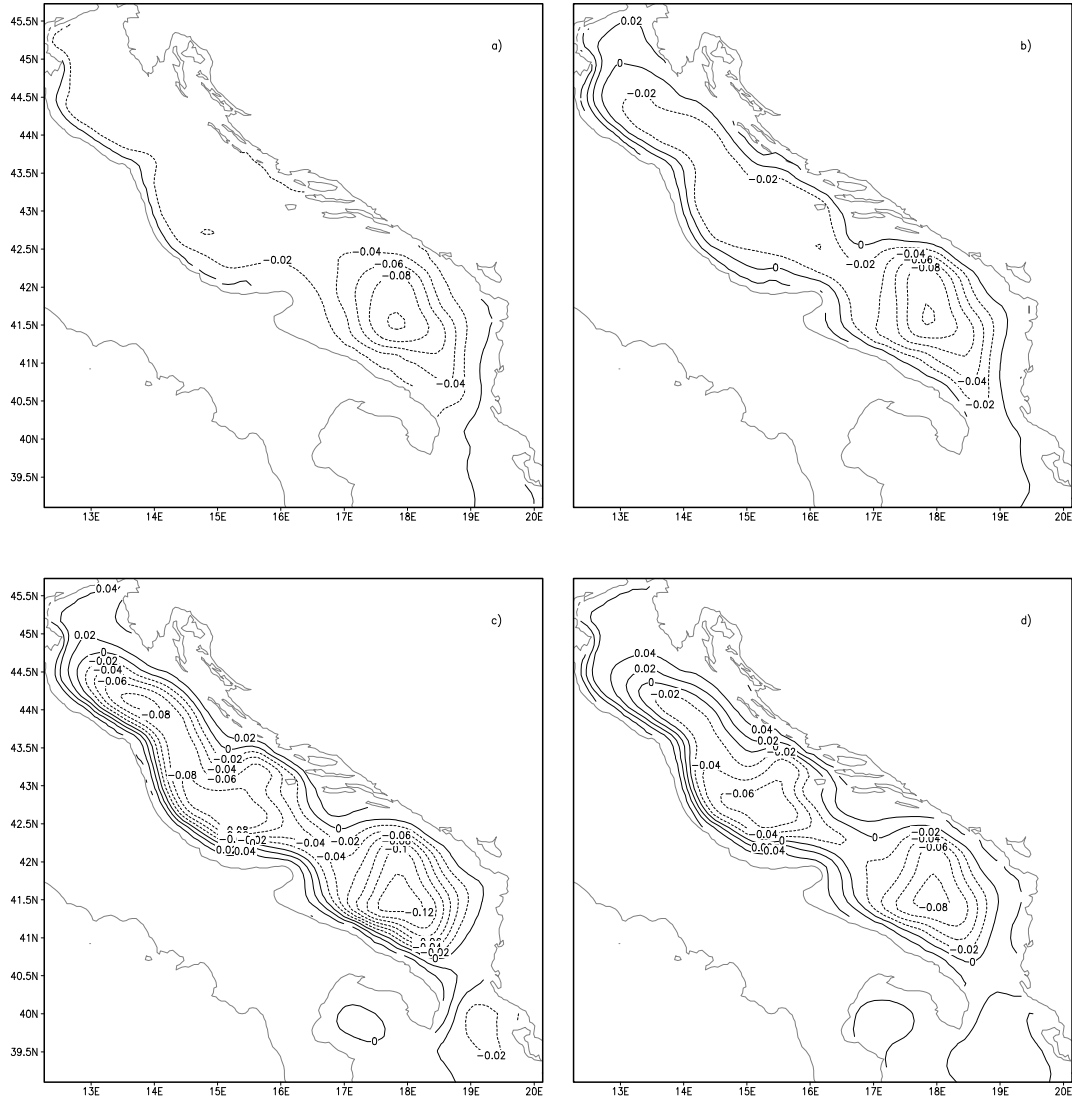


Figure 4.5: Seasonal sea surface elevation fields simulated by the high resolution coupled model ( $m$ ). a) winter, b) spring, c) summer, d) autumn

south. The South-eastern Adriatic Current still brings the water from the Ionian Sea into the southern part of the Adriatic. It becomes broader and gets connected with the Southern Adriatic Gyre. Gyres in the central and the northern part of the Adriatic are not well defined in the surface circulation field, although the global circulation is cyclonic.

In summer the Western Adriatic Current becomes the major surface circula-

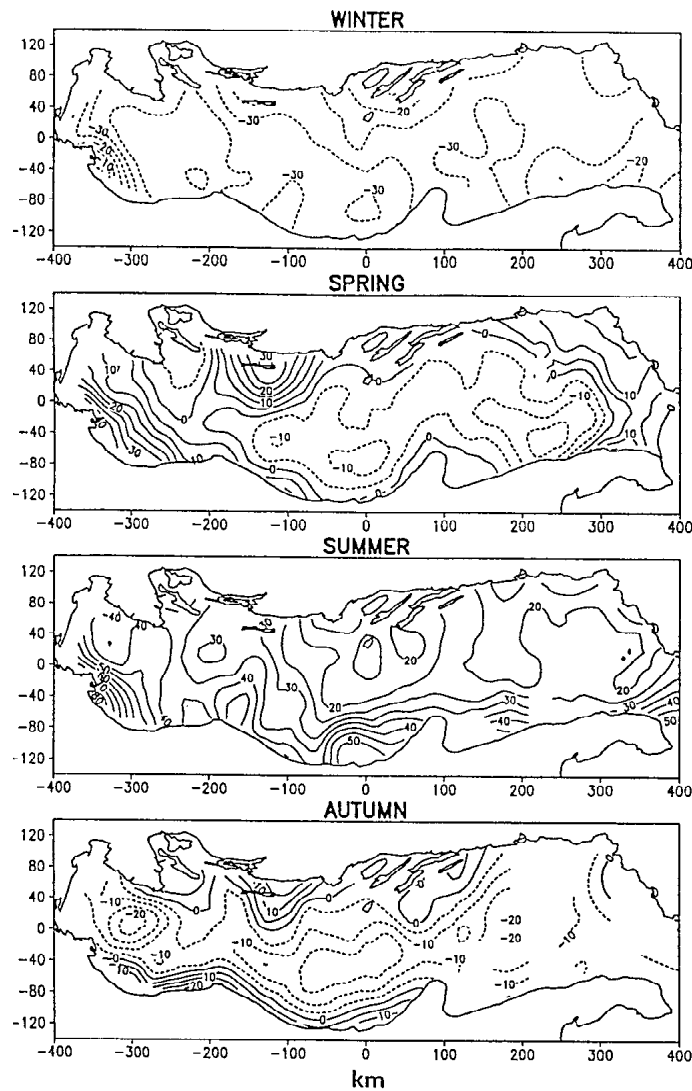


Figure 4.6: Seasonal fields of climatological dynamic height anomalies (*dyn mm*) relative to 30m depth (from Artegiani et al. 1997b).

tion feature. It extends to the Otranto Strait forming the outflow at the surface from the Adriatic Sea into the Ionian Sea along the western coast of the Otranto Strait. The current is partially detached from the coast in the northern part of the Adriatic. The surface water inflow from the Ionian Sea is significantly suppressed near the Otranto Strait. The South-eastern Adriatic Current is relatively weak along the Albanian coast, but it becomes strong further to the north. Now, the Southern Adriatic Gyre and the Central Adriatic Gyre are clearly visible in the surface circulation. In autumn the Western Adriatic Current again becomes

reduced in intensity and its extension towards the south becomes more limited. The South-eastern Adriatic Current becomes more dominant, with the large and wide inflow from the Ionian Sea over the whole Otranto Strait and it spreads far to the north.

In comparison with observations (e.g. Poulain 2001) and climatological calculations (e.g. Artegiani et al. 1997b) we can see that all major features of the surface circulation and their seasonal variability are simulated well by the model. One explanation for the relatively weak intensity of the seasonally averaged surface circulation in winter, in comparison to other seasons, may be the reduction of horizontal buoyancy gradients due to the larger vertical mixing in winter and due to the density compensation process in the North Adriatic (Zavaratelli et al. 1999, Zavaratelli et al. 2002). Another reason could be the larger variability in the direction of winds which results in the weaker averaged velocity field at the surface. On the other hand, the intensification of surface buoyancy gradients in summer and the strong Scirocco wind in autumn may result in a relatively larger intensity of the seasonally averaged surface circulation.

Seasonal averages of the circulation field at the depth of 5m are displayed in Fig.4.4. When comparing the circulation at the 5m depth with the surface circulation displayed in Fig.4.3 we can see that all circulation features are similar to those at the surface, with the major difference that the circulation intensity is generally weaker and that in winter the Western Adriatic Current is less pronounced than at the surface. On the other hand, in summer the Western Adriatic Current has the almost identical shape and the relative intensity at the 5m depth as at the surface. Also, we can see that the South-eastern Adriatic Current is less pronounced at the 5m depth than at the surface in all seasons.

Seasonal averages of the surface elevation are displayed in Fig.4.5. Again, we can see the main surface circulation structures visible in seasonal averages of the surface velocity field, but in winter the sea surface elevation gradient is very weak in the northern part of the Adriatic. In winter only the South Adriatic Gyre is clearly visible, while in summer all three Adriatic gyres are visible in the seasonally averaged field. In autumn the Northern Adriatic Gyre disappears again. The western coastal current and the South Adriatic Gyre are much more pronounced features in seasonal averages of the surface elevation field simulated by the model than in climatological seasonal dynamic height fields calculated by Artegiani et al. (1997b) (Fig.4.6). The main reasons for this difference can be that the coarse resolution dynamic height climatologically estimated by Artegiani

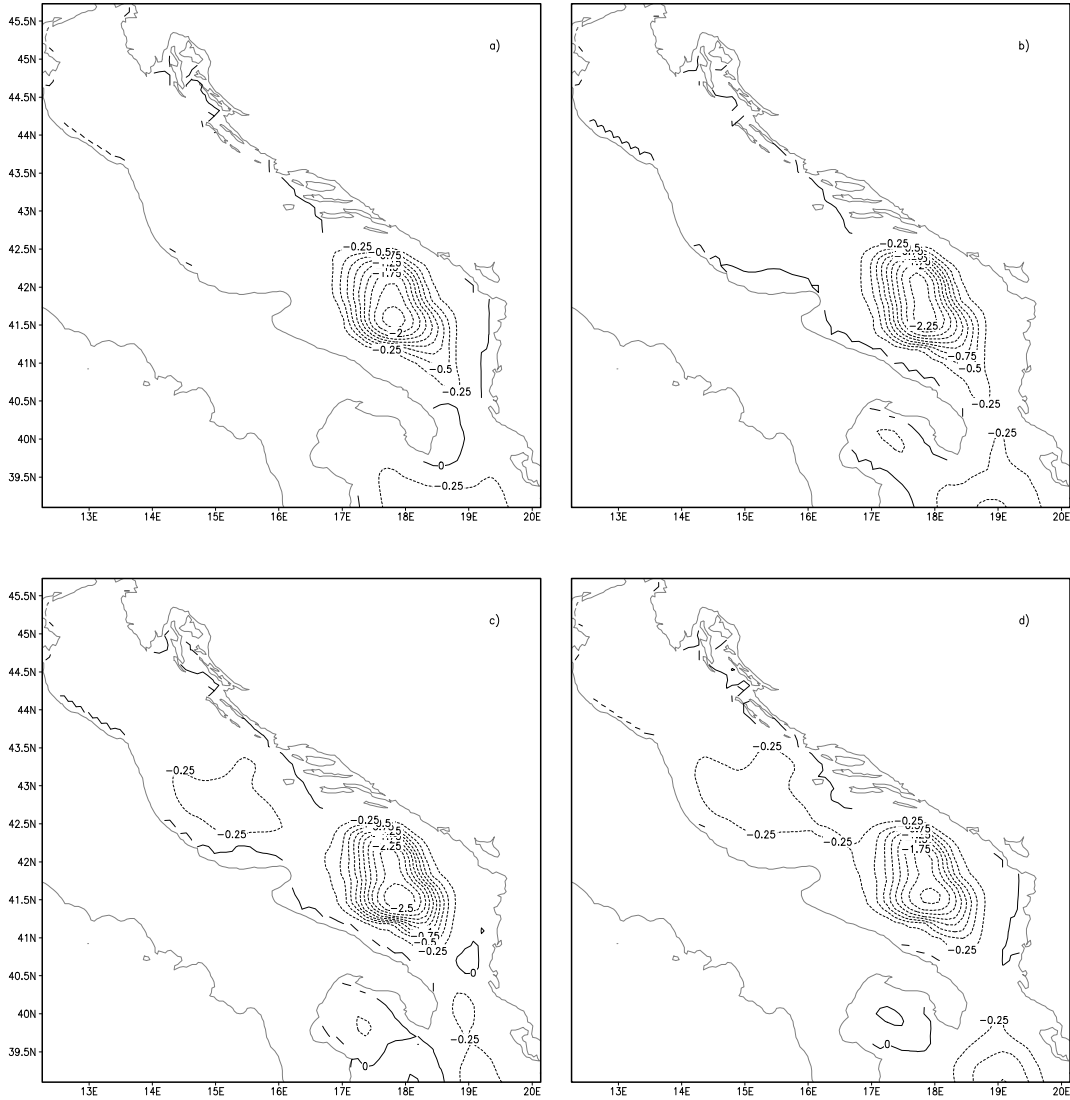


Figure 4.7: Seasonal total transport stream function fields simulated by the high resolution coupled model ( $10^6 m^3 s^{-1}$ ). a) winter, b) spring, c) summer, d) autumn

et al. (1997b) may not detect the narrow coastal current, that it does not account for the wind driven part of the flow and that the subjective estimate of the layer of no motion in Artegiani et al. (1997b), which is the reference for the calculation of the dynamic height, may introduce large errors in their climatological estimate.

Seasonal averages of the total transport stream function are displayed in Fig.4.7. The main feature in the total transport field is the southern Adriatic

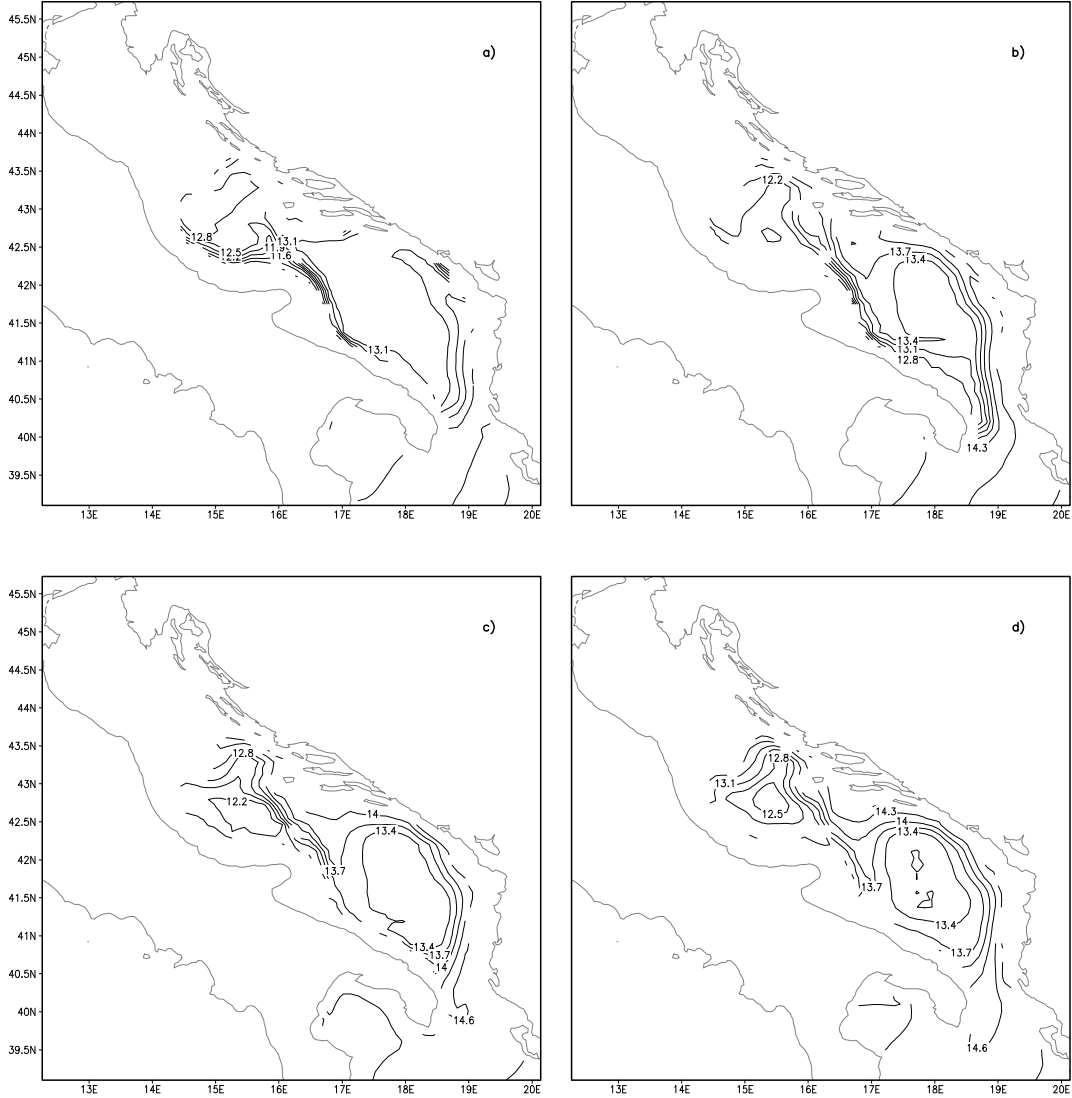


Figure 4.8: Seasonal averages of temperature fields at 100m depth simulated by the high resolution coupled model ( $^{\circ}\text{C}$ ). a) winter, b) spring, c) summer, d) autumn

Gyre. It dominates the total transport field because the southern part of the Adriatic is much deeper than the central and the northern parts of Adriatic resulting in the larger net volume of the total transport, and because the southern Adriatic Gyre simulated by the model is a very stable circulation feature which does not have significant variations of the intensity or any reversal of the cir-

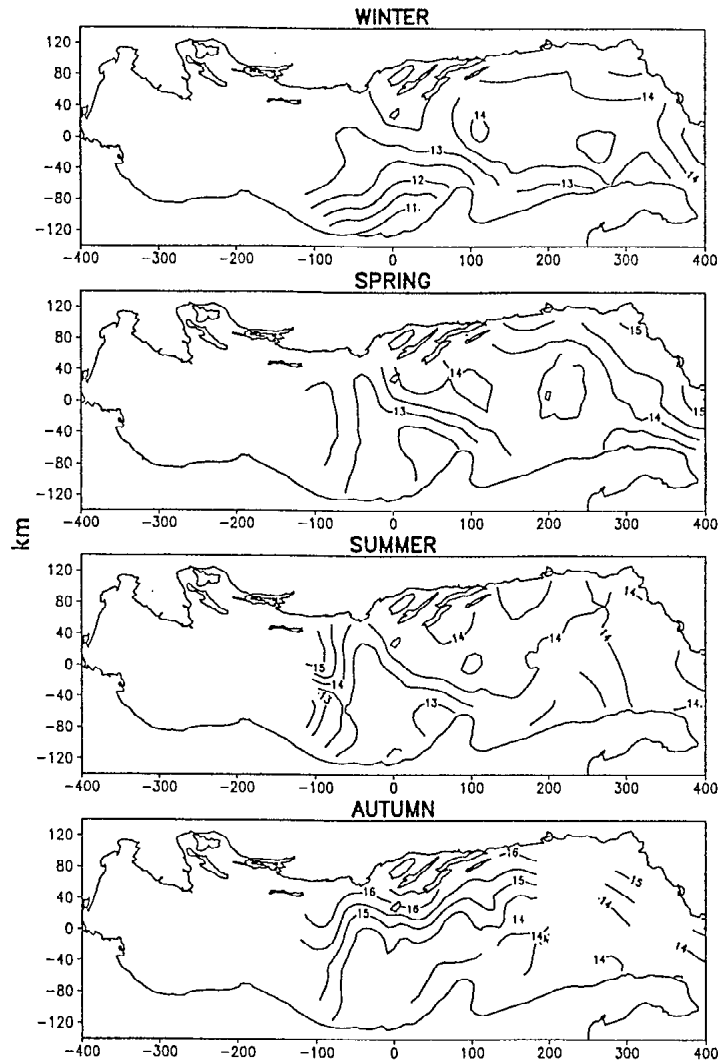


Figure 4.9: Seasonal averages of climatological temperature fields at 100m depth ( $^{\circ}\text{C}$ ) (from Artegiani et al. 1997b).

ulation direction. The central Adriatic gyre is also visible in summer and in autumn. A more detailed investigation of the total transport field shows that the total transport is cyclonic in the whole Adriatic in all seasons, but, due to the more shallow northern part, quantitatively it is less significant than in the southern part (not shown).

Seasonal averages of the temperature field at 100m depth are displayed in Fig.4.8. Seasonally averaged temperature fields have the north-south gradient with the relatively cold water in the Pomo Depression and the relatively warm

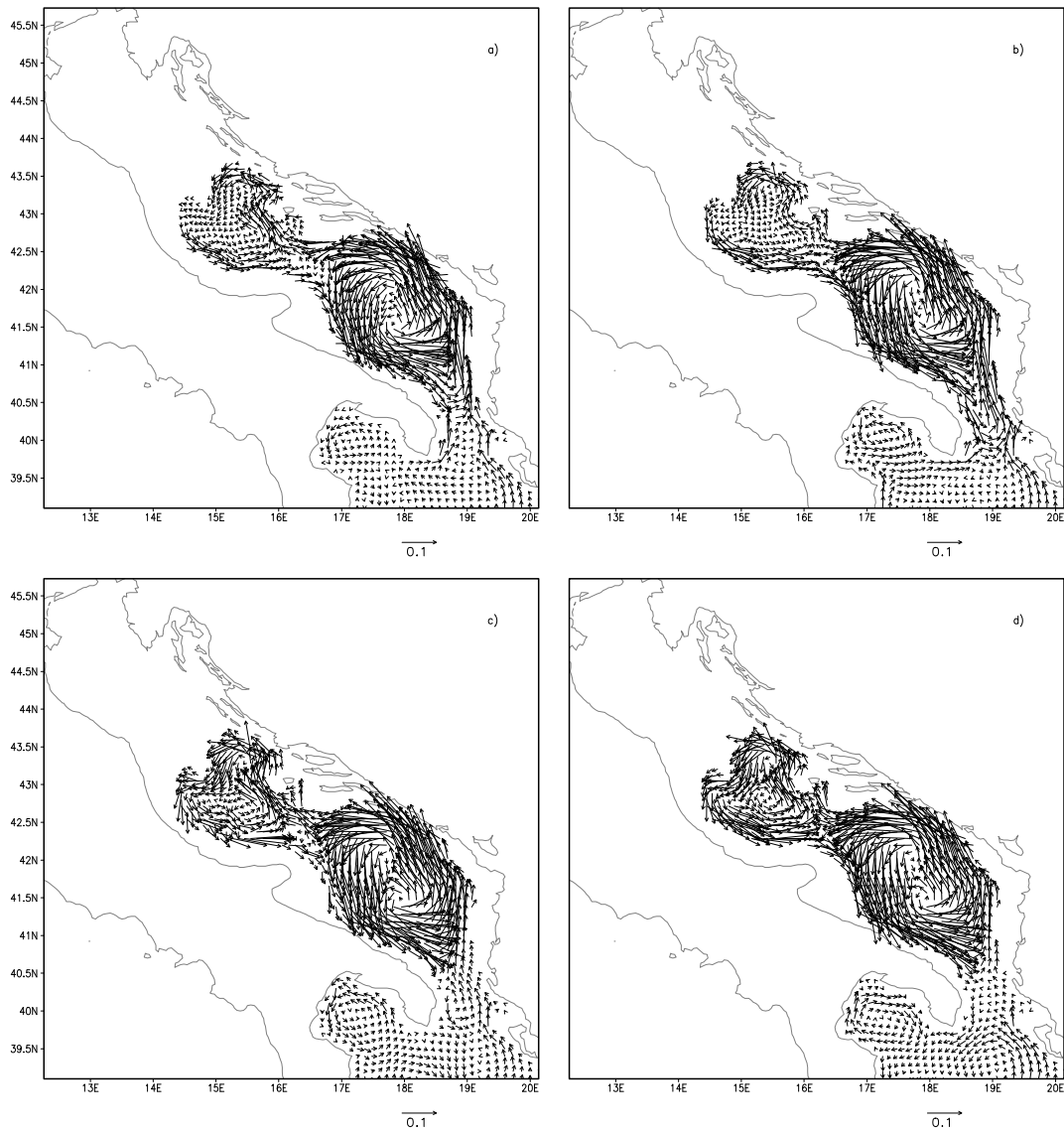


Figure 4.10: Seasonal averages of velocity fields at 100m depth simulated by the high resolution coupled model ( $ms^{-1}$ ). a) winter, b) spring, c) summer, d) autumn

water in the South Adriatic Depression and in the Ionian Sea. It can be seen from seasonal averages that there is a permanent inflow of relatively warm Levantine water from the Ionian Sea through the Otranto strait and along the south-eastern coast. Relatively warm Levantine water partially recirculates in the South Adriatic Gyre. In summer and in autumn it is partially advected along the eastern

coast further to the north into the Pomo Depression. In winter cold water appears along the western coast in the Pomo Depression and along the Palagruza Sill. The distribution of horizontal gradients indicates that there is the transport of relatively warm water from the South Adriatic Depression into the Pomo Depression in the east and the transport of relatively cold water from the Pomo Depression into the South Adriatic Depression in the west. The gradients are especially large in winter, when also the temperature in the central part of the South Adriatic Depression is lower than in other seasons. The main reason for this specific distribution of temperature in winter months may be the sinking of the cold surface water along the western shelf (Artegiani et al. 1997b) and the convection in the centre of the South Adriatic Depression due to the strong cooling of the surface water (Pollak 1951, Ovchinnikov et al. 1985).

The mean value of seasonal averages of the temperature and the intensity of horizontal gradients simulated at 100m depth are lower than the climatology based on in-situ measurements made by Artigiani et al. (1997b) and displayed in Fig.4.9. The difference is relatively small in winter and it is larger in autumn. On the other hand the spatial distribution is in good agreement with the climatology, especially during winter when an area with cold water and minimum temperatures appears next to the western coastal shelf. One reason for the colder simulated mean temperature may be the data set used for the southern boundary condition. In the MODB climatological data set temperatures at the 100m depth are lower than the corresponding temperatures in the climatological analysis by Artigiani et al. (1997b). Due to the horizontal advection of the temperature from the Ionian Sea into the South Adriatic Depression along the eastern coast the simulated temperature at the 100m depth is significantly influenced by climatological values at the boundary.

Seasonal averages of the velocity field at 100m depth are displayed in Fig.4.10. In all seasons the circulation is cyclonic in both depressions. We can see that the largest intensity of the velocity is in the South Adriatic Depression and close to internal boundaries. There is an almost permanent inflow from the Ionian Sea along the eastern coast. Again, we can see that there is the inflow from the South Adriatic Depression into the Pomo Depression along the eastern side of the Palagruza Sill and that there is the outflow from the Pomo Depression into the South Adriatic Depression along the western side of the Palagruza Sill.

## 4.2 Discussion and validation of atmospheric model results

The most important parameters simulated by the atmospheric model, used in simulations by oceanographic models, are the surface heat fluxes and the wind stress. Therefore, to evaluate the atmospheric model simulation, first we will concentrate on the evaluation of the calculation of surface fluxes over the sea. Also, the evaluation will include simulated evaporation and precipitation fields, which influence the simulation of the surface salinity.

YEAR	1991	1992	1993	1994	1995	1996	1997	Mean
Short wave radiation	211.0	190.3	201.3	200.4	201.8	193.0	206.4	200.6
Long wave radiation	-102.6	-97.6	-97.0	-98.1	-101.1	-98.0	-103.5	-99.7
Latent heat flux	-103.6	-91.4	-93.8	-90.0	-105.2	-106.3	-107.6	-99.7
Sensible heat flux	-26.0	-19.5	-22.7	-17.7	-27.6	-25.0	-21.9	-22.9
Total heat flux	-21.2	-18.2	-12.2	-5.4	-32.1	-36.3	-26.6	-21.7
Evaporation	1.31	1.24	1.23	1.24	1.34	1.35	1.36	1.30
Precipitation	0.45	0.47	0.43	0.40	0.55	0.63	0.51	0.49
Evaporation-Precipitation	0.86	0.77	0.80	0.84	0.79	0.72	0.75	0.79

Table 4.1: Yearly averages of all components of surface heat flux for the Adriatic simulated by the atmospheric model ( $Wm^{-2}$ ). The last column on the right gives the seven-year mean value for each heat flux component and the total mean flux simulated in the period 1991-1997. Spatially and temporary averaged precipitation and evaporation per unit surface, with their seven-year mean values, are given at the bottom of the table ( $m^{-1}$ ).

The atmospheric model is used in a seven-year simulation during the time period 1991-1997 to produce averaged climatological forcing fields for the ocean model. The model is applied in the one-way forcing mode, using sea surface

	May (1986)	Artegiani et al. (1997a)	Maggiore et al. (1998)
Short wave radiation	172.0	162.9	218.0
Long wave radiation	-67.9	-72.1	-91.0
Latent heat flux	-108.2	-92.5	-122.0
Sensible heat flux	-17.7	-17.7	-22.0
Total heat flux	-21.8	-19.4	-17.0
Evaporation		1.17	1.58
Precipitation		1.02	0.70
Evaporation-Precipitation		0.15	0.88

Table 4.2: Climatological estimates and calculations of the spatially and temporally averaged heat flux components ( $Wm^{-2}$ ), evaporation and precipitation per unit surface ( $m^{-1}$ ) in the Adriatic from other studies.

temperature fields analysed from satellite observations available for this time period. Yearly averages of each of the components of the heat flux, calculated in the model and spatially averaged over the Adriatic Sea, are given in Table 4.1. Results of calculations and climatological estimates originating from other studies are given in Table 4.2.

The yearly averaged short wave radiation simulated by the model varies between  $190Wm^{-2}$  in 1992 and  $211Wm^{-2}$  in 1991, with the seven-year mean of  $201Wm^{-2}$ . This value is higher than the value obtained in the climatological estimate by May (1986) and in the calculation by Artégiani et al. (1997a), but it is lower than the value obtained in the calculation by Maggiore et al. (1998).

The seven-year averaged long wave radiation is  $-100Wm^{-2}$ , and the value varies between  $-104Wm^{-2}$  in 1997 and  $-97Wm^{-2}$  in 1993. The seven-year averaged value is somewhat higher than values estimated and calculated by May (1986), by Artégiani et al. (1997a) and by Maggiore et al. (1998). One explanation for this difference is that other studies performed simplified parameteri-

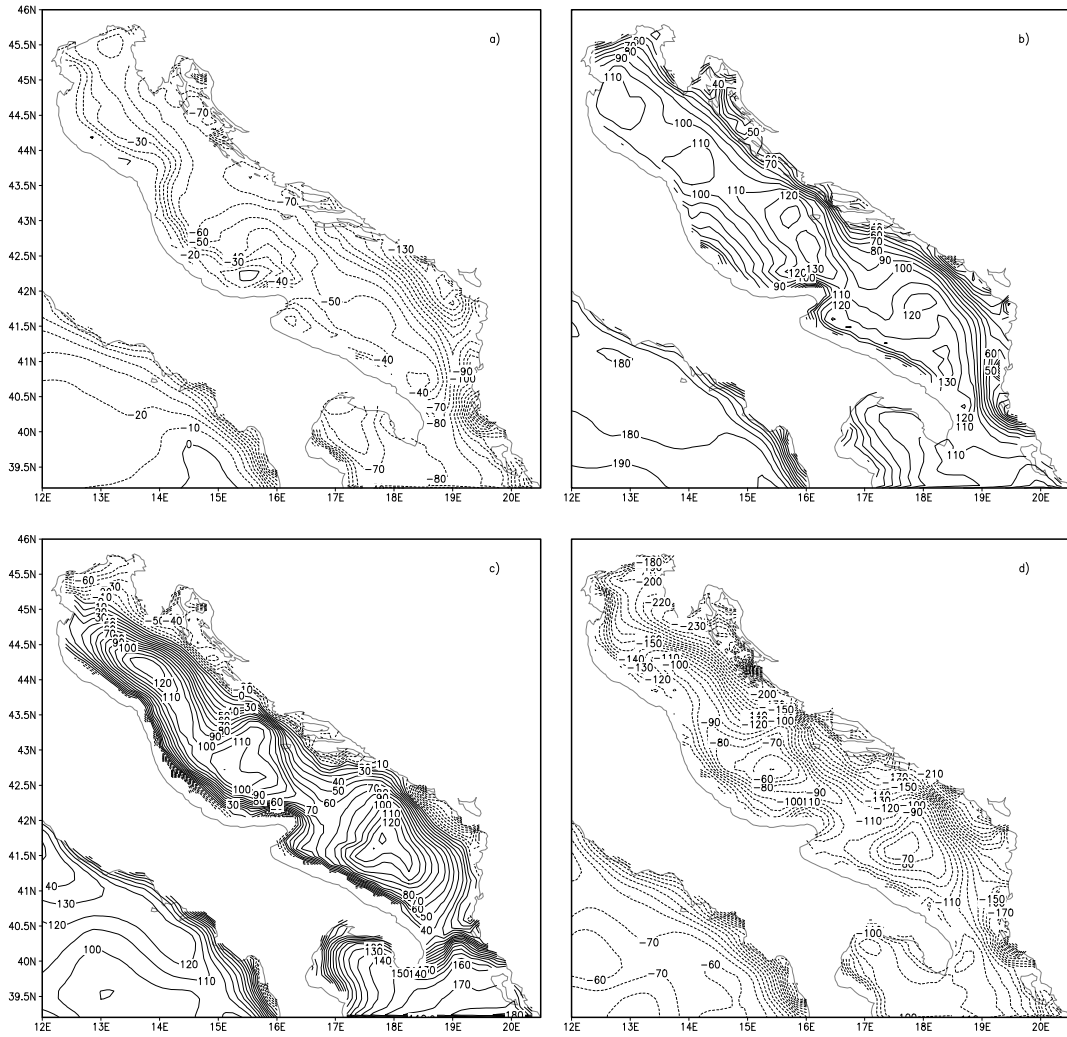


Figure 4.11: Seasonal averages of the total heat flux simulated by the high resolution coupled model ( $Wm^{-2}$ ). a) winter, b) spring, c) summer, d) autumn

sations of the long wave radiation using only the two-dimensional climatological percentage of the cloud cover together with the information on the near-surface temperature and water vapour, while in the atmospheric model the long wave radiation is parameterised using emissivity functions calculated from full vertical profiles of temperature, water vapour and clouds.

The simulated latent heat flux averaged over each year has the maximum heat loss of  $-108Wm^{-2}$  in 1997 and the minimum heat loss of  $-90Wm^{-2}$  in 1994. The simulated seven-year mean heat loss is  $-100Wm^{-2}$ . This value is between climatological values calculated by May (1986) and by Artegiani et al.

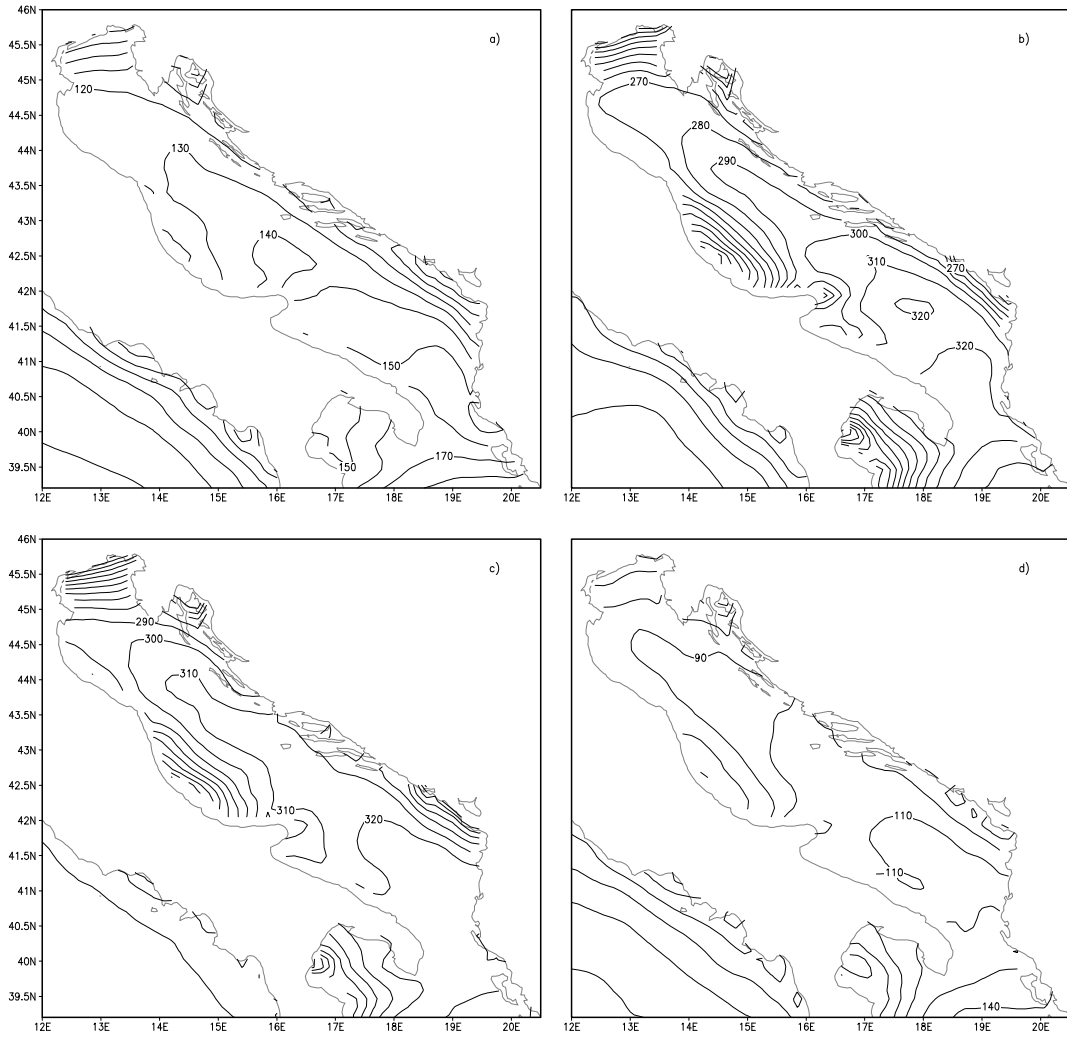


Figure 4.12: Seasonal averages of the short wave radiation simulated by the high resolution coupled model ( $Wm^{-2}$ ). a) winter, b) spring, c) summer, d) autumn

(1997a), and it gives a smaller heat loss than the value calculated by Maggiore et al. (1998).

Yearly averages of the sensible heat flux vary between  $-25Wm^{-2}$  in 1996 and  $-18Wm^{-2}$  in 1994 with the mean flux of  $-22Wm^{-2}$ . The heat loss due to the sensible heat flux is larger than the estimate by May (1986) and the calculation by Artegiani et al. (1997a), but it is very similar to the calculation by Maggiore et al. (1998).

The simulated total heat flux over the Adriatic, averaged in the seven-year period, is  $-21.7Wm^{-2}$ . The calculated value is in very good agreement with

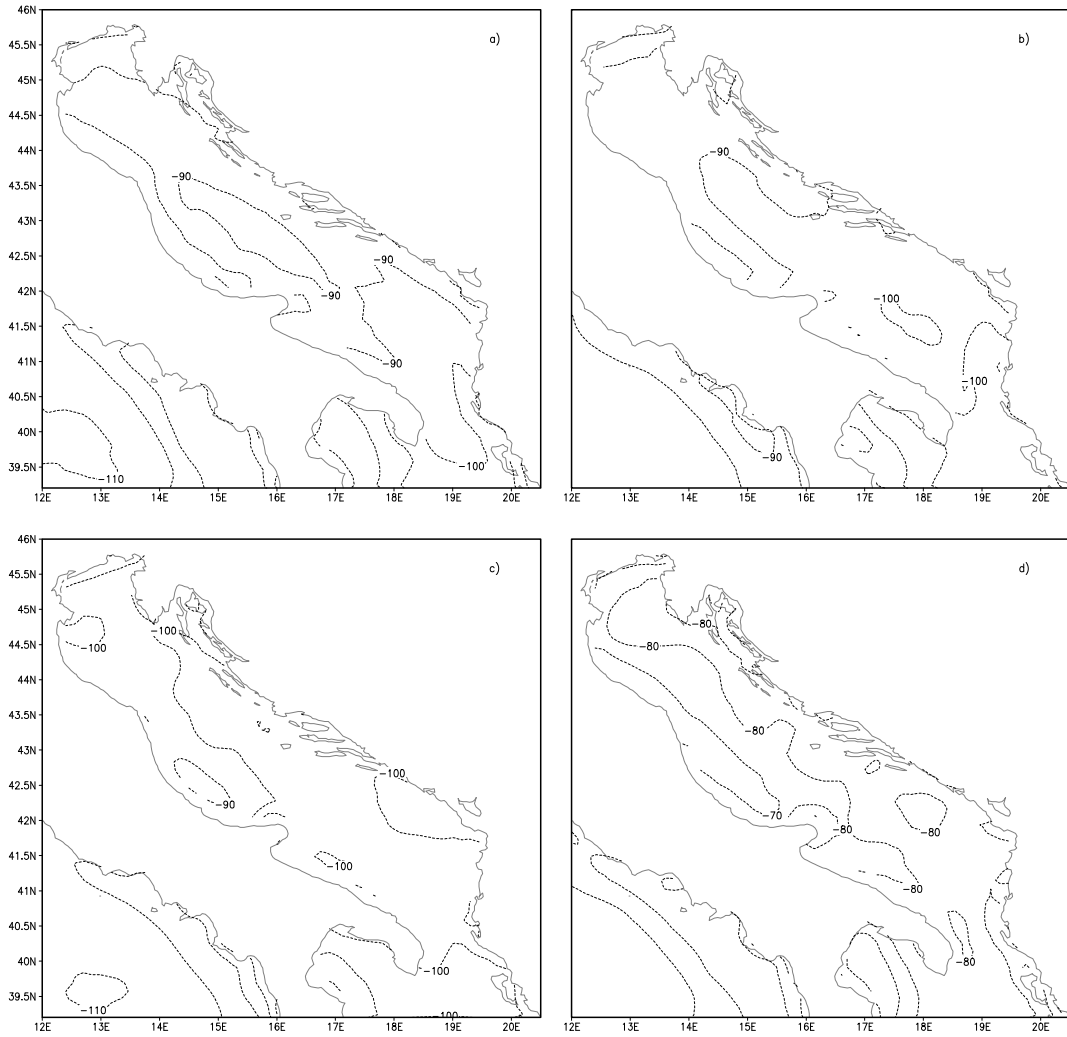


Figure 4.13: Seasonal averages of the long wave radiation simulated by the high resolution coupled model ( $Wm^{-2}$ ). a) winter, b) spring, c) summer, d) autumn

other studies. The best agreement is with the climatological estimate by May (1986), while the calculations by Artegiani et al. (1997a) and by Maggiore et al. (1998) give somewhat lower values. The simulated total heat flux averaged over each year shows a relatively large variation between the maximum heat loss of  $-36.3Wm^{-2}$  in 1996 and the minimum heat loss of  $-5.4Wm^{-2}$  in 1994. However, the oscillation of the heat loss is smaller than that obtained in the calculation by Maggiore et al. (1998) in the four-year period 1991-1994. Also, it can be noticed that in this study the averaged value significantly depends on the averaging period. For instance, in the four-year period 1991-1994 it would

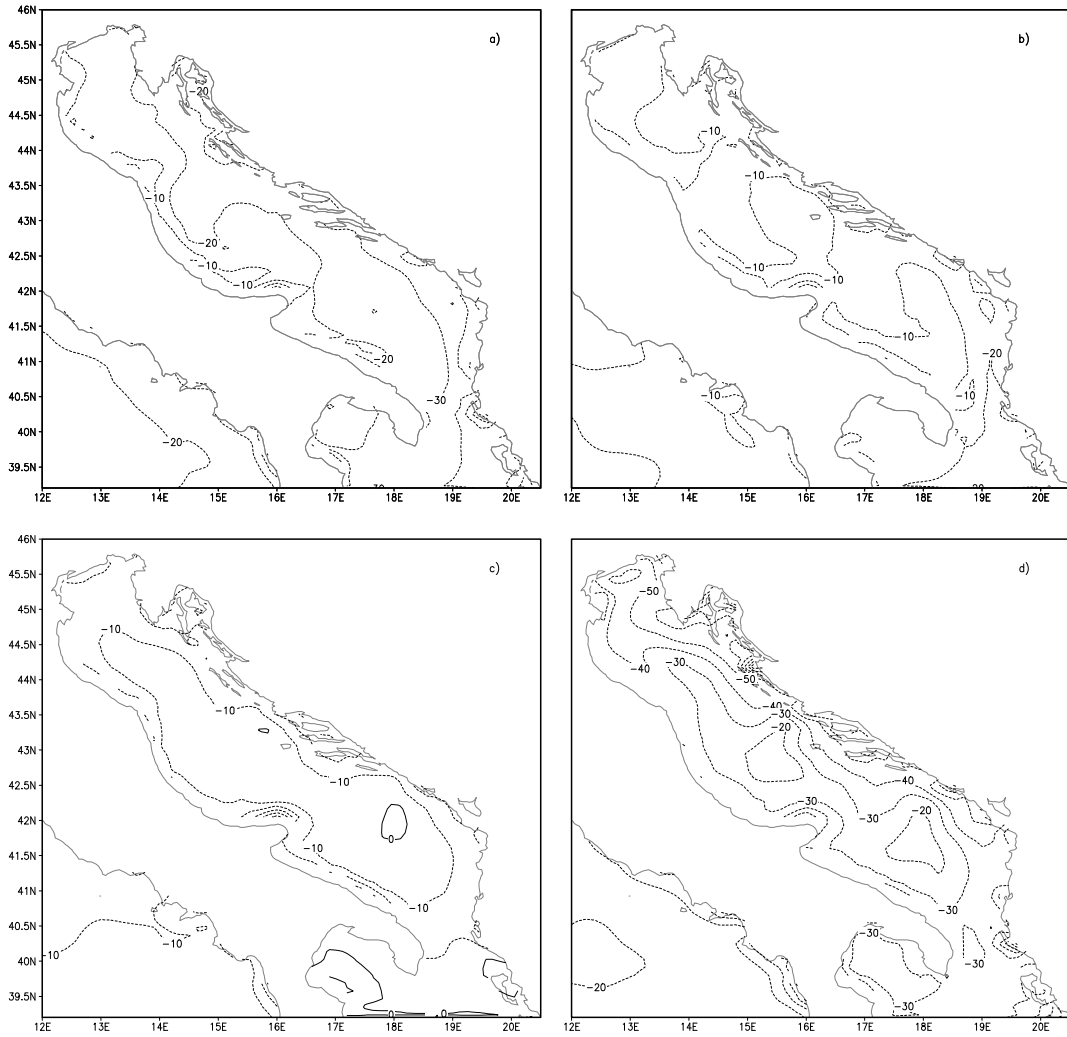


Figure 4.14: Seasonal averages of the sensible heat flux simulated by the high resolution coupled model ( $Wm^{-2}$ ). a) winter, b) spring, c) summer, d) autumn

be  $-14.3Wm^{-2}$ , what is very close to the value calculated during the same time period by Maggiore et al. (1998).

Another difference in comparison to the calculation by Maggiore et al. (1998) is that they attribute the yearly variability of the total heat flux mainly to the variation in the latent and sensible heat flux components. In the coupled model simulation only the long wave radiation component of the heat flux has a small annual variation, and the short wave radiation contributes significantly to the variation of the yearly averaged heat flux. This difference in the result may be explained by the fact that Maggiore et al. (1998) calculated the short wave

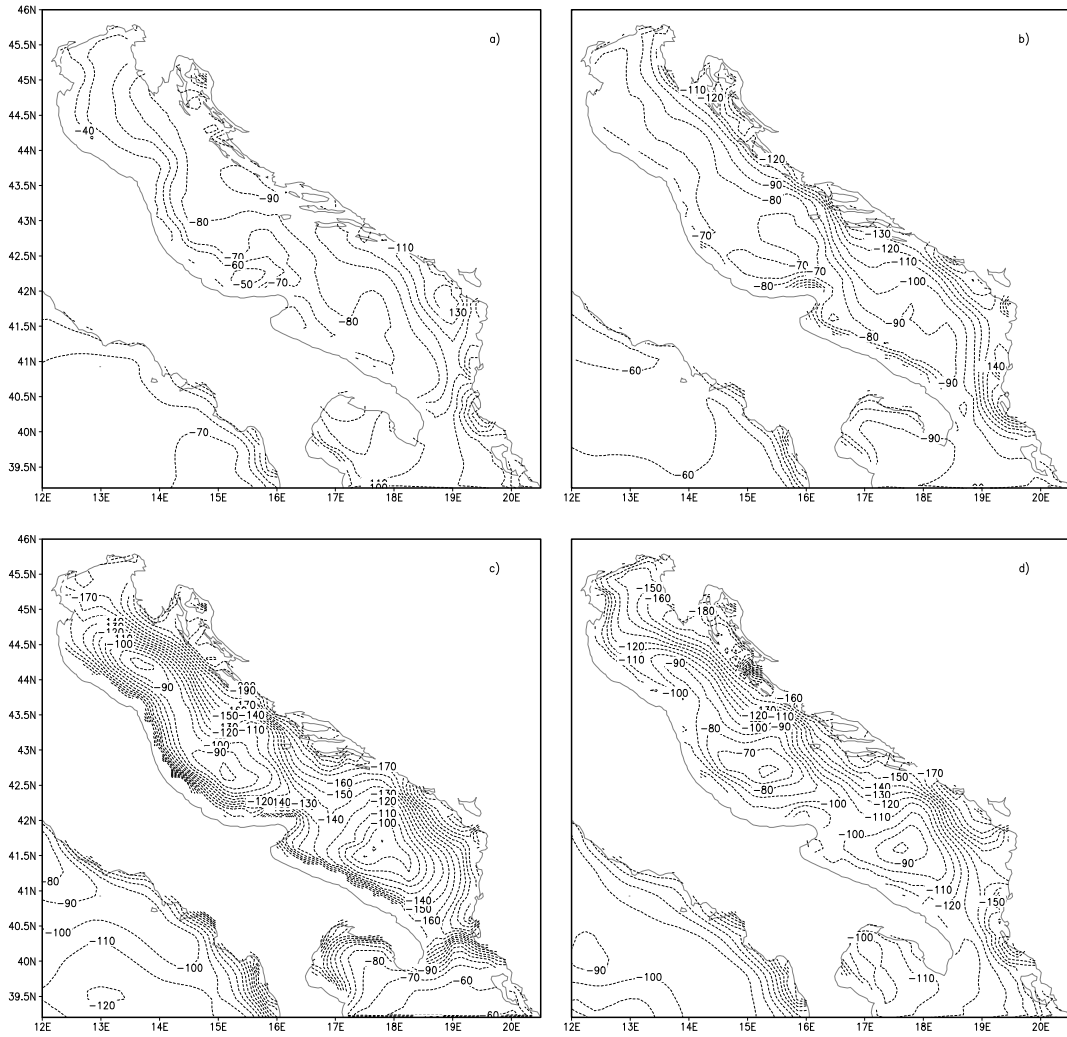


Figure 4.15: Seasonal averages of the latent heat flux simulated by the high resolution coupled model ( $Wm^{-2}$ ). a) winter, b) spring, c) summer, d) autumn

radiation using the climatological cloud cover which is identical in each year, while they calculated sensible and latent heat fluxes from ECMWF analyses using the realistic temporal variation of meteorological parameters during each year. On the other hand, it appears from the result of the coupled model that the temporal variability of the cloud cover distribution may significantly influence the yearly averaged short wave radiation and the yearly averaged total heat flux.

Annual averages of the evaporation and the precipitation per unit surface in the Adriatic simulated by the model are given in the bottom of Table 4.1. The seven-year averaged difference between the evaporation and the precipitation per

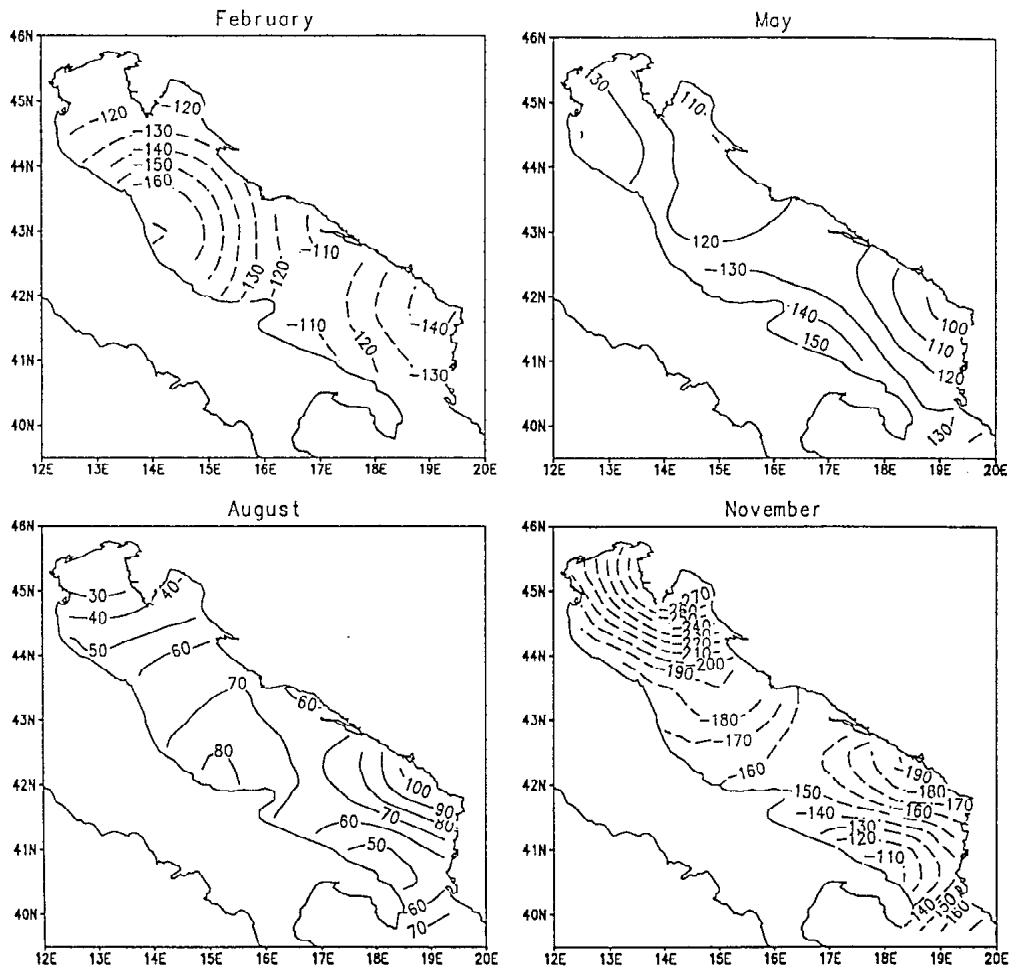


Figure 4.16: The climatological total heat flux ( $Wm^{-2}$ ) for selected months calculated by May (1986) (from Artegiani et al. 1997b).

unit surface is  $0.79m^{-1}$ , with the variation of the yearly mean value between the minimum of  $0.72m^{-1}$  in 1996 and the maximum of  $0.86m^{-1}$  in 1991. The yearly variation is mainly the consequence of the variation in the precipitation. The seven-year averaged difference between the evaporation and the precipitation is significantly larger than that obtained in the calculation by Artegiani et al. (1997a) and it is smaller than the value obtained in the calculation by Maggiore et al. (1998). On the other hand, the seasonally averaged precipitation obtained in the coupled model simulation is in very good agreement with the climatological estimate by Zore-Armanda (1969) calculated using offshore observations. We can see that the calculation using the coupled model gives the yearly averaged evaporation which is similar to that calculated in other studies. On the other

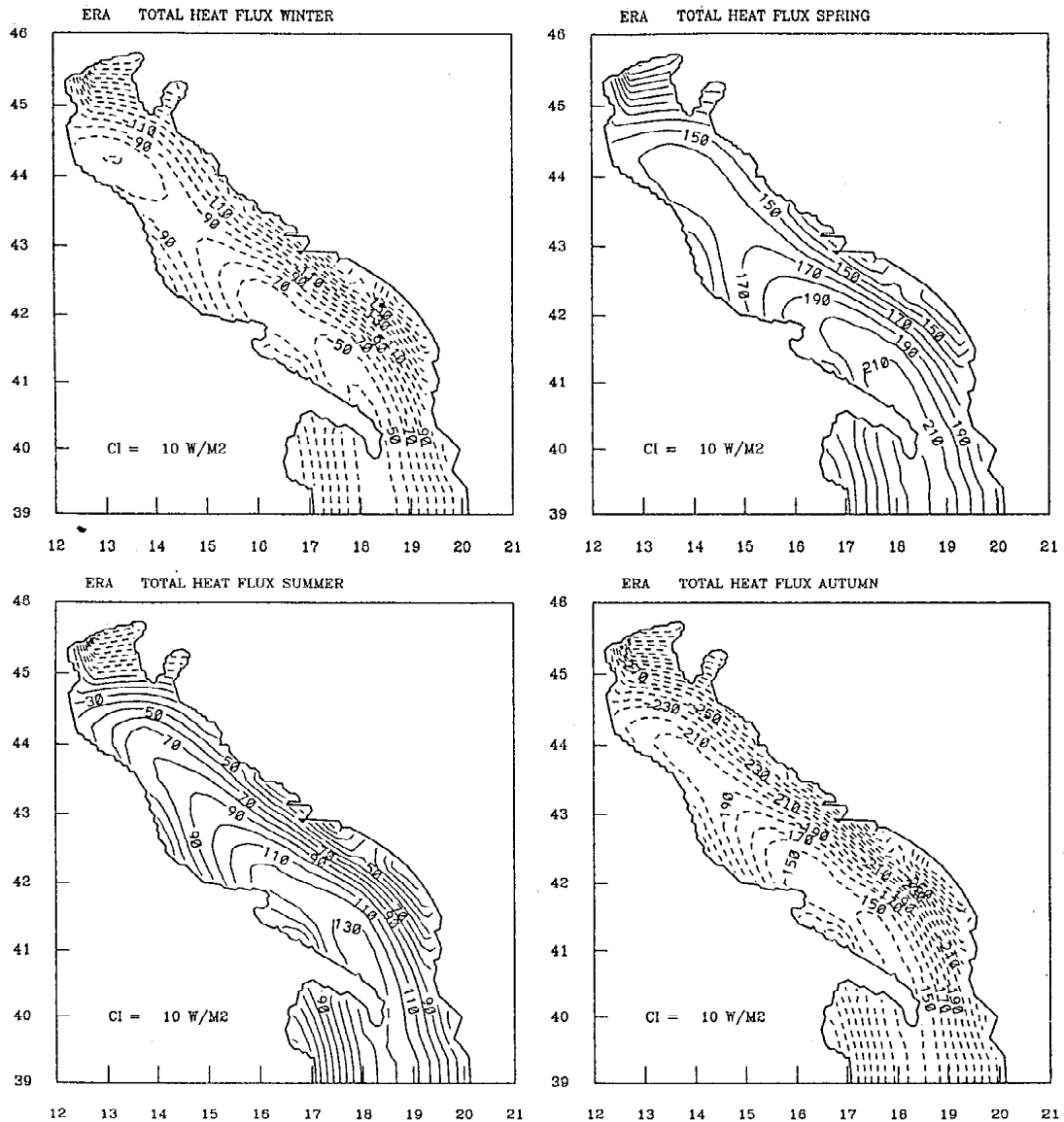


Figure 4.17: Seasonal averages of the climatological total heat flux ( $W m^{-2}$ ) calculated by Maggiore et al. (1998) (from Zavaratelli et al. 2002).

hand, the the yearly averaged precipitation is smaller then that calculated in studies presented in Table 4.2, but it is in relatively good agreement with the COAMPS estimate given in Maggiore et al. (1998).

The spatial distribution of seasonal averages of the total heat flux for 1997, simulated by the high resolution coupled model, is displayed in Fig.4.11. There is the average heat loss in the Adriatic in winter and in autumn, and the average

heat gain in spring and in summer. In winter the largest heat loss is in the south-eastern part of the Adriatic, and the smallest heat loss is along the western coast. In spring the largest heat gain is in the south of the Adriatic along the western coast, and in summer the largest heat gain is offshore. In summer there is the heat loss in a narrow band along almost all coasts. In autumn the largest heat loss is along coasts, with the maximum in the north-eastern part of the Adriatic.

Seasonal averages of the short wave radiation in the Adriatic for 1997 show a relatively permanent spatial structure in all seasons (Fig.4.12), but there is a large variability in the mean intensity. In all seasons the maximum of the short wave radiation is in the southern part of the Adriatic, along the western coast, and the minimum is along the coast in the northern and south-eastern parts of the Adriatic. On the other hand, fields of seasonally averaged long wave radiation (Fig.4.13) show a larger spatial variability, but a much smaller variability in the intensity of the spatially averaged value. In autumn there is the largest heat loss due to the long wave radiation in the north-eastern part of the Adriatic.

The seasonal mean of the sensible heat flux for 1997 (Fig.4.14) is relatively small during winter, spring and summer, when it reaches the minimum, and it is significantly larger in autumn, with the largest heat loss along the eastern coast. The latent heat flux has a relatively large seasonal variability of the mean value and a large variation of the spatial distribution (Fig.4.15). The heat loss due to the latent heat flux is the lowest in winter and it is the highest in summer. It has the largest value along the eastern coast. The minimum is in the north-western part of the Adriatic in winter, along the western coast in spring and offshore in summer and autumn.

The comparison between different components of the total heat flux in the Adriatic demonstrates that the high spatial variability of the total heat flux in the summer and in autumn is mainly the consequence of the spatial variability of the latent heat flux, while in winter and in spring it is mainly caused by the combination of the spatial variability of the latent heat flux and of the short wave radiation. Clearly, the seasonal change of the spatially averaged total heat flux is the consequence of the change in the short wave radiation in all seasons, but in autumn it is also determined by the increase of the magnitude of other components of the total heat flux along the eastern coast.

In general, the spatial distribution of the total heat flux and its components for 1997 is in good agreement with other studies which calculated the climatological heat flux in the Adriatic. In all other studies (May 1986, Artegiani et al. 1997a,

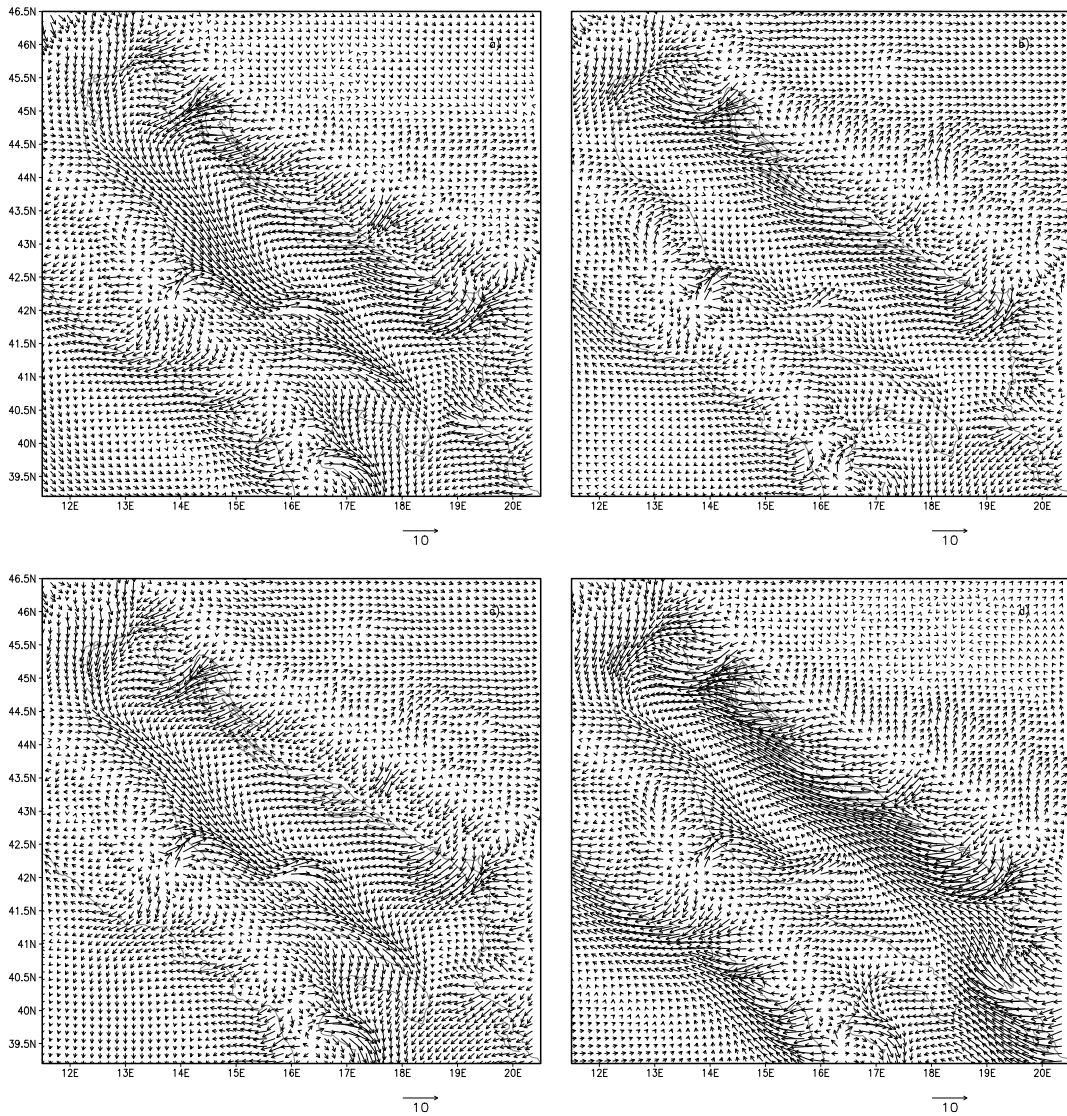


Figure 4.18: Seasonal averaged wind velocity vectors 10m above the ground simulated by the high resolution coupled model ( $ms^{-1}$ ). a) winter, b) spring, c) summer, d) autumn

Maggiore et al. 1998) there is generally the heat loss in winter and in autumn, and there is the heat gain in spring and in summer.

In comparison with the climatological calculation by May (1986), displayed in Fig.4.16, the spatial structure of the total heat flux computed by the coupled model contains many more details. In winter another major difference is that the climatology by May (1986), like the reported result by Artegiani et al. (1997a), gives the largest total heat loss close to the north-western coast, while in the

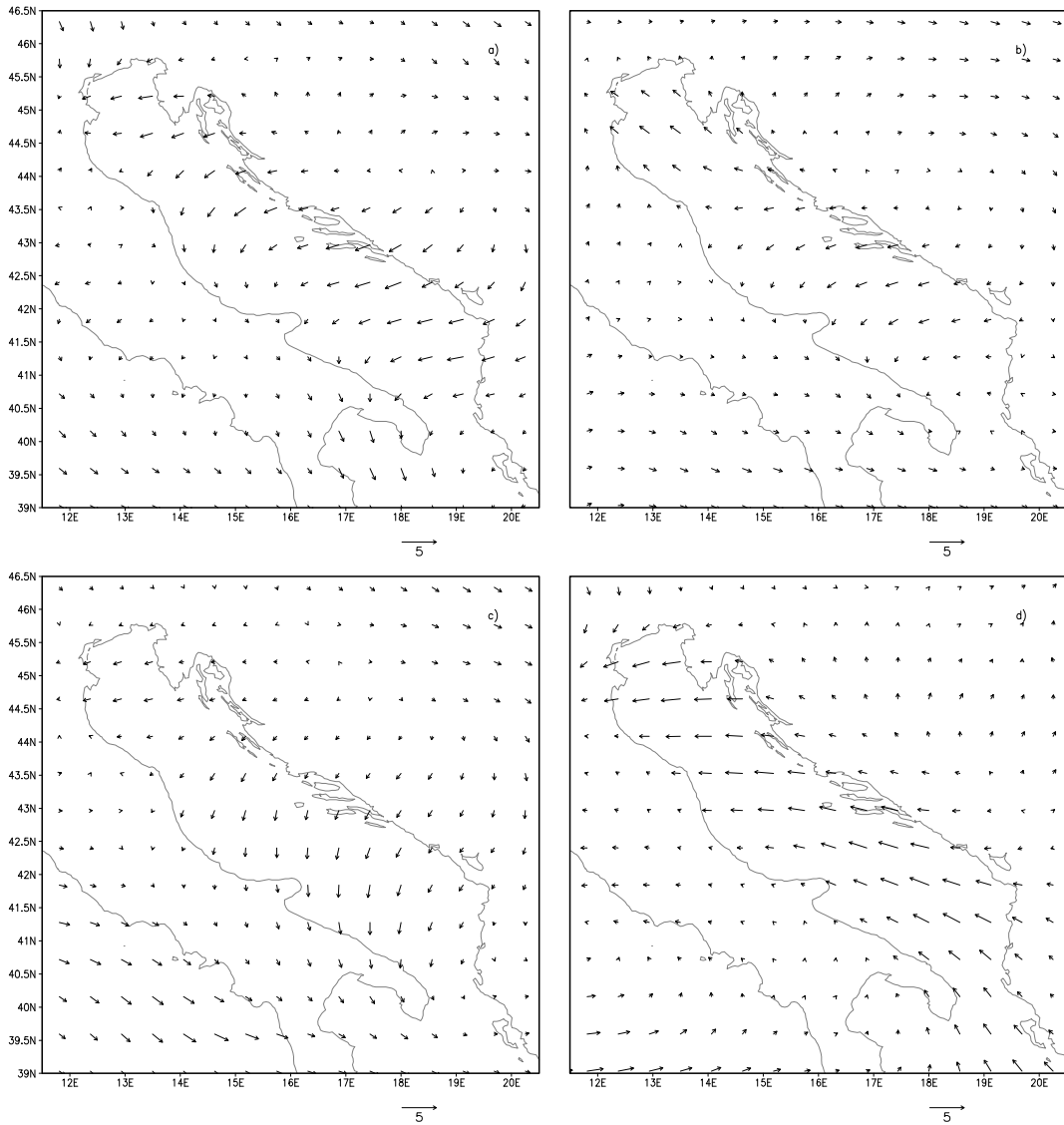


Figure 4.19: Seasonal averaged wind velocity vectors 10m above the ground from ECMWF reanalyses ( $ms^{-1}$ ). a) winter, b) spring, c) summer, d) autumn

coupled model result the largest heat loss is along the south-eastern coast, and there is a minimum in the heat loss along the western coast. In other seasons, spatial structure of the outputs of the simulation performed by the coupled model are generally in good qualitative agreement with the climatological calculation by May (1986).

The spatial distribution of the seasonal mean of the total heat flux computed for 1997 may be also compared to the results of the calculation by Maggiore et al. (1998), presented in Zavaratelli et al. (2002) and displayed in Fig.4.17. Again, the

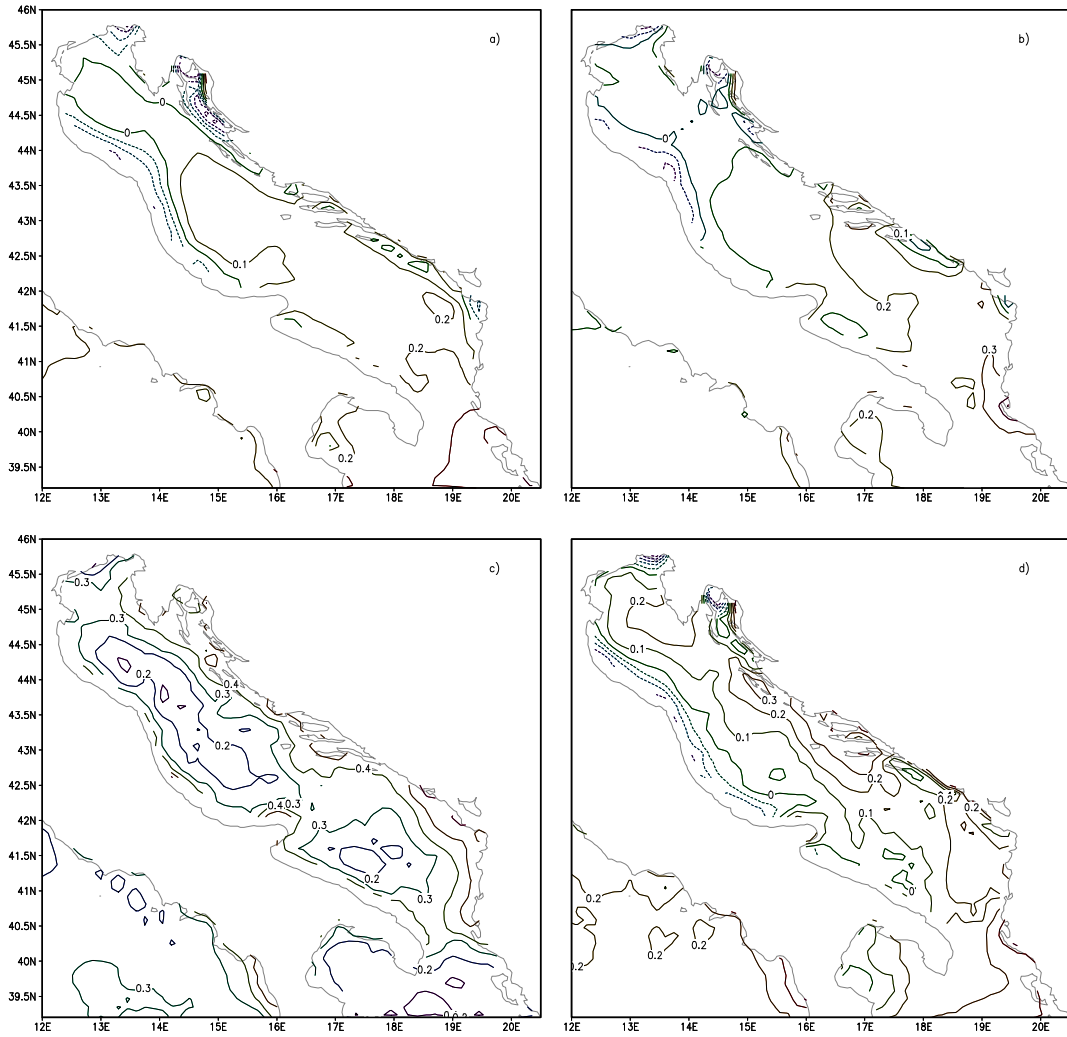


Figure 4.20: Seasonal averages of the difference between the evaporation and the precipitation per unit surface ( $m^{-1}$ ) simulated by the high resolution coupled model ( $m^{-1}$ ). a) winter, b) spring, c) summer, d) autumn

seasonal mean of the total heat flux computed in the coupled model simulation contains much more spatial detail. However, this time main spatial features of the winter distribution of the total heat flux in Maggiore et al. (1998) are generally very similar to those computed by the coupled model, with the maximum heat loss along the eastern coast. Also, in other seasons, there is a good qualitative agreement between two calculations.

One larger difference between the seasonally averaged total heat flux computed by the coupled model (Fig.4.11) and that computed by Maggiore et al.

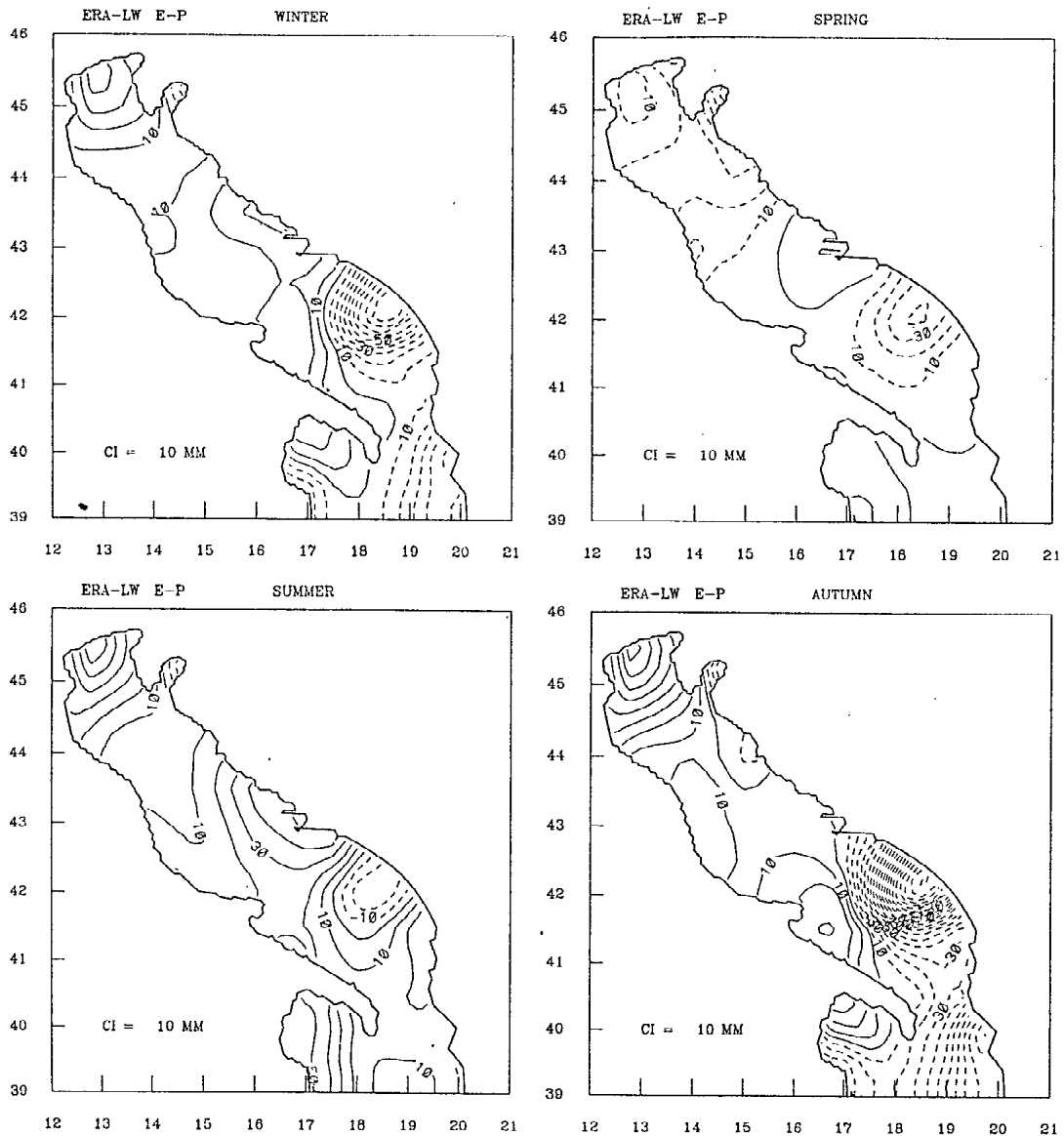


Figure 4.21: Seasonal averages of the climatological difference between the evaporation and the precipitation per unit surface ( $m^{-1}$ ) calculated by Maggiore et al. (1998) (from Zavaratelli et al. 2002).

(1998) (Fig.4.17) is the intensity of the spatially averaged heat flux in each season. In all seasons the intensity of the spatially averaged heat flux calculated by Maggiore et al. (1998) is larger than the value calculated in this study. On the other hand, seasonally averaged amplitudes of the total heat flux calculated in this study are in relatively good agreement with those calculated by May (1986).

However, the yearly mean heat loss resulting from all studies appears to have a very similar magnitude (Table 4.1 and Table 4.2).

Seasonal averages of the simulated field of wind vectors 10m above the ground are displayed in Fig.4.18. We can see that in the Adriatic the simulated wind field is strongly channelled by the coastal topography. There are several local maxima in the intensity of the 10m wind along the eastern coast formed along valleys in the Julian Alps and the Dinaric Alps (Fig.1.2). The strongest winds are in winter and autumn. In winter there is a stronger influence of the Bora wind in the North Adriatic, while in autumn there is the prevalence of the Scirocco wind along the eastern coast. In spring the wind is weaker with the prevailing south-east direction. In summer the north-eastern Bora wind dominates again, but its magnitude is weaker than in winter. Along the western coast the simulated 10m wind has mostly the north-western direction. Its mean value has the largest magnitude in winter, while it is very weak in spring.

Generally, offshore the direction and intensity of the wind velocity over the Adriatic Sea is in relatively good agreement with climatological fields calculated by May (1986) and displayed in Fig.2d in Artegiani et al. (1997b), and with ECMWF reanalyses fields displayed in Fig.4.19. On the other hand, along coasts the coupled model simulation results in stronger winds with the higher spatial variability. However, a direct comparison along coasts can not be performed, because coarse resolution climatological calculations and ECMWF reanalyses do not account for the high spatial variability of the topography along the coast.

Seasonal averages of the difference between the evaporation and the precipitation are displayed in Fig.4.20. We can see that offshore the evaporation significantly exceeds the precipitation in all seasons, and that the structure of the field is very similar to that of the seasonally averaged latent heat flux which determines the evaporation. On the other hand, along the coast there is a relatively large seasonal and spatial variability due to the significant influence of the precipitation.

In winter, in spring and in autumn the precipitation reduces the effect of the evaporation along the south-eastern coast of the Adriatic. At the same time, at some places the seasonally averaged precipitation exceeds the evaporation along the north-eastern coast, and there is a relatively wide belt where the precipitation exceeds the evaporation along the western coast. We can see that along the eastern coast main spots with large precipitation are close to places where mountain ridges are very close to the coast (Fig.1.2), indicating that the precip-

itation is intensified by the coastal topography. The relatively wide belt where the precipitation exceeds the evaporation along the western coast, may be explained by the larger precipitation along the coast compared to the precipitation offshore and by the fact that the simulated latent heat flux and therefore the evaporation have their minimum along the western coast. In summer, due to the very small seasonally averaged precipitation, the whole field mainly reflects the spatial distribution of the latent heat flux.

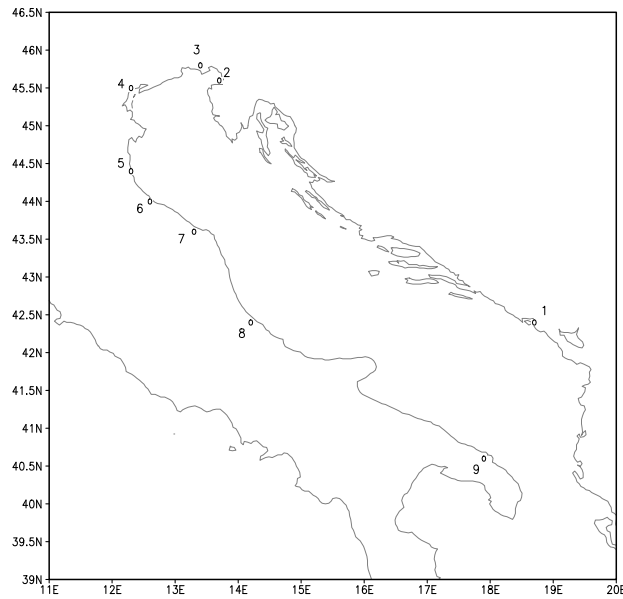


Figure 4.22: Geographical position of coastal meteorological stations used for the evaluation of model outputs. Numbers represent following stations: 1 - Tivat, 2 - Trieste, 3 - Ronchi dei Legionari, 4 - Venezia Tesserà, 5 - Punta Marina, 6 - Rimini, 7 - Falconara, 8 - Pescara and 9 - Brindisi.

Seasonal averages of the difference between the evaporation and the precipitation somewhat differ from fields calculated by Maggiore et al. (1998) and presented in Zavaratelli et al. (2002) (Fig.4.21). The main difference is that in this study the evaporation exceeds the precipitation offshore in all seasons, while in Maggiore et al. (1998), in spring there is the net negative flux over almost all the Adriatic Sea. Another difference is that in Maggiore et al. (1998) the precipitation significantly exceeds the evaporation along the south-eastern coast and it covers the large part of the South Adriatic, while in this study it only reduces the evaporation in a narrow band along the coast. The lower precipitation and

its concentration along the coast in this study, results in a lower yearly mean precipitation simulated by the coupled model in comparison to calculations by Maggiore et al. (1998) and by Artegiani et al. (1997a) (Table 4.1 and Table 4.2).

One reason for this disagreement may be that climatological estimates of the precipitation in other studies are made by the interpolation of observations at coastal stations without available values offshore, while in the coupled model result the simulated precipitation is concentrated in a very narrow band along the coast, and it is relatively weak offshore. Also, this may explain the very good agreement of the yearly mean precipitation simulated by the coupled model with the climatological estimate by Zore-Armanda (1969) performed using the offshore observations.

Atmospheric parameters simulated by the model may be compared with measurements at meteorological stations. For this purpose, 9 stations are selected along the Adriatic coast. Measured values at those stations belong to a larger data set, originating from the German Weather Service, that also includes data from several other stations positioned inland, but it is found that, due to the complex topography and complex influence of local factors, it is very difficult to directly compare values measured at surface stations with the model simulation. The geographical position of selected coastal stations is displayed in Fig.4.22.

The high resolution atmospheric model, with the sea surface temperature obtained from the analyses of satellite observations, is used as the reference experiment for the comparison with measurements. It is assumed that it provides the most accurate simulation of atmospheric parameters, because it uses the boundary condition which is the closest to the observations. However, in Section 5.2 we will analyse in detail the sensitivity of the atmospheric model results to the sea surface temperature calculation and to the horizontal resolution of the model.

In Fig.4.23 and Fig.4.24 we can see the daily variation of the difference between the measured and the simulated 2m temperature during 1997 at 9 coastal stations. Station measurements used for the validation correspond to 6:00UTC on each day, because it is found that at that time there is a sufficiently long record of available measurements at selected stations, and it is estimated that at the same time there is a less significant influence of the heating of the land by the short wave radiation on the 2m temperature. The measured value at each station is compared with the 6 hours mean of the simulated value between 3:00UTC and 9:00UTC.

We can see in Fig.4.23 that at the Station 1 there is a relatively large difference

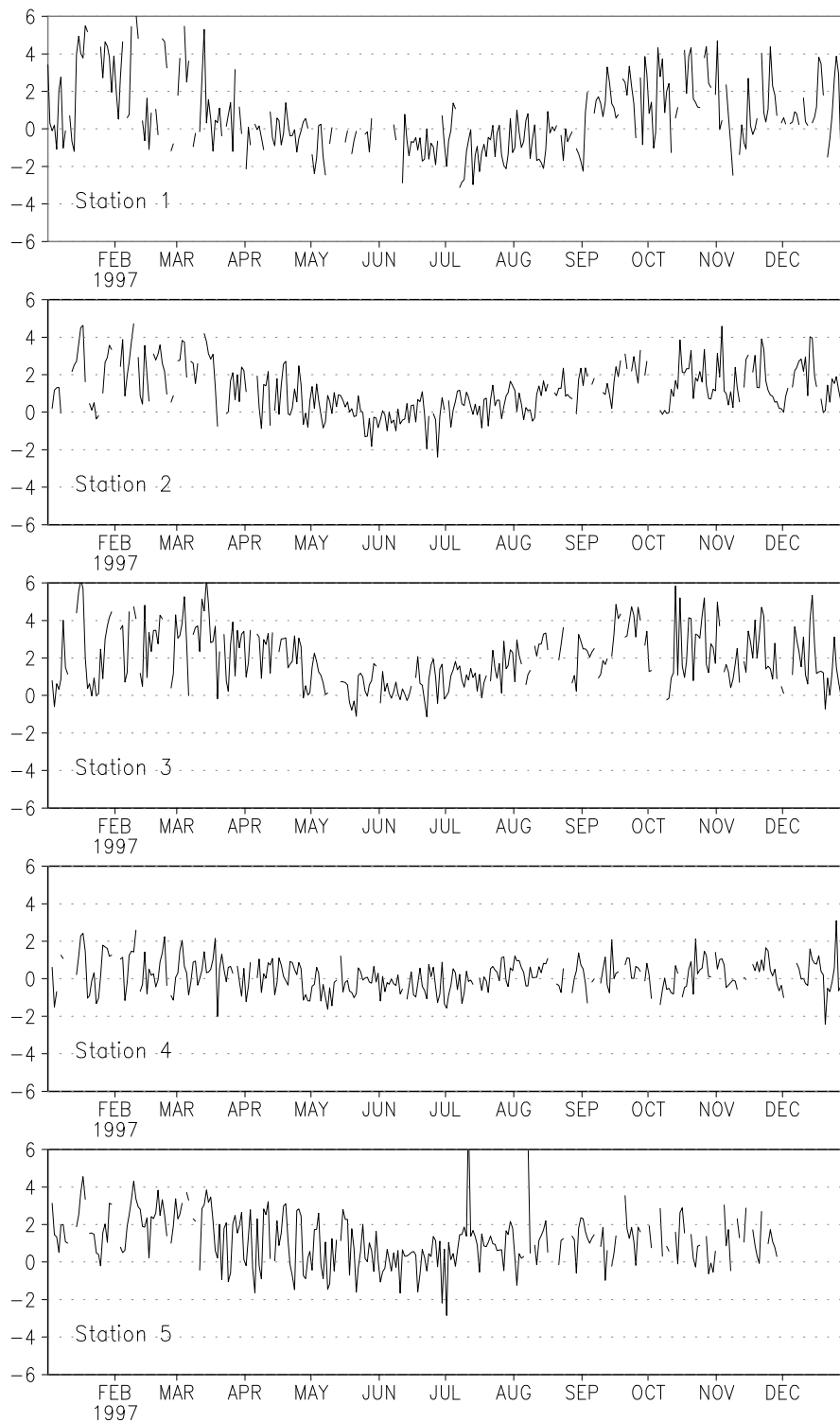


Figure 4.23: Difference between simulated and measured 2m temperature at coastal stations 1 - 5 ( $^{\circ}C$ ).

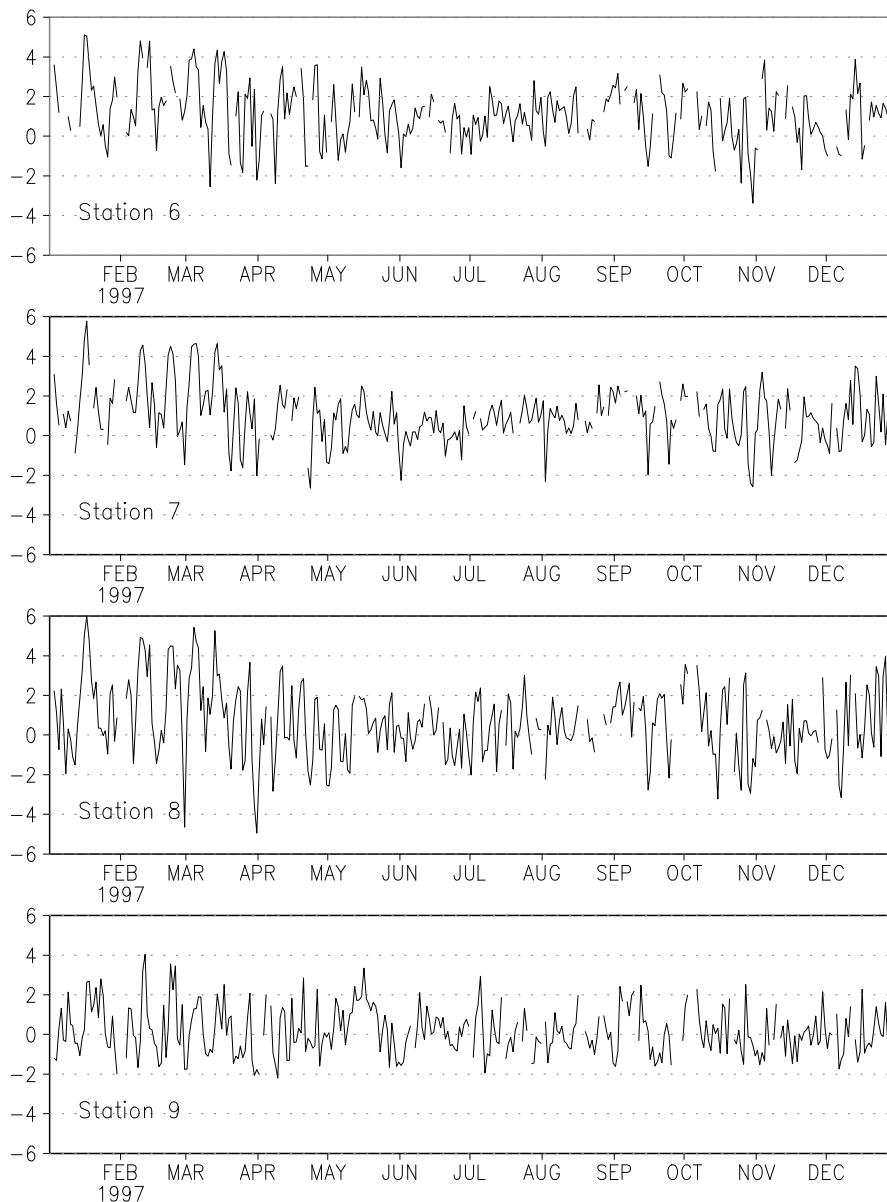


Figure 4.24: Same as Fig.4.23, but for stations 6 - 9.

between the observed and the simulated value, with a relatively large variation, in winter and autumn, while in spring and summer the difference and its variation are significantly reduced. Stations 2 and 3 show a very similar general behavior, with simulated values generally larger than observed values during the whole year, especially in winter and in autumn. The similarity originates from the fact that stations 2 and 3 are geographically very close to each other. The only visible difference between two stations is that station 2 has a somewhat smaller variation of the temperature difference around the mean. At station 4 there is a very good

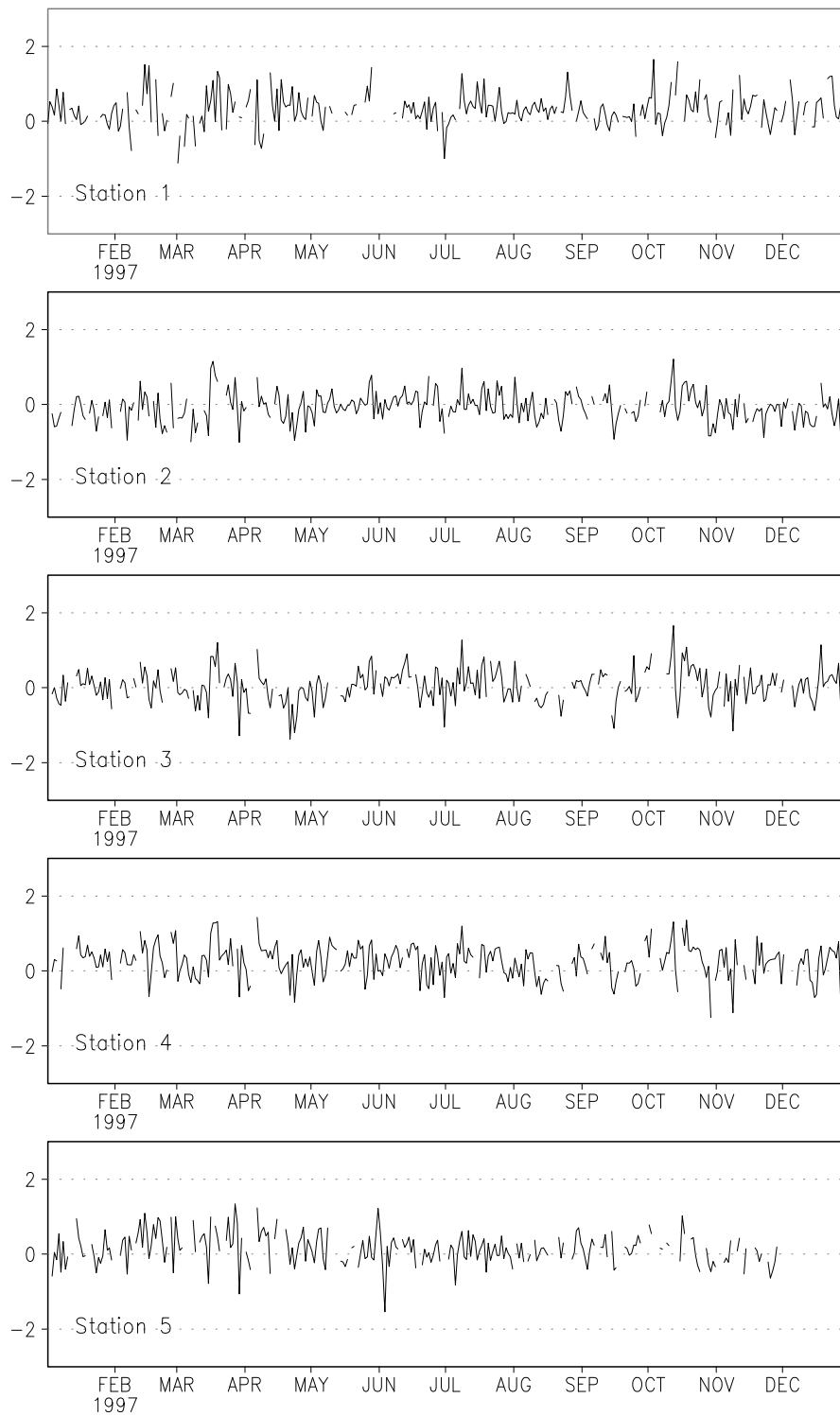


Figure 4.25: Difference between simulated and measured sea level pressure at coastal stations 1 - 5 (*mb*).

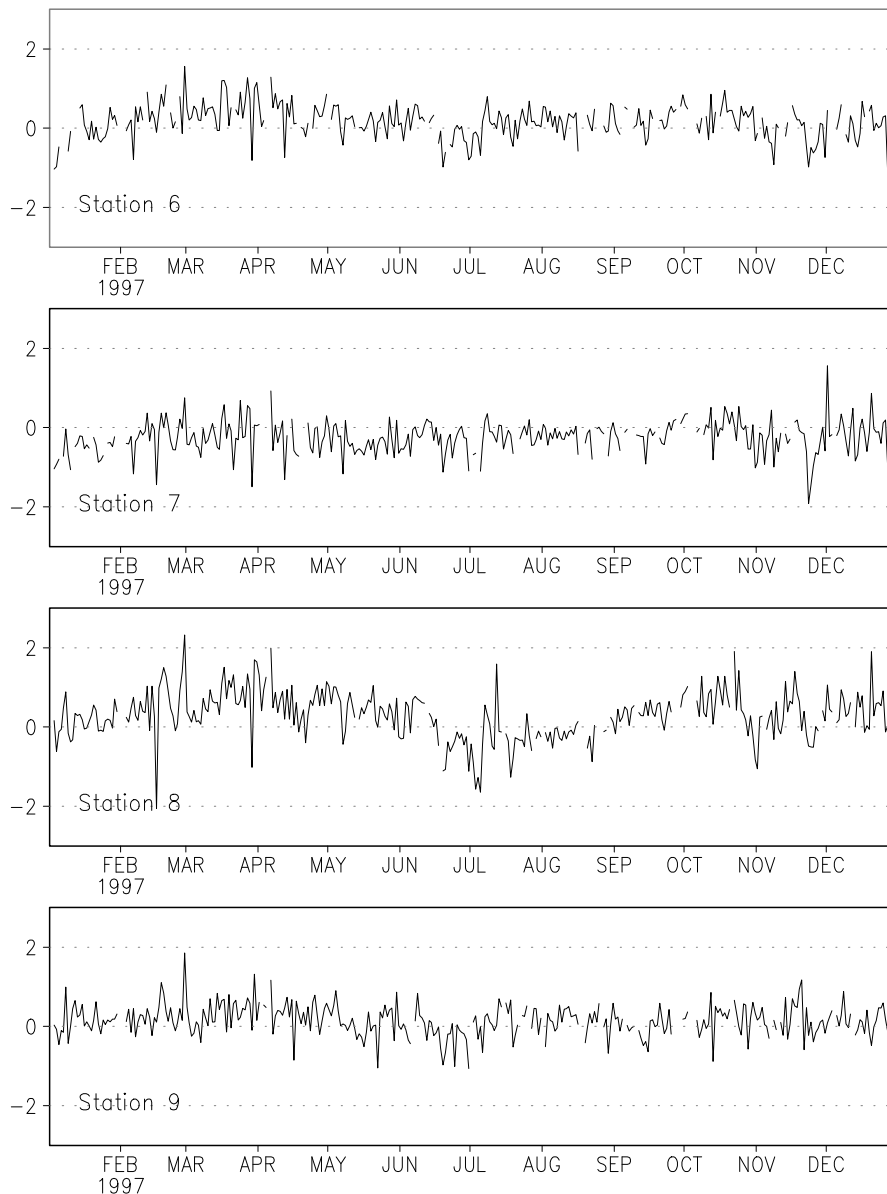


Figure 4.26: Same as Fig.4.25, but for stations 6 - 9.

agreement between the simulated and the measured 2m temperature, and in average at station 5 the simulated value is slightly higher than the measured value during the whole year.

Stations 6, 7 and 8 show a relatively large variation of the difference between the simulated and the observed 2m temperature, with a general overestimation by the model (Fig.4.24). The variation is especially pronounced at station 8 in winter. At station 9 there is a relatively good agreement between the simulated and observed temperature during the whole year.

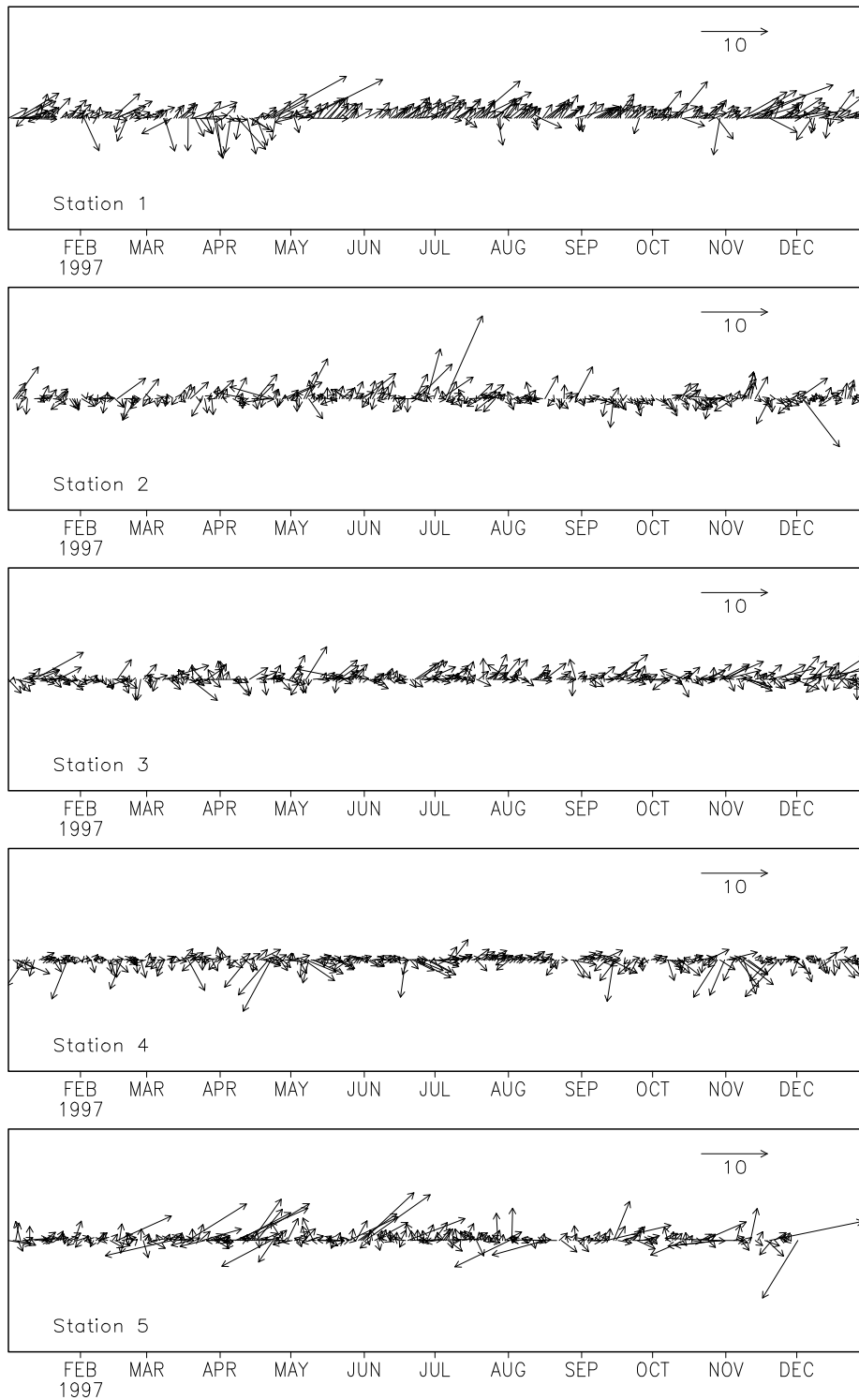


Figure 4.27: Difference between simulated and measured wind at coastal stations 1 - 5 ( $m s^{-1}$ ).

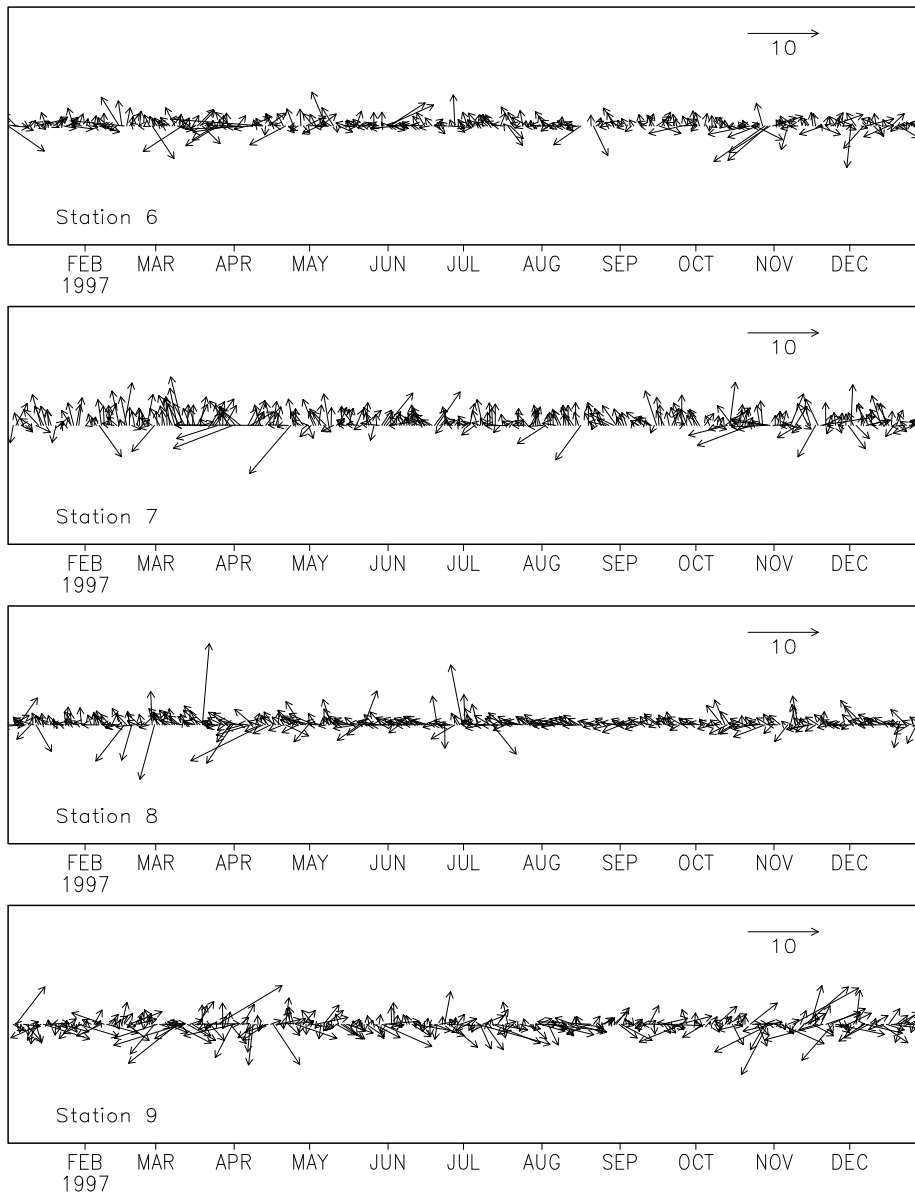


Figure 4.28: Same as Fig.4.25, but for stations 6 - 9.

The differences in the quality of the model simulation of the 2m temperature at different coastal stations may be explained by different local meteorological conditions at each station. When comparing the position of meteorological stations (Fig.4.22) with the local coastal topography displayed in Fig.1.2, and approximated in the atmospheric model, we can see that stations 1, 2 and 3 are close to high coastal mountains. As a consequence, there is a possibility that the complex topography significantly influences the local 2m temperature and that the atmospheric model is not able to simulate correctly local meteorological

conditions. As a confirmation for this statement, the correspondence between the measured and the simulated 2m temperature is generally better at stations positioned along the western coast which has the simpler coastal topography.

On the other hand, monthly averaged and instantaneous values of the difference between the simulated and the measured 2m temperature at coastal stations are generally in good agreement with differences between simulated and analysed fields in the same geographical area obtained by several other limited area atmospheric models which used similar horizontal resolutions, e.g. results of several limited area models displayed in Fig.5 and Fig.6 in Christensen et al. (1997).

The difference in the sea level pressure is much less dependent on the position of the station (Fig.4.25 and Fig.4.26). There appears to be a quite homogeneous distribution of the variance of the difference between the simulated and the measured sea level pressure at all stations throughout the year. Only station 8 shows a significant seasonal variation of the difference with a higher simulated than observed sea level pressure in spring and in autumn. The better correspondence between the simulated and the observed sea level pressure compared with the correspondence between the simulated and the observed 2m temperature can be explained by the fact that the sea level pressure field depends much less on local meteorological conditions than the 2m temperature field. Its value and spatial distribution are significantly influenced by lateral boundary conditions of the atmospheric model, and in the coupled model lateral boundary conditions are obtained from very accurate ECMWF reanalyses. Again, there is a high level of agreement of monthly averaged and instantaneous differences between the simulated and the measured sea level pressure, with monthly averaged differences between simulated and analysed fields obtained by other limited area atmospheric models in the same geographical area, e.g. those displayed in Fig.3 and Fig.4 in Christensen et al. (1997).

The difference between the simulated and measured 10m wind at 9 coastal stations is displayed in Fig.4.27 and in Fig.4.28. When comparing these figures with Fig.4.18 we can see that in general the intensity of the difference between the simulated and the observed wind is smaller than the simulated wind intensity itself, although at several particular dates and at some stations the difference is large. There is no general similarity in the difference between the simulated and the observed value at different stations indicating that it may be caused by local meteorological conditions at each station. At station 1 the difference between the simulated and the observed winds indicates that the simulated winds

generally have a too weak component from the north-east direction. Also, at station 7 the simulated wind in general has a too weak component from the north-western direction. At all other stations the disagreement between the simulated and the observed winds has no dominant direction. The differences between the simulated and observed 10m wind could not be directly compared with results from other limited area models. However, we could expect that at least the quality of the simulation of the geostrophic part of the surface wind should be similar to that obtained by other limited area models, because the difference between the simulated and the observed surface pressure is similar to those originating from other limited area models given in Christensen et al. (1997).

# Chapter 5

## Sensitivity experiments

### 5.1 Differences between experiments

Five oceanographic model experiments are performed in the study. Differences between experiments are summarized in Table 5.1. In the control experiment GCM the surface heat fluxes and the wind stress are calculated from the ECMWF reanalyses, using the method described in Subsection 3.3.

Experiment	Horizontal resolution	Two-way interaction	Time step for surface fluxes
GCM	50km	no	6h
S25	25km	no	1h
S13	13km	no	1h
C25	25km	yes	1h
C13	13km	yes	1h

Table 5.1: Differences between experiments.

In experiment S25 surface heat fluxes and the wind stress are computed using the low resolution atmospheric model set-up and the analysed sea surface temperature, while in experiment S13 the computation is made with the high resolution atmospheric model set-up and the analysed sea surface temperature. Experiment C25 is performed using the fully coupled model with the coarse resolution atmospheric model set-up, and in experiment C13 the fully coupled model is applied with the fine resolution atmospheric model set-up.

To perform the comparison between ocean model outputs resulting from annual simulations with five different experimental configurations, daily averaged outputs of each experiment are decomposed into EOF modes. In this way it becomes possible to represent highly variable annual fields only by the coefficients of time series and by the spatial distribution of the most important EOF modes, assuming that those EOF modes account for the major part of the variance. Only two-dimensional fields are compared, and the transformation is made from the spatially and temporally varying field represented by the matrix  $\mathbf{T}(m, n)$ , where  $m$  are all ocean model points in the horizontal, and  $n = 365$  are output time steps. The matrix transformation is performed using the mathematical libraries LAPACK and BLAS.

## 5.2 Sensitivity of oceanographic outputs

### 5.2.1 Surface temperature

The surface temperature is the first and the most important ocean model parameter for the comparison between experiments. One reason for this choice is that the sea surface temperature is the parameter which reacts most sensitively to the change of surface heat fluxes. Another reason is that each day a relatively large number of satellite observations is available, covering the whole Adriatic and containing the information about the high spatial and temporal variability of the surface temperature.

Objective analyses of the sea surface temperature are performed on the ocean model grid using “night pass” satellite observations and the method described in Subsection 3.2.3. Only “night pass” satellite observations are used to eliminate the possible occurrence of large measurement errors during the day due to the skin effect. Then the EOF analysis is performed using the transformation of fields of the difference between the simulated and analysed surface temperature. Prior to the computation of EOF modes, the mean value of each field of differences is subtracted at each time step from each point value. Consequently, the variance of EOF modes represents the variance of the spatial variability of the difference between the simulated and analysed surface temperature.

The temporal variation of the spatially averaged difference between the simulated and the analysed surface temperature and the temporal and spatial variation of dominant EOF modes in experiment GCM, in which the ocean model is forced by surface fluxes computed from ECMWF parameters, are displayed in Fig.5.1 and Fig.5.2.

In Fig.5.1a we can see that from January until May the spatially averaged surface temperature is in relatively good agreement with the analysis, with a small underestimation until the middle of March. In the middle of May the spatial mean of the simulated surface temperature becomes almost  $4^{\circ}\text{C}$  warmer than the analysed value. Then, in following two weeks the difference between the simulated and the analysed surface temperature becomes reduced with the minimum at the beginning of June, but it rises again reaching the maximum in the second half of June. Then the difference starts to oscillate, but there is a clear tendency of the simulated mean to be higher by about  $3^{\circ}\text{C}$  than the analysed mean, with the maximum difference at the beginning of September. After this peak the difference is reduced, but still in autumn and at the end of December its mean is about  $1^{\circ}\text{C}$  higher than the analysed mean.

The time variation of the first temporal EOF coefficient, displayed in Fig.5.1b, shows a good agreement between the simulated and the analysed surface temperature until the middle of May, but then there starts a period with a relatively large difference. Again the simulated value is larger than the analysed. This EOF is by far the most important mode which accounts for 77.5% of the total variance. The spatial structure of the first EOF mode is displayed in Fig.5.2a. We can see that it is practically flat over the Adriatic, with the significant gradient only close to the southern open boundary in the Otranto Strait. Negative values in the Otranto Strait and in the Ionian Sea in summer and in autumn, in combination with large positive coefficients, indicate that in this area simulated values are in better agreement with analyses than in the Adriatic Sea.

The reason is that the large positive mean difference between the simulation and the analysis (Fig.5.1a) at the same time corresponds to the large positive first EOF coefficient (Fig.5.1b). On the other hand, close to the southern model boundary, simulated fields are significantly influenced by climatological values imposed at the boundary, which are in better agreement with the analyses. Consequently close to the southern model boundary the first EOF mode (Fig.5.2a) is negative indicating that there the positive deviation of the simulated temperature is reduced.

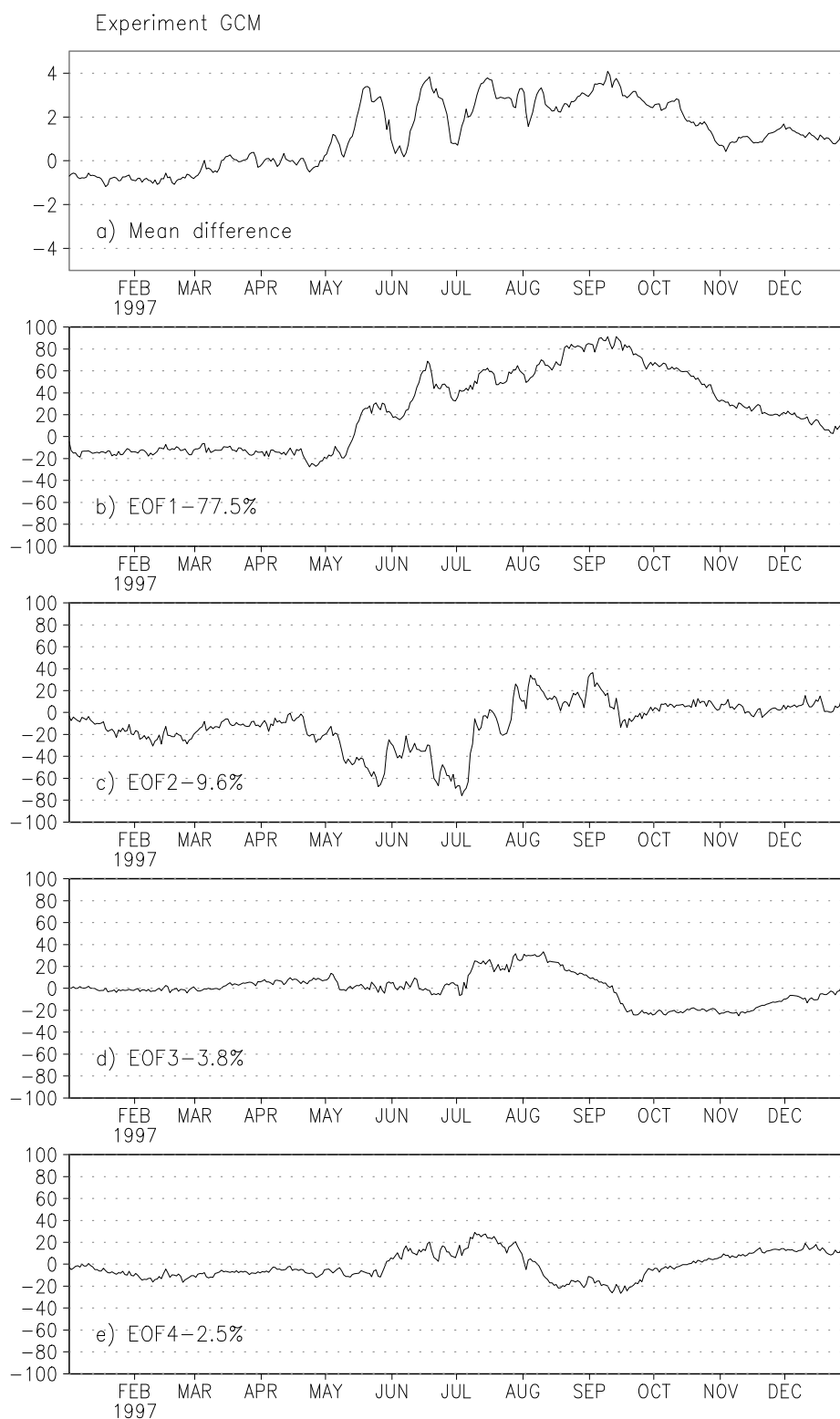


Figure 5.1: Experiment GCM: the mean difference and coefficients of the first four EOF modes of the difference between simulated and measured surface temperature ( $^{\circ}C$ ).

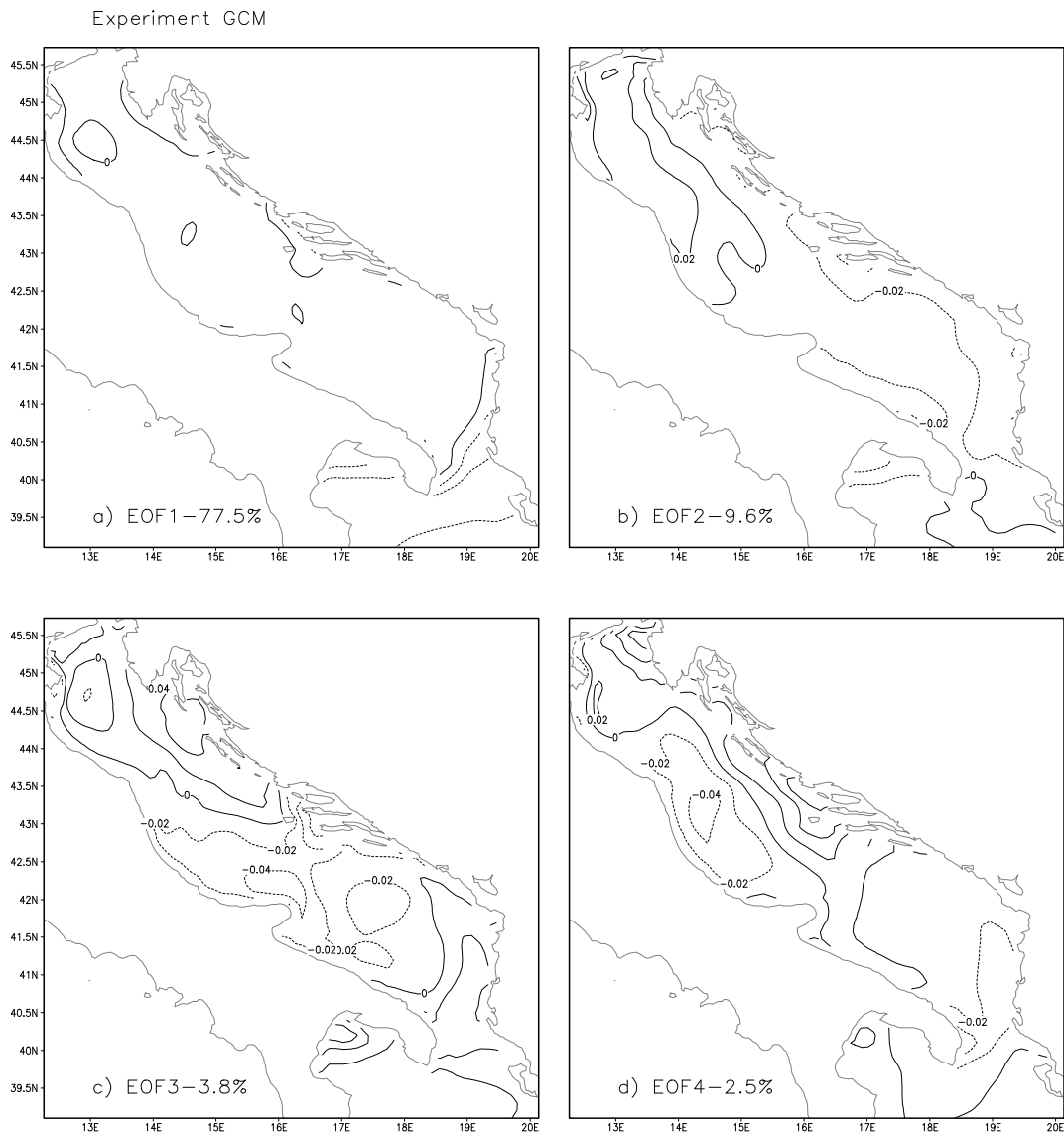


Figure 5.2: Experiment GCM: the first four EOF modes of the difference between simulated and measured surface temperature.

Also, the time variation of the second EOF coefficient (Fig.5.1c) shows a good agreement until May, and then the coefficient becomes negative until August. In August the coefficient changes the sign and becomes positive until the middle of September, when it becomes relatively small until the end of December. This EOF mode accounts for 9.6% of the total variance. The spatial structure of the second EOF mode is displayed in Fig.5.2b. It can be seen that from May until

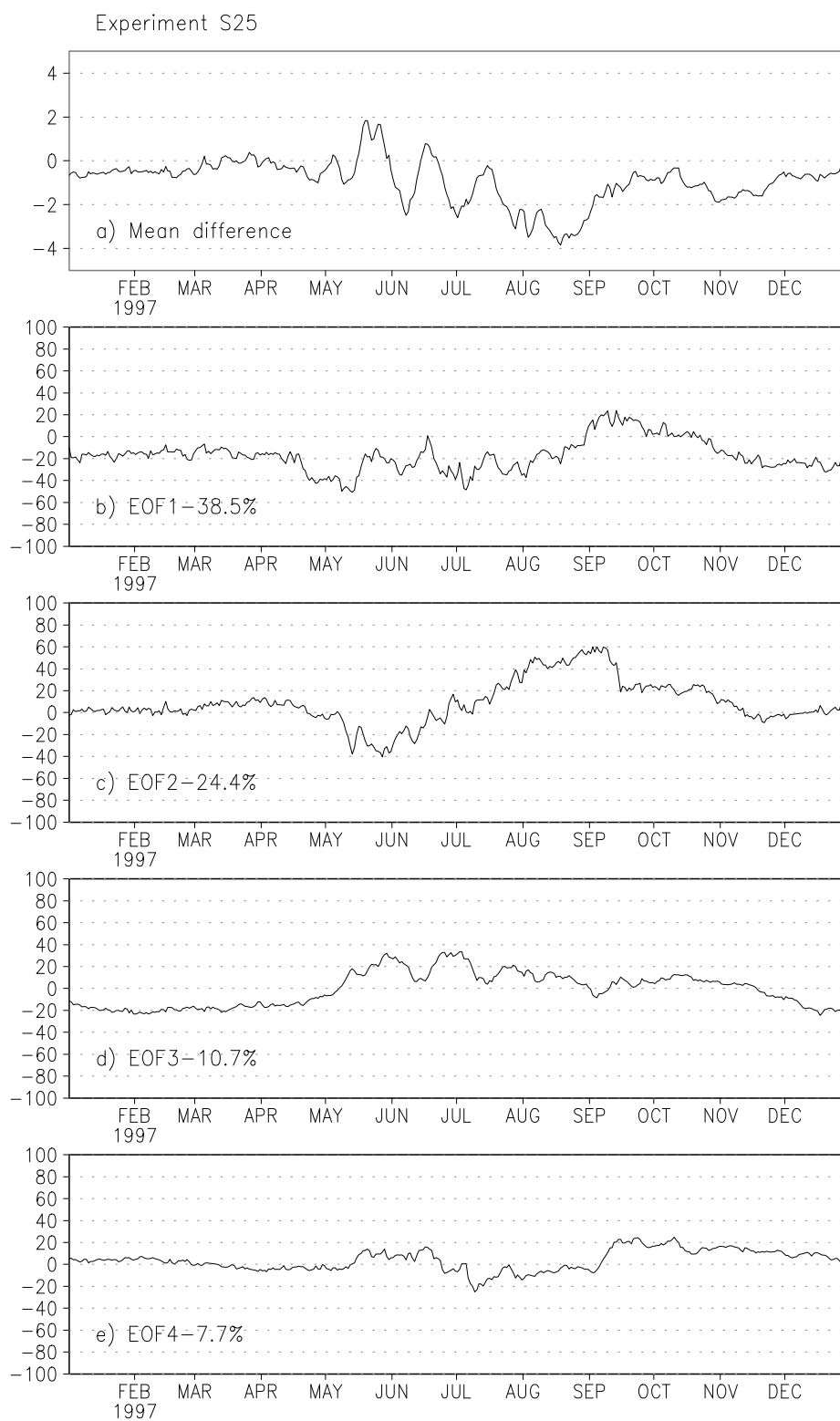


Figure 5.3: Same as Fig.5.1, but for experiment S25

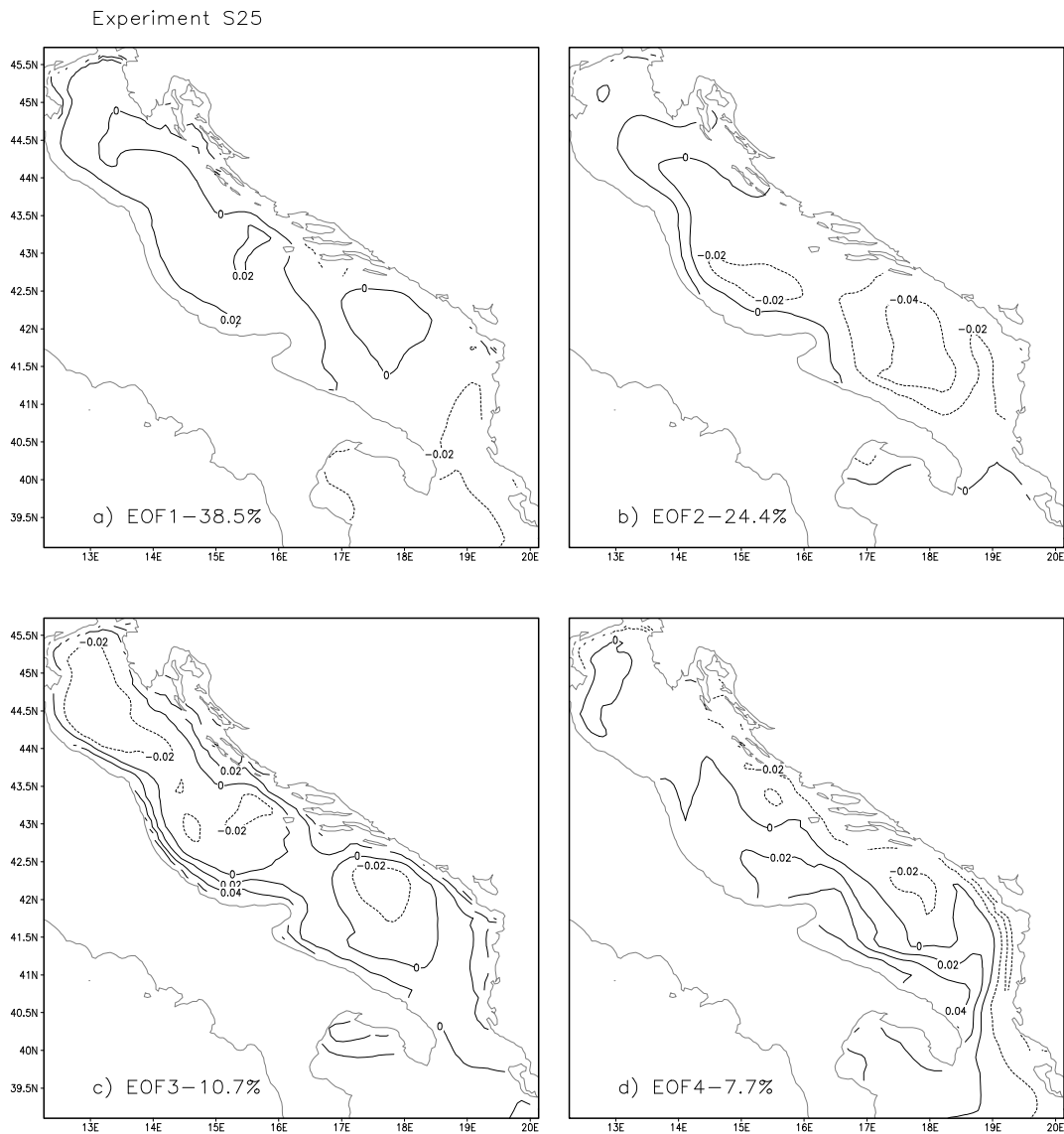


Figure 5.4: Same as Fig.5.2, but for experiment S25

the middle of August the simulated positive north-south gradient is larger than observed, and from the beginning of August until the middle of September the negative north-south gradient is larger than observed. The third and the fourth EOF modes account only for the 3.8% and 2.5% of the total variance respectively and therefore they are statistically less significant.

The time variation of the spatially averaged difference between the simulated and the analysed surface temperature and the time variation of dominant EOF

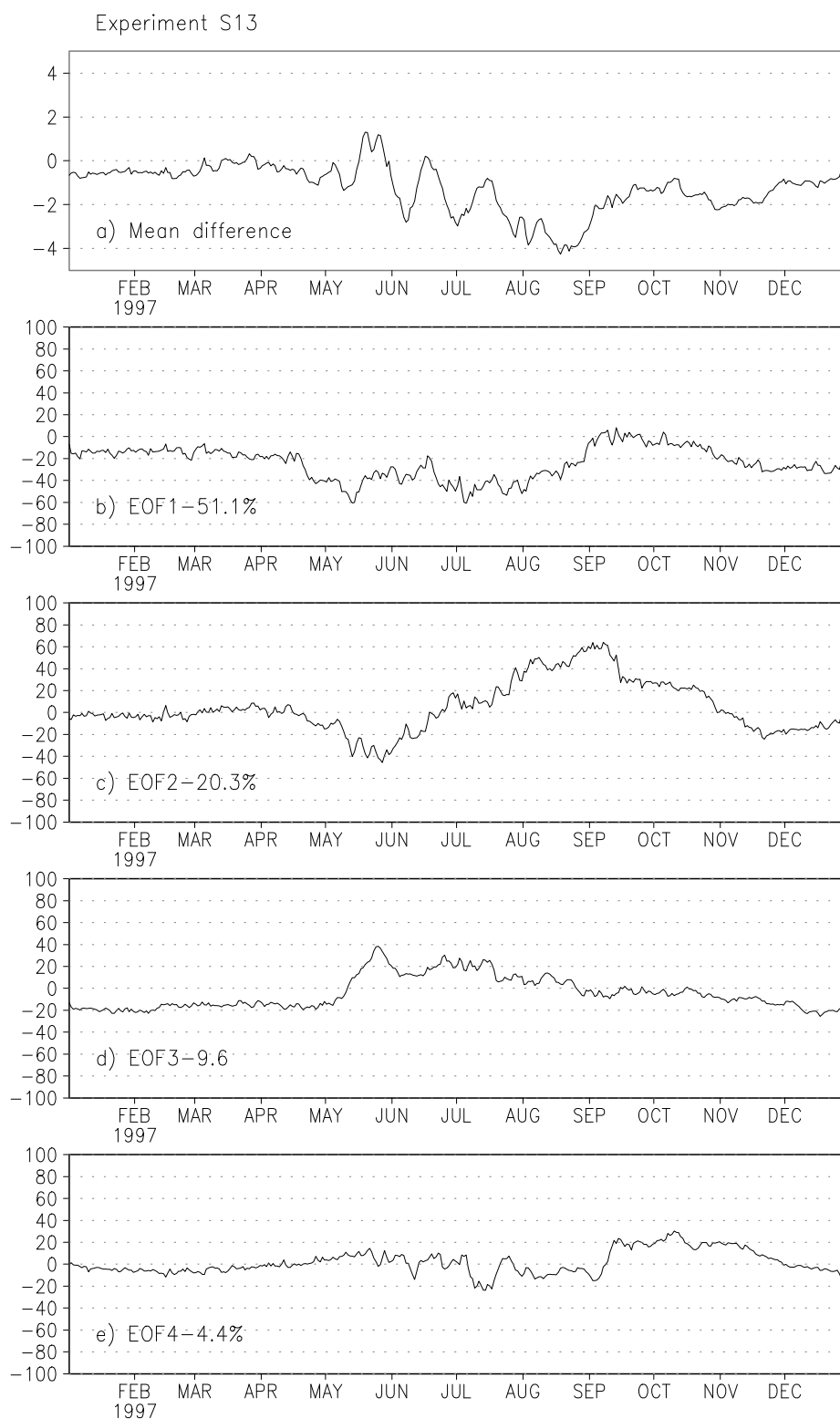


Figure 5.5: Same as Fig.5.1, but for experiment S13

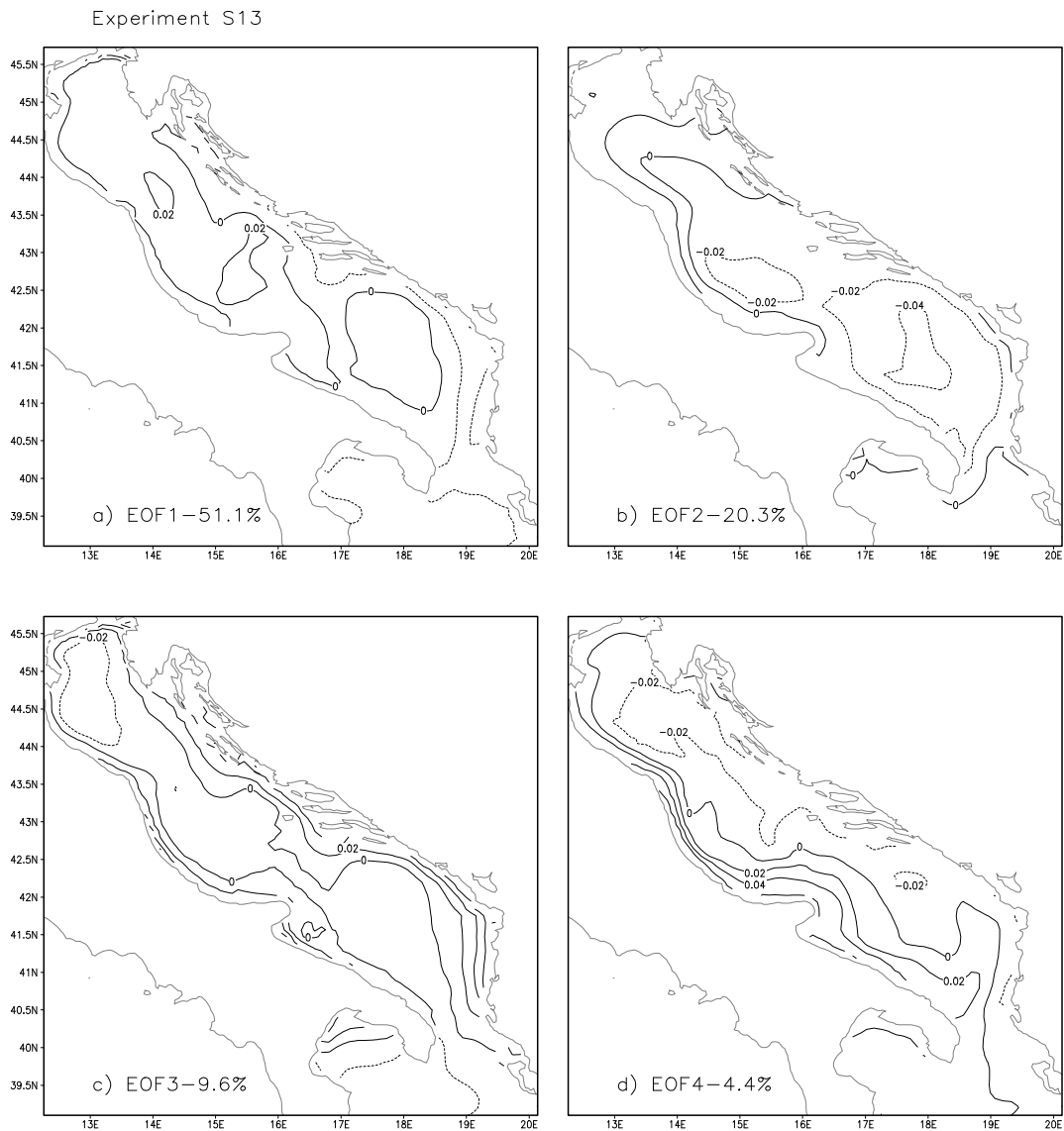


Figure 5.6: Same as Fig.5.2, but for experiment S13

modes obtained in experiment S25, in which the ocean model is forced by surface fluxes computed by the coarse resolution atmospheric model using the one-way forcing, are displayed in Fig.5.3 and Fig.5.4.

We can see in Fig.5.3a that during the first four months, from the beginning of the simulation until the middle of May there is a relatively small averaged difference between simulated and analysed fields. Again, in the middle of May the mean simulated surface temperature becomes significantly higher than analysed.

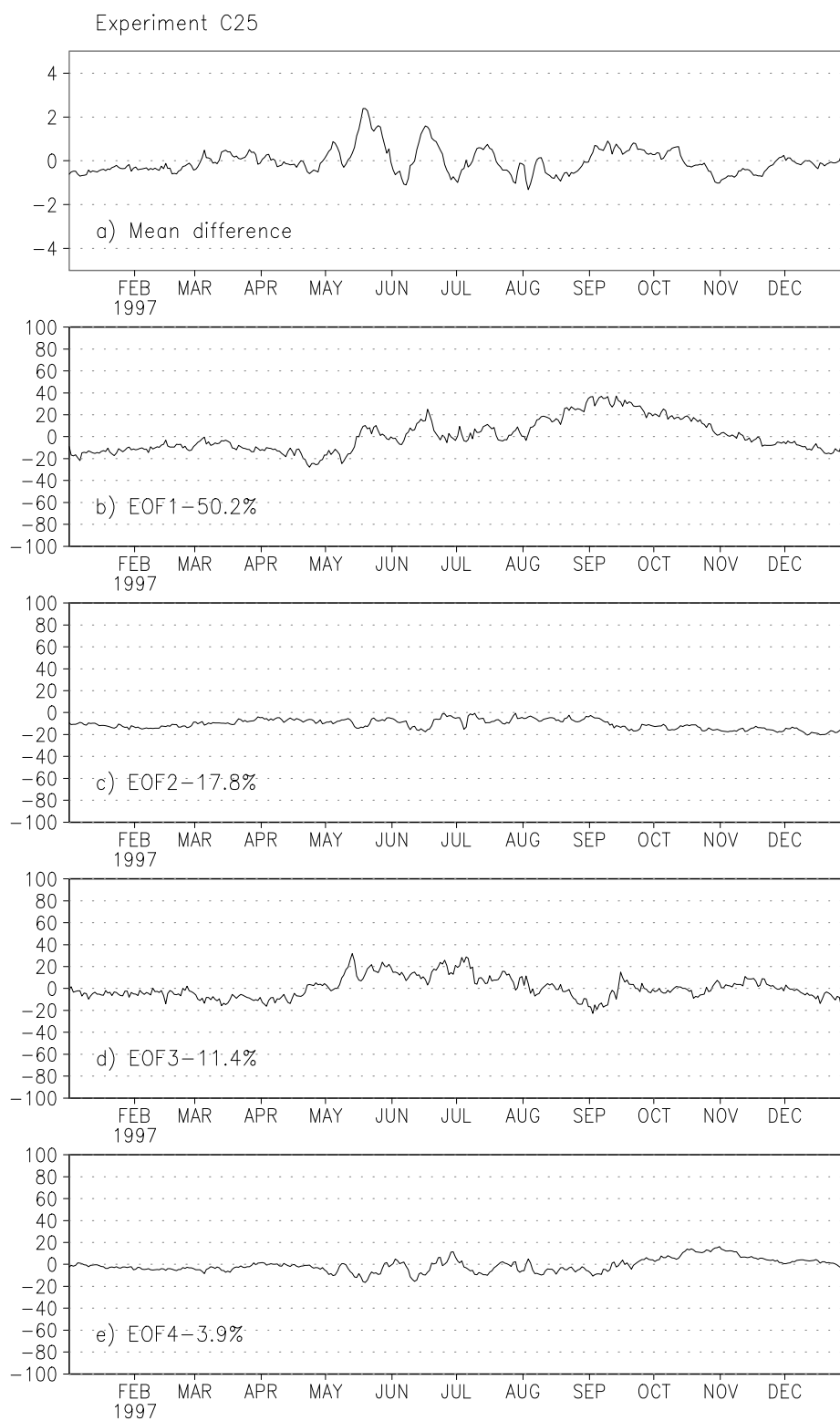


Figure 5.7: Same as Fig.5.1, but for experiment C25

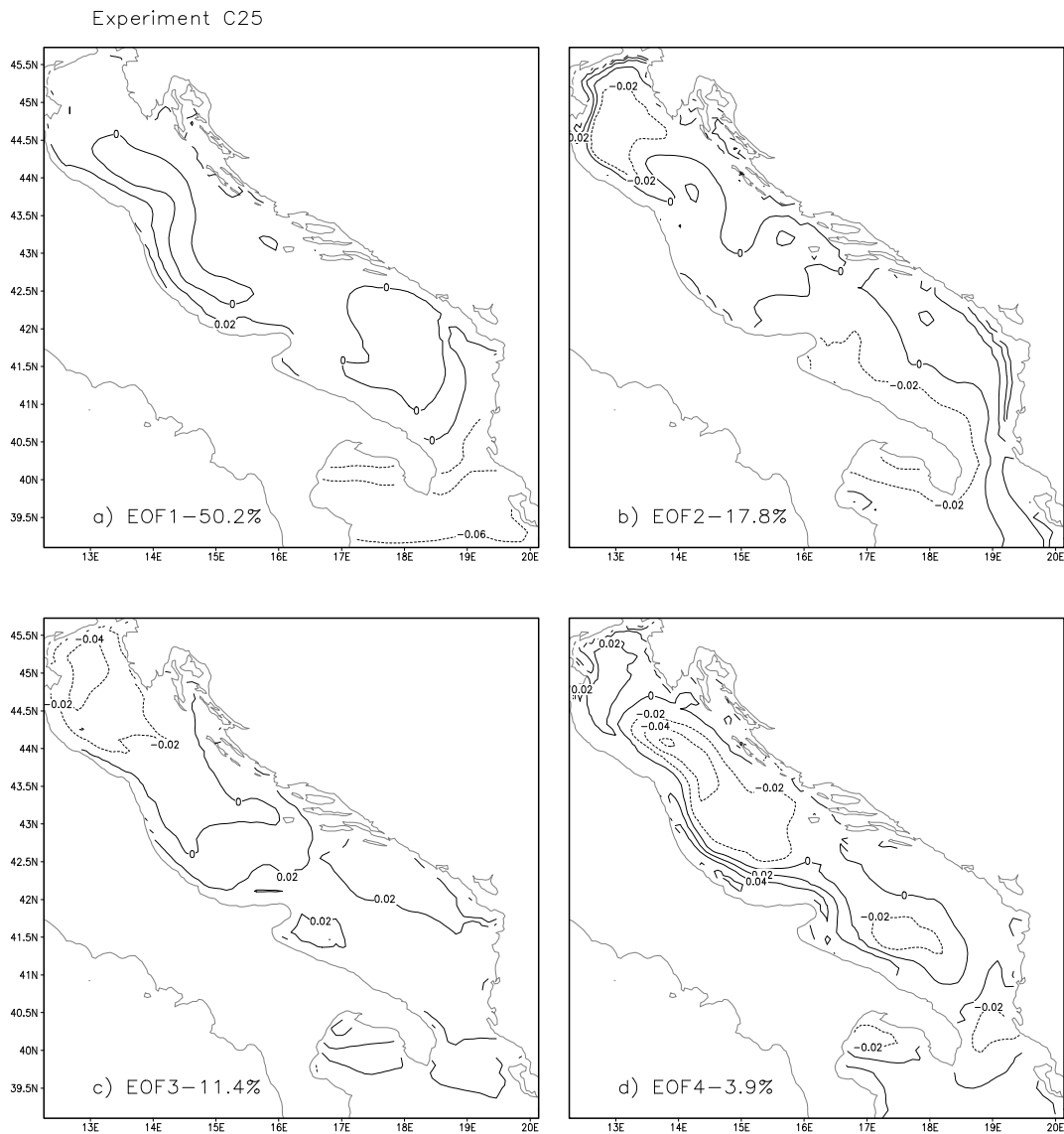


Figure 5.8: Same as Fig.5.2, but for experiment C25

However, this time the difference of  $2^{\circ}C$  is two times smaller than in the case of experiment GCM. Starting from May the difference between the mean simulated and analysed surface temperature starts to oscillate again until August with the similar coefficient of the oscillation like in the case of experiment GCM, but with the tendency that the simulated mean is lower than the analysed mean. However, in comparison to experiment GCM, in experiment S25 the mean of the coefficient is closer to zero. In August the simulated mean surface temperature

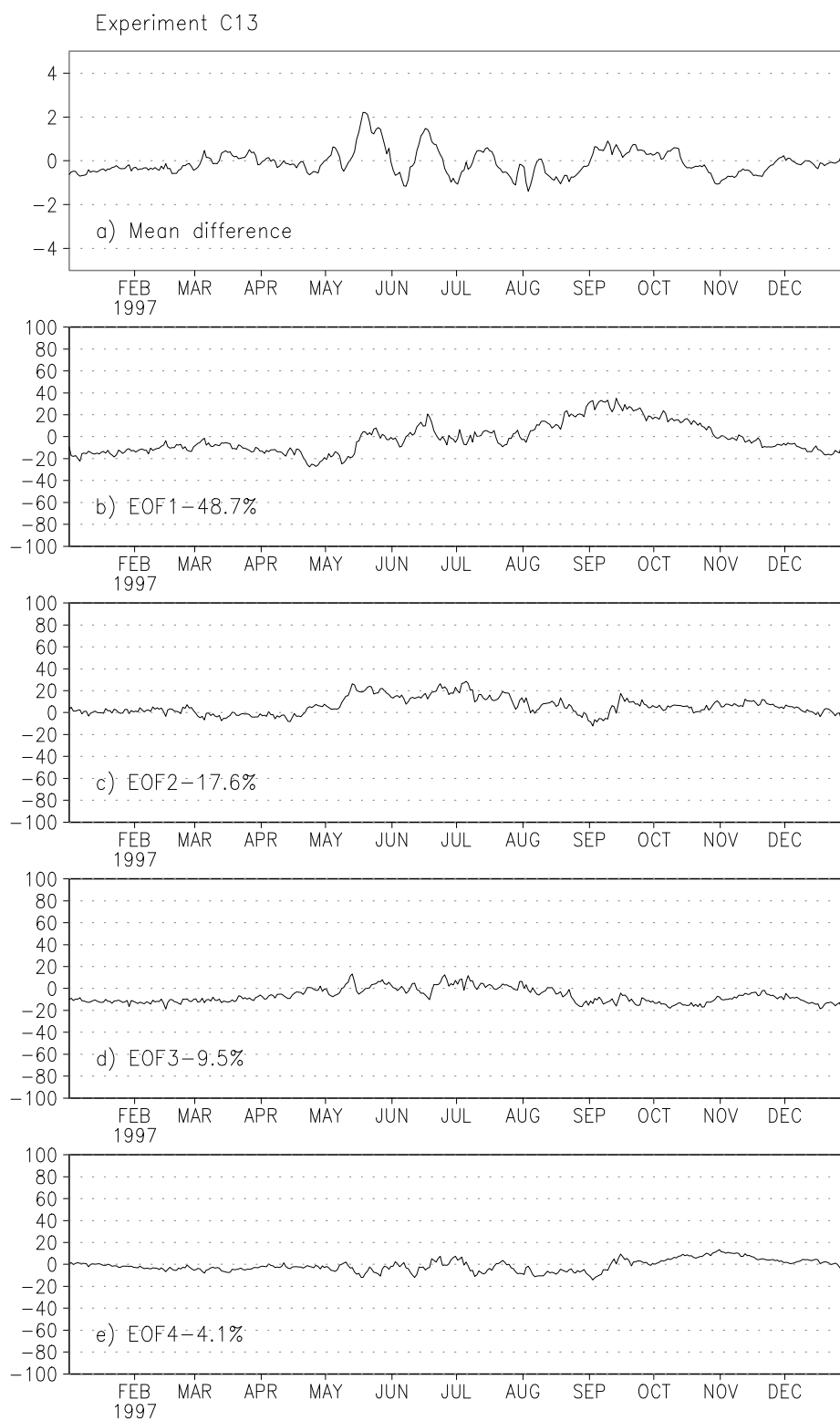


Figure 5.9: Same as Fig.5.1, but for experiment C13

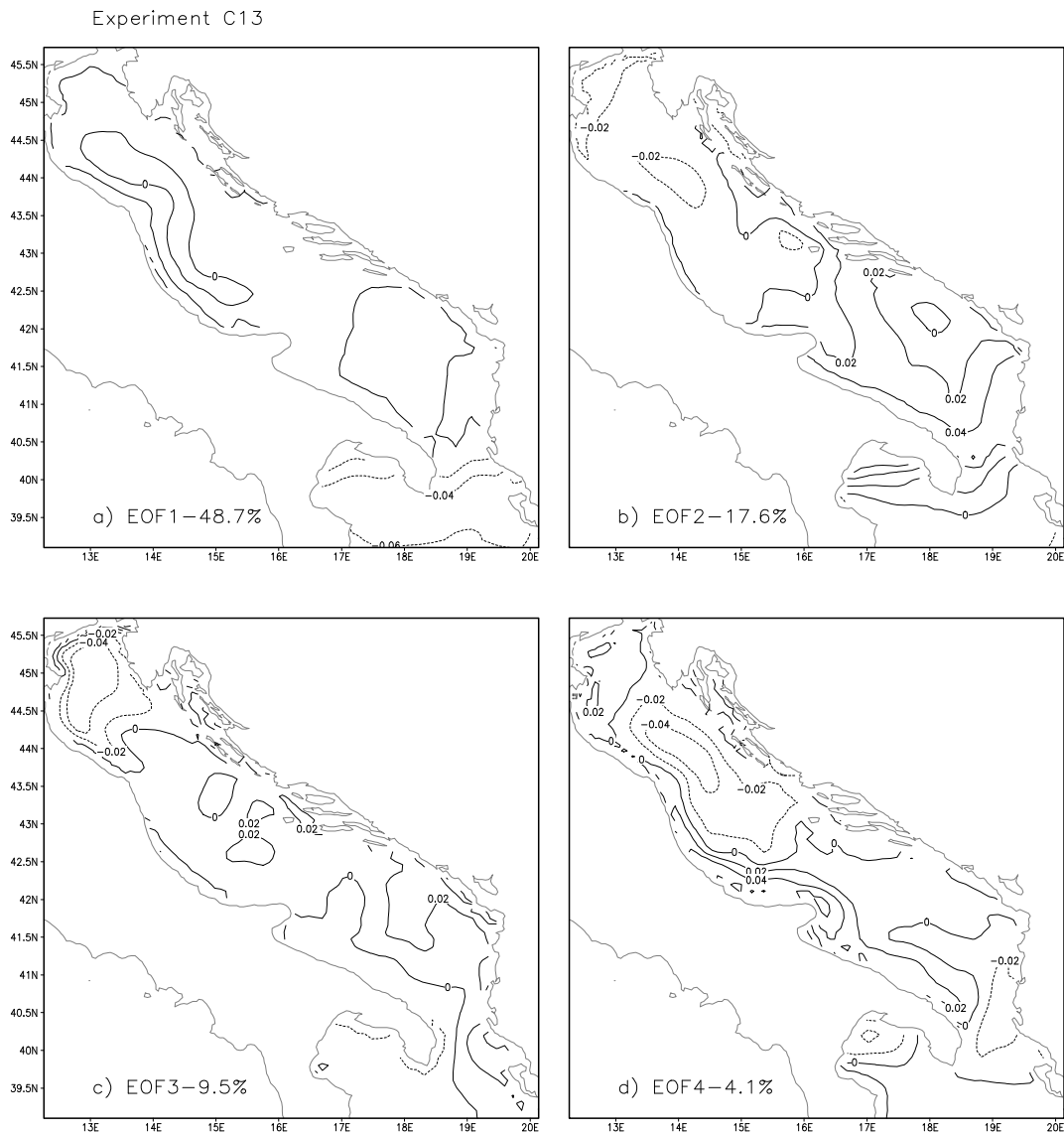


Figure 5.10: Same as Fig.5.2, but for experiment C13

becomes  $4^{\circ}\text{C}$  lower than the analysed mean value. From this moment the shape of the time variation of the difference between the simulated and the analysed mean in experiment GCM and in experiment S25 look very similar, but there is a relatively large shift between the two functions of more than  $4^{\circ}\text{C}$  until the beginning of September.

In fact, we may see from the difference between the simulated and the analysed surface temperature that, while in summer in experiment GCM the mean of the

simulated field is much higher than the mean of the analysed field (Fig.5.1a), at the same time in experiment S25 the mean of the simulated field is much lower than the mean of the analysed field (Fig.5.3a). The same tendency to simulate higher than analysed values in experiment GCM and lower than analysed values in experiment S25 continues until the end of the year, but we may notice that from the middle of November the mean simulated surface temperature in experiment S25 is closer to the analysed mean.

The temporal variation of the coefficient of the first EOF mode of the difference between the simulated and analysed surface temperature in experiment S25 is displayed in Fig.5.3b, and its spatial variability is displayed in Fig.5.4a. This EOF mode accounts for 38% of the total variance. Its coefficient is relatively small, but it is negative during the whole year, except from September until November when it is positive.

In Fig.5.4a we can see that the negative temporal coefficient corresponds to the simulated surface temperature distribution which is further lower than the analysed values in the Northern Adriatic and in the Central Adriatic, while in the Otranto Strait and the Ionian Sea the mismatch is reduced. On the other hand, the positive coefficient from September until November reduces the negative difference between the simulated and the analysed mean of the surface temperature.

The second EOF mode accounts for 24% of the total variance. Its coefficient (Fig.5.3c) is negative from May until July and it reaches relatively high positive values in August and September, while in autumn it slowly decays towards zero. Its spatial distribution (Fig.5.4b) indicates that its negative coefficient is associated with the increase of the difference between the simulated and analysed fields in the Northern Adriatic and with the reduction of the difference in the Central and the Southern Adriatic. On the other hand, the large positive coefficient at the end of the summer indicates the reduction of the difference in the Northern Adriatic. At the same time there is an increase of the difference between simulated and analysed values in the middle of the South Adriatic Gyre, with the simulated surface temperature lower than the analysed.

The coefficient time series and the spatial distribution of the third EOF mode, which accounts for 11% of the total variance, are displayed in Fig.5.3d and in Fig.5.4c. Its coefficient is negative from January until May and at the end of the year, and it is positive during summer. Its negative value corresponds to the simulated field which is slightly warmer than observed offshore and colder than observed along coasts.

The fourth EOF mode, displayed in Fig.5.3e and in Fig.5.4d, has a relatively small coefficient during the whole year except in autumn, when it is positive, indicating a better matching between the simulation and the analysis in the south-western part of the Adriatic.

The time variation of the spatially averaged difference between the simulated and the analysed surface temperature and the time variation of dominant EOF modes in experiment S13, in which the ocean model is forced by surface fluxes computed from the high resolution atmospheric model using the one-way forcing, are displayed in Fig.5.5 and Fig.5.6. It can be immediately noticed that there is no evident difference between the result of experiment S13 (Fig.5.5a) and of experiment S25 (Fig.5.3a), because the difference between two experiments is much smaller than the difference between simulated and analysed fields (not shown). Also, the coefficient and the spatial structure of the most significant EOF modes are very similar to those obtained in experiment S25. The only significant difference is that in experiment S13 the first EOF mode with 50% accounts for the larger part of the total variance.

The temporal and the spatial variation of dominant EOF modes and the temporal variation of the mean difference between the simulated and the analysed surface temperature in experiment C25, in which the ocean model is forced by surface fluxes computed by the coarse resolution fully coupled model, are displayed in Fig.5.7 and in Fig.5.8.

Again, the temporal variation of the spatially averaged difference between the simulated and the analysed surface temperature (Fig.5.7a) shows that there is a relatively good agreement between simulated and analysed fields until May, when the mean simulated surface temperature becomes higher than the analysed mean surface temperature. In summer the mean of the difference between the simulation and the analysis oscillates, but now, contrary to experiments GCM, S25 and S13, the equilibrium around which it oscillates is almost zero. At the beginning of autumn the mean difference between simulated and analysed fields is small and it is further attenuated towards the end of the year.

The coefficient of the first EOF mode which accounts for the 50% of the total variance, displayed in Fig.5.7b, has a small negative value until June and in December, and it is positive during summer and autumn with the maximum in September. However, its spatial distribution (Fig.5.8a) indicates that it has a very small influence over the Adriatic, except in a very narrow band confined to the central part of the western coast.

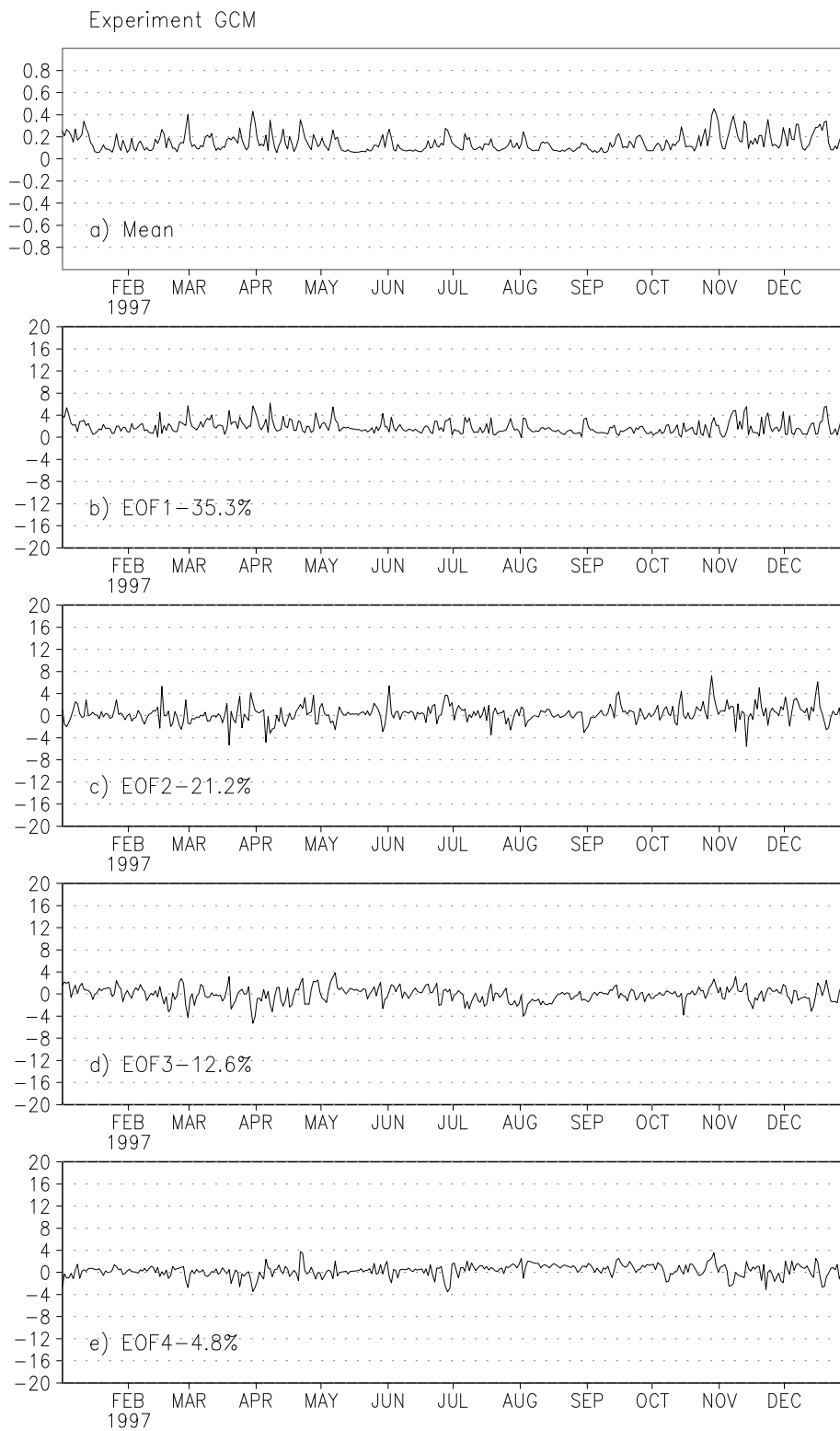


Figure 5.11: Experiment GCM: the spatial average and coefficients of first four EOF modes of the magnitude of surface velocity ( $ms^{-1}$ ).

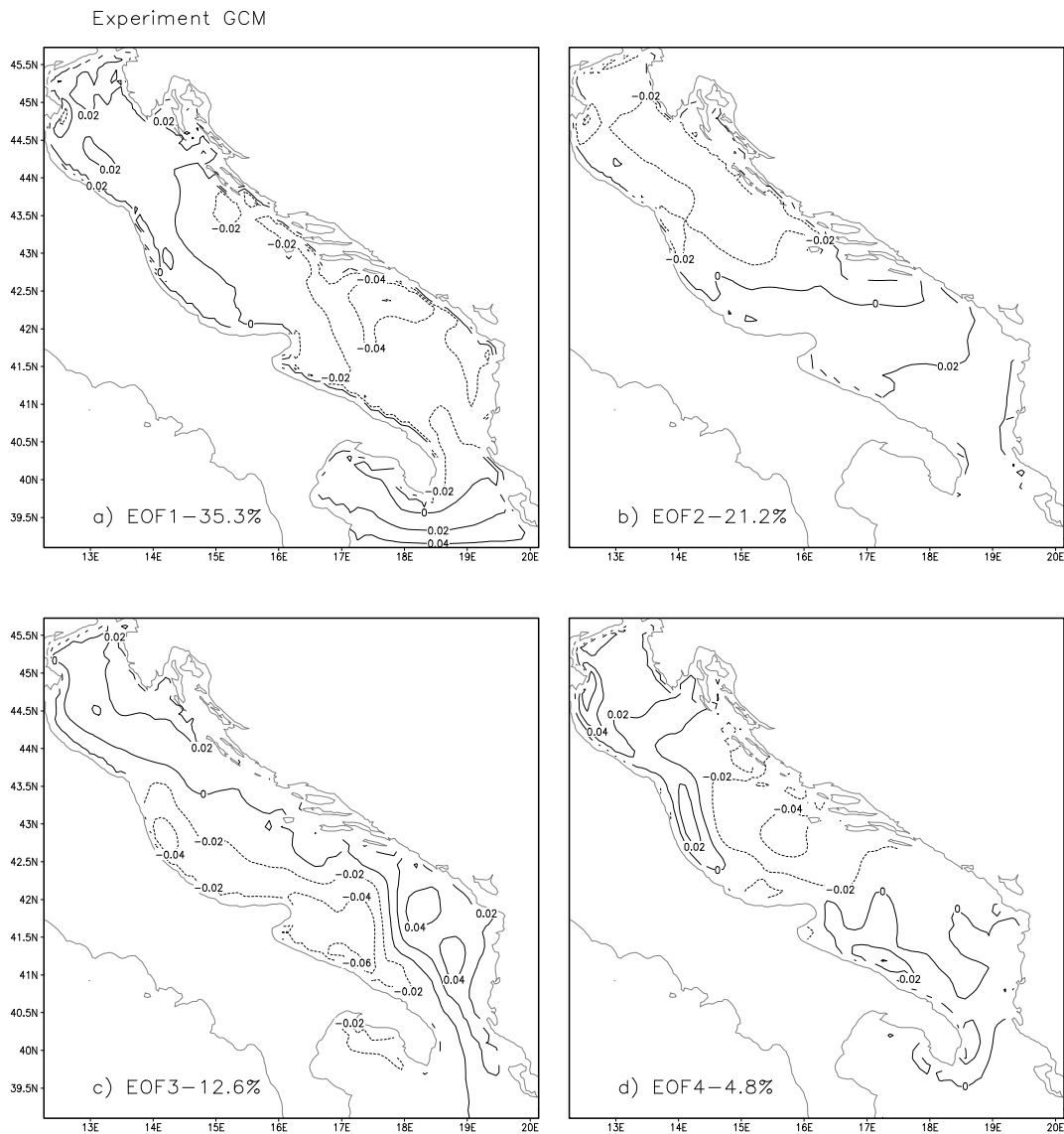


Figure 5.12: Experiment GCM: the first four EOF modes of the magnitude of surface velocity ( $ms^{-1}$ ).

It is relatively significant only in the Ionian Sea and in the Otranto Strait, where it indicates that in this area, strongly influenced by prescribed values at the open model boundary, the simulated surface temperature is somewhat lower than analysed in summer and at the beginning of autumn, and it is higher than analysed in the rest of the year.

The coefficient of the second EOF mode, accounting for 18% of the total

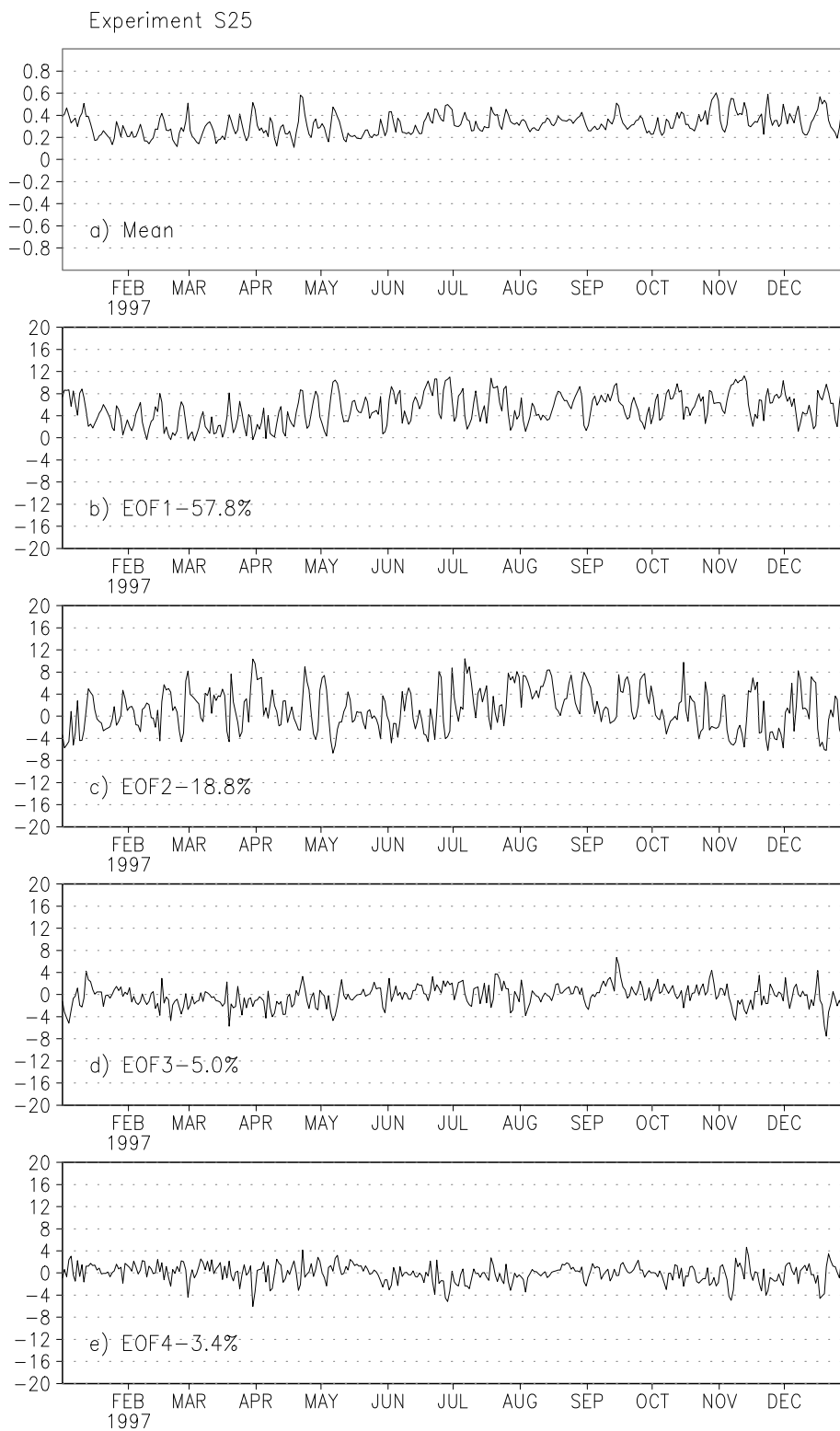


Figure 5.13: Same as Fig.5.11, but for experiment S25

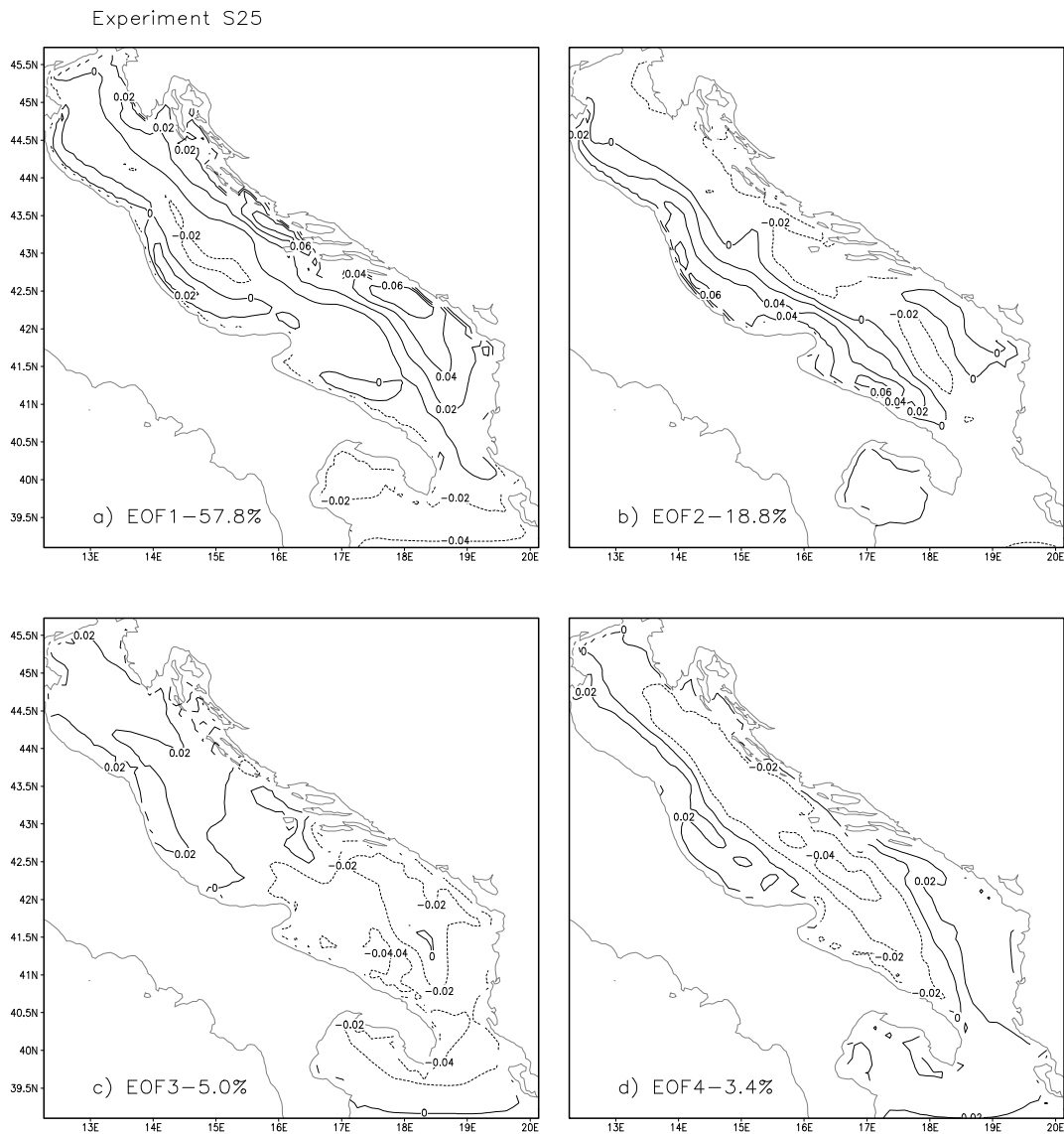


Figure 5.14: Same as Fig.5.12, but for experiment S25

variance (Fig.5.7c), has a relatively small negative value throughout the year. Its spatial distribution (Fig.5.8b) indicates that simulated values are slightly lower than analysed values along the eastern coast and they are slightly higher than analysed values in the Northern Adriatic. However, this effect is reduced in summer, when the coefficient of the third EOF mode is positive having a similar spatial structure in the North Adriatic (Fig.5.7d). The fourth EOF mode is less significant because it accounts for a relatively small part of the total variance

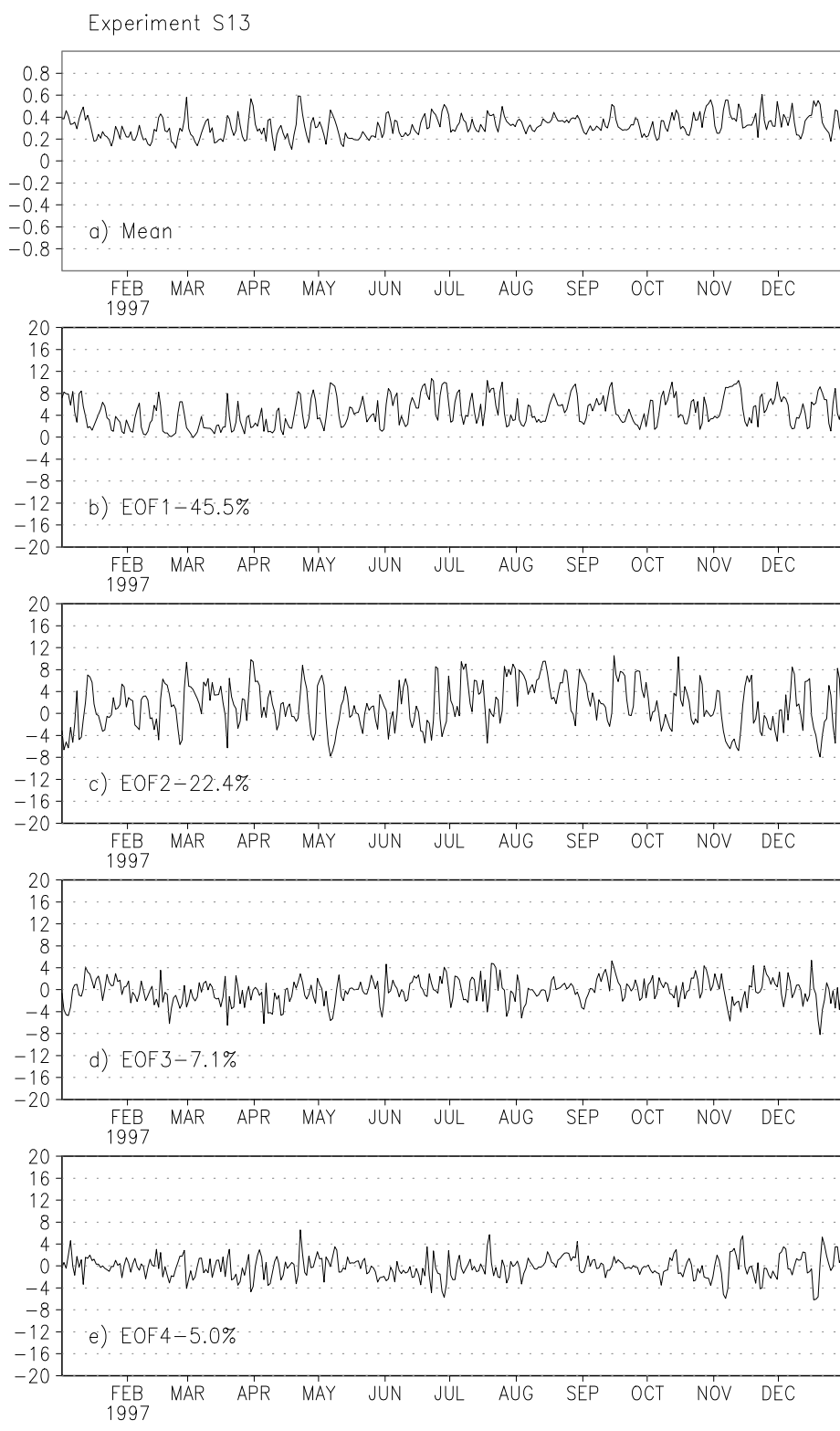


Figure 5.15: Same as Fig.5.11, but for experiment S13

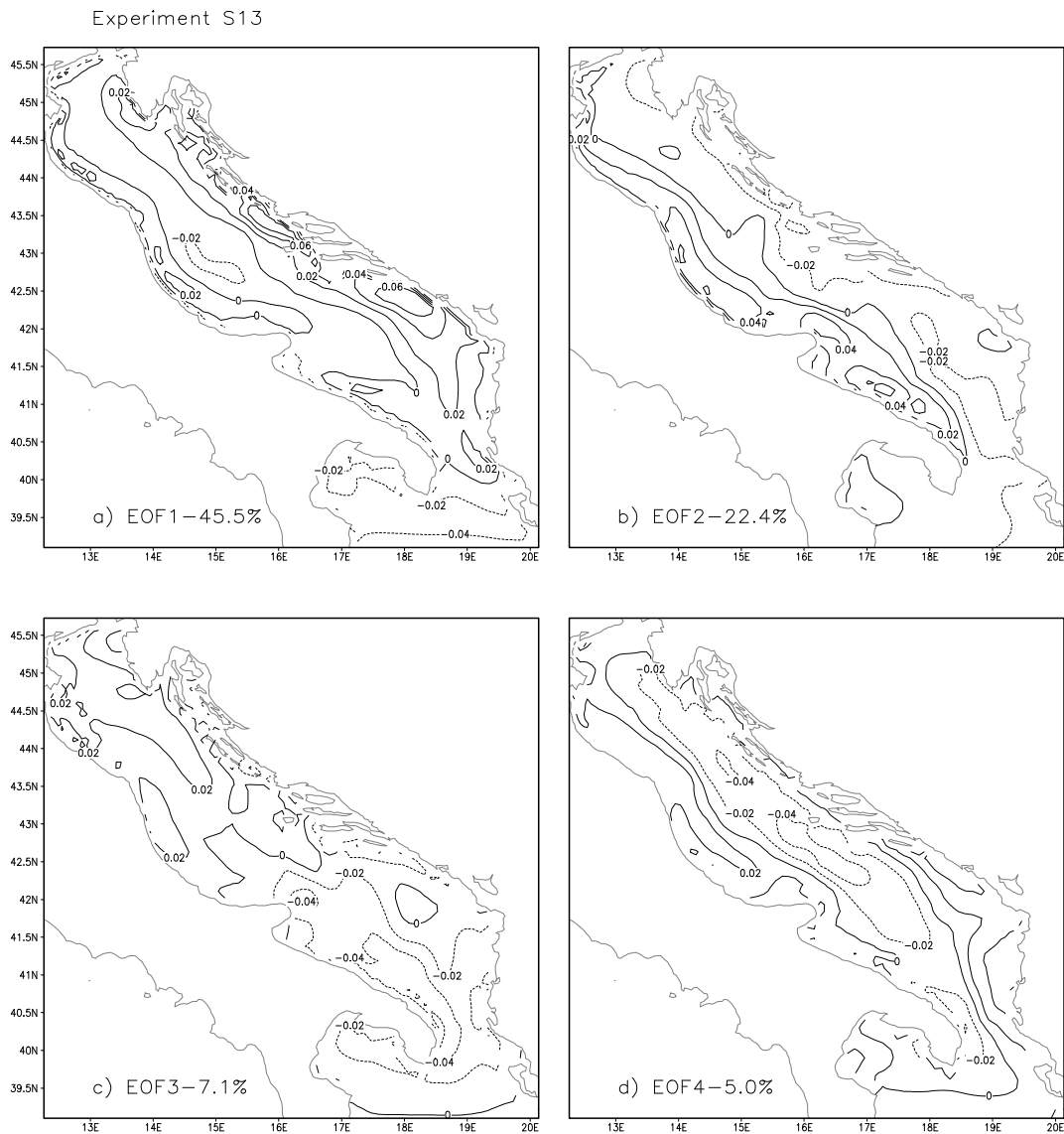


Figure 5.16: Same as Fig.5.12, but for experiment S13

(4%) and its coefficient is relatively small throughout the year.

The temporal variation of the mean difference between the simulated and the analysed surface temperature and the temporal and the spatial variation of its dominant EOF modes in experiment C13, performed using the high resolution fully coupled model, are displayed in Fig.5.9 and in Fig.5.10.

We can see that, like in the comparison between experiments S25 and S13, the temporal variation of the mean difference in the experiment C13 is almost

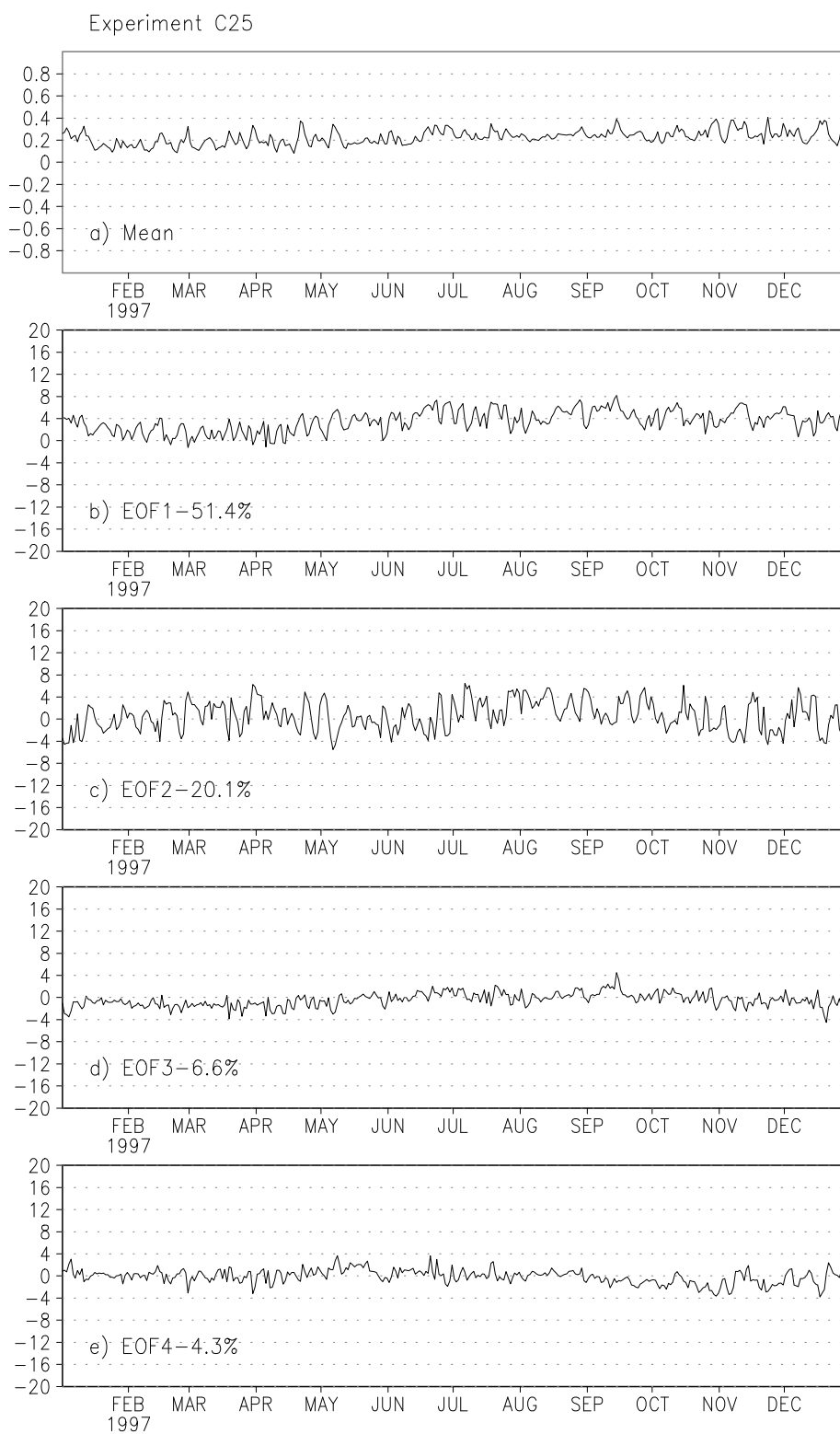


Figure 5.17: Same as Fig.5.11, but for experiment C25

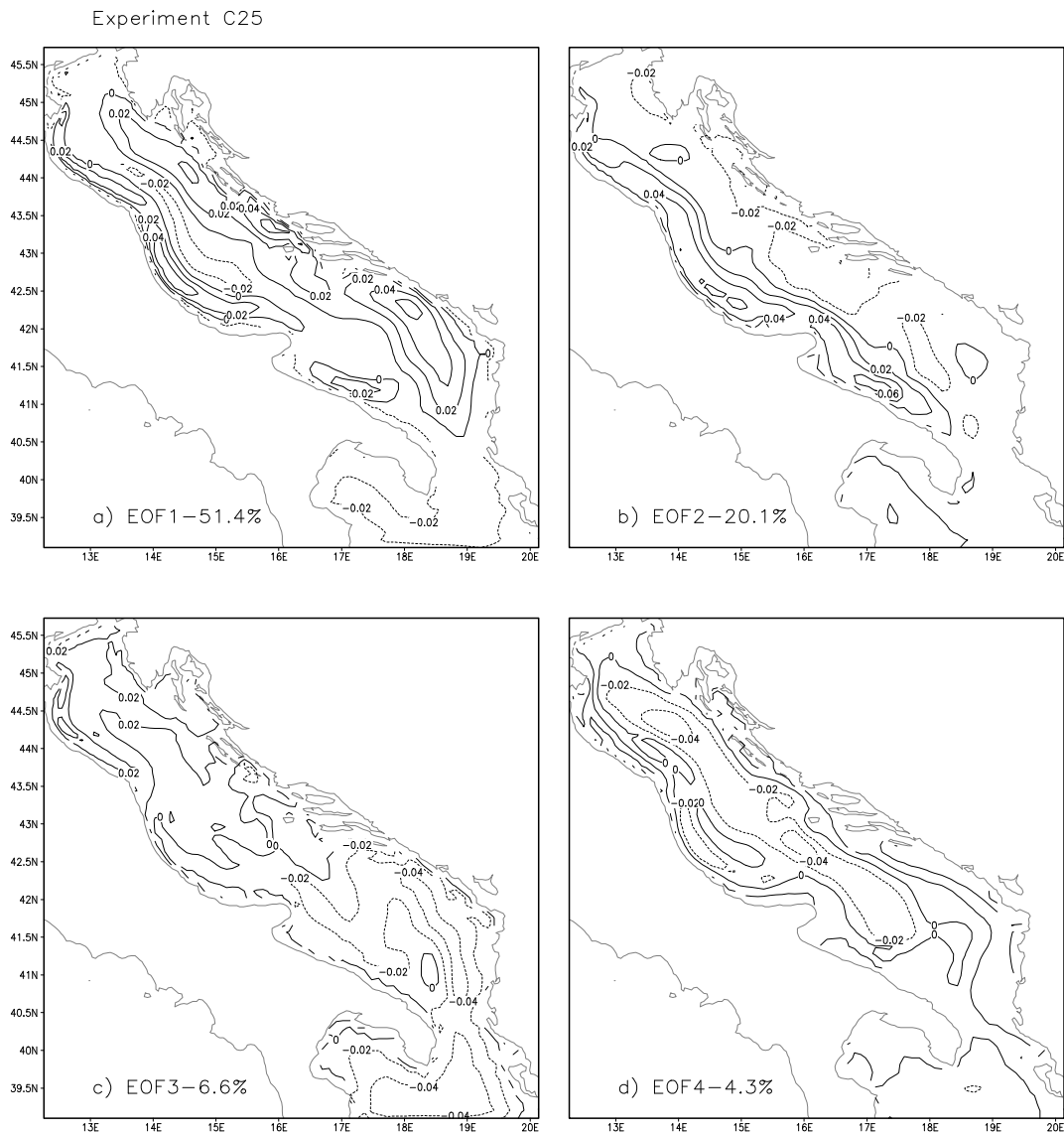


Figure 5.18: Same as Fig.5.12, but for experiment C25

identical to that obtained in experiment C25. Also, the temporal variation of the coefficient and the spatial distribution of the first EOF mode are very similar to those simulated in experiment C25. On the other hand, the coefficient of the second EOF mode is larger in experiment C13 than in experiment C25, but it has a much smaller spatial variability in the experiment C13. The third and the fourth EOF modes have relatively small coefficients during the whole year, and the fourth EOF mode explains a relatively small part of the total variance.

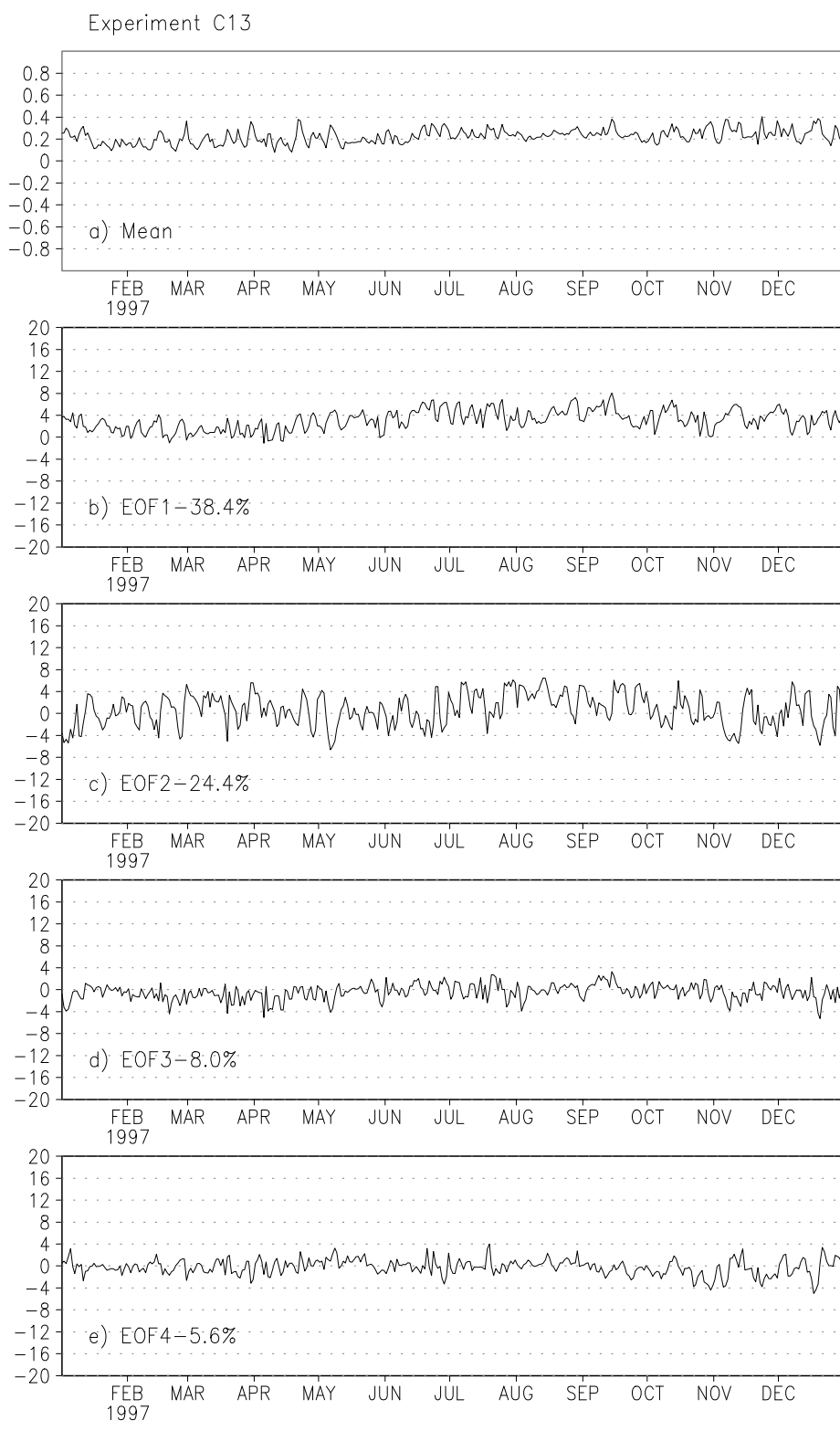


Figure 5.19: Same as Fig.5.11, but for experiment C13

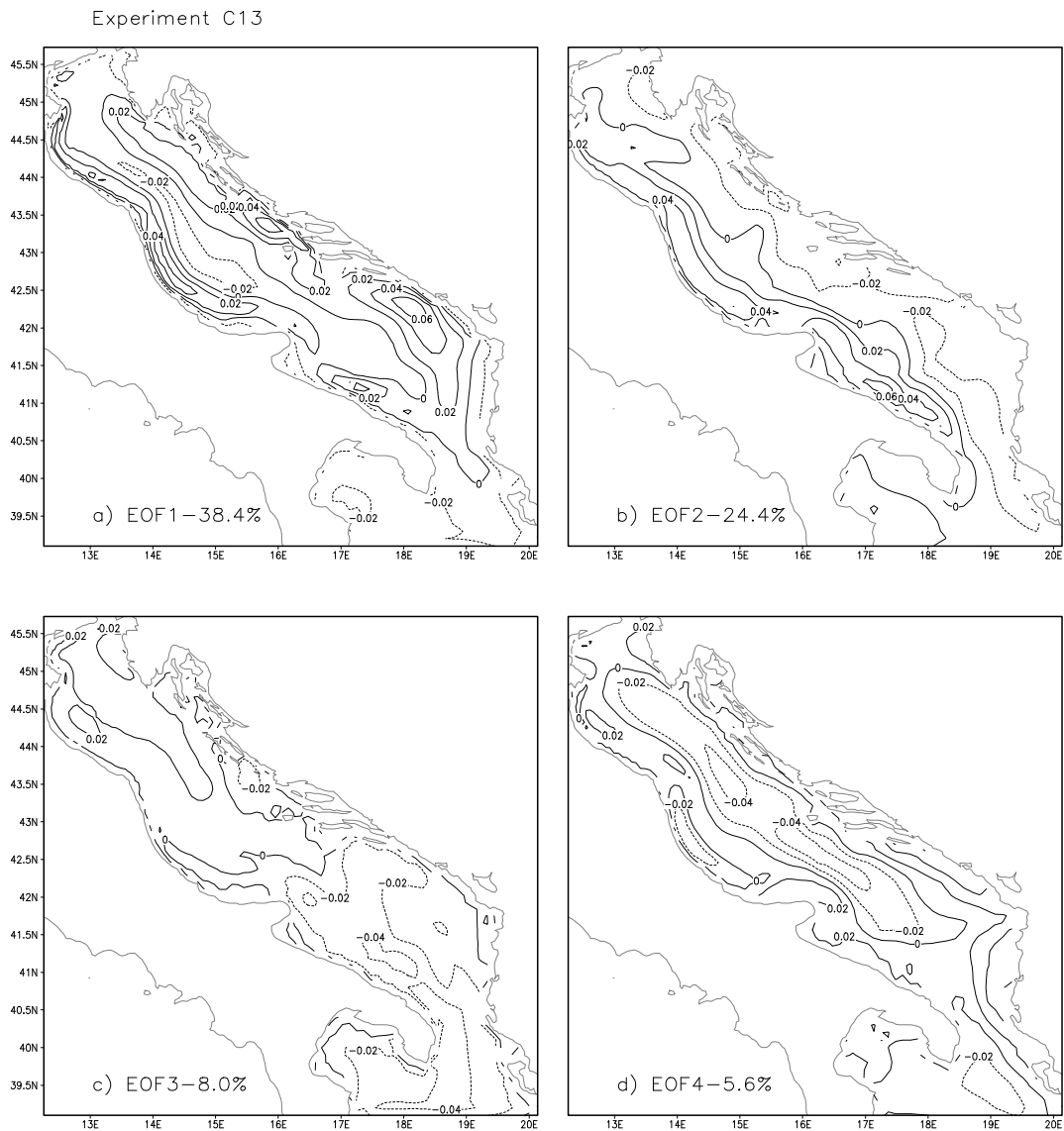


Figure 5.20: Same as Fig.5.12, but for experiment C13

In experiment GCM the simulated surface field has a positive deviation of the mean value. It starts in early summer and it is still present at the end of the year. Furthermore, the temporal and the spatial structure of the most important EOF modes of the difference between the simulated and the analysed fields in experiment GCM indicates that from the beginning of summer until the end of the year there is a relatively large spatial disagreement between simulated and analysed fields.

In experiment S25 the disagreement between the simulation and the analysis is reduced. Nevertheless, the model simulates lower mean surface temperature than the analysed values, and from the beginning of summer there is a negative deviation of the mean simulated temperature. Furthermore, during several periods of time there is still a relatively large spatial disagreement between simulated and analysed fields. The higher resolution atmospheric model forcing applied in experiment S13 does not change significantly the result obtained in experiment S25.

On the other hand, in experiment C25 with the fully coupled model there is a much better correspondence between the simulated and the analysed mean, and the drift of the mean simulated surface temperature is not visible. Furthermore, the spatial and the temporal distribution of the most significant EOF modes shows that there is good correspondence between spatial features simulated by the coupled model and the analyses. Like in one-way forcing experiments, the use of the higher resolution atmospheric model in experiment C13 does not change significantly the result obtained in experiment C25.

### 5.2.2 Surface currents

Another oceanographic parameter that may be significantly influenced by surface fluxes is the surface velocity. We will analyse only its magnitude, assuming that it is representative for all major circulation features at the surface. The direction will be presented for the entire water column in the form of stream-function. The sensitivity of surface currents to the coupling scheme will be investigated only on skin-layer fields. The sensitivity analysis of currents at the 5m depth is qualitatively very similar to the analysis at the skin-layer, but the influence of the coupling scheme on the result is less evident.

The mean magnitude of the surface velocity and the temporal and the spatial variation of its dominant EOF modes in experiment GCM, with the T213 ECMWF model surface forcing, are displayed in Fig.5.11 and Fig.5.12. We can see in Fig.5.11 that there is a relatively large short-term variability of the mean intensity and of coefficients of dominant EOF modes of surface currents. The spatially averaged magnitude of the surface velocity (Fig.5.11a) has a relatively low value in summer in comparison with other seasons. The main reason for this minimum may be the weakening of the wind intensity in summer.

The first EOF mode accounts for 35% of the total variance. We can see in

Fig.5.11b that its temporal coefficient is positive during the whole year with the maximum in autumn. Its spatial structure, displayed in Fig.5.12a, shows that it corresponds to larger than average surface velocities in the North Adriatic and along the north-western coast, and to weaker than average surface velocity in the Southern Adriatic and along the eastern coast. The second EOF mode, which accounts for 21% of the total variance, has a temporal coefficient which is close to zero, but has relatively high temporal variation (Fig.5.11c). Its spatial variability (Fig.5.12b) shows a similar spatial structure as the first EOF mode, with a gradient in the north-south direction. The third EOF mode accounts for 13% of the total variance, and it is mostly determined by the relative importance of the South-eastern Adriatic Current (Fig.5.12c). Its coefficient is relatively small, oscillating around the zero value (Fig.5.11d). The fourth EOF mode, which accounts for 5% of the total variance, represents the relative importance of the Western Adriatic Current (Fig.5.12d). The temporal variation of its coefficient shows that it is very small, varying around zero (Fig.5.11e).

In Fig.5.13 and in Fig.5.14 we can see the temporal variability of the mean intensity of surface currents and the temporal and the spatial variability of dominant EOF modes in experiment S25, in which the ocean model is forced by fluxes computed by the coarse resolution atmospheric model. The mean intensity of surface currents (Fig.5.13a) is generally larger in experiment S25 than in experiment GCM. Now, in experiment S25, the minimum occurs in spring and the maximum in autumn.

From the spatial distribution of the first EOF mode (Fig.5.14a), which accounts for 58% of the total variance, we can see that it mainly accounts for relatively intense coastal currents along the eastern and western coasts and relatively weak currents offshore. The South-eastern Adriatic Current is the dominant feature, while the Western Adriatic Current is less pronounced. In Fig.5.13b we can see that this EOF mode has a highly variable coefficient with large short-term fluctuations. However, it is positive throughout the year. The spatial distribution of the second EOF mode, displayed in Fig.5.14b, indicates that this mode mainly accounts for the intensification of the Western Adriatic Current in the central and the southern parts of the Adriatic and the intensification of the South Adriatic Gyre. It accounts for 19% of the total variance. The highly variable time evolution of its relatively large coefficient indicates that in average these features are more constantly pronounced in summer and early autumn, while in the rest of the year they exhibit large short-term variations.

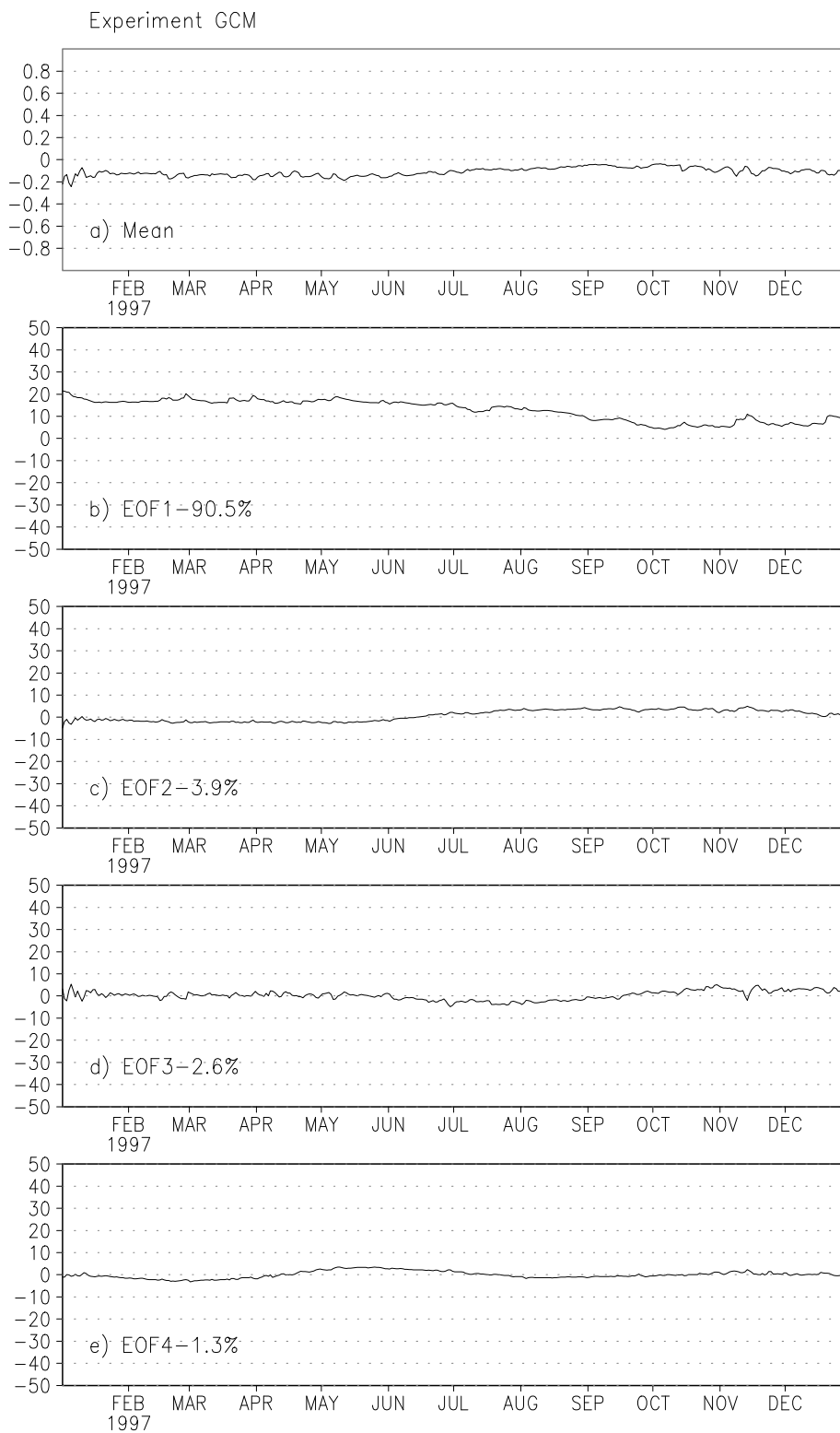


Figure 5.21: Experiment GCM: the spatial average and coefficients of first four EOF modes of the stream function ( $10^6 m^3 s^{-1}$ ).

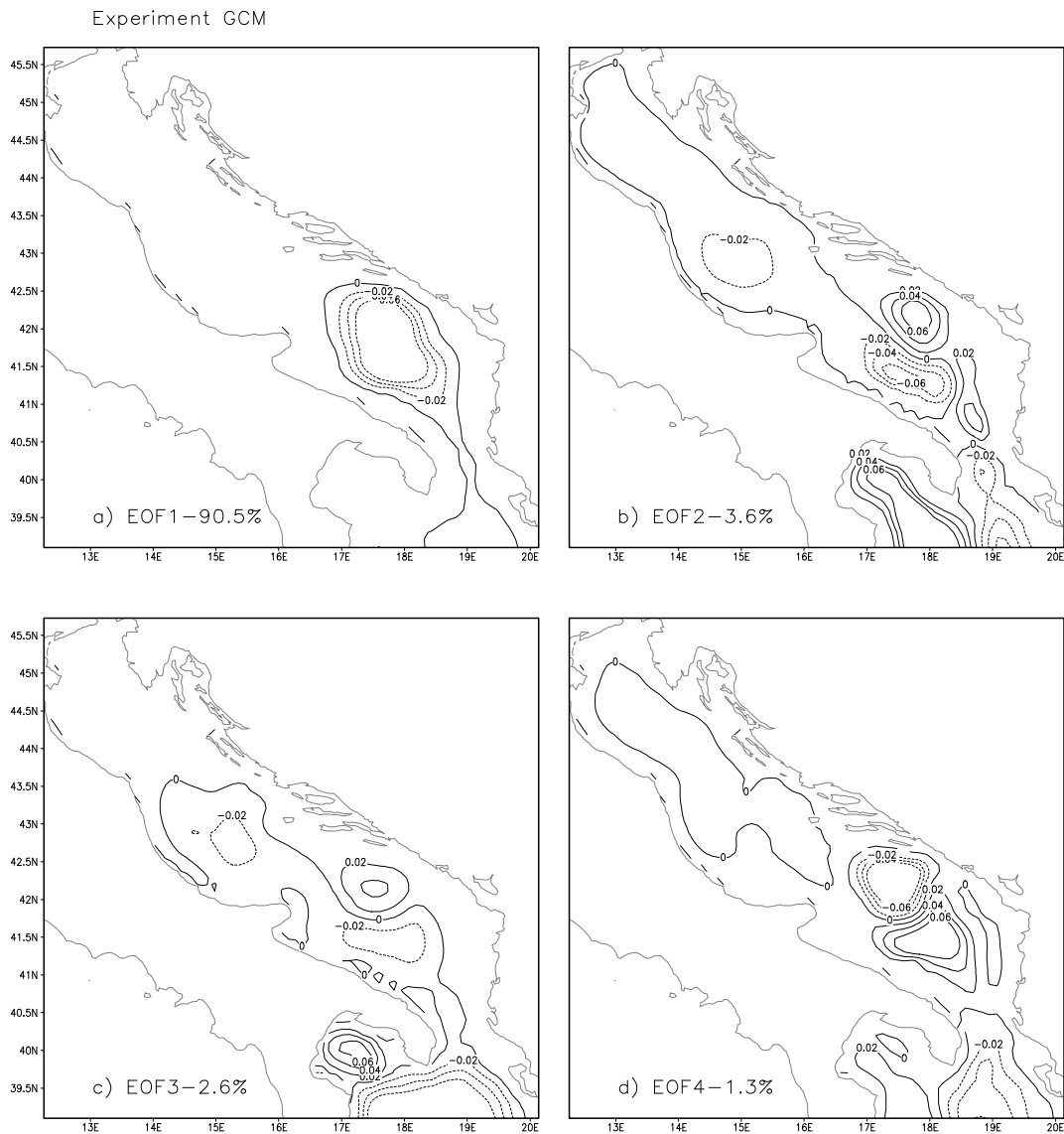


Figure 5.22: Experiment GCM: the first four EOF modes of the stream function.

In Fig.5.13d and Fig.5.13e we can see that the remaining two EOF modes explain relatively small parts of the total variance, 5% and 3% respectively, and that their temporal coefficients are relatively small. Consequently, they are relatively less significant for the analysis.

The temporal variability of the mean magnitude of the surface velocity and the temporal and the spatial variability of its dominant EOF modes in experiment S13, in which the ocean model is forced by fluxes computed in the high resolution

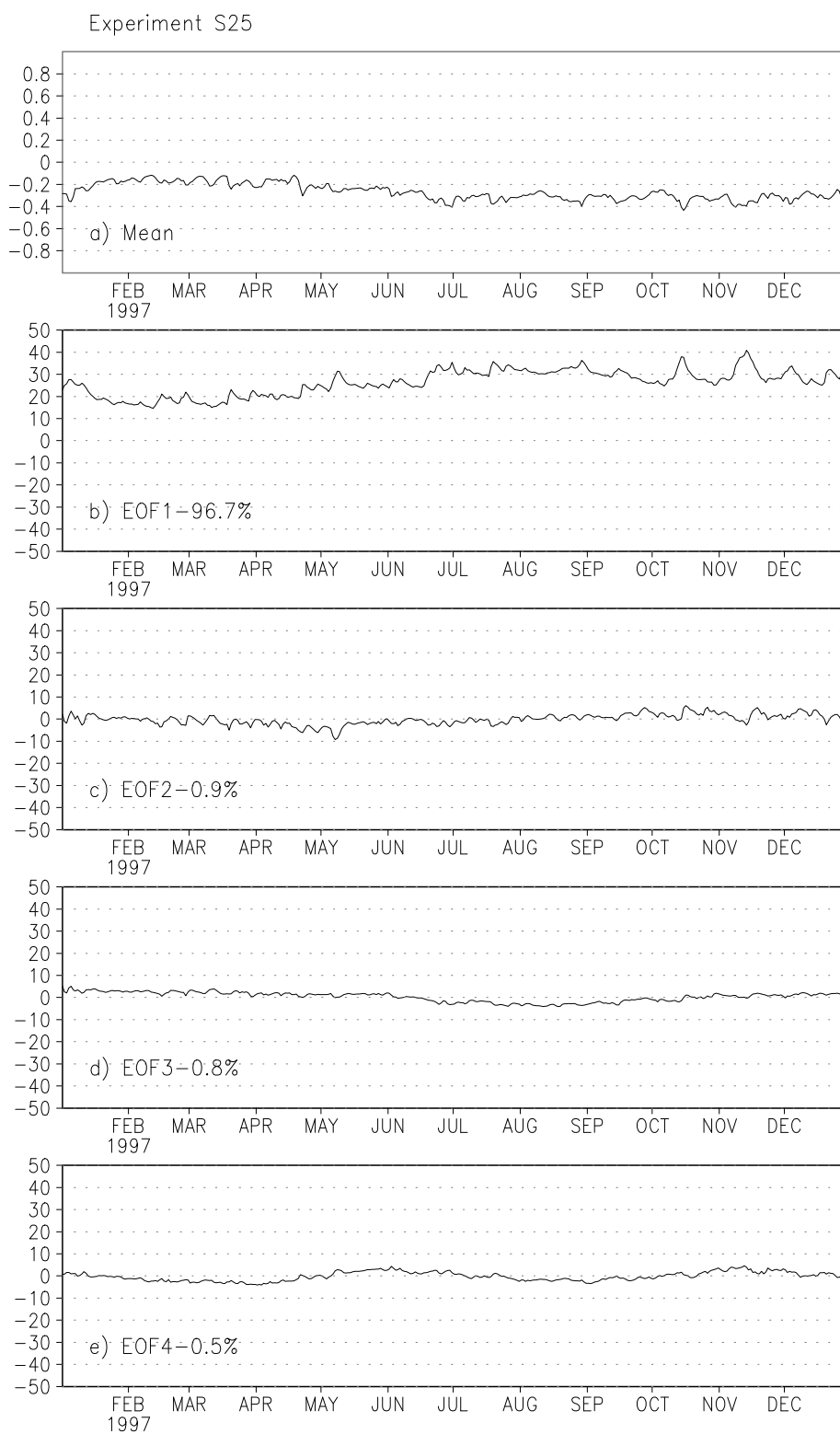


Figure 5.23: Same as Fig.5.21, but for experiment S25

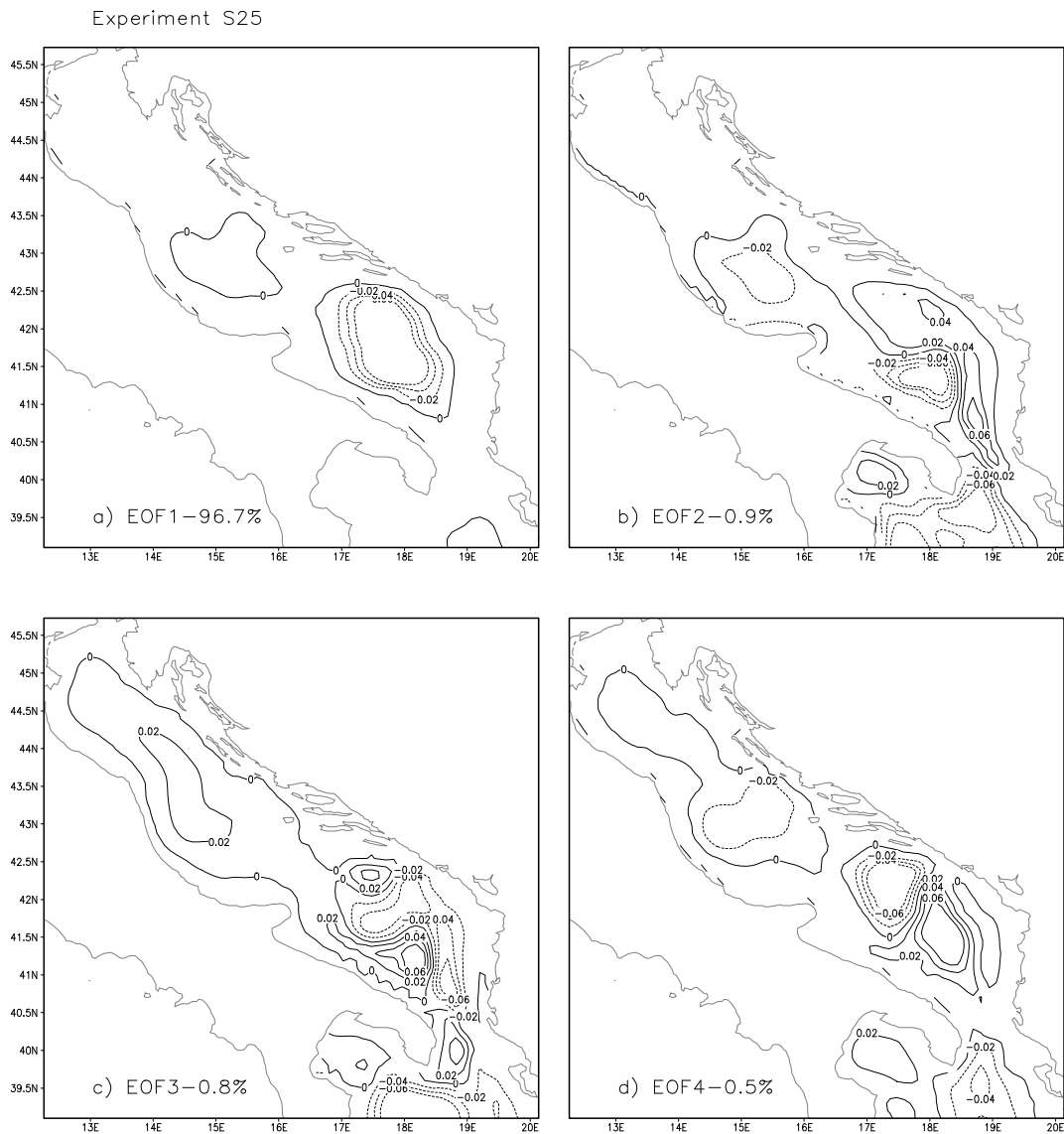


Figure 5.24: Same as Fig.5.22, but for experiment S25

atmospheric model are displayed in Fig.5.15 and Fig.5.16. We can see that the temporal variation of the mean intensity of surface currents and the temporal and the spatial variation of major EOF modes are almost identical to those obtained in experiment S25. The only significant difference is that now the first EOF mode accounts for 46%, the second EOF mode accounts for 22%, the third EOF mode accounts for 7% and the fourth EOF mode accounts for 5% of the total variance, indicating that there is more variability in surface velocity fields, because the

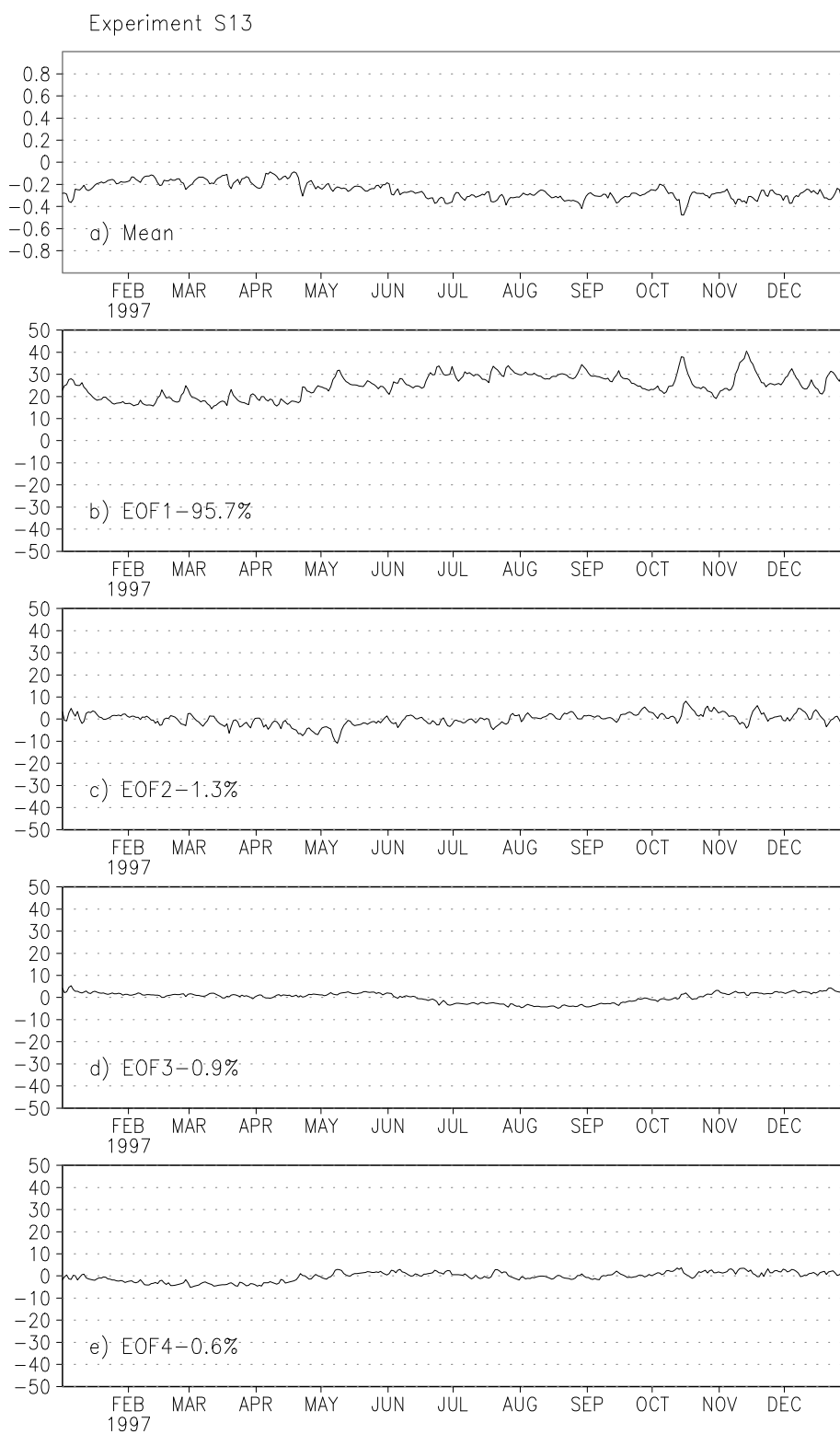


Figure 5.25: Same as Fig.5.21, but for experiment S13

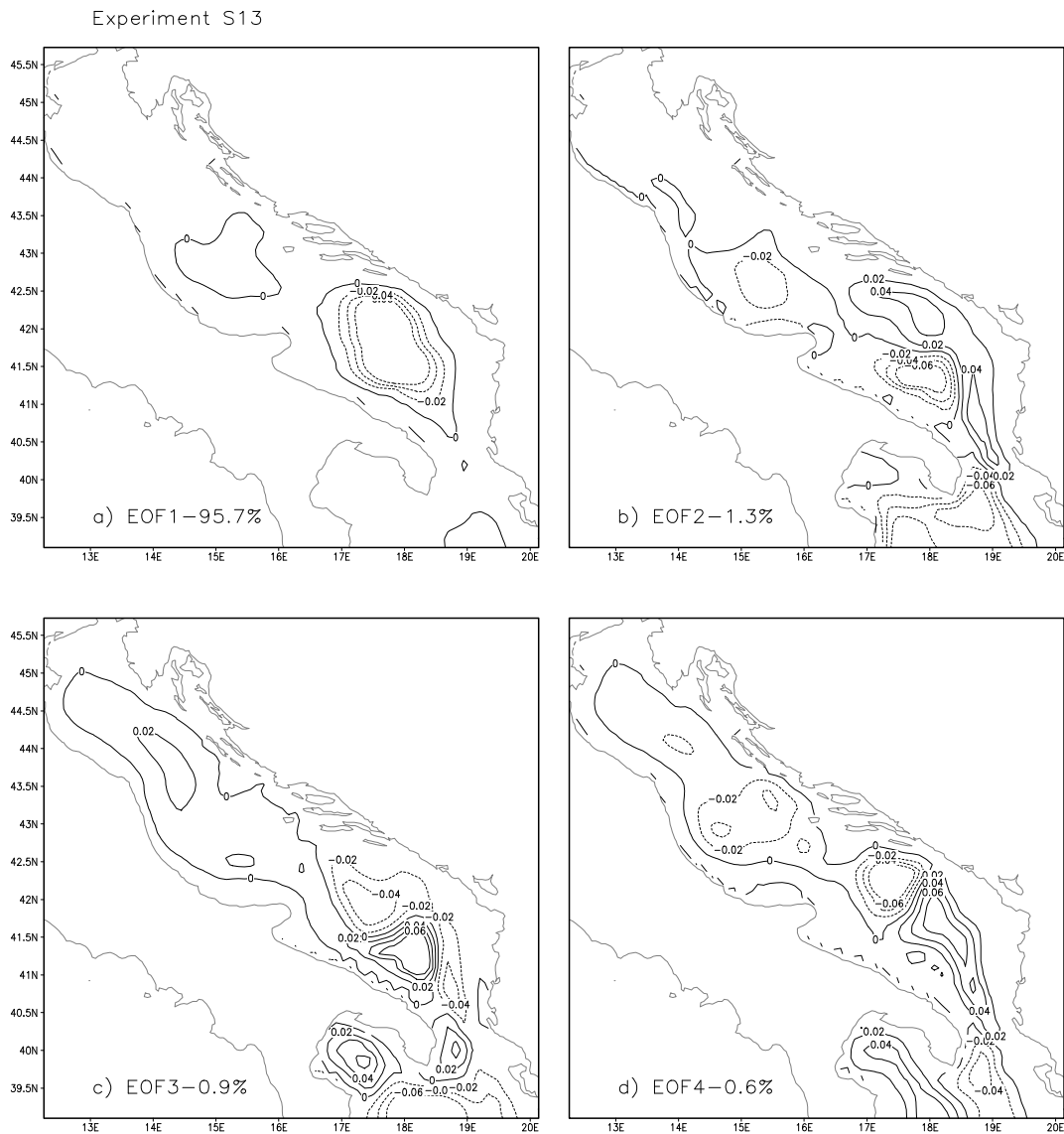


Figure 5.26: Same as Fig.5.22, but for experiment S13

total variance is more equally distributed between EOF modes.

The temporal variability of the mean magnitude of the surface velocity and the temporal and the spatial variability of its dominant EOF modes resulting from experiment C25 with the coarse resolution fully coupled model are displayed in Fig.5.17 and Fig.5.18. The temporal variability of the mean velocity is very similar to that in experiments S25 and S13, but the mean magnitude is slightly lower during the whole year. The first EOF mode accounts for 51% of the total

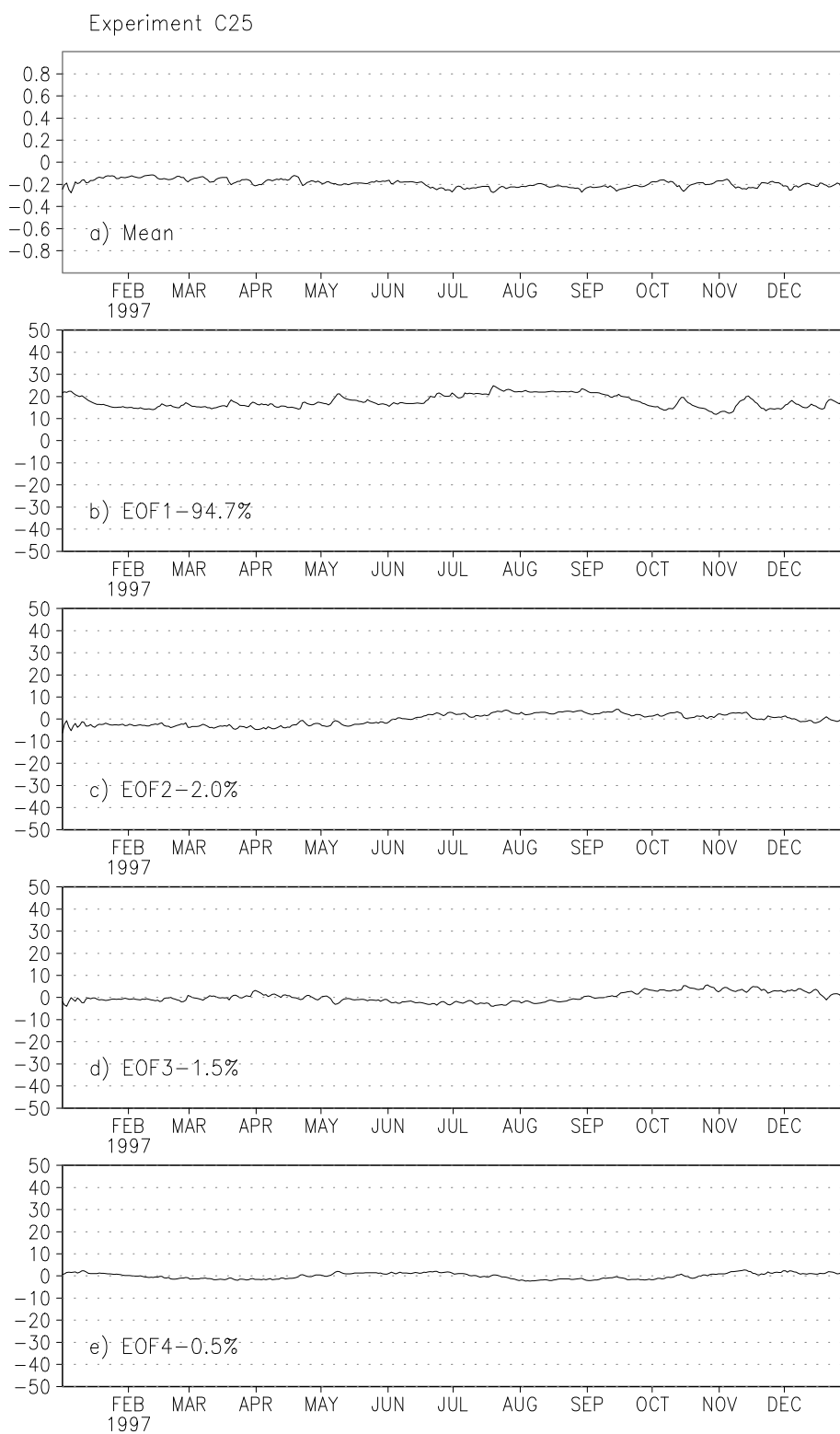


Figure 5.27: Same as Fig.5.21, but for experiment C25

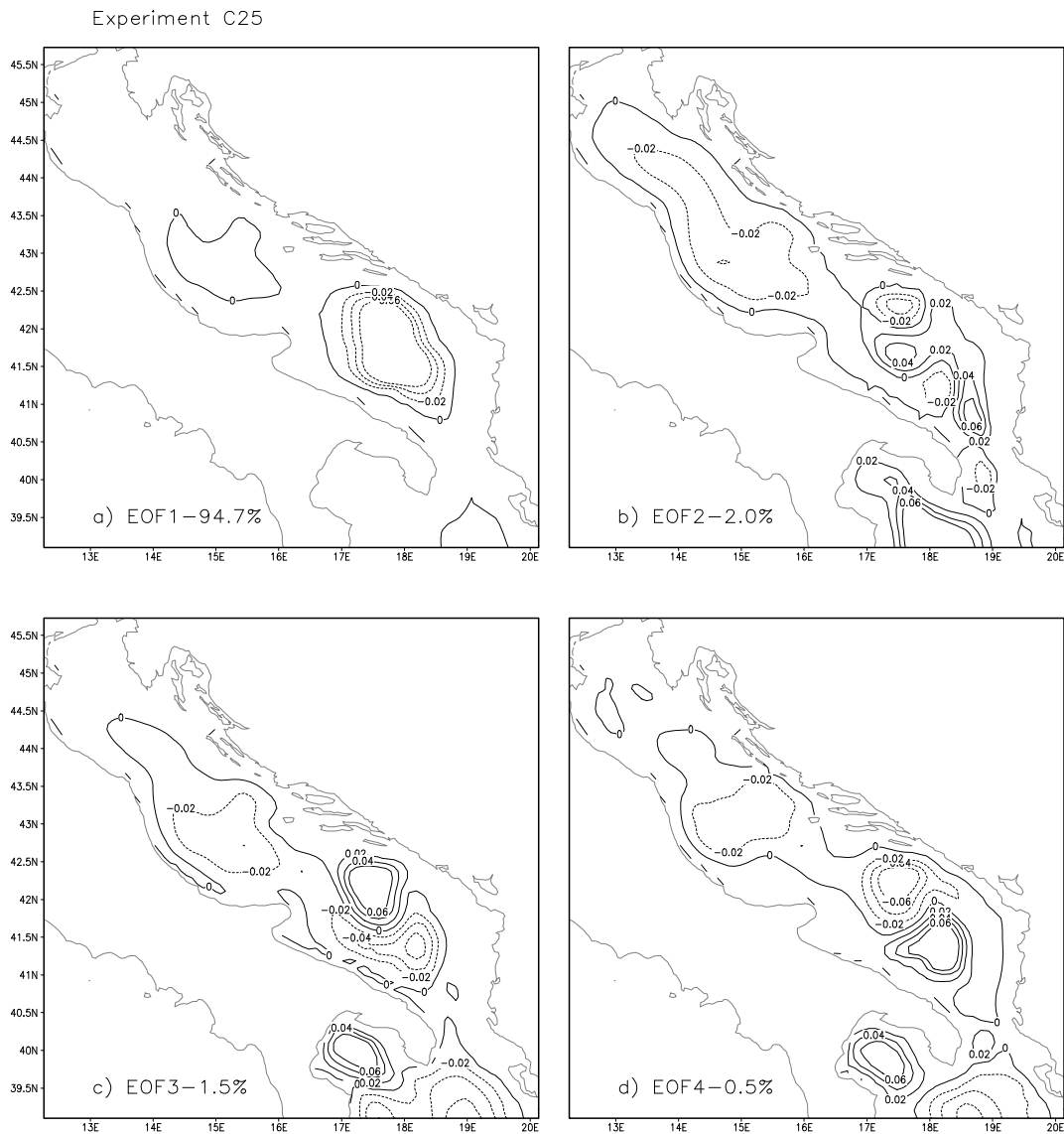


Figure 5.28: Same as Fig.5.22, but for experiment C25

variance. Its spatial distribution, displayed in Fig.5.18a, is very similar to that obtained in experiments S25 and S13, although now the Western Adriatic Current is more pronounced in comparison to the South-eastern Adriatic Current. The spatial structure of the second EOF mode, which accounts for 20% of the total variance, is very similar to the one obtained in experiments S25 and S13 indicating that it describes the intensification of the Western Adriatic Current in the central and the southern part of the Adriatic. Its coefficient (Fig.5.17c) is smaller than in

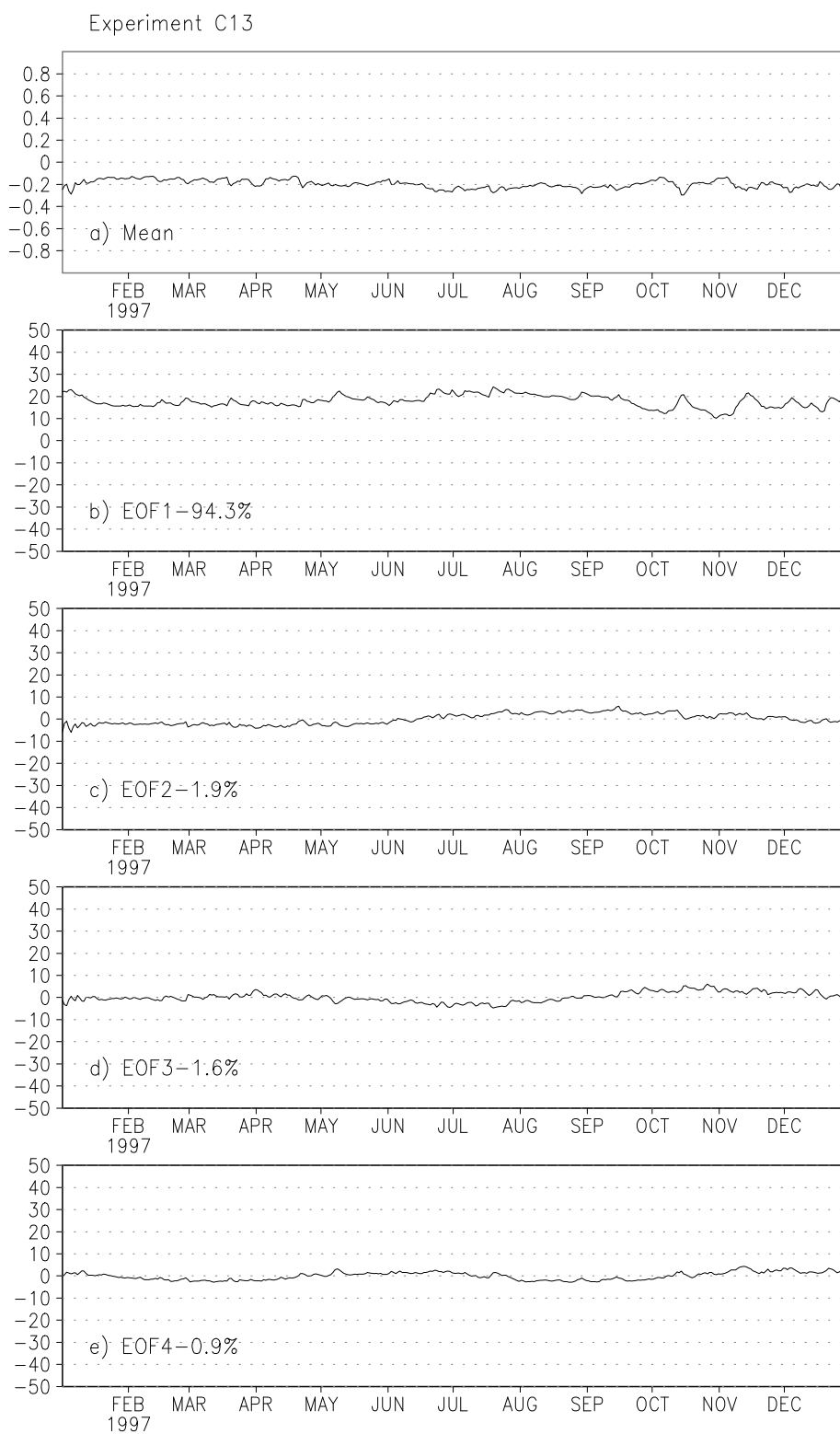


Figure 5.29: Same as Fig.5.21, but for experiment C13

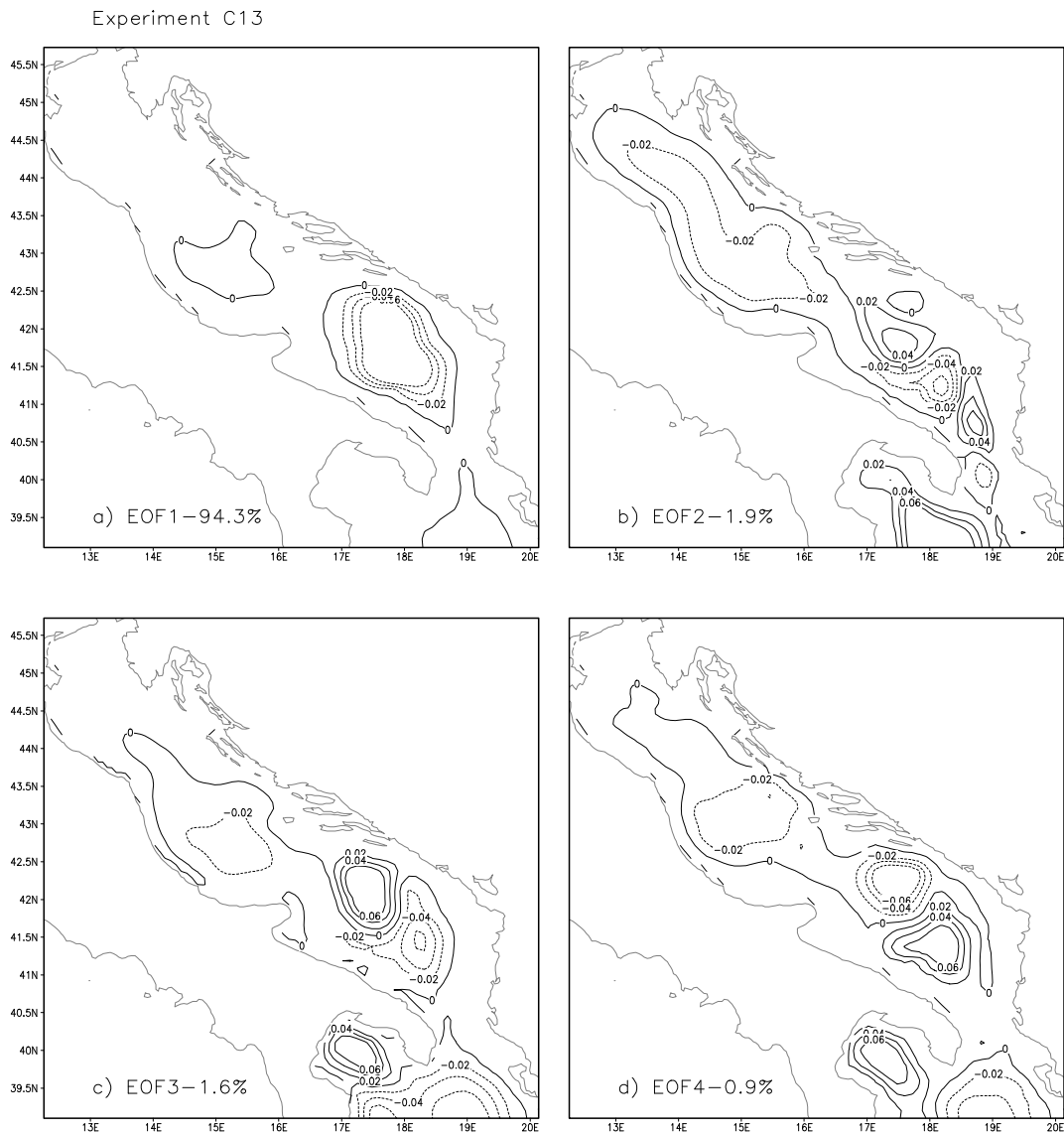


Figure 5.30: Same as Fig.5.22, but for experiment C13

experiments S25 and S13, indicating that now the Western Adriatic Current is less intensified in the Central Adriatic and in the Southern Adriatic in summer and later in autumn. The third and the fourth EOF modes explain respectively 7% and 4% of the total variance. They explain more complex spatial structures than the corresponding EOF modes in experiments S25 and S13, but their temporal coefficients are relatively small during the whole year.

The variation of the mean magnitude of the surface velocity with time and the

temporal and the spatial variability of its dominant EOF modes resulting from experiment C13 with the high resolution fully coupled model are displayed in Fig.5.19 and Fig.5.20. Like in the comparison between experiments S25 and S13, we can see that the mean intensity and the spatial and the temporal variability of the first and of the second EOF mode of the surface velocity are very similar to those simulated in experiment C25. The main difference in comparison with experiment C25 is that now the first EOF mode explains only 38% and the second EOF mode explains 24% of the total variance. The third and the fourth EOF mode, with 8% and 6% of the total variance, differ from those calculated from the experiment C25, but their magnitude is relatively small. Again, like in experiments S25 and S13, the outputs of the higher resolution model contain a larger variability, because the percentage of the total variance is more equally distributed between the most significant EOF modes.

In experiment GCM the main coastal currents, like the Western Adriatic Current and the South-eastern Adriatic Current, are not clearly visible in the most significant EOF modes. The South-eastern Adriatic Current appears clearly only in the third EOF mode and the Western Adriatic Current is clearly visible only in the fourth EOF mode. On the other hand, the simulation using the higher resolution atmospheric model in experiment S25 results in the larger mean intensity of surface currents. Furthermore, already in the first EOF mode, both the western and eastern coastal currents are clearly the dominant spatial structures. Also, there is a larger short term variability of the temporal coefficient of main EOF modes. The forcing with the high resolution atmospheric model (experiment S13) results in an even higher variability in the circulation. The use of the fully coupled model in experiments C25 and C13 generally repeats the result of one-way forcing experiments S25 and S13, with the highest variability of the surface velocity in experiment C13.

It should be noticed that the analysis of the velocity field just below the surface, at the depth of 5m, would be somewhat different, because in that case coastal currents are also clearly visible in the first EOF mode resulting from experiment GCM. However, the result of the analysis of currents at the 5m depth is qualitatively very similar to the analysis of the surface velocity on the skin layer, with the general increase in the variability of the surface circulation with the increase of the horizontal resolution of the atmospheric forcing. Therefore this analysis is not shown.

### 5.2.3 Total transport stream function

The total transport stream function may indicate the differences in the vertically integrated quantities, resulting from the higher resolution or from the coupled mode forcing. The time variability of the mean total transport stream function and the time and the space variability of the most significant EOF modes, obtained from the experiment GCM, are displayed in Fig.5.21 and in Fig.5.22. In Fig.5.21a we can see that the mean value is always negative, indicating that the mean simulated circulation in the Adriatic is cyclonic throughout the year. However, the mean cyclonic circulation is attenuated at the end of the summer and in the early autumn.

We can see from the temporal (Fig.5.21b) and the spatial (Fig.5.22a) variation of the first EOF mode, which represents the relative importance of the South Adriatic Gyre with 90% of the total variance, that the attenuation of the general cyclonic circulation is mainly the consequence of the weakening of the South Adriatic Gyre. We can also see from the temporal and the spatial distribution of the second and the third EOF modes that at the same time the centre of the south Adriatic gyre is shifted closer to the western coast, while there appears a weak anticyclonic circulation along the eastern coast.

In Fig.5.23 and in Fig.5.24 we can see the time variability of the mean total transport stream function and the time and the space variability of the most significant EOF modes obtained from the experiment S25. This time the generally cyclonic total transport is more intense than in the experiment GCM with a higher short-term variation (Fig.5.23a). In this case the mean of the total transport decreases in spring and starting from early summer it increases until November, when again it starts to decrease. Again, the first EOF mode displayed in Fig.5.24a, which accounts for 97% of the total variance, represents the relative importance of the South Adriatic Gyre. Now it can be seen in Fig.5.23b that the South Adriatic Gyre is intensified at the end of summer and that it is further intensified in autumn. The comparison between magnitudes of coefficients of the first EOF mode and other EOF modes shows that this EOF mode is by far the most important and it completely dominates the total transport.

The analysis of the mean total transport stream function and the time and space variability of the most significant EOF modes obtained in experiment S13, displayed in Fig.5.25 and Fig.5.26, shows that there is no significant difference in comparison to experiment S25.

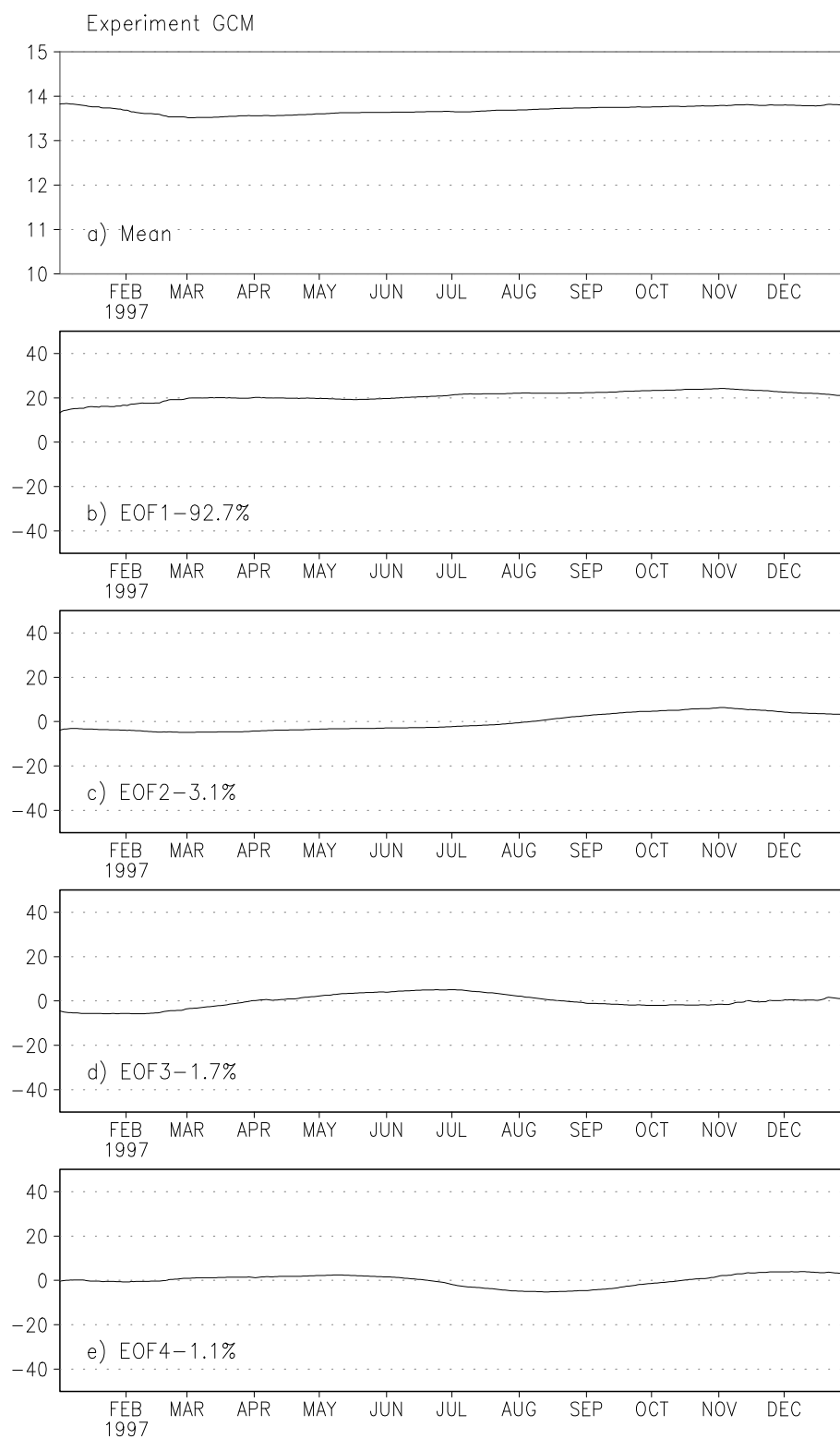


Figure 5.31: Experiment GCM: the spatial average and coefficients of first four EOF modes of the temperature at 100m depth ( $^{\circ}C$ ).

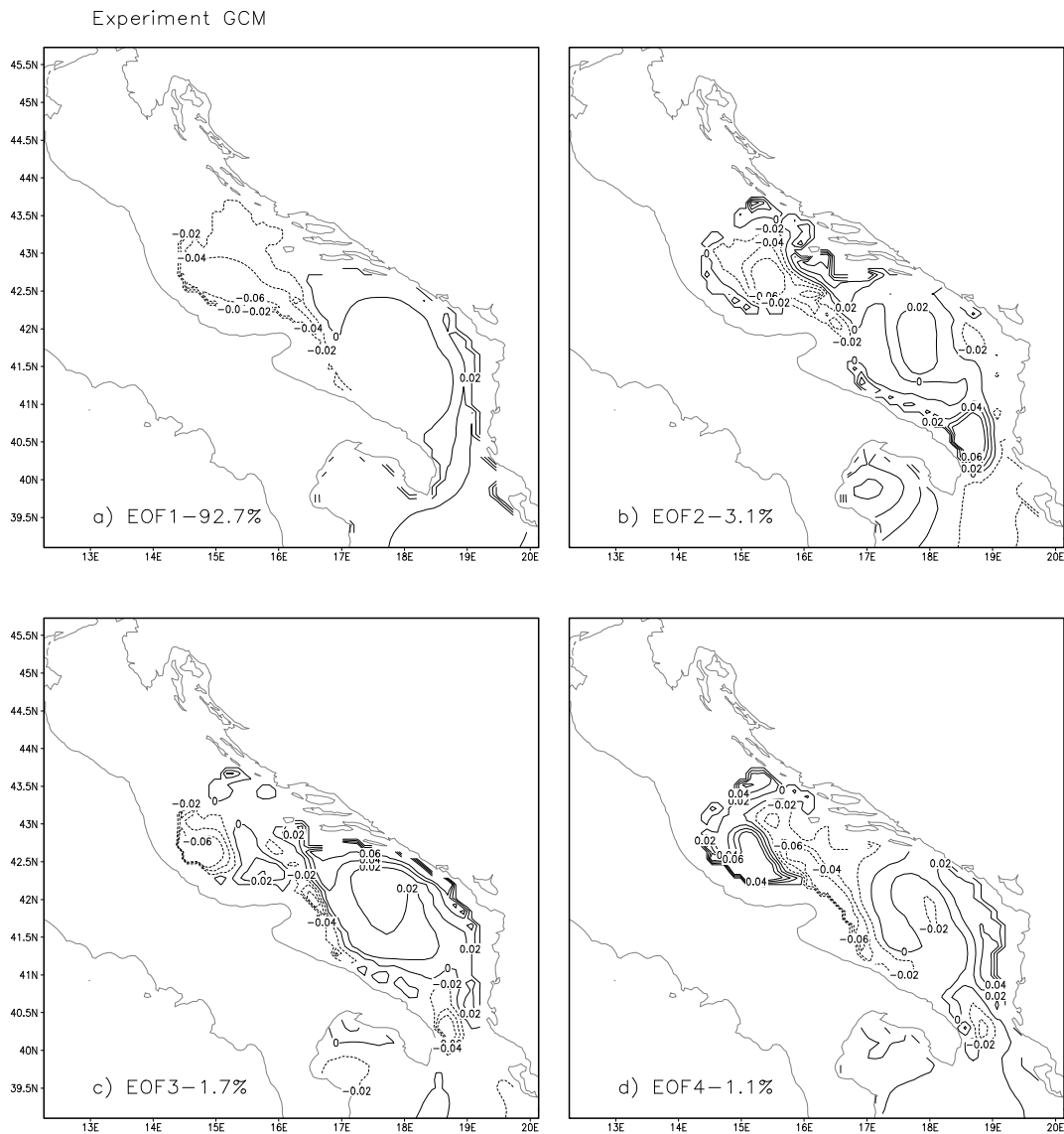


Figure 5.32: Experiment GCM: the first four EOF modes of the temperature at 100m depth.

The mean total transport stream function and the time and the space variability of the most significant EOF modes, obtained in experiment C25 with the coarse resolution coupled model are displayed in Fig.5.27 and Fig.5.28. Now we can see in Fig.5.27a that the mean total transport is very stable without significant short-term or long term variations. Again, like in experiments S25 and S13, the temporal variation of the coefficient of the first EOF mode (Fig.5.27b), ac-

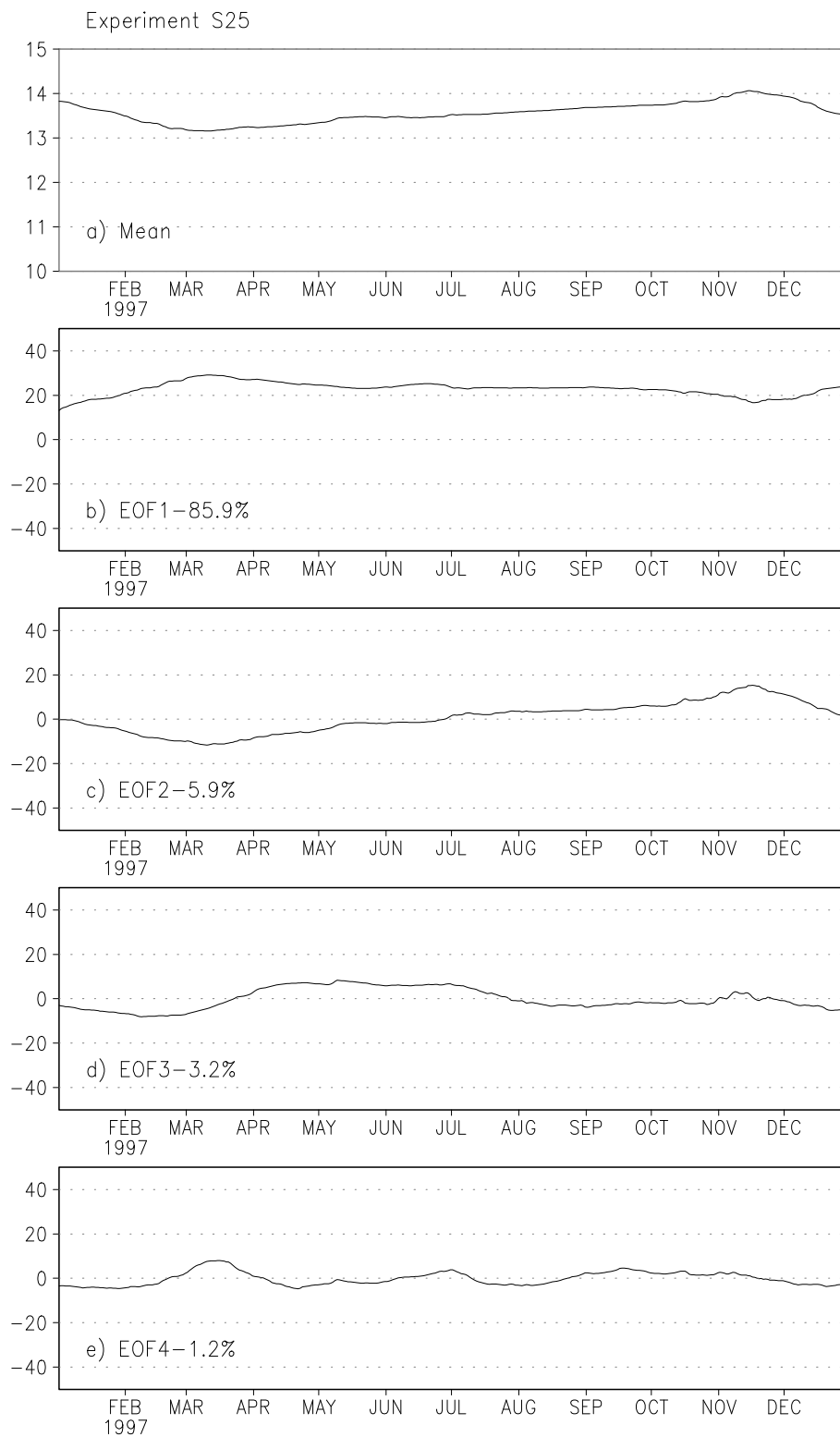


Figure 5.33: Same as Fig.5.31, but for experiment S25

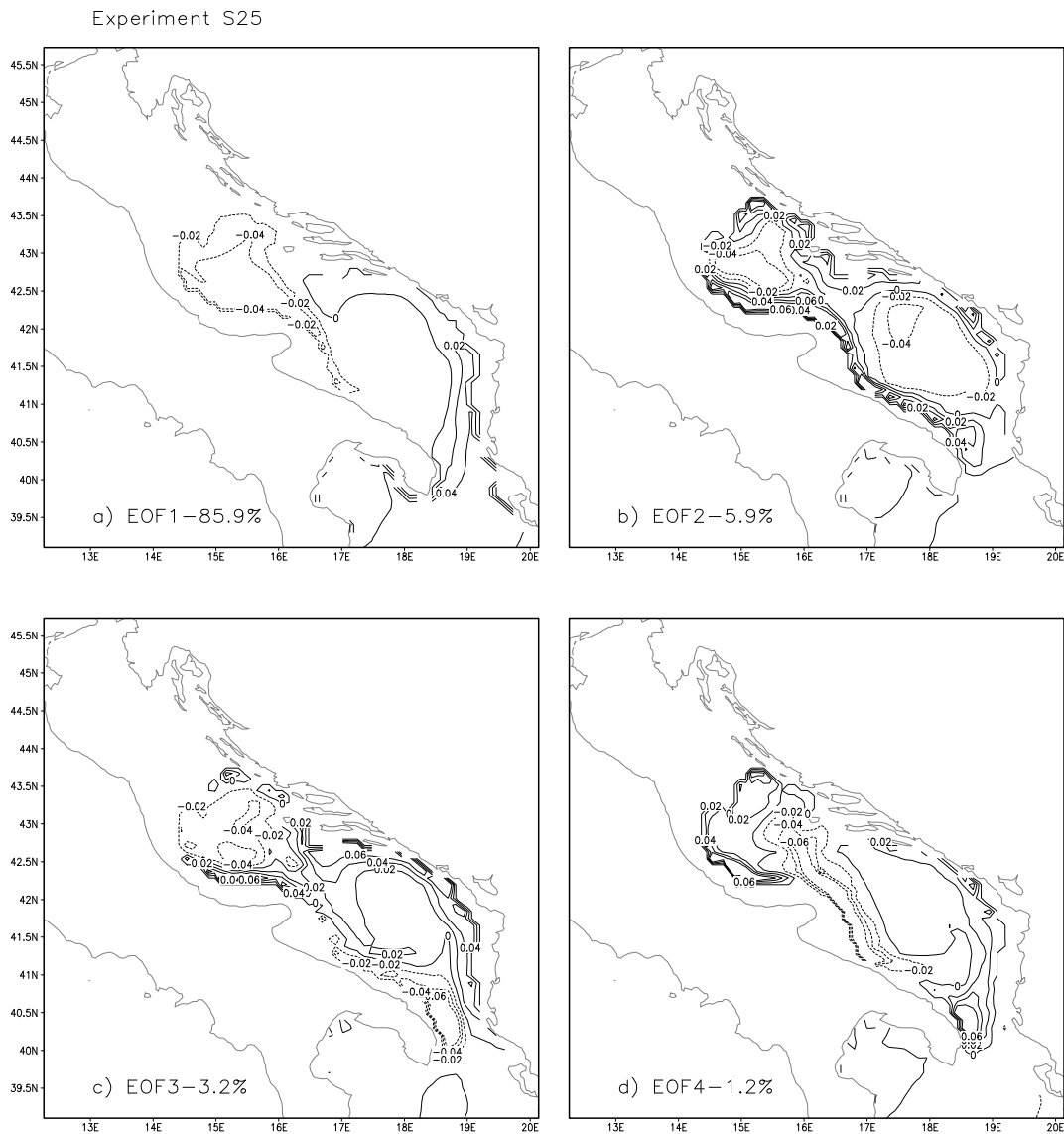


Figure 5.34: Same as Fig.5.32, but for experiment S25

counting for 95% of total variance, indicates that this EOF mode dominates the structure of the total transport. However, in this case it shows more attenuated short-term and long term variability, without the drift of the intensity from the initial value, which occurred in experiments S25 and S13. Again, increasing the horizontal resolution in the atmospheric model in the experiment C13 does not result in any significant change of the result in comparison to experiment C25 (Fig.5.29 and Fig.5.30).

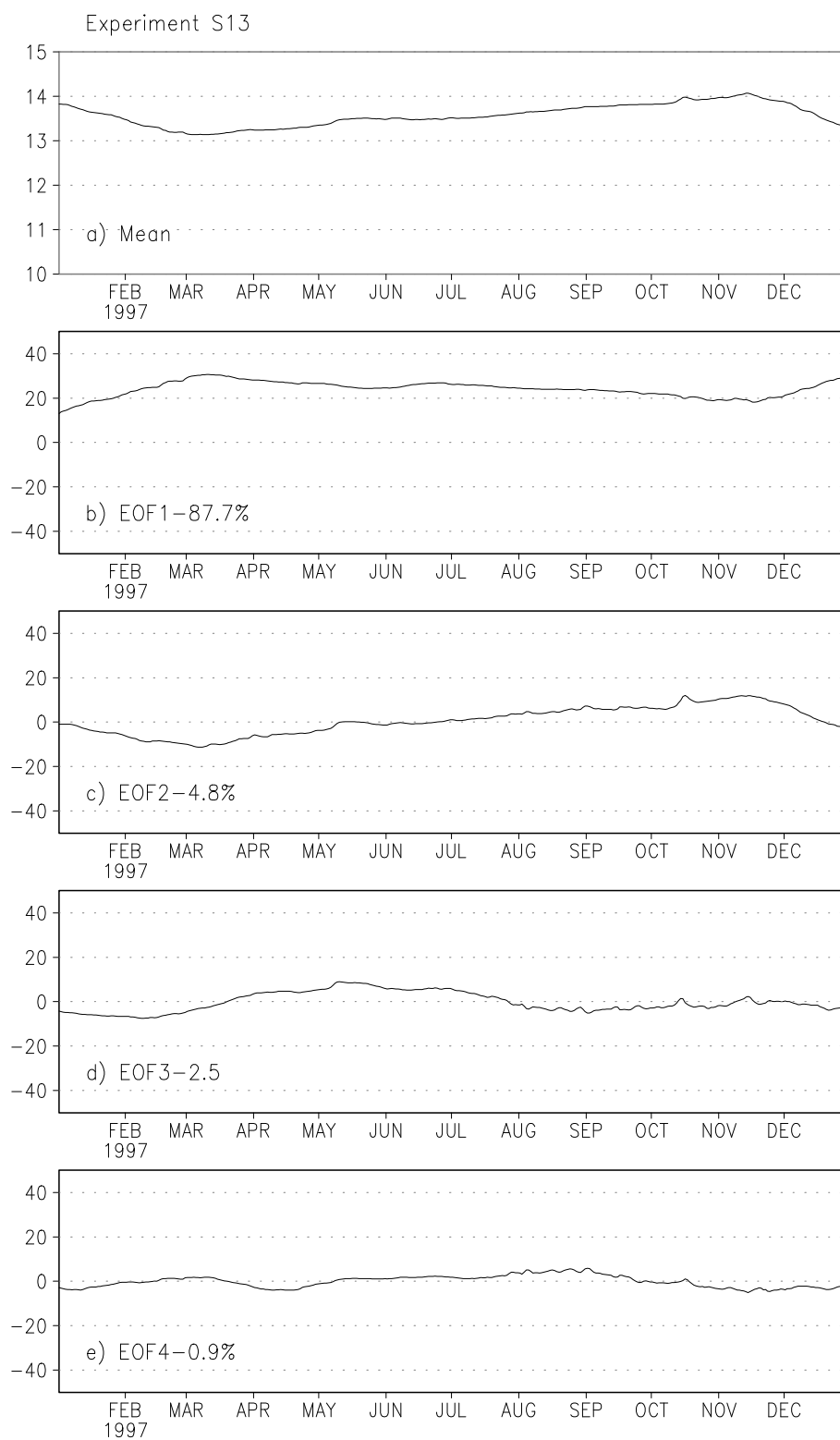


Figure 5.35: Same as Fig.5.31, but for experiment S13

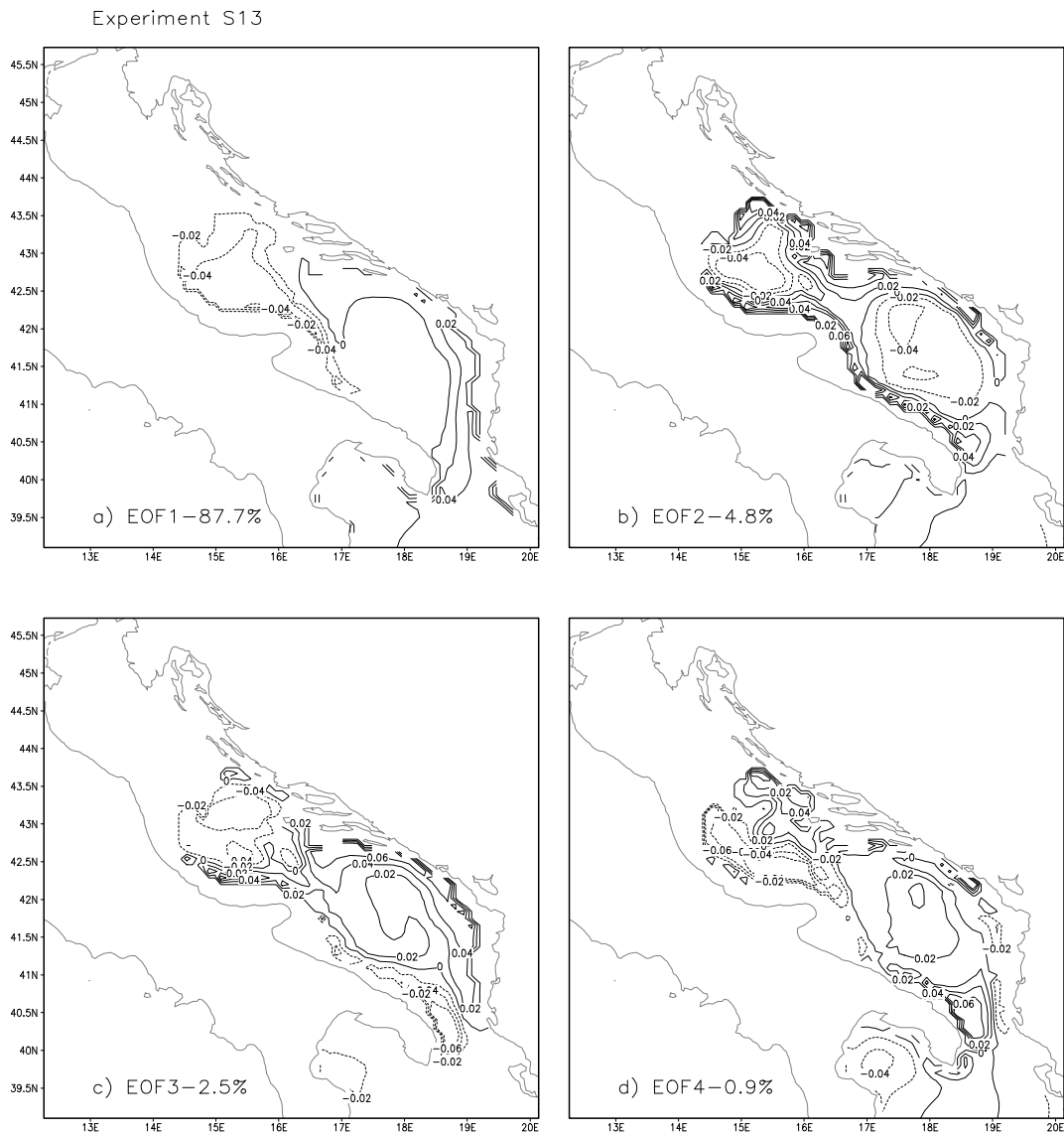


Figure 5.36: Same as Fig.5.32, but for experiment S13

We can conclude from the comparison between experiment GCM and experiment S25, that the higher horizontal resolution in the atmospheric model results in more stable spatial structures with an almost permanent South Adriatic Gyre, while there is a larger short-term variability in its intensity. The further increment of the atmospheric model horizontal resolution in experiment S13 does not result in any significant change of the total transport field in comparison with experiment S25. The use of the fully coupled model in experiment C25 results

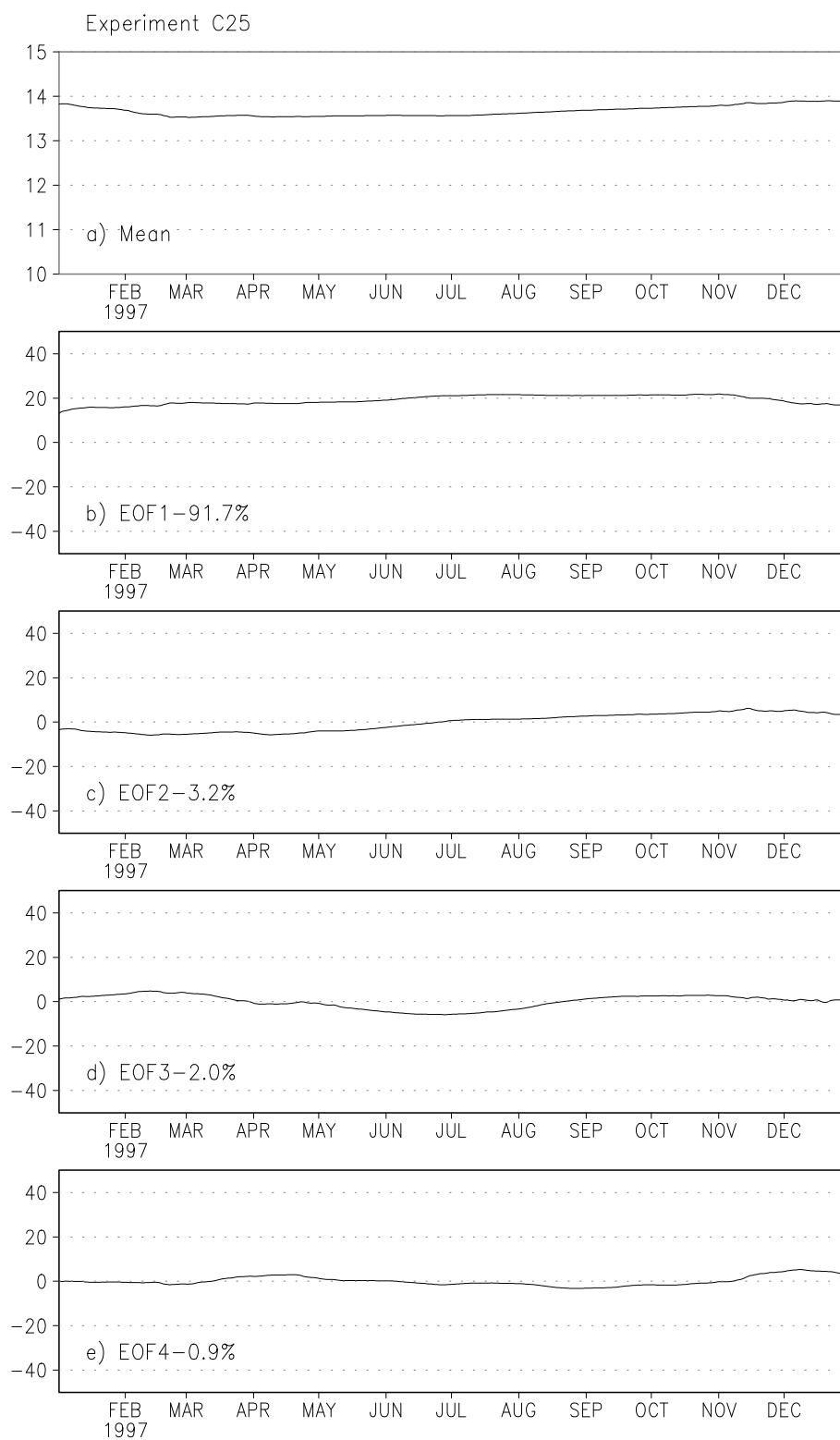


Figure 5.37: Same as Fig.5.31, but for experiment C25

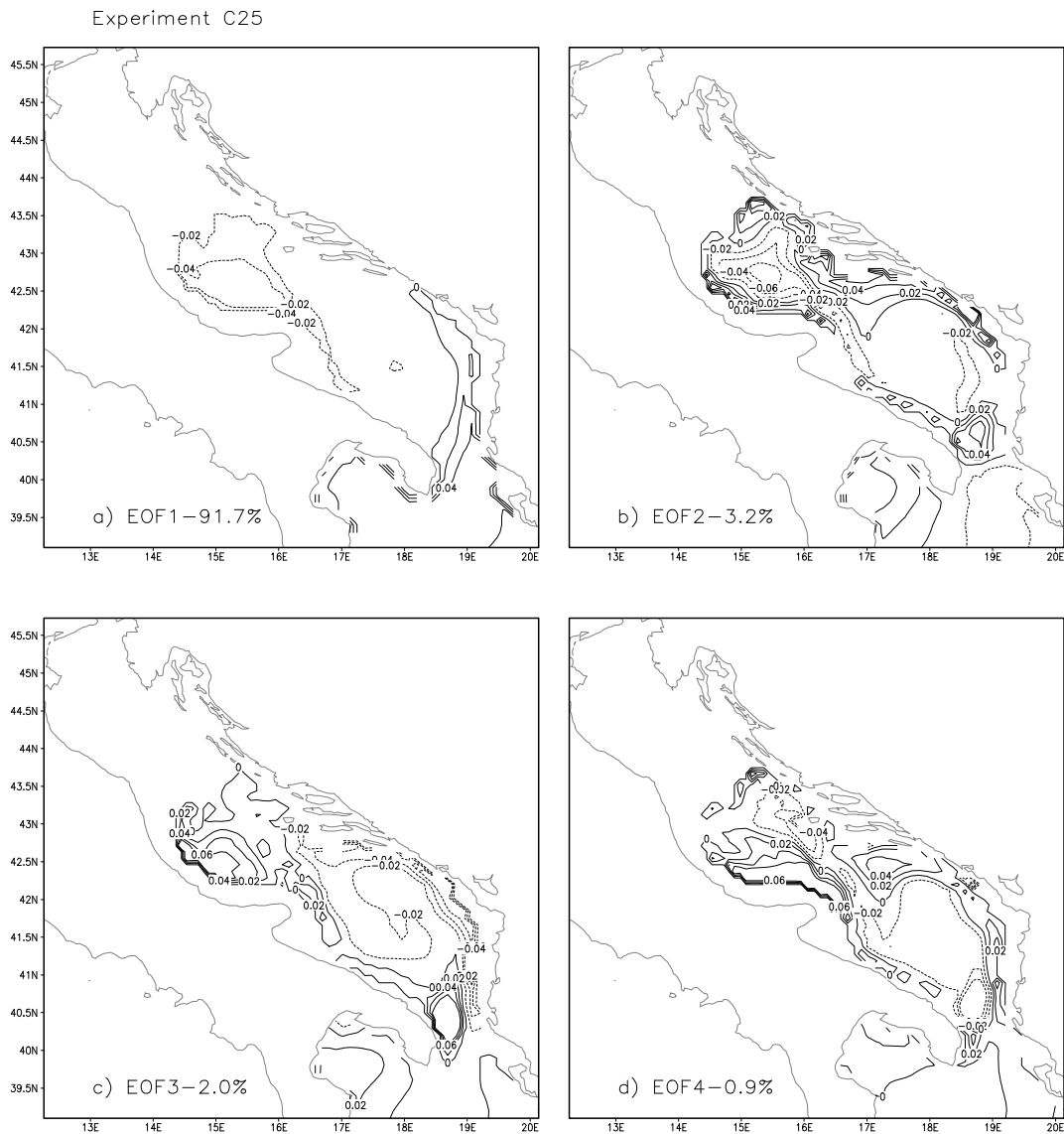


Figure 5.38: Same as Fig.5.32, but for experiment C25

in a temporary more stable simulation of the total transport stream function in comparison with one-way forcing experiments S25 and S13. Furthermore, now there is no positive drift from the initial value of the intensity of the mean total transport at the end of the year. Again, in comparison with experiment C25, the further increase of the atmospheric model horizontal resolution in experiment C13 does not result in any significant change in the result.

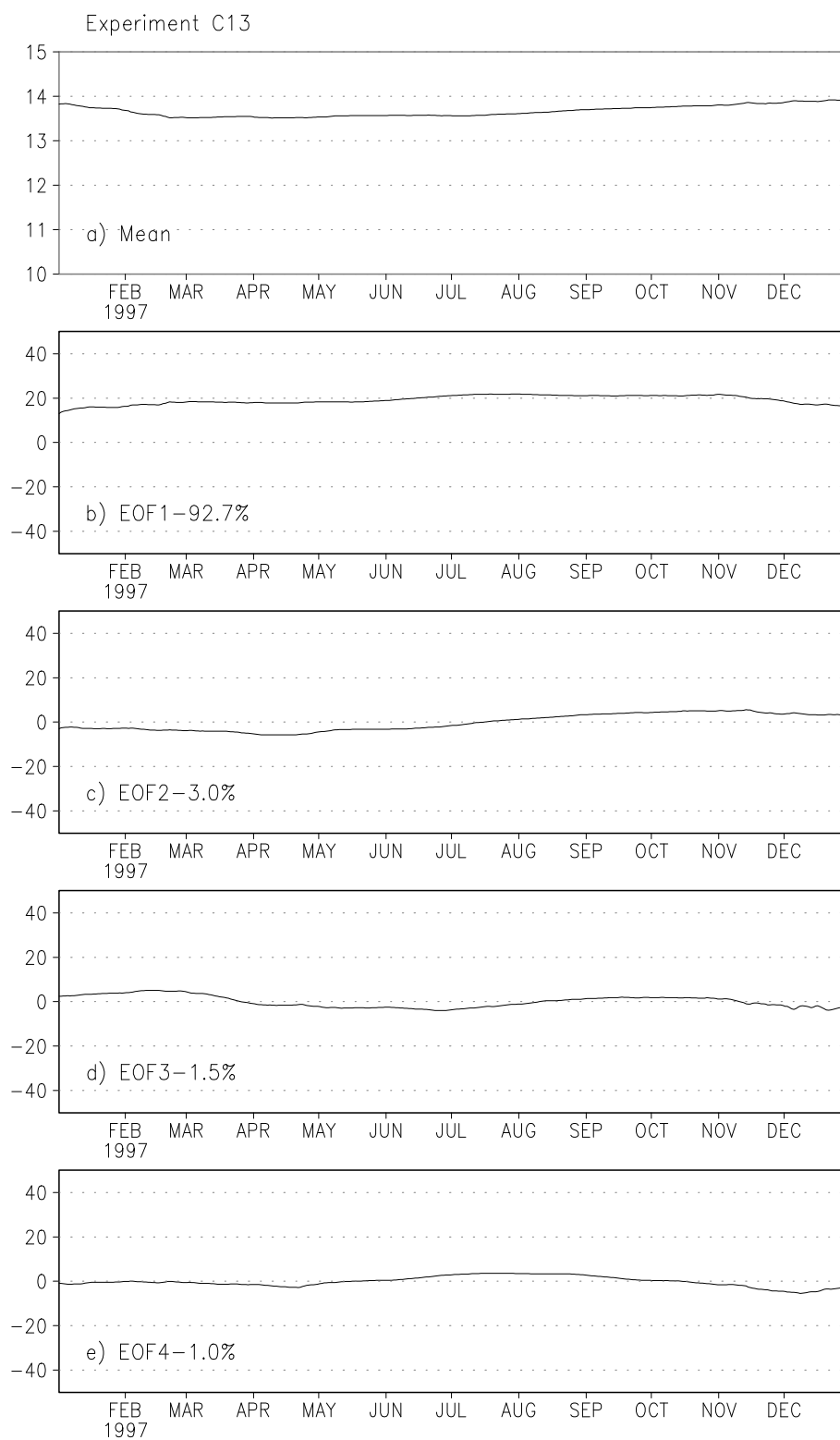


Figure 5.39: Same as Fig.5.31, but for experiment C13

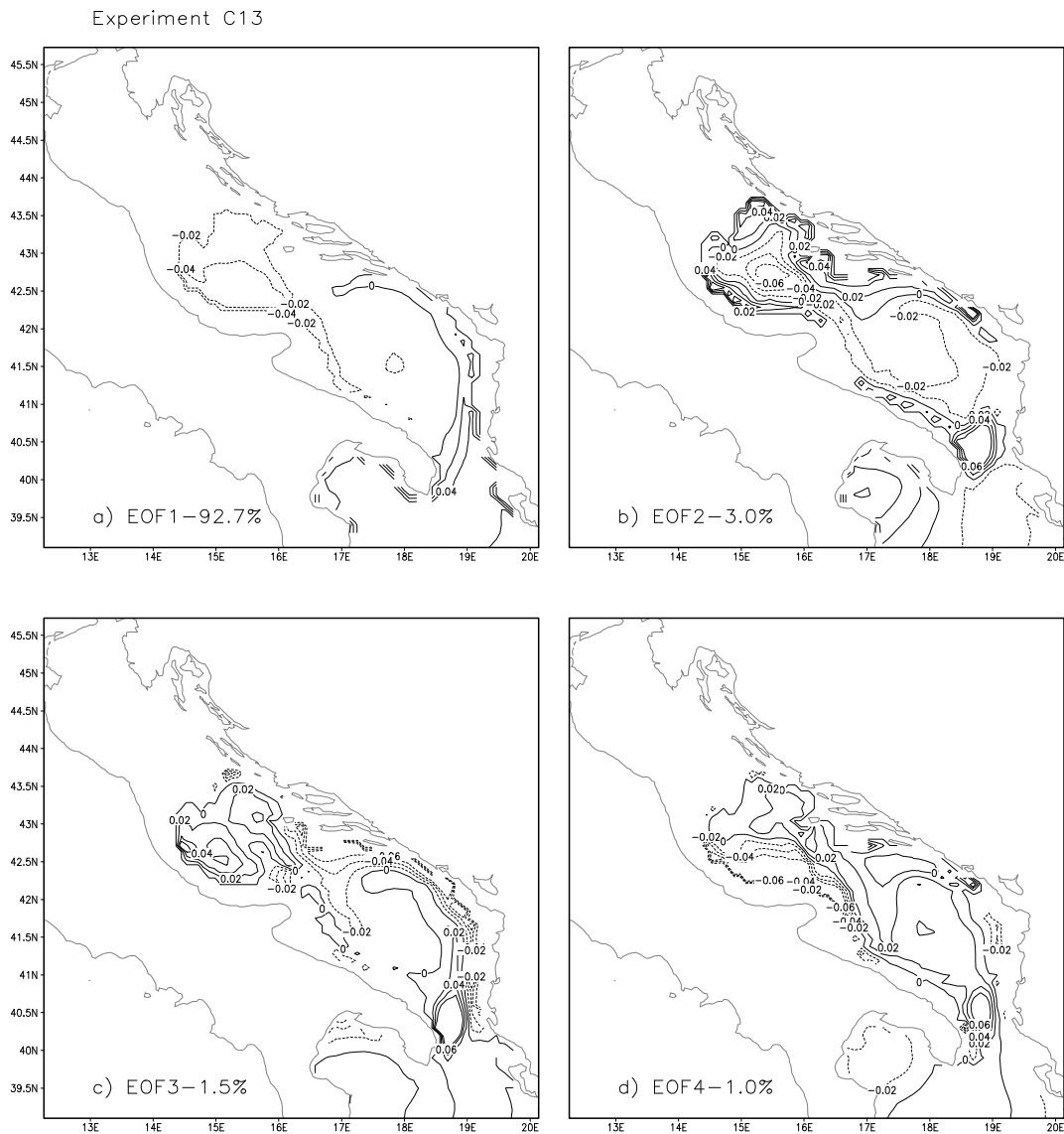


Figure 5.40: Same as Fig.5.32, but for experiment C13

## 5.2.4 Temperature at 100m depth

The time variability of the mean temperature at the 100m depth and the time and the space variability of the most significant EOF modes obtained from the experiment GCM are displayed in Fig.5.31 and Fig.5.32. From the temporal variation of the mean temperature, displayed in Fig.5.31a, we can see that there is the cooling in winter months, with the minimum mean temperature at the

end of February and at the beginning of March, and that there is the heating in the rest of the year. The spatial distribution of the first EOF mode (Fig.5.32a), in the combination with the coefficient which is positive during the whole year (Fig.5.31b), shows that there is a permanent inflow of relatively warm water from the Ionian Sea along the south-eastern coast, and the outflow of the relatively cold water from the Pomo Depression into the South Adriatic Depression. This is the most significant EOF mode, with 93% of the total variance and the coefficient which is much larger than in any other EOF mode.

In Fig.5.33 and Fig.5.34 we can see the temporal variability of the mean temperature and the temporal and spatial variability of the most significant EOF modes calculated from outputs of experiment S25. Again, the mean value has a minimum at the end of February and the beginning of March, but now it is much deeper than in the case of experiment GCM. The heating which starts in early March now stops in the middle of November, and then there starts the cooling. The temporal and spatial variation of the first EOF mode (Fig.5.33b and Fig.5.34a) indicates higher gradients between the warmer water from the Ionian Sea and the colder water from the Pomo Depression than in experiment GCM. The gradient becomes especially large at the end of the year during the cooling in December. In this experiment the second EOF mode becomes relatively important when its temporal variation reaches local extremes. This happens when at the same time the mean temperature reaches local extremes. When the mean temperature has the minimum value the negative minimum in the coefficient of the second EOF indicates that the temperature along coasts is lower than the temperature in the middle of depressions. When the mean temperature reaches the maximum the positive maximum in the second EOF mode indicates that the temperature along coasts is higher than the temperature in the middle of depressions. The remaining two EOF modes contribute less significantly to the structure of the simulated temperature field. We can see in Fig.5.35 and Fig.5.36 that the temporal and spatial variation of the mean simulated temperature and of its most significant EOF modes in experiment S13 is very similar to that obtained in experiment S25.

The temporal variation of the mean simulated temperature and the temporal and the spatial variation of its principal EOF modes calculated from outputs of the coupled model experiment C25 are displayed in Fig.5.37 and Fig.5.38. Again, like in other experiments, the mean temperature reaches the minimum at the end of February and at the beginning of March (Fig.5.37a). Then, like in

experiment GCM, it slowly raises until the end of the year. The temporal and spatial variation of the first EOF mode (Fig.5.37b and Fig.5.38a) indicate that, in comparison to experiments S25 and S13, the gradient between the water from the Ionian Sea and from the Pomo Depression is relatively smaller. Furthermore, the comparison of the first EOF mode with other EOF modes shows that this EOF mode is by far the most significant. In fact, it is very similar to the gradient obtained in experiment GCM. The temporal variation of the mean simulated temperature and the temporal and spatial variations of its principal EOF modes (Fig.5.39 and Fig.5.40), obtained in the fine resolution coupled model experiment C13, are very similar to those obtained in the coarse resolution coupled model experiment C25.

The comparison between ocean model outputs of the temperature at the 100m depth shows that there is a relatively large difference between the outputs from experiments GCM, C25 and C13 and the outputs from experiments S25 and S13. In experiments S25 and S13 the cooling in winter is more intensive and the new cooling starts in autumn. This temporal variation may be the result of wrong surface heat fluxes in experiments S25 and S13. It is shown in Subsection 5.1.1. that in experiments S25 and S13 appears the relatively large negative surface temperature deviation in comparison with the analyses. The unrealistically large cooling of the surface temperature reduces the vertical stability in the ocean model and it may result in the increased vertical mixing. As a consequence, at the end of the year the temperature at the 100m depth may become significantly lower than the initial value at the beginning of the year. On the other hand, the large positive deviation of the surface temperature in experiment GCM results in the higher vertical stability in the ocean model. Therefore, in experiment GCM the positive surface temperature deviation is not reflected in the temperature field at the depth of 100m.

Furthermore, it may be noticed that the high-frequent temporal variability of temperature fields at the surface is strongly reduced at the 100m depth, because at this depth the synoptic weather scale is mostly filtered out.

## 5.3 Sensitivity of atmospheric outputs

The main objective of the comparison between experiments is the evaluation of the simulation of oceanographic parameters. However, during the two-way interaction in the coupled model atmospheric parameters close to the sea surface are influenced by the surface temperature simulated in the ocean model. To estimate the sensitivity of the atmospheric model outputs to the change of the sea surface temperature between coupled and uncoupled experiments, simulated atmospheric model parameters are compared at the 9 meteorological stations displayed in Fig.4.22. In this way we can also compare the outputs of each sensitivity experiment with the observations at coastal stations.

The reference experiment for the comparison is experiment S13. Previously in Section 4.2, its outputs were compared with observations at meteorological stations. Now the outputs of experiment S13 are compared with the outputs simulated in the coarser resolution simulation S25, in which, like in experiment S13, the sea surface temperature is obtained using daily analysis from satellite measurements. Furthermore, the outputs from experiment S13 are compared with the outputs obtained in the coupled model experiment C13 with the same horizontal resolution as in experiment S13, but with the sea surface temperature simulated by the ocean model.

### 5.3.1 Temperature at 2m

Differences between the 2m temperature simulated in experiment S13 and in experiment S25 are displayed in Fig.5.41 and Fig.5.42. Now, in comparison with Fig.4.23 and Fig.4.24, the range of the vertical axes is reduced to  $(-2^{\circ}C, 2^{\circ}C)$ , while in Fig.4.23 and Fig.4.24 it was  $(-6^{\circ}C, 6^{\circ}C)$ , to highlight details of the difference. We can see that at station 1 the 2m temperature simulated in experiment S13 is higher than the 2m temperature simulated in experiment S25 during the whole year. However, this difference does not give any preference to either experiment, because the difference does not seem to be related to the difference between the simulated value in experiment S13 and observations (Fig.4.23). At station 2 the difference between experiment S13 and experiment S25 is very small, while at the geographically nearby station 3 the difference is relatively large with

a high short term variability. At station 4 the difference between simulations is relatively small in comparison to differences at other stations, but it is relatively large in comparison to the difference between the simulation and the observation (Fig.4.23). Again, it is difficult to estimate which simulation is in better agreement with observations.

At station 5 there are relatively large differences between experiments in spring when outputs from experiment S13 are in better agreement with observations. Differences between simulated values in experiment S13 and in experiment S25 at stations 6 and 7 are relatively small in comparison with differences between simulated and observed values (Fig.4.24). However, at both stations the 2m temperature simulated in experiment S13 is slightly higher than the one simulated in experiment S25 during the whole year. As the 2m temperature simulated in experiment S13 is higher than observations, this means that outputs from experiment S25 are in slightly better agreement with observations. On the other hand, there is a relatively large difference between simulated values at station 8 with higher values of the 2m temperature simulated in experiment S13 resulting in better agreement with observations (Fig.4.24). At station 9 the significant difference between simulations exists only in the middle of May and in June, when in comparison with Fig.4.24 we can see that outputs obtained from experiment S25 are in better agreement with observations.

The difference between the 2m temperature, simulated in experiment S13 using the analysed sea surface temperature and simulated in experiment C13 using the simulated sea surface temperature, are displayed in Fig.5.43 and Fig.5.44. Again, the range of the vertical axes is set to  $(-2^{\circ}C, 2^{\circ}C)$  to highlight details of the difference between experiments. We can see that generally, at all stations, differences between values simulated in experiments S13 and in experiment C13 are smaller than differences between values simulated in experiment S13 and in experiment S25. At station 1 the only significant difference occurs at the beginning of summer, but the comparison with differences between simulated and observed values (Fig.4.23) does not indicate which simulation is better. The relatively large difference at the beginning of summer is also evident at station 2 and especially at station 3. In this period and at the beginning of autumn outputs from experiment C13 seem to be in slightly better agreement with observations (Fig.4.23). The similar conclusion may be drawn also for stations 4 and 5, while at other stations the difference between simulations is not noticeable in comparison with the difference between the simulation and observations.

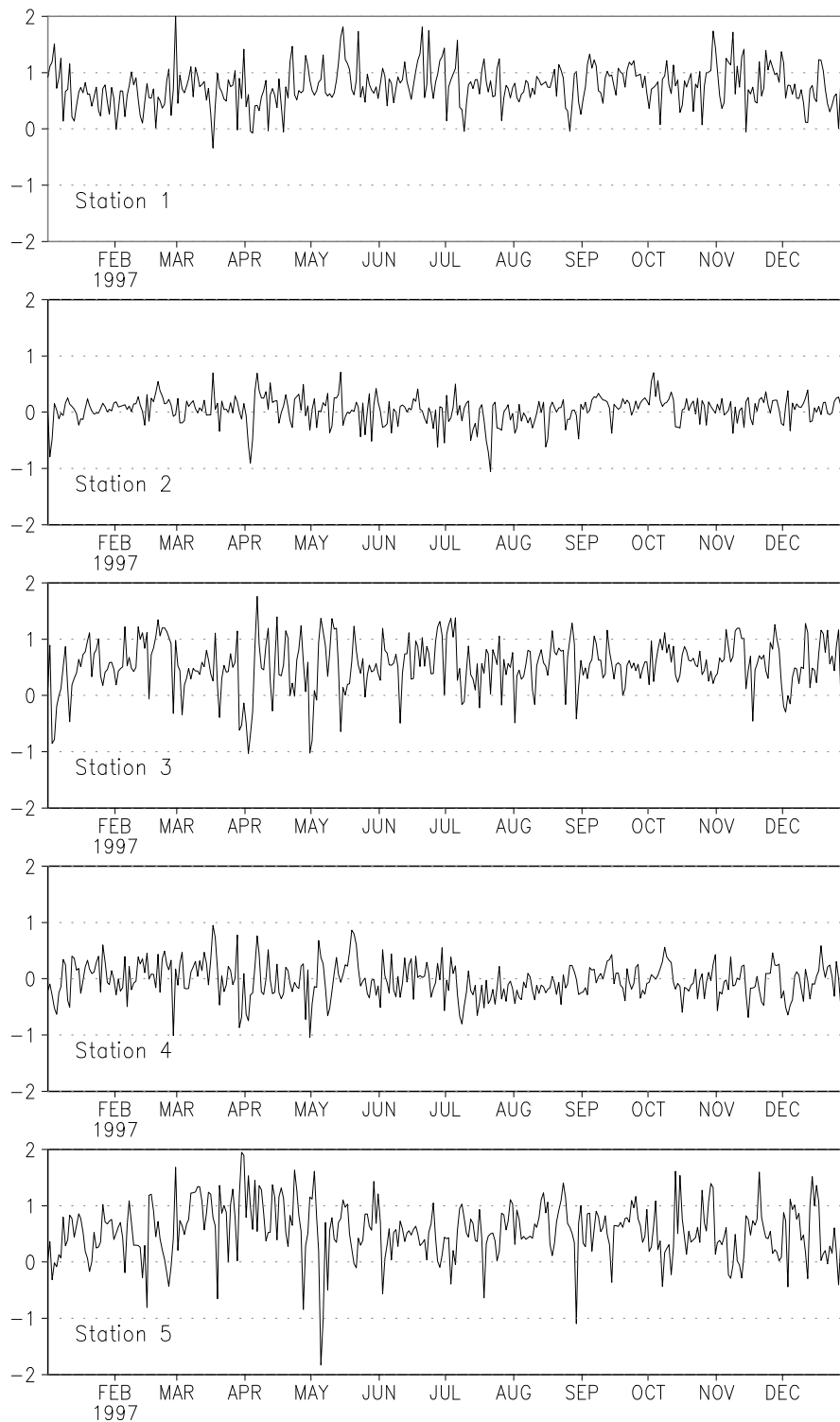


Figure 5.41: Difference between 2m temperature simulated in experiment S13 and in experiment S25 at coastal stations 1 - 5 ( $^{\circ}C$ )

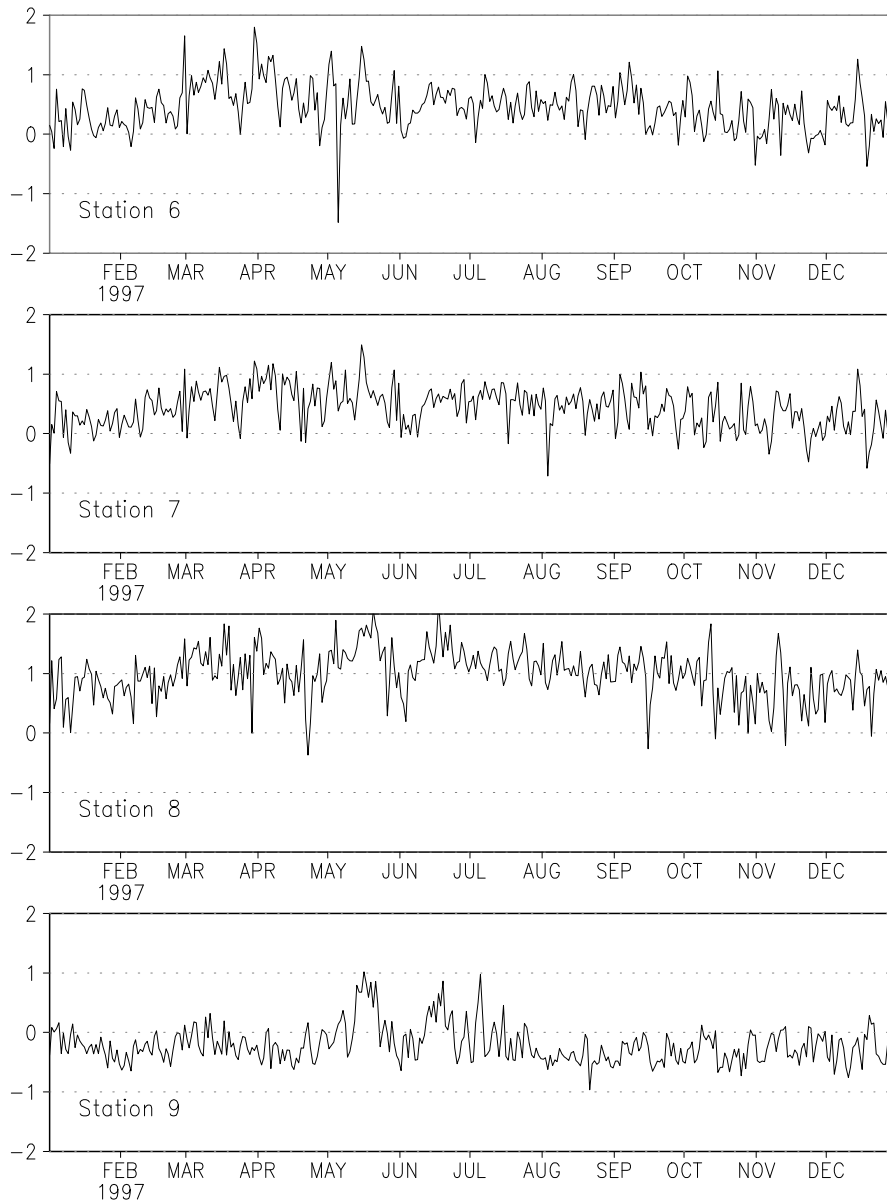


Figure 5.42: Same as Fig.5.41, but for stations 6 - 9.

### 5.3.2 Sea level pressure

Differences between the sea level pressure simulated in experiment S13 and in experiment S25 are displayed in Fig.5.45 and Fig.5.46. In comparison to Fig.4.25 and Fig.4.26, and to show details of the difference between experiments, the range of the vertical axes is reduced from  $(-3mb, 3mb)$  to  $(-2mb, 2mb)$ . At station 1 the sea level pressure simulated in experiment S25 is significantly lower than the one simulated in experiment S13 during the whole year. The comparison with

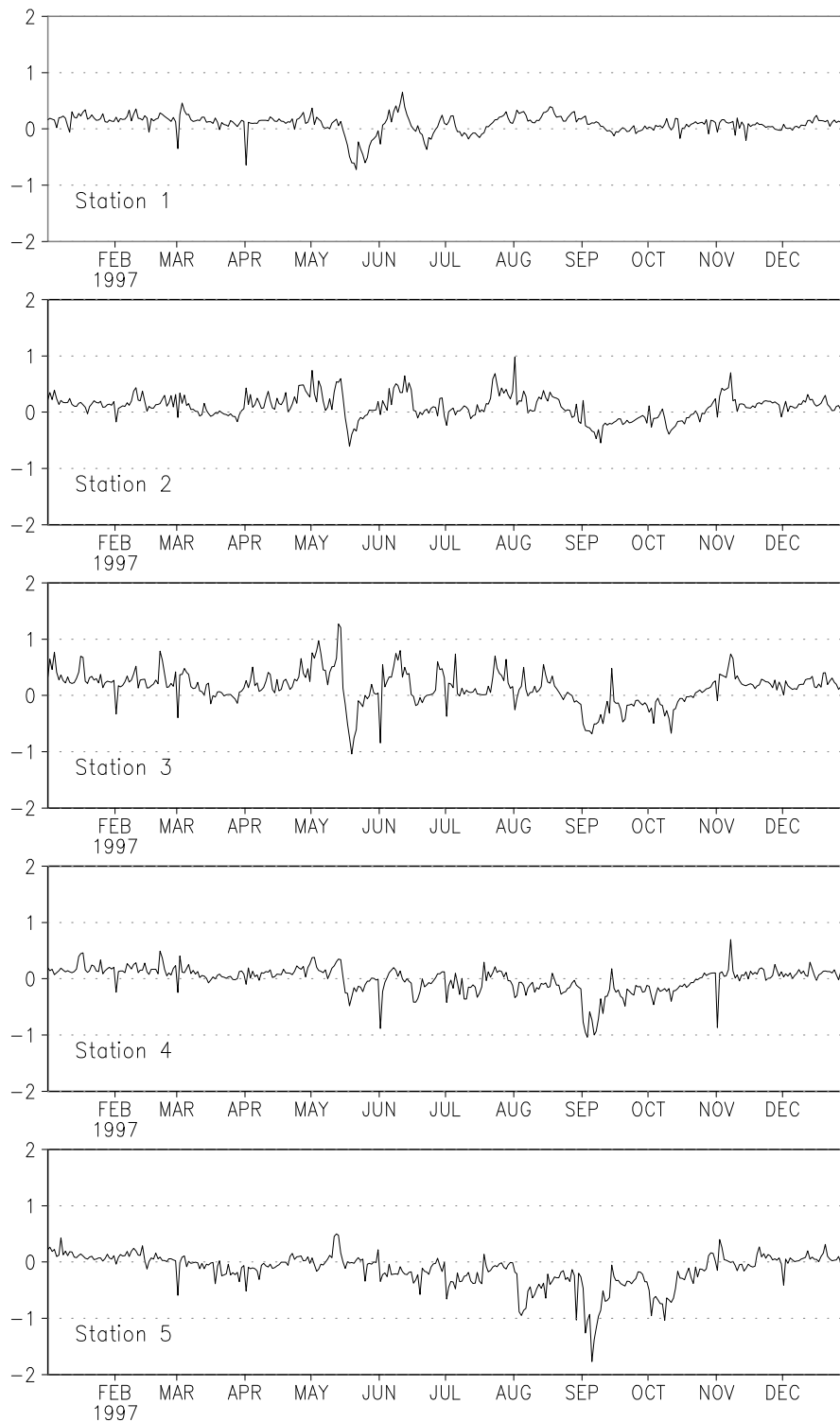


Figure 5.43: Difference between 2m temperature simulated in experiment S13 and in experiment C13 at coastal stations 1 - 5 ( $^{\circ}C$ )

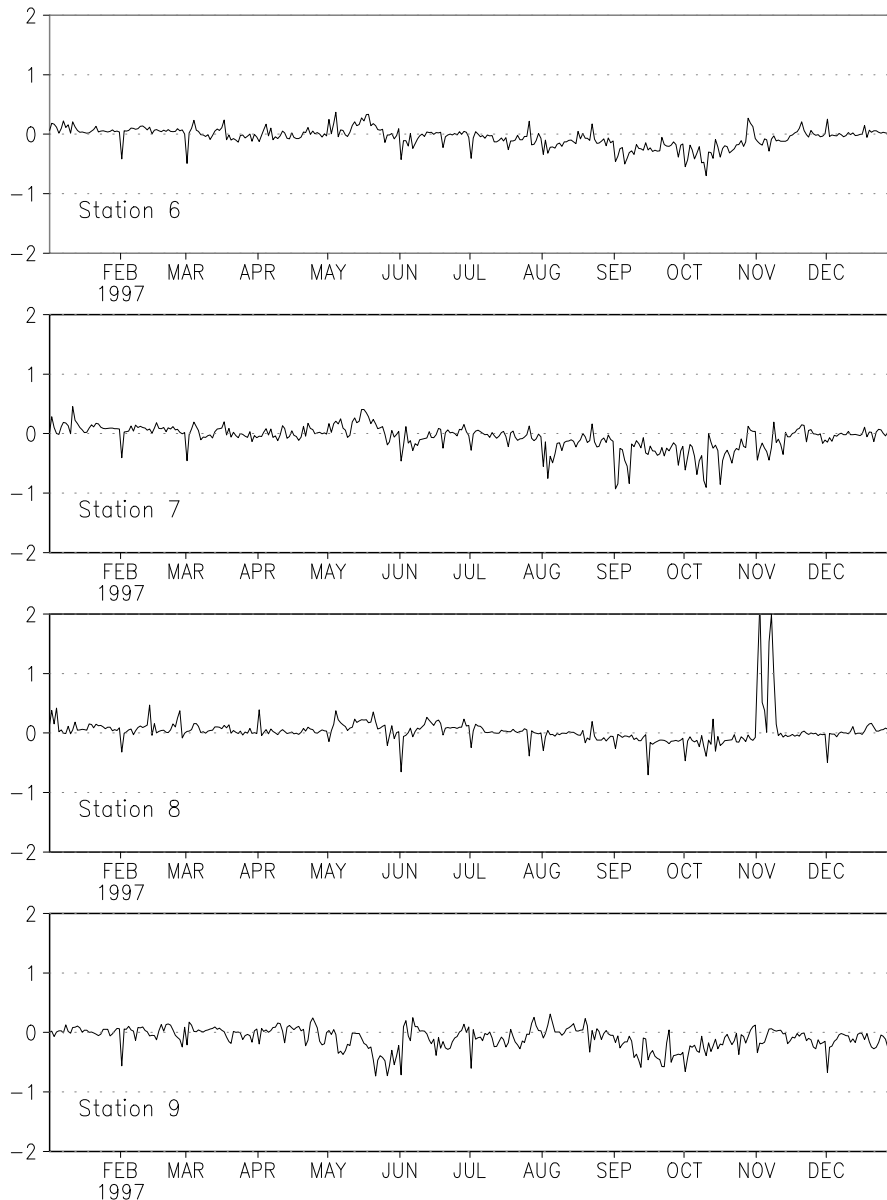


Figure 5.44: Same as Fig.5.43, but for stations 6 - 9.

Fig.4.25 indicates that values obtained in experiment S13 are in better agreement with observations. The difference may be explained by the different model topography in experiments S13 and S25, assuming that in the experiment S25 the sea level pressure at the station point is calculated with the systematic error due to the extrapolation from the surface pressure at the point which is high above the sea level. A relatively small systematic difference between experiments S13 and S25 is also visible at stations 3 and 4. Other variations in the difference between the sea level pressure simulated in experiments S13 and S25 at station points are

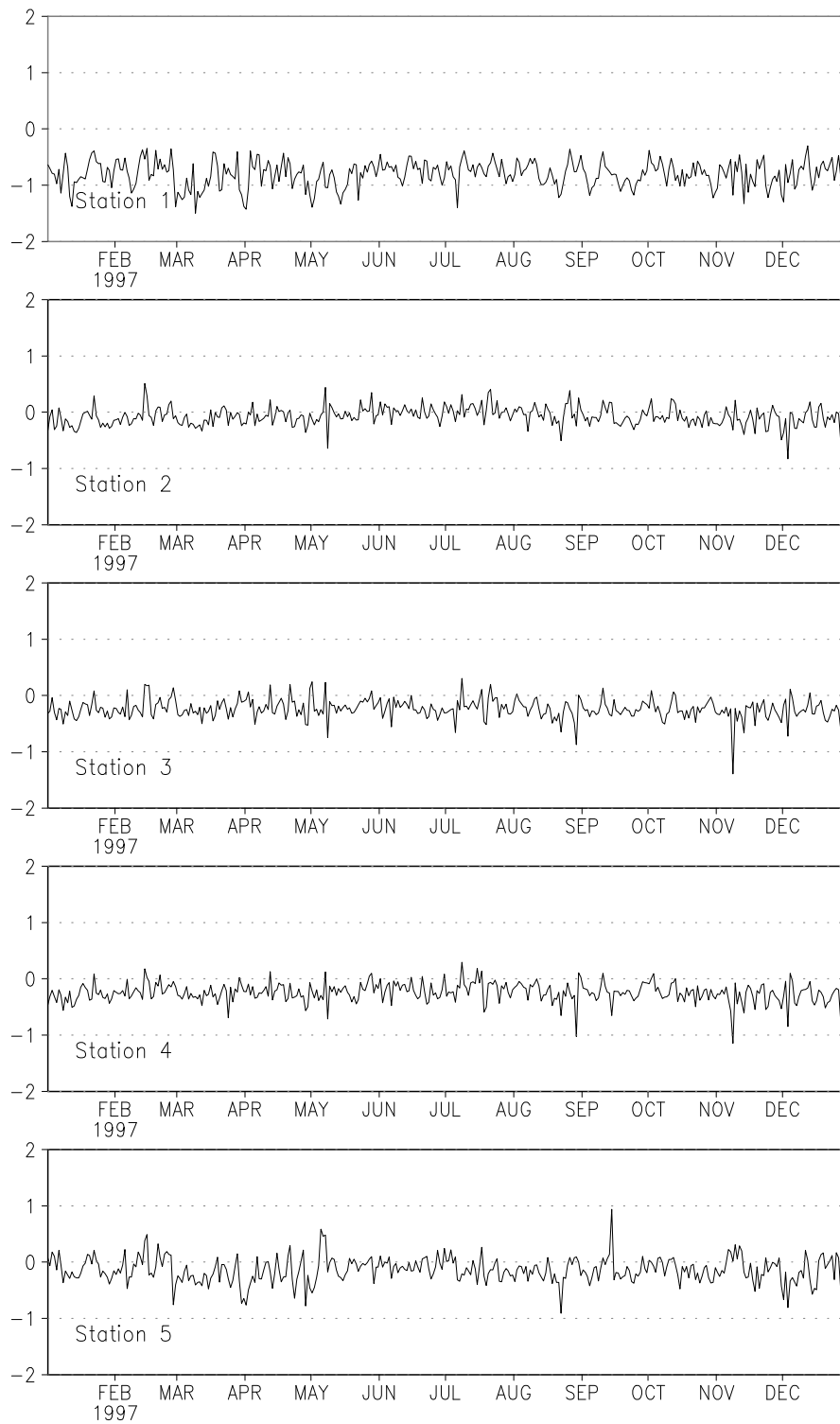


Figure 5.45: Difference between sea level pressure simulated in experiment S13 and in experiment S25 at coastal stations 1 - 5 (*mb*)

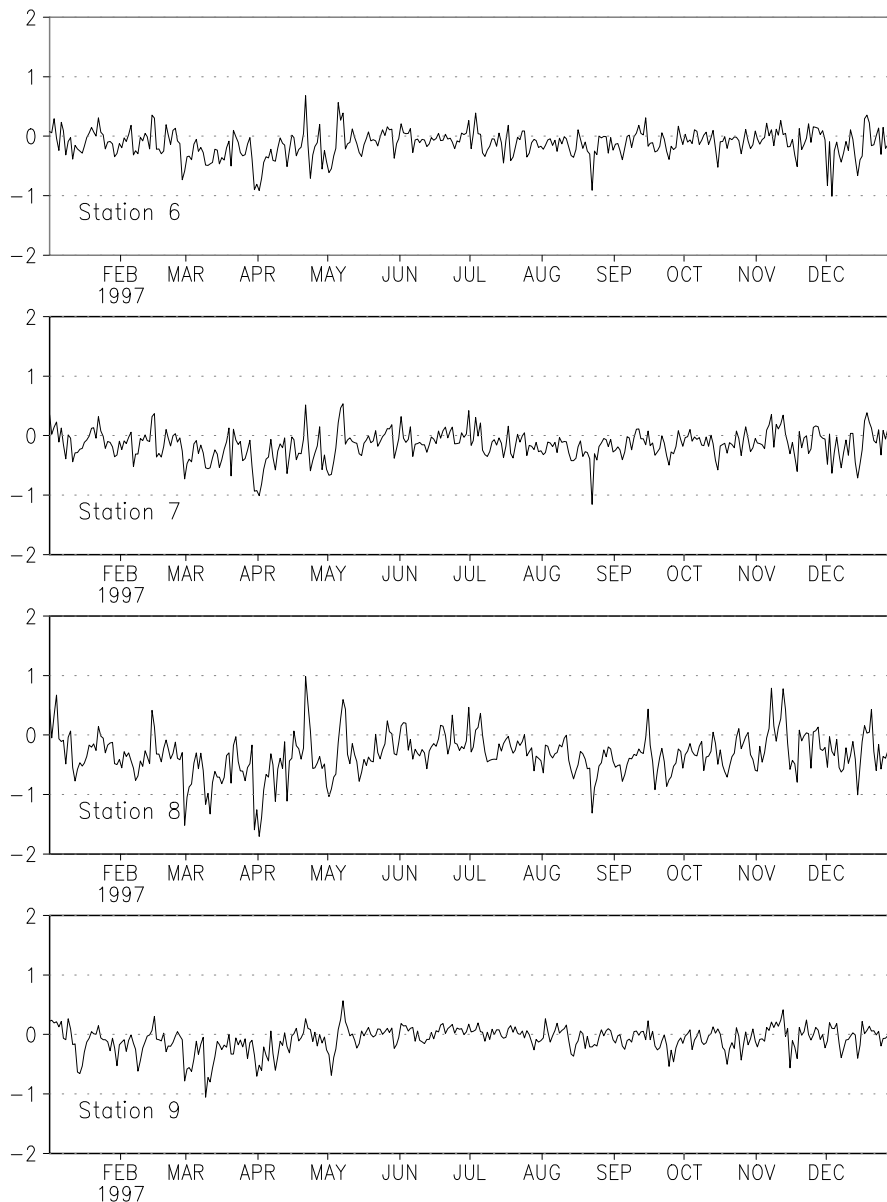


Figure 5.46: Same as Fig.5.45, but for stations 6 - 9.

relatively small and they do not seem to change significantly the difference between simulated and observed values. The only exception can be found at station 8 showing a relatively large variation of the difference between values obtained in experiments S13 and S25. The comparison with differences between simulated and observed values (Fig.4.26) indicates that in comparison to experiment S25 both the instantaneous and time averaged values obtained in experiment S13 are in better agreement with observations.

Differences between the sea level pressure in experiment S13 and in experiment

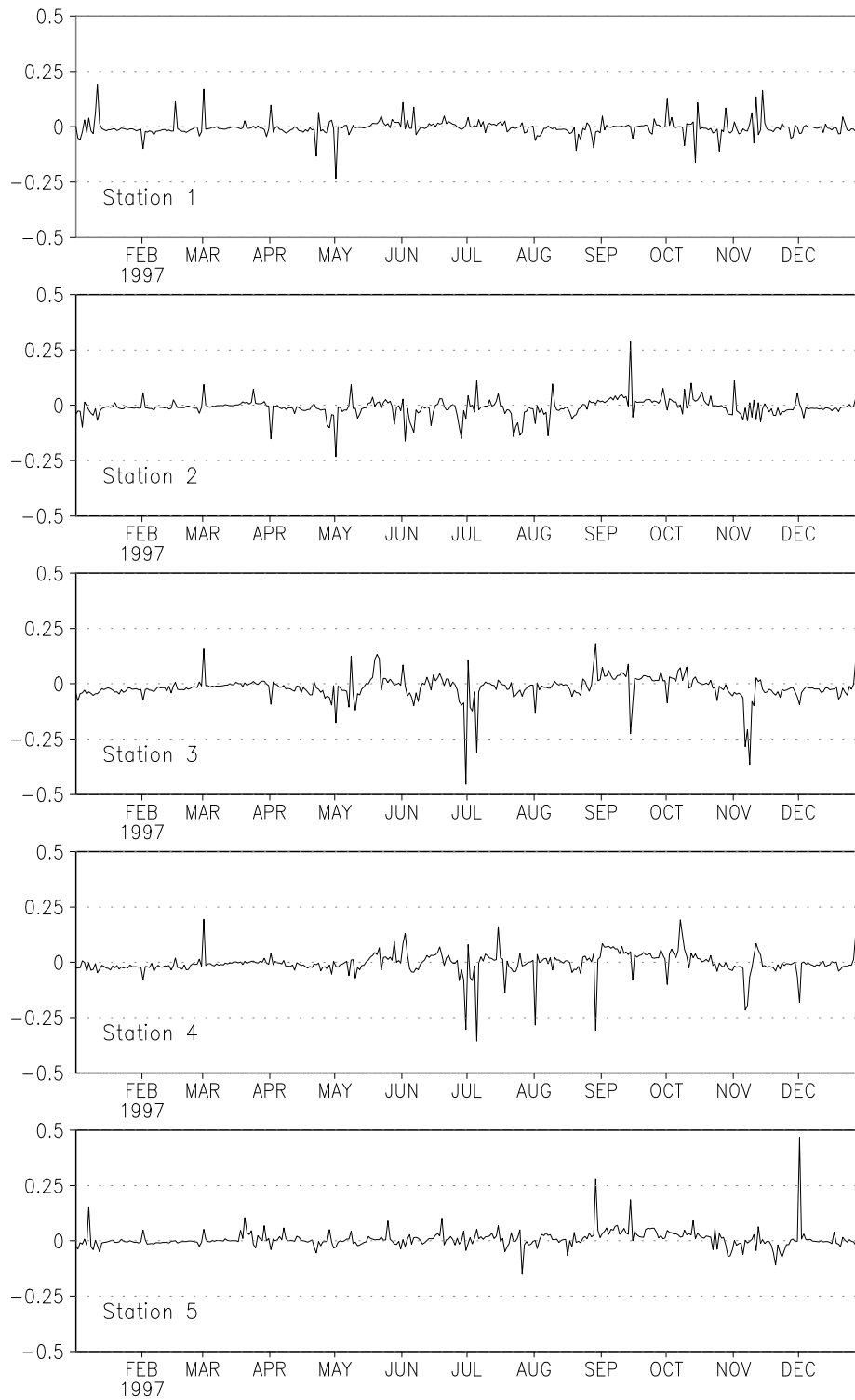


Figure 5.47: Difference between sea level pressure simulated in experiment S13 and in experiment C13 at coastal stations 1 - 5 (*mb*)

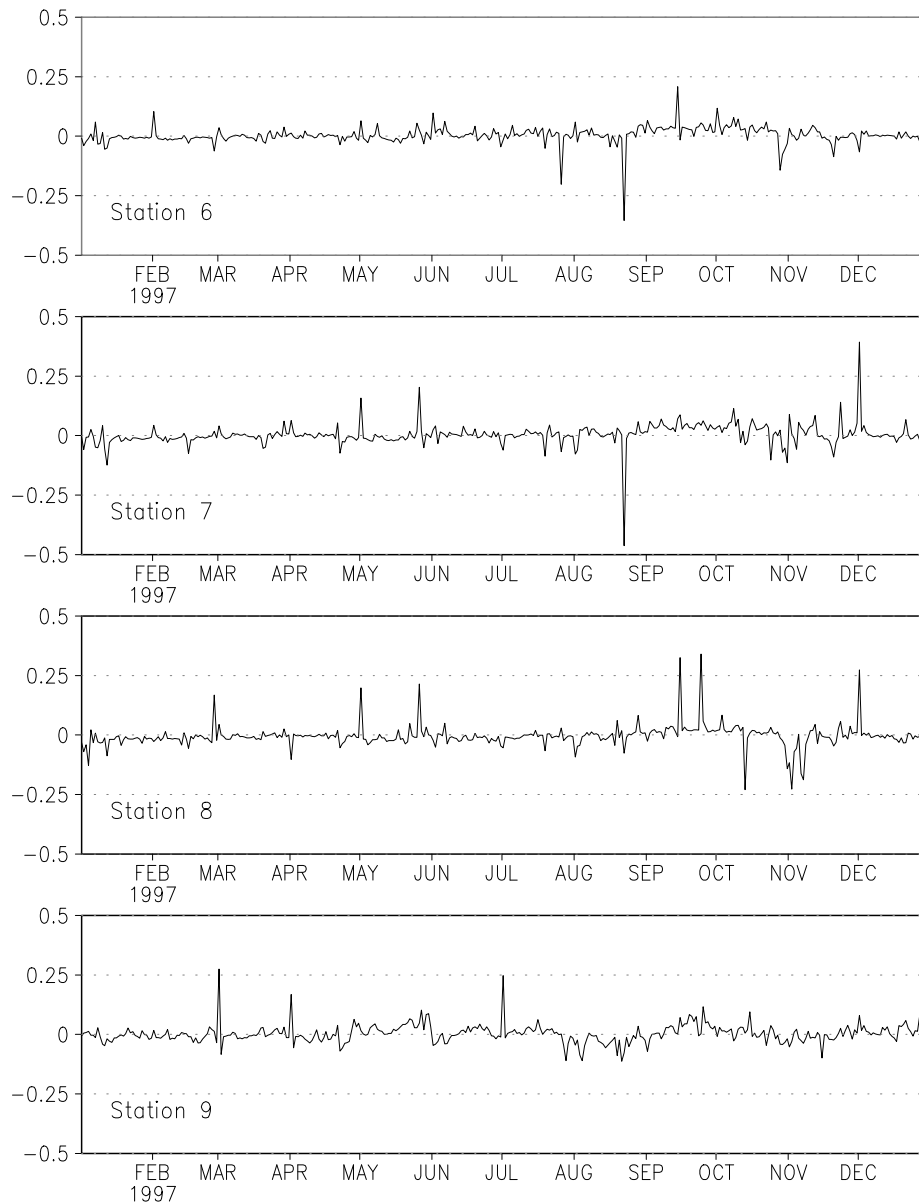


Figure 5.48: Same as Fig.5.47, but for stations 6 - 9.

C13 are displayed in Fig.5.47 and Fig.5.48. Now the vertical axis range is further reduced to  $1mb$ . We can see that differences in the simulated sea level pressure, resulting from different sea surface temperature fields in atmospheric models, are relatively small at all station points.

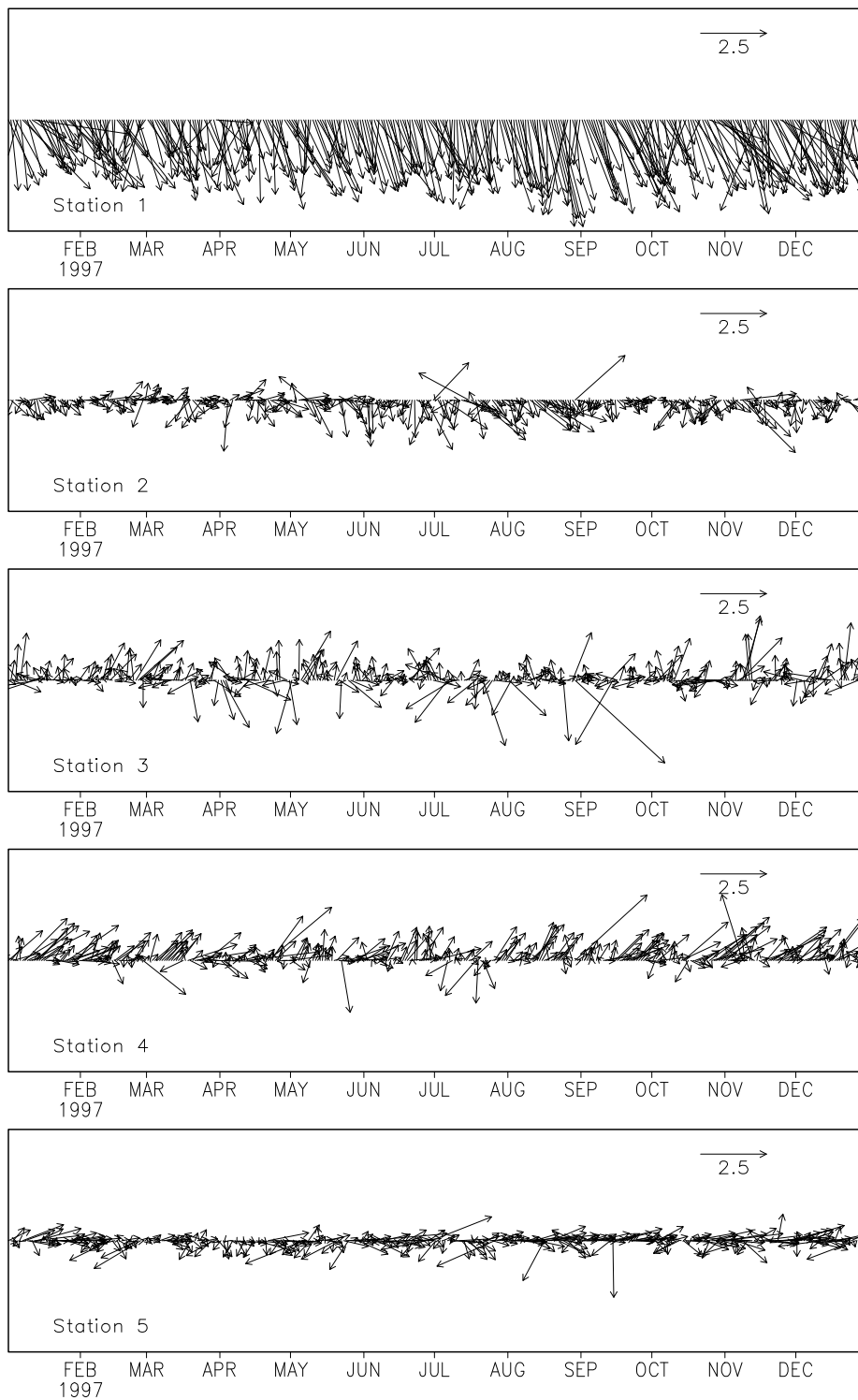


Figure 5.49: Difference between 10m wind simulated in experiment S13 and in experiment S25 at coastal stations 1 - 5 ( $m s^{-1}$ )

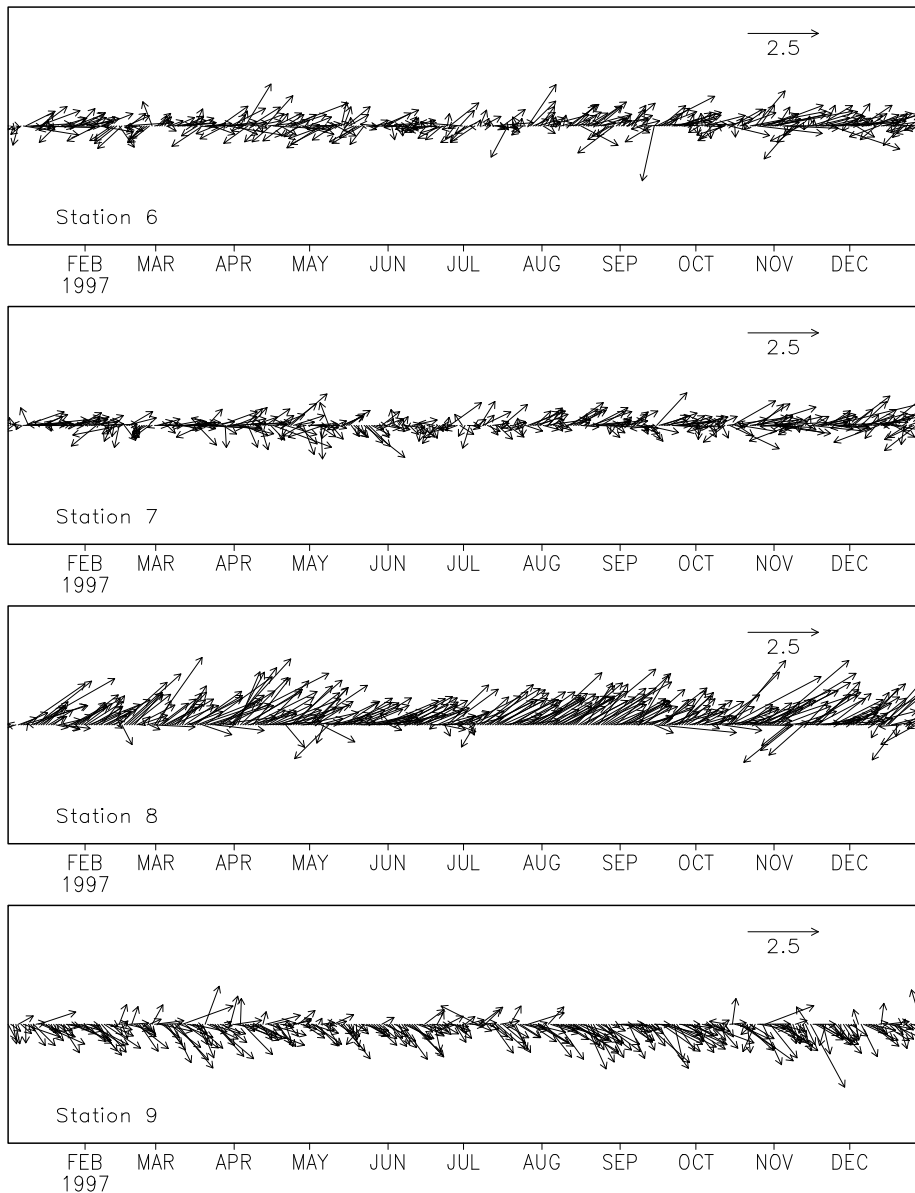


Figure 5.50: Same as Fig.5.49, but for stations 6 - 9.

### 5.3.3 Surface wind

The difference between the 10m wind in experiment S13 and in experiment S25 are displayed in Fig.5.49 and Fig.5.50. To highlight details, the length of the unit vector is reduced from  $10\text{m s}^{-1}$  in Fig.4.27 and Fig.4.28 to  $2.5\text{m s}^{-1}$ . Again, at station 1 there is a systematic difference between the experiments, which may be explained by the different topography representation in the low and in the high resolution model. A less pronounced systematic difference is also evident at station 8. At other stations the difference seems to be more random. In compar-

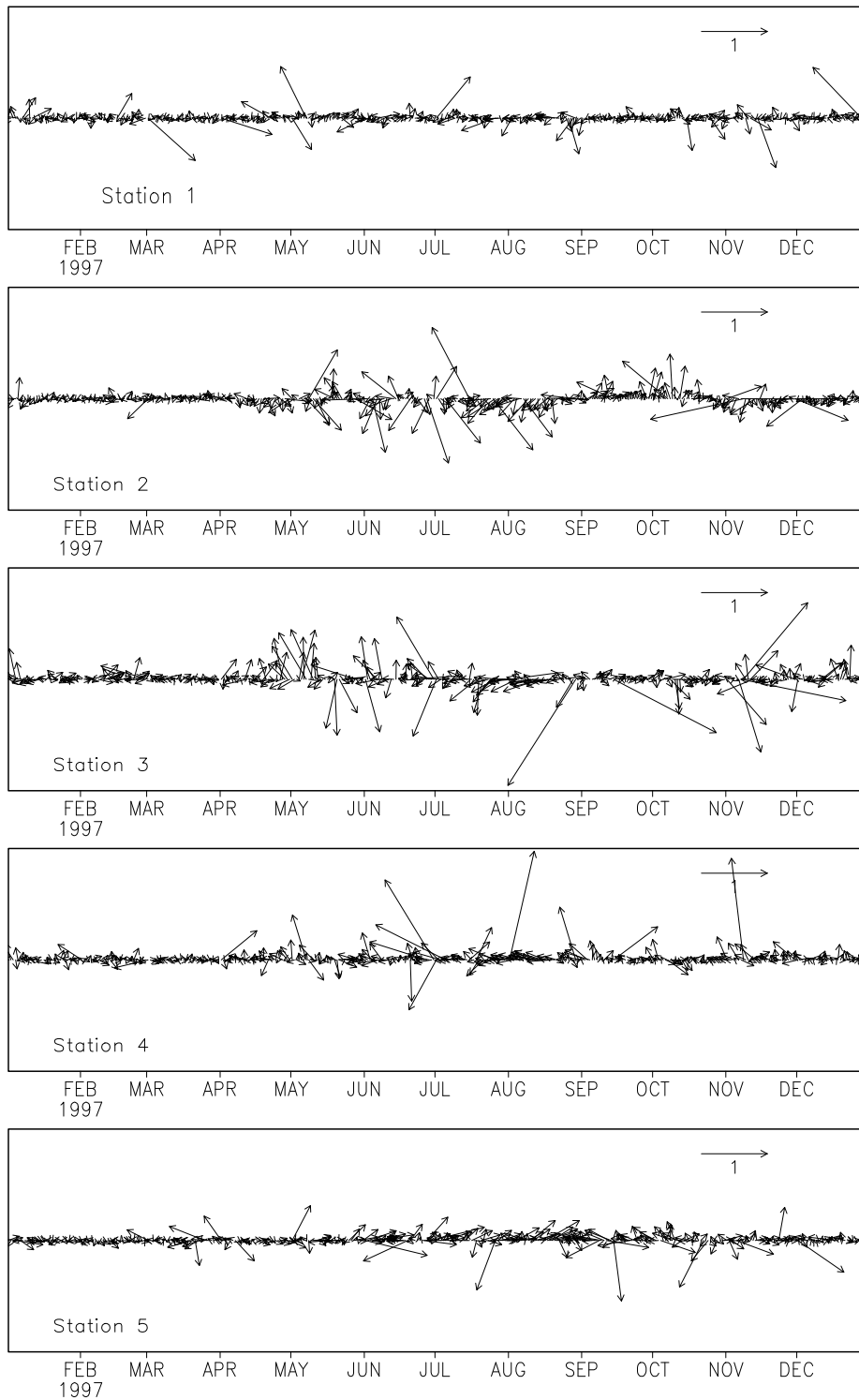


Figure 5.51: Difference between 10m wind simulated in experiment S13 and in experiment C13 at coastal stations 1 - 5 ( $ms^{-1}b$ )

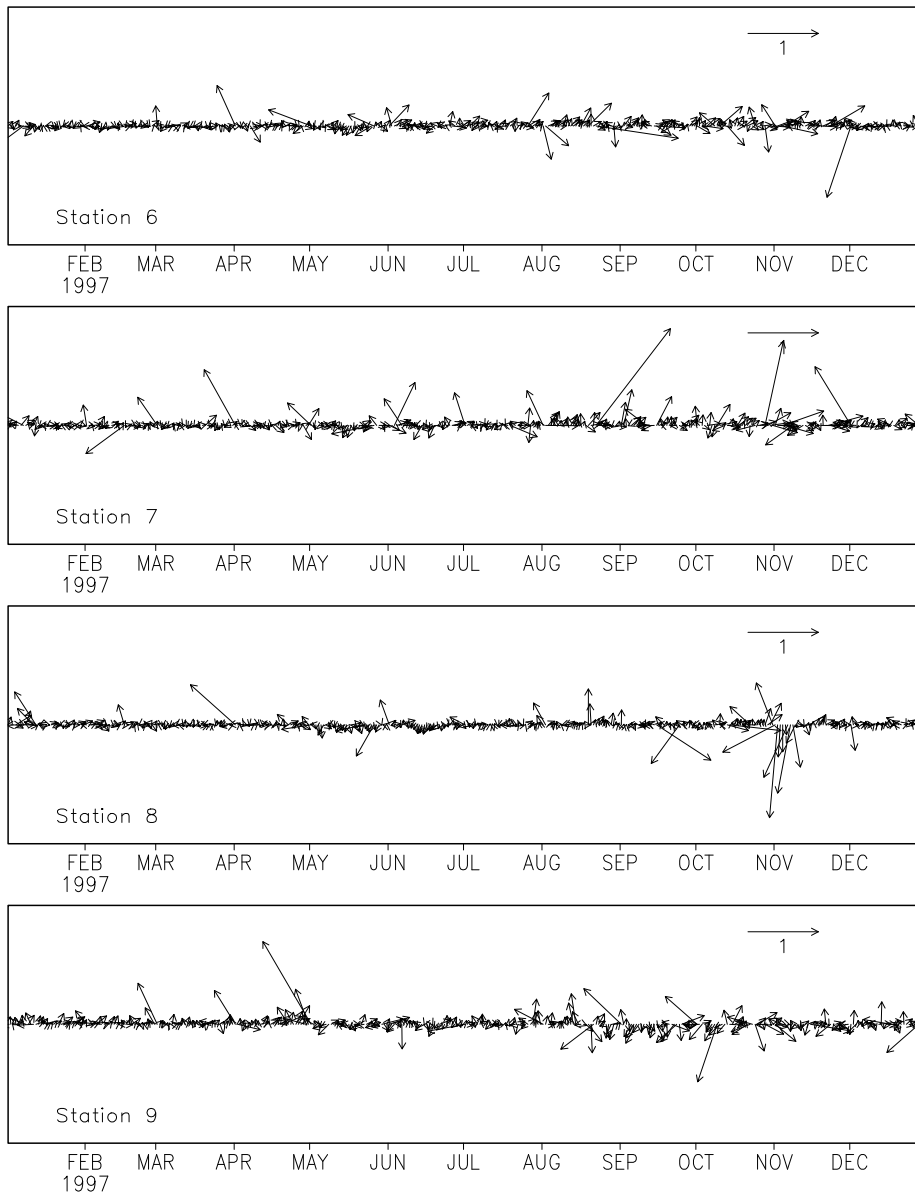


Figure 5.52: Same as Fig.5.51, but for stations 6 - 9.

ison with the difference between the simulation and the observations at station 1 (Fig.4.27) we can see that the south-north component of the velocity is simulated better in experiment S13, while the west-east component is simulated better in experiment S25. Overall, the wind simulated in the experiment S13 seems to be in better agreement with observations. At the station 8 both components of the wind seem to be better simulated in comparison to observations in experiment S13. On the other hand, at other stations there is no evident significant difference between experiments S13 and S25 which would improve the matching between

the model simulation and observations.

In Fig.5.51 and Fig.5.52 we can see the difference between the 10m wind in experiment S13 and in experiment S25. To show the details, the length of the unit vector is further reduced from  $2.5\text{ms}^{-1}$  in Fig.5.49 and Fig.5.50 to  $1\text{ms}^{-1}$ . Evidently, differences in simulated surface winds at coastal stations, resulting from the different sea surface temperature are very small and they do not significantly change the matching between the model simulation and the observations.

# Chapter 6

## Summary and conclusions

In this study a limited area coupled ocean-atmosphere model is applied in the Adriatic Sea in order to demonstrate its sensitivity to the coupling scheme. In Chapter 4 the seasonally averaged outputs of the oceanographic model are qualitatively validated, by comparing with climatological data, climatological analyses and measurements. The simulated surface temperature is further quantitatively compared with a large number of satellite observations.

The validation of the sea surface temperature simulated by the model shows that in all seasons the major features, and even several localized features of the sea surface temperature, are well simulated by the coupled model, both qualitatively and quantitatively. Furthermore the quantitative daily comparison of the sea surface temperature with satellite observations showed a high level of agreement between the simulated and the analysed fields during the whole year.

Simulated seasonal fields of surface currents are in qualitatively good agreement with climatological estimates and with drifter observations. At the depth of 100m simulated seasonal fields of the temperature and of the circulation show a good qualitative and quantitative correspondence with climatological analyses. Also, the seasonal variation of the surface elevation and the total transport are in very good agreement with climatological analyses and historical observations.

The most important parameters for the validation of the atmospheric model were surface heat fluxes, because they are the most significant influence on the ocean model simulation and moreover could be quantitatively compared with climatological estimates and calculations from other studies. The 7-year-averaged heat loss in the Adriatic Sea computed with the atmospheric model from the analysed sea surface temperature is  $21.7Wm^{-2}$ . This value is in very good agreement

with other climatological estimates and calculations. The comparison of single surface heat flux components shows a relatively larger difference with other studies, but always the mean values are close to or between values obtained in other studies. The comparison of the spatial variation of the seasonally averaged total heat flux, and of its components, shows that fields obtained with the application of the high resolution coupled ocean-atmosphere model contain a much higher spatial variability than other climatological calculations.

The comparison of the difference between the evaporation and precipitation calculated in this and in other studies shows that the mean evaporation is comparable to that calculated in other studies, while the mean precipitation is significantly lower. The reason is clear when one compares the spatial distribution of seasonal precipitation in this and other studies: in other studies the precipitation is calculated using observations at coastal stations, whereas the model shows that the precipitation is mostly concentrated along the coast and it is much smaller offshore, resulting in a smaller mean value.

Meteorological parameters are further compared with measurements at 9 stations positioned along the Adriatic coast. Quantitatively, the differences between the observed 2m temperatures and sea level pressures at coastal stations and those simulated by the coupled model, are comparable to those obtained by other limited-area atmospheric models in the same geographical area. Differences between simulated and observed 2m temperature values, which are mostly determined by local conditions, are relatively larger than differences in the sea level pressure which are mostly determined by lateral boundary conditions. It was not possible to directly compare the simulation accuracy for surface winds at coastal stations with results of other limited area models. However, it is evident that generally the model is able to simulate relatively well the wind direction and intensity, because the intensity of the differences between simulated and measured winds is generally much smaller than the measured wind intensity at coastal stations.

The temporal and the spatial variation of the most significant EOF modes obtained from oceanographic model outputs of 5 model experiments were used to assess the model sensitivity to the coupling scheme and on the horizontal resolution of the atmospheric model.

The most important oceanographic parameter for the assessment of the model sensitivity is the surface temperature, because it has a high spatial and temporal variability which is highly influenced by surface heat fluxes. Furthermore, for the

Adriatic Sea there are a large number of satellite measurements of the sea surface temperature available on a daily basis. The analysis of the temporal variation of the spatially averaged surface temperature, obtained in the experiment in which the ocean model is forced by fluxes from a general circulation model, shows a relatively large positive deviation of the simulated mean surface temperature that starts in early summer, and remains as a positive temperature drift at the end of the year. Furthermore, the analysis of the most important EOF modes shows that the main structures of the surface temperature field for this computation significantly deviate from the analysed structures.

The computation of surface fluxes using the higher resolution limited area atmospheric model leads to a somewhat better correspondence between the mean simulated values and the mean analysed values. There is a better spatial agreement between the simulation and the analysis, but again there is a positive surface temperature deviation. It starts in early summer, but it becomes negative and results in a negative drift by the end of the year. Also, for several periods there is still a relatively large spatial disagreement between the simulation and the analysis. Further increase of the horizontal resolution of the atmospheric model does not result in better correspondence between the simulation and the analysis.

On the other hand, the use of the limited-area coupled model significantly reduces the difference between the spatially averaged simulated and analysed surface temperature throughout the simulation period, and there is no evident drift of the simulated value towards the end of the year. The temporal and the spatial analysis of the most significant EOF modes shows that also spatial structures of the simulated surface temperatures are in good agreement with the analysis during the whole year. Again, the further increase of the horizontal resolution of the atmospheric model in the coupled mode did not result in a significant improvement of the simulation result.

The analysis of the most significant EOF modes of the surface currents simulated using the surface forcing from the global circulation model shows that in this experiment some major features observed in the surface flow were not simulated very well. On the other hand, the use of the higher resolution limited area model to calculate surface fluxes results in qualitatively good agreement of major simulated surface circulation features with observations, including a larger temporal variability of the surface flow. The use of an even higher horizontal resolution in the atmospheric model results in a further increase of the short-term variability of the surface flow.

The outputs of the coupled limited area model have spatial features similar to those obtained by the one-way surface forcing, but there is a higher stability of the surface circulation with a lower amplitude of the short-term variations. Again the use of the higher resolution atmospheric model leads to a higher short-term variation of the surface circulation.

The analysis of the total transport stream functions shows again that the increase of the horizontal resolution of the atmospheric model leads to an improved accuracy in the result including a permanent maintenance of the South Adriatic Gyre. However, the mean total transport increases during the year, and further increase of the horizontal resolution does not improve the result significantly. The use of the coupled model results in a more stable South Adriatic Gyre and there is no drift of the intensity of the mean total transport.

The analysis of the temperature at the depth of 100m shows that one-way surface forcing with the high resolution atmospheric model resulted in a relatively large disagreement between the simulation and the climatology, because, due to the enhanced vertical mixing, the negative surface temperature deviation penetrates down to the depth of 100m. On the other hand the outputs of the coupled model were in relatively good agreement with the climatology, because in this case both the surface fluxes and the vertical mixing were much more realistic.

One important finding of the study is that the use of the coupled model resulted in a qualitatively and quantitatively better simulation for all analysed oceanographic parameters in comparison to observations. As expected the largest and most significant improvement was in the simulation of the surface temperature, but the better simulation of the surface temperature resulted also in the more stable simulation and better agreement of other oceanographic parameters with observations. The only oceanographic parameters whose simulation was improved more by increasing resolution of the atmospheric model than by applying the coupled model, were surface currents. However, when coupling was applied to the high resolution atmospheric model, surface currents were even better simulated and more stable.

In this study, in order to better assess the sensitivity of the model purely to the coupling scheme, in both modes (coupled and uncoupled) there was no artificial flux correction of the simulated heat and momentum flux. The improvement of the simulation result, could possibly be obtained by some artificial correction method like the relaxation of the simulated surface temperature towards the climatology or by the assimilation of surface temperature observations. However,

data assimilation can also be applied to the coupled model. In that case it should give an even better result than the data assimilation with the uncoupled model, because of the better initial agreement between the simulation and the observations.

The sensitivity of the coupled model to the coupling scheme was further assessed for atmospheric parameters at 9 meteorological stations along the Adriatic coast. Changing the horizontal resolution of the atmospheric model generally influenced the results at coastal stations much more than changing the sea surface temperature from the analyses to the simulated values. However, it was difficult to assess in which experiment atmospheric parameters were better simulated, because while at most stations higher resolution slightly improved the simulation result, at some stations the coarser resolution simulations resulted in slightly better agreement with observations. It seems that complex local conditions, which may significantly influence meteorological parameters at coastal stations, were not resolved with a sufficient accuracy even by the highest resolution atmospheric model.

The only meteorological parameter whose simulation was changed relatively significantly by applying the bidirectional coupling in comparison to the increasing the horizontal resolution of the atmospheric model, was the 2m temperature recorded at several stations, but even this parameter was more influenced by the increasing the horizontal resolution of the atmospheric model than by the bidirectional coupling. One reason for the relatively small influence of the coupling scheme on the result is that during the whole simulation period sea surface temperature fields simulated in the coupled model are in relatively good agreement with analyses used in the one-way forcing experiment, resulting in small differences between the simulated air temperature in the two experiments. Another reason is that at coastal stations the 2m temperature is strongly influenced by the land surface temperature calculated by the soil and vegetation model which strongly depends on the horizontal resolution of the atmospheric model.

The study confirmed the ability of the coupled model, which includes the ISPRAMIX oceanographic model, to simulate oceanographic parameters in the Adriatic Sea with a high level of agreement with satellite observations during the whole simulation period even without the use of data assimilation. It was shown that coupling the atmospheric model with the oceanographic model improved the simulation of oceanographic parameters much more than increasing the horizontal resolution of the uncoupled atmospheric model. However, there was a less evident

influence of the coupling scheme on the simulation of atmospheric parameters at coastal meteorological stations.

The improved simulation accuracy of physical oceanographic parameters by bidirectional coupling should produce more accurate studies of the biological productivity and of eutrophication in the Adriatic Sea than ones which use one-way forcing by atmospheric fluxes obtained from global circulation models or from high resolution limited area atmospheric models (e.g. Zavaratelli et al. 2002, Horton et al. 1997).

In this study the coupled model is applied in the Adriatic Sea, which is characterized by high spatial and temporal variability of momentum and the heat fluxes due to the complex coastal topography and the relatively high variability of the weather on the synoptic scale. However, the method can be applied also to other coastal areas with complex meteorological conditions and with the complex topography at the neighbouring land surface.

## Acknowledgments

I would like to express my gratitude to Prof. Dr. Jürgen Sündermann for his help, guidance and support during my work on the thesis. I would like to thank Dr. K. Heinke Schlünzen for her instructions, support and help. I am thankful to Dr. Volker Reinhardt for providing atmospheric observations. The use of meteorological observations was made available for my study by the Deutsche Wetterdienst. I am especially grateful to Dr. Thomas Pohlmann for his full support, guidance and help. I have performed the work on my thesis at the Institute for Environment and Sustainability of the Joint Research Centre, Ispra. I have been supported by the Category 20 FP5 grant of the European Commission. I would like to especially thank Dr. Walter Eifler who introduced me to the Ph.D. study, Dr. Peter Schlittenhardt, Dr. Wolfram Schimpf and Dr. Steven Eisenreich for their encouragement and support during the work on my thesis. I am thankful to Dr. Robert Edwards and Dr. Judith Challis for their help.

# Bibliography

- Arakawa, A., and V.R. Lamb, 1977: Computational Design of the Basic Dynamical Processes of the UCLA General Circulation Model. *Meth. in Comp. Phys.*, **17**, 173-265.
- Arakawa, A., and V.R. Lamb, 1981: A potential enstrophy and energy conserving scheme for the shallow water equations. *Mon. Wea. Rev.*, **100**, 18-36
- Artegiani, A., D. Bregant, E. Paschini, N. Pinardi, F. Raicich, and A. Russo, 1997a: The Adriatic Sea general circulation, Part I, Air Sea interactions and water mass structure. *J. Phys. Oceanogr.* **27**, 1492-1514
- Artegiani, A., D. Bregant, E. Paschini, N. Pinardi, F. Raicich, and A. Russo, 1997b: The Adriatic Sea general circulation, Part II, Baroclinic circulation structure. *J. Phys. Oceanogr.* **27**, 1515-1532
- Backhaus, J.O., 1985: A three-dimensional model for the simulation of shelf sea dynamics. *Deutsche hydrographische Zeitschrift*, **38**, 165-187
- Bao, J.-W., J.M. Wilczak, J.-K. Choi, and L.H. Kantha, 2000: Numerical simulations of air-sea interaction under high wind conditions using a coupled model: A study of hurricane development. *Mon. Wea. Rev.*, **128**, 2190-2210
- Barthelet, P., L. Terray, and S. Valcke, 1998: Transient CO2 experiment using the ARPEGE/OPAICE non flux corrected coupled model. *Geophys. Res. Lett.*, **25**, 2277-2280.
- Beg-Paklar, G., V. Isakov, D. Koracin, V. Kourafalou, and M. Orlic, 2001: A case study of bora-driven flow and density changes on the Adriatic Shelf (January 1987) *Cont. Shelf Res.*, **21**, 1751-1783

- Bender, M.A., and I. Ginis, 2000: Real case simulations of hurricane-ocean interaction using a high resolution coupled model: Effects on hurricane intensity. *Mon. Wea. Rev.*, **128**, 917-946
- Betts, A.K., 1986: A new convective adjustment scheme. Part I: Observational and theoretical basis. *Quart. J. Roy. Meteor. Soc.* **112**, 1306-1335
- Bergamasco, A., and M. Gacic, 1996: Baroclinic response of the Adriatic Sea to an episode of Bora wind, *J. Phys. Oceanogr.*, **26**, 1354-1369
- Bone, M., 1993: Development of a non-linear levels model application to Bora-driven circulation on the Adriatic shelf. *Estuarine Coastal Shelf Sci.* **37**, 475-496
- Blackadar, A.K., 1962: The vertical distribution of wind and turbulent exchange in a neutral atmosphere. *J. Geophys. Res.*, **67**, 3095-3101.
- Boville, B.A., and P.R. Gent, 1998: The NCAR Climate Systems Model, Version One. *J. Climate*, **11**, 1115-1130.
- Brasseur, P., J.M. Beckers, J.M. Brankart, and R. Schoenauen, 1996: Seasonal temperature and salinity fields in the Mediterranean Sea: Climatological analyses of a historical data set. *Deep Sea Res.*, **43(2)**, 159-192
- Bratseth, A.M., 1986: Statistical interpolation by means of successive corrections. *Tellus*, **38A**, 439-447
- Buljan, M., and M. Zore-Armanda, 1976: Oceanographical properties of the Adriatic Sea. *Oceanogr. Mar. Biol. Ann. Rev.*, **14**, 11-98
- Businger, J. A., J. C. Wyngaard, Y. Izumi, and E. F. Bradley, 1971: Flux-profile relationships in the atmospheric surface layer. *J. Atmos. Sci.*, **28**, 181-189.
- Castellari S., N. Pinardi, and K. Leaman, 1998: A model study of air-sea interactions in the Mediterranean area. *J. Mar. Sys.* **18**, 89-114
- Charnock, H., 1955: Wind stress on a water surface. *Quart. J. Roy. Meteor. Soc.*, **81**, 639-640.
- Chen, F., Z. Janjic, and K. Mitchell, 1997: Impact of atmospheric-surface layer parameterizations in the new land-surface scheme of the NCEP mesoscale Eta numerical model. *Boundary-Layer Meteorol.* **85**, 391-421

- Christensen, J.H., B. Machenhauer, R.G. Jones, C. Schär, P.M. Ruti, M. Castro, and G. Visconti, 1997: Validation of present-day regional climate simulations over Europe: LAM simulations with observed boundary conditions. *Climate Dynamics* **13**, 489-506
- Demirov E., W. Eifler, M. Ouberdous, and N. Hibma, 1998: ISPRAMIX - a three dimensional free surface model for coastal ocean simulations and satellite data assimilation on parallel computers. *JRC report. EUR 19129 EN*.
- Demirov E., W. Eifler, and M. Ouberdous, 1998: ISPRAMIX - a three dimensional free surface model for coastal ocean simulations and satellite data assimilation on parallel computers. Part III. Nested grid approach for coastal modeling. Case study - Simulation of seasonal and mesoscale variability of Northwest African coastal upwelling. *JRC report. EUR 18129 EN*
- Devos, J.J, 1997: Atmosphere-ocean forcing with ECMWF data: Seafflux2 algorithms. *JRC Technical Note. No. I.97.46*
- Dobricic, S., W. Eifler, and E. Demirov, 1998: Coupled limited area ocean-atmosphere model for coastal zone studies: Model development and application to Adriatic. *JRC report. EUR 18140 EN*
- EEA, 1999: State and pressure of the marine and coastal Mediterranean environment. *Environmental assessment report 5, European Environment Agency*.
- Eifler, W., 1993: A hypothesis on momentum and heat transfer near the sea-atmosphere interface and a related simple model. *J. Mar. Sys.*, **4**, 133-153
- Eifler, W., T. Kupusovic, and W. Schrimpf, 1991: Numerical verification and exercises with different models for simulating sea circulation pattern: The vertical diffusion of momentum in forced barotropic sea. *CEC Environment and Quality of Life Report, EUR 13370 EN*.
- Eifler, W., and W. Schrimpf, 1992: ISPRAMIX, a hydrodynamic program for computing regional sea circulation patterns and transfer processes *CEC Report, EUR 14856 EN*.
- Fairall, C.W., E.F. Bradley, D.P. Rogers, J.B. Edson, and G.S. Young, 1996: Bulk parameterization of air-sea fluxes for TOGA COARE. *J. Geophys. Res.*, **101**, 3747-3764

- Gadd, A.J., 1978: A split-explicit scheme for numerical weather prediction. *Quart. J. Roy. Meteor. Soc.* **104**, 569-582
- Gacic, M., S. Marullo, R. Santoleri, and A. Bergamasco, 1997: Analysis of the seasonal and interannual variability of the sea surface temperature field in the Adriatic Sea from AVHRR data (1984-1992). *J. Geophys. Res.* **102**, 22937-22946
- Hodur, R., 1997: The Naval Research Laboratory Coupled Ocean/Atmosphere Mesoscale Prediction System (COAMPS). *Mon. Wea. Rev.*, **125**, 1414-1430
- Horton, C., M. Clifford, and J. Schmitz, 1997: A real-time oceanographic now-cast/forecast system for the Mediterranean Sea. *J. Geophys. Res.*, **102**, 25123-25156
- Janjic, Z.I., 1994: The step mountain eta coordinate model: Further developments of the convection, viscous sublayer and turbulence closure schemes. *Mon. Wea. Rev.* **122**, 927-945
- Killworth, P.D., D.A. Smeed, and A.G. Nurser, 2000: The effects on ocean models of relaxation toward observations at the surface. *J. Phys. Oceanogr.*, **30**, 160-175
- Kolmogorov, A., 1942: Equations of turbulent motion of an incompressible fluid. *Izv. Akad. Nauk. SSSR, Seria fizicheskaya*, (English translation: Imperial College, Mech. Eng. Dep. Rept. ON/6) 5: 56-58
- Kourafalou, V.H., 1999: Process studies on the Po river plume, *J. Geophys. Res.*, **104**, 29963-29985
- Kuzmic, M., 1991: Exploring the effects of Bura over the northern Adriatic: CZCS imagery and a mathematical model prediction. *Int. J. Remote Sens.*, **12**, 207-214
- Lacis, A.A., and J.E. Hansen, 1974: A parameterization for the absorption of solar radiation in the Earth's atmosphere. *J. Atmos. Sci.*, **31**, 118-133
- Laprise, R., 1992: The Euler equations of motion with hydrostatic pressure as an independent variable. *Mon. Wea. Rev.* **120**, 197-207

- Leonard, B.P., 1979: A stable and accurate convective modeling procedure based on quadratic upstream interpolation. *Comp. Methods Appl. Mech. Engr.*, **19**, 58-98
- Lionello, P., and P. Malguzzi, 1997: Coupled atmosphere-wave-ocean prediction in the Mediterranean Sea. INM/WMO International Symposium on Cyclones and Hazardous Weather in the Mediterranean, Palma de Mallorca, 1997, Spain, 779-784
- Liu, W.T., K.B. Katsaros, and J.A. Businger, 1979: Bulk parameterization of air-sea exchanges of heat and water vapor including the molecular constraints at the interface. *J. Atmos. Sci.* **36**, 1722-1735
- Lobocki, L., 1993: A procedure for the derivation of surface layer bulk relationships from simplified second order closure models. *J. Appl. Meteorol.* **32**, 126-138
- Maggiore A., M. Zavatarelli, M.G. Angelucci, and N. Pinardi, 1998: Surface heat and water fluxes in the Adriatic Sea: Seasonal and interannual variability. *Phys. Chem. Earth* **23**, 561-567
- Mahrt, L., and H.L. Pan, 1993: A two layer model of soil hydrology. *Boundary-Layer Meteorol.* **29**, 1-20
- Malanotte-Rizzoli, P., and A. Bergamasco, 1983: The dynamics of the coastal region of the northern Adriatic Sea. *J. Phys. Oceanogr.*, **13**, 1105-1130
- Manabe, S., R.J. Stouffer, M.J. Spelman, and K. Bryan, 1991: Transient responses of a coupled ocean-atmosphere model to gradual changes of atmospheric CO<sub>2</sub>. Part I: Annual Mean Response. *J. Climate*, **4**, 785-818
- May, P.W., 1986: A brief explanation of Mediterranean heat and momentum flux calculations. *NORDA Code 322, Nav. Oceanogr. and Atmos. Res. Lab., Stennis Space Cent., Miss.*, 5pp.
- Mellor, G.L., and T. Yamada, 1982: Development of a turbulence closure model for geophysical fluid problems. *Rev. Geophys. Space Phys.* **20**, 851-875
- Mesinger, F., 1984: A blocking technique for representation of mountains in atmospheric models. *Rev. Meteor. Aeronaut.* **44**, 195-202

- Nihoul, J.C.J., 1986: Three dimensional mathematical model of the marine environment - Application to the Adriatic Sea. *Final report Vol 1., CEC Contract 2831-85-11 PC ISPB*
- Nitz, T., 1998: Untersucung der Sensitivität eines wattenauflösdnen Modells bezüglich der iterativen Kopplung mit einem mesoskaligen meteorologischen Modell für den Bereich der Deutschen Bucht. *PhD thesis, Zentrum für Meeres und Klimaforschung der Universität Hamburg*, 119pp.
- Oberhuber, J.M., 1988: The budgets of heat, buoyancy and turbulent kinetic energy at the surface of the global ocean: An atlas based on the COADS data set. *Max Planck Inst. Meteorol. Rep. 15*, 20pp.,Hamburg
- Orlic, M., M. Kuzmic, and Z. Pasaric, 1993: Response of the Adriatic Sea to the Bora and Scirocco forcing. *Cont. Shelf Res.*, **14**, 91-116
- Ovchinnikov, I.M., V.I. Zats, V.G. Krivosheia, and A.I. Udodov, 1985: Formation of deep Eastern Mediterranean waters in the Adriatic Sea. *Oceanology*, **25**, 704-707
- Pan, H.L., and L. Mahrt, 1987: Interaction between soil hydrology and boundary layer development. *Boundary-Layer Meteor.* **38**, 185-202
- Paulson, C.A., 1970: Mathematical representation of wind speed and temperature profiles in the unstable atmospheric surface layer. *J. Appl. Meteor.*, **9**, 857-861
- Poulain, P.M., 2001: Adriatic Sea surface circulation as derived from drifter data between 1990 and 1999. *J. Mar. Sys.*,**29**, 3-32
- Pollak, M.J., 1951: The sources of deep water of the Eastern Mediterranean Sea. *J. Mar. Res.*,**10**, 128-152
- Prandtl, L., 1945: Über ein neues Formelsystem für die ausgebildete Turbulenz. *Nachr. Akad. Wiss., Göttingen, Math.-Phys. Klasse*, 6
- Raicich, F., 1994: Note on flow rates of Adriatic rivers. *Tech. Rep. RF02/94*, 8pp, Istituto Talassografico Sperimentale Trieste, Italy
- Raicich, F., 1996: On the fresh water balance of the Adriatic Sea. *J. Mar. Sys.*,**9**, 305-319

- Reed, R.K, 1977: On estimating insolation over the ocean. *J. Phys. Oceanogr.*, **6**, 781-800
- Sausen, R., K. Barthel, and K. Hasselmann 1988: Coupled ocean-atmosphere models with flux adjustment. *Climate Dynamics*, **2**, 145-163.
- Schrimpf, W., W. Eifler, and T. Kupusovic, 1992: Barotropic simulation in the northern Adriatic during a Bura-wind episode by three different numerical models. in *Computer Methods in Water Resources II*, vol. **2**, *Computational Hydraulics and Hydrology*, edited by D. Ouzar et al., pp. 377-392, Comput. Mech., Billerica, Mass.
- Smith, S.D., 1988: Coefficients for sea surface wind stress, heat flux, and wind profiles as a function of wind speed and temperature. *J. Geophys. Res.*, **93**, 15467 - 15472.
- Smolarkiewicz, P.K., and W. W. Grabowski, 1990: The multidimensional positive definite advection transport algorithm: Nonoscillatory option, *J. Comput. Phys.*, **86**, 355-375
- Stephens, G.L., 1978: Radiation profiles in extended water clouds II: Parameterization schemes. *J. Atmos. Sci.*, **35**, 2123-2132
- UNESCO, 1981: Tenth report on oceanographic tables and standards. *UNESCO Technical Papers in Marine Sci., No. 36, UNESCO, Paris*
- Vintzileos, A., and R. Sadourny, 1997: A general interface between an atmospheric general circulation model and underlying ocean and land surface models: Delocalized physics Scheme. *Mon. Wea. Rev.*, **125**, 926-941
- Vested, H.J., P. Berg, and T. Uhrenholdt, 1996: Dense water formation in the northern Adriatic Sea. *J. Mar. Sys.*, **18**, 135-160
- Wilson, M.F., and A. Henderson-Sellers, 1985: Land cover and soils data sets for use in general circulation climate models. *J. Climatol.*, **5**, 119-143
- Zavaratelli, M., N. Pinardi, and A. Maggiore, 1999: Winter density compensation in the Northern Adriatic Sea. A numerical model process study. in *Ecosystem Research Report: The Adriatic Sea, EU Environ. Ser.*, **EUR-32**, 141-156

- Zavaratelli, M., J.W. Baretta, J.G. Baretta-Bekker, and N. Pinardi, 2001: The dynamics of the Adriatic Sea ecosystem: an idealised model study. *Deep-Sea Res. I*, **47**, 937-970
- Zavaratelli, M., N. Pinardi, V.H. Kourofalou, and A. Maggiore, 2002: Diagnostic and prognostic model studies of the Adriatic Sea general circulation: Seasonal variability. *J. Geophys. Res.*, **4**, 1-20
- Zhao, Q., and F.H. Carr, 1997: A prognostic cloud scheme for operational NWP models. *Mon. Wea. Rev.* **125**, 1931-1953
- Zore, M., 1956: On gradient currents in the Adriatic Sea. *Acta Adriatica* **8 (6)**, 1-38 (in Croatian, abstract in English)
- Zore-Armanda, M., 1969: Evaporation of the Adriatic Sea. *Hidrog. God.* **1968**, 47-56 (in Croatian, abstract in English)

# List of Figures

1.1	The bottom topography (depth in m) of the Adriatic Sea. . . . .	6
1.2	The topography surrounding the Adriatic. . . . .	7
1.3	Main features of the surface circulation. Northern, central and southern cyclonic gyres are labelled 1, 2 and 3. The Western Adriatic Current is labelled 4 and the South-eastern Adriatic Current is labelled 5. . . . .	9
2.1	The sketch of the model vertical coordinate. . . . .	16
2.2	The illustration of the turbulence parameterisation with the near-interface shape function (from Eifler and Schrimpf 1992). . . . .	19
2.3	The vertical $\eta$ coordinate . . . . .	22
2.4	The schematic representation of the coupling scheme between the oceanographic and the atmospheric model . . . . .	31
2.5	The splitting with time of the calculation of surface fluxes and sea surface temperature. . . . .	32
3.1	The horizontal grid of the ocean model. Grid points marked with dots are land points. . . . .	34
3.2	The estimated climatological inflow rate ( $m^3s^{-1}$ ) from major rivers in the Adriatic (after Raicich 1994). . . . .	36
3.3	Coarse resolution model land-sea mask (up) and topography (down) Land points are marked with dots, and the topography elevation is given in metres. . . . .	40
3.4	High resolution model land-sea mask (up) and topography (down) Land points are marked with dots, and the topography elevation is given in metres. . . . .	41
3.5	The horizontal grid of the T213 ECMWF model. Grid points marked with dots are land points. . . . .	43

4.1	Seasonal fields of temperature ( $^{\circ}C$ ) at 1m depth simulated by the high resolution coupled model. a) winter, b) spring, c) summer, d) autumn . . . . .	47
4.2	Seasonal fields of the difference between the surface temperature simulated by the high resolution coupled model and daily analyses obtained from satellite observations ( $^{\circ}C$ ). a) winter, b) spring, c) summer, d) autumn . . . . .	48
4.3	Seasonal velocity fields at the surface simulated by the high resolution coupled model ( $ms^{-1}$ ). a) winter, b) spring, c) summer, d) autumn . . . . .	50
4.4	Seasonal velocity fields at the depth of 5m simulated by the high resolution coupled model ( $ms^{-1}$ ). a) winter, b) spring, c) summer, d) autumn . . . . .	51
4.5	Seasonal sea surface elevation fields simulated by the high resolution coupled model ( $m$ ). a) winter, b) spring, c) summer, d) autumn . . . . .	52
4.6	Seasonal fields of climatological dynamic height anomalies ( $dyn\ mm$ ) relative to 30m depth (from Artegiani et al. 1997b). . . . .	53
4.7	Seasonal total transport stream function fields simulated by the high resolution coupled model ( $10^6m^3s^{-1}$ ). a) winter, b) spring, c) summer, d) autumn . . . . .	55
4.8	Seasonal averages of temperature fields at 100m depth simulated by the high resolution coupled model ( $^{\circ}C$ ). a) winter, b) spring, c) summer, d) autumn . . . . .	56
4.9	Seasonal averages of climatological temperature fields at 100m depth ( $^{\circ}C$ ) (from Artegiani et al. 1997b). . . . .	57
4.10	Seasonal averages of velocity fields at 100m depth simulated by the high resolution coupled model ( $ms^{-1}$ ). a) winter, b) spring, c) summer, d) autumn . . . . .	58
4.11	Seasonal averages of the total heat flux simulated by the high resolution coupled model ( $Wm^{-2}$ ). a) winter, b) spring, c) summer, d) autumn . . . . .	62
4.12	Seasonal averages of the short wave radiation simulated by the high resolution coupled model ( $Wm^{-2}$ ). a) winter, b) spring, c) summer, d) autumn . . . . .	63

4.13	Seasonal averages of the long wave radiation simulated by the high resolution coupled model ( $Wm^{-2}$ ). a) winter, b) spring, c) summer, d) autumn . . . . .	64
4.14	Seasonal averages of the sensible heat flux simulated by the high resolution coupled model ( $Wm^{-2}$ ). a) winter, b) spring, c) summer, d) autumn . . . . .	65
4.15	Seasonal averages of the latent heat flux simulated by the high resolution coupled model ( $Wm^{-2}$ ). a) winter, b) spring, c) summer, d) autumn . . . . .	66
4.16	The climatological total heat flux ( $Wm^{-2}$ ) for selected months calculated by May (1986) (from Artegiani et al. 1997b). . . . .	67
4.17	Seasonal averages of the climatological total heat flux ( $Wm^{-2}$ ) calculated by Maggiore et al. (1998) (from Zavaratelli et al. 2002). . . . .	68
4.18	Seasonal averaged wind velocity vectors 10m above the ground simulated by the high resolution coupled model ( $ms^{-1}$ ). a) winter, b) spring, c) summer, d) autumn . . . . .	70
4.19	Seasonal averaged wind velocity vectors 10m above the ground from ECMWF reanalyses ( $ms^{-1}$ ). a) winter, b) spring, c) summer, d) autumn . . . . .	71
4.20	Seasonal averages of the difference between the evaporation and the precipitation per unit surface ( $m^{-1}$ ) simulated by the high resolution coupled model ( $m^{-1}$ ). a) winter, b) spring, c) summer, d) autumn . . . . .	72
4.21	Seasonal averages of the climatological difference between the evaporation and the precipitation per unit surface ( $m^{-1}$ ) calculated by Maggiore et al. (1998) (from Zavaratelli et al. 2002). . . . .	73
4.22	Geographical position of coastal meteorological stations used for the evaluation of model outputs. Numbers represent following stations: 1 - Tivat, 2 - Trieste, 3 - Ronchi dei Legionari, 4 - Venezia Tesserà, 5 - Punta Marina, 6 - Rimini, 7 - Falconara, 8 - Pescara and 9 - Brindisi. . . . .	75
4.23	Difference between simulated and measured 2m temperature at coastal stations 1 - 5 ( $^{\circ}C$ ). . . . .	77
4.24	Same as Fig.4.23, but for stations 6 - 9. . . . .	78
4.25	Difference between simulated and measured sea level pressure at coastal stations 1 - 5 ( $mb$ ). . . . .	79

4.26	Same as Fig.4.25, but for stations 6 - 9. . . . .	80
4.27	Difference between simulated and measured wind at coastal stations 1 - 5 ( $ms^{-1}$ ). . . . .	81
4.28	Same as Fig.4.25, but for stations 6 - 9. . . . .	82
5.1	Experiment GCM: the mean difference and coefficients of the first four EOF modes of the difference between simulated and measured surface temperature ( $^{\circ}C$ ). . . . .	88
5.2	Experiment GCM: the first four EOF modes of the difference between simulated and measured surface temperature. . . . .	89
5.3	Same as Fig.5.1, but for experiment S25 . . . . .	90
5.4	Same as Fig.5.2, but for experiment S25 . . . . .	91
5.5	Same as Fig.5.1, but for experiment S13 . . . . .	92
5.6	Same as Fig.5.2, but for experiment S13 . . . . .	93
5.7	Same as Fig.5.1, but for experiment C25 . . . . .	94
5.8	Same as Fig.5.2, but for experiment C25 . . . . .	95
5.9	Same as Fig.5.1, but for experiment C13 . . . . .	96
5.10	Same as Fig.5.2, but for experiment C13 . . . . .	97
5.11	Experiment GCM: the spatial average and coefficients of first four EOF modes of the magnitude of surface velocity ( $ms^{-1}$ ). . . . .	100
5.12	Experiment GCM: the first four EOF modes of the magnitude of surface velocity ( $ms^{-1}$ ). . . . .	101
5.13	Same as Fig.5.11, but for experiment S25 . . . . .	102
5.14	Same as Fig.5.12, but for experiment S25 . . . . .	103
5.15	Same as Fig.5.11, but for experiment S13 . . . . .	104
5.16	Same as Fig.5.12, but for experiment S13 . . . . .	105
5.17	Same as Fig.5.11, but for experiment C25 . . . . .	106
5.18	Same as Fig.5.12, but for experiment C25 . . . . .	107
5.19	Same as Fig.5.11, but for experiment C13 . . . . .	108
5.20	Same as Fig.5.12, but for experiment C13 . . . . .	109
5.21	Experiment GCM: the spatial average and coefficients of first four EOF modes of the stream function ( $10^6m^3s^{-1}$ ). . . . .	112
5.22	Experiment GCM: the first four EOF modes of the stream function. . . . .	113
5.23	Same as Fig.5.21, but for experiment S25 . . . . .	114
5.24	Same as Fig.5.22, but for experiment S25 . . . . .	115
5.25	Same as Fig.5.21, but for experiment S13 . . . . .	116

5.26	Same as Fig.5.22, but for experiment S13 . . . . .	117
5.27	Same as Fig.5.21, but for experiment C25 . . . . .	118
5.28	Same as Fig.5.22, but for experiment C25 . . . . .	119
5.29	Same as Fig.5.21, but for experiment C13 . . . . .	120
5.30	Same as Fig.5.22, but for experiment C13 . . . . .	121
5.31	Experiment GCM: the spatial average and coefficients of first four EOF modes of the temperature at 100m depth ( $^{\circ}C$ ). . . . .	124
5.32	Experiment GCM: the first four EOF modes of the temperature at 100m depth. . . . .	125
5.33	Same as Fig.5.31, but for experiment S25 . . . . .	126
5.34	Same as Fig.5.32, but for experiment S25 . . . . .	127
5.35	Same as Fig.5.31, but for experiment S13 . . . . .	128
5.36	Same as Fig.5.32, but for experiment S13 . . . . .	129
5.37	Same as Fig.5.31, but for experiment C25 . . . . .	130
5.38	Same as Fig.5.32, but for experiment C25 . . . . .	131
5.39	Same as Fig.5.31, but for experiment C13 . . . . .	132
5.40	Same as Fig.5.32, but for experiment C13 . . . . .	133
5.41	Difference between 2m temperature simulated in experiment S13 and in experiment S25 at coastal stations 1 - 5 ( $^{\circ}C$ ) . . . . .	138
5.42	Same as Fig.5.41, but for stations 6 - 9. . . . .	139
5.43	Difference between 2m temperature simulated in experiment S13 and in experiment C13 at coastal stations 1 - 5 ( $^{\circ}C$ ) . . . . .	140
5.44	Same as Fig.5.43, but for stations 6 - 9. . . . .	141
5.45	Difference between sea level pressure simulated in experiment S13 and in experiment S25 at coastal stations 1 - 5 ( $mb$ ) . . . . .	142
5.46	Same as Fig.5.45, but for stations 6 - 9. . . . .	143
5.47	Difference between sea level pressure simulated in experiment S13 and in experiment C13 at coastal stations 1 - 5 ( $mb$ ) . . . . .	144
5.48	Same as Fig.5.47, but for stations 6 - 9. . . . .	145
5.49	Difference between 10m wind simulated in experiment S13 and in experiment S25 at coastal stations 1 - 5 ( $ms^{-1}$ ) . . . . .	146
5.50	Same as Fig.5.49, but for stations 6 - 9. . . . .	147
5.51	Difference between 10m wind simulated in experiment S13 and in experiment C13 at coastal stations 1 - 5 ( $ms^{-1}$ ) . . . . .	148
5.52	Same as Fig.5.51, but for stations 6 - 9. . . . .	149

# List of Tables

4.1	Yearly averages of all components of surface heat flux for the Adriatic simulated by the atmospheric model ( $Wm^{-2}$ ). The last column on the right gives the seven-year mean value for each heat flux component and the total mean flux simulated in the period 1991-1997. Spatially and temporary averaged precipitation and evaporation per unit surface, with their seven-year mean values, are given at the bottom of the table ( $m^{-1}$ ). . . . .	60
4.2	Climatological estimates and calculations of the spatially and temporary averaged heat flux components ( $Wm^{-2}$ ), evaporation and precipitation per unit surface ( $m^{-1}$ ) in the Adriatic from other studies. . . . .	61
5.1	Differences between experiments. . . . .	85